New Techniques in Astronomical Spectroscopy for 8-M Telescopes

David Lee

Department of Physics,
University of Durham,
August 1998.

A thesis submitted to the University of Durham in accordance with the regulations for admittance to the Degree of Doctor of Philosophy.

New Techniques in Astronomical Spectroscopy for 8-M Telescopes

David Lee

A thesis submitted for the degree of Doctor of Philosophy.
Department of Physics, University of Durham, 1998.

Abstract

The purpose of this thesis is to investigate new instrument technology to enhance the capabilities of 8-m telescopes.

This thesis first describes the theory, design, construction, and testing of an immersed grating. Immersed gratings can be used to provide R$\geq 10^4$ with a multi-object and/or integral field spectrograph on an 8-m telescope. Immersed gratings allow high resolution to be achieved whilst maintaining the required pupil size at a level similar to that on 4-m telescopes. This thesis describes laboratory tests which verify that immersed gratings provide high resolution. The throughput penalty in using an immersed grating is shown to be small with losses due to air-glass reflections ,which can be eliminated with antireflection coatings, and metal-dielectric losses. This work demonstrates that immersed gratings provide a good method to reach R=10^4 (and above) with a multi-aperture spectrograph on an 8-m telescope.

The second part of this thesis describes the construction of a microlens-fibre based integral field unit (IFU): the SMIRFS-IFU. This instrument provides a unique J and H-band integral field capability for use with the CGS4 spectrograph at UKIRT. The optical design, assembly, laboratory testing, and telescope commissioning of the SMIRFS-IFU are described. The microlens arrays for use with SMIRFS-IFU were tested in detail and found to provide excellent image quality but with some scattered light. The assembly of the SMIRFS-IFU was achieved with high precision. The overall performance of the SMIRFS-IFU was found to be high and close to theoretical expectations. This instrument demonstrates that the technology of microlenses linked to fibres does provide a means of constructing high performance (i.e. high throughput, high spatial and spectral resolution) IFUs. Integral field spectroscopy is even more important for 8-m telescopes to take advantage of their enormous light gathering power. The SMIRFS-IFU is an important upgrade to CGS4 to perform high spatial resolution integral field spectroscopy.

Preface

The work described in this thesis was undertaken by the author as a PPARC research student at the University of Durham, Department of Physics, under the supervision of Dr. Jeremy Allington-Smith during the period October 1994 to October 1997. No part of this thesis has been submitted for a degree at the University of Durham or at any other University.

The work presented in this thesis was carried out solely by the author with the exception of chapters 5 and 7. Dr. Robert Content was responsible for the optical design of the SMIRFS-IFU described in chapter 5 and his work is acknowledge in the text. Dr. Roger Haynes was responsible for some of the work described in chapter 7 and his work is also acknowledged in the text.

Some of the work presented in this thesis has appeared in the following publications:

D. Lee, R. Haynes, R. Content and J. R. Allington-Smith, "Characterisation of microlens arrays for use in integral field spectroscopy", Proc. SPIE 3355 (1998).

R. Haynes, R. Content, J. R. Allington-Smith and D. Lee, "TEIFU: a thousand element integral field unit for the WHT", Proc. SPIE 3355 (1998).

R. Haynes, R. Content, J. R. Allington-Smith and D. Lee, "SMIRFS-II: multiobject and integral field near-IR spectroscopy", Proc. SPIE 3354 (1998).

R. Haynes, R. Content, J. R. Allington-Smith and D. Lee, "TEIFU: a thousand element integral field unit for the WHT", in Fibre optics in Astronomy-III (1998).

R. Haynes, J. R. Allington-Smith, R. Content and D. Lee, "SMIRFS-II Multi-object and Integral Field Unit Spectroscopy at the UKIRT", in Fibre optics in Astronomy-III (1998).

R. L. Davies and *et al.*, "GMOS: the GEMINI Multiple Object Spectrographs", Proc. SPIE 2871 (1997).

J. R. Allington-Smith *et al.*, "The Gemini Multiobject Spectrographs", Proceedings of wide field spectroscopy, Kluwer (1996).

Acknowledgements

Initially I would like to thank the Department of Physics at the University of Durham for providing an excellent location in which to conduct research. I also acknowledge the Particle Physics and Astronomy Research Council for the receipt of a PPARC studentship.

I would like to thank Jeremy Allington-Smith for his excellent supervision during my PhD. Jeremy was always available for questions, provided lots of helpful advice, and was very good at reminding me what I was supposed to be doing. I would also like to thank George Dodsworth and John Webster for their expert help in producing mechanical drawings. I couldn't have done half the experiments without their help. I would also like to thank Ray Sharples and Roger Davies for their useful advice. Despite the fact that we never agreed on anything I would like to thank Robert Content for some excellent arguments and for passing on some of his valuable knowledge of optical design and testing.

I am grateful to my office mates; Paul Young, Nigel Andrews, and Andrew Vick for tolerating my complaints, for computing advice, and for installing Maelstrom! We had an excellent time in room 11. I'm not sure whether to thank Mark 'clanger' Chang or not, who insisted on dismantling my experiments and breaking equipment. However, I'm sure I got my revenge on a number of occasions. What are friends for if you can't borrow their optical equipment? Thanks also to Colin Dunlop, who can align a spatial filter faster than anybody, and Peter Doel for help with various experiments. Thank you to Scott Croom for his help with thesis preparation and also to Douglas Burke and the other members of the YTA.

I'd like to acknowledge the staff of the Department of Physics for their help during my PhD, particularly the staff of the mechanical workshops. I'd also like to thank my flat-mates in Durham; Gail Radcliffe, Matthew Slater, and Rene Rodgers for their support and advice over the years. Cheers to Jason Wilde for always being available for a beer. Above all I'd like to thank Dr. Roger Haynes, good friend and fellow instrument builder. The two of us made a great instrument building double act.

Finally I would like to thank the Anglo-Australian Observatory for waiting so patiently for me to write my PhD thesis and for the provision of excellent facilities.

Contents

Chapter 1

Introduction

Abstract

This chapter provides an introduction to the work presented in this PhD thesis. The motivation for the work presented in this thesis is to provide a high spectral resolution capability and an integral field spectroscopy capability for use with the Gemini multi-object spectrograph.

1.1 Introduction

To say this is the era of 8-m telescopes is a bit of an understatement. There are approximately ten 8-m telescope projects which are either completed, in the process of being commissioned, or under construction. The two Keck telescopes (10-m) have already been in operation for a few years (Nelson & Mast, 1986). The first VLT telescope (4×8-m) has had first light with Gemini North (2×8-m with another telescope in the Southern hemisphere) and Subaru (8.2-m) soon to follow. Other large telescope projects include: the Hobby-Everly telescope (9-m), the two Magellan telescopes (6.5-m), the converted Multi mirror telescope (MMT, 6.5-m), and the Large Binocular telescope (LBT, 2×8.4-m). There are also other large telescope projects, such as the Gran Telescopio Canarias (10-m), in the planning stage. In total these telescopes will increase the currently available collecting area by a factor of approximately five.

The new breed of telescopes are not just bigger: they are also better. Each telescope is optimised for a slightly different purpose but mostly there is a common theme: high image quality in order to take advantage of the best seeing conditions available. For instance

the median seeing at Mauna Kea is 0.4 arcseconds FWHM and ideally this should not be degraded by the telescope. They are expected to produce improved image quality through the use of high performance mirrors and active mirror figure control. The telescope itself is also to cause less degradation of the incoming wavefront due to effects such as dome seeing and mirror seeing. The Gemini telescope specification even predicts near diffraction limited performance in the K-band (and at longer wavelengths) via the use of adaptive optics (Robertson & Mountain, 1997). The Gemini adaptive optics system will also provide 0.1-0.2 arcsecond image quality at visible wavelengths. New telescopes are also expected to operate over a much larger range of wavelengths, from the atmospheric UltraViolet cut off to $\sim 30\mu$m in the case of Gemini. Some of the features and improvements in the design of the new 8-m telescopes are summarised as follows:

- Large apertures to provide increased collecting area,
- Lower emissivity in the infrared via the use of optimised coatings,
- Higher reflectivity via optimised coatings,
- Very high image quality specifications,
- Active correction of the primary mirror figure,
- Adaptive optics capability, via fast tip/tilt secondary mirrors, and higher order AO correction.
- Lower telescope enclosure and support structure seeing degradation
- Stable telescope environments.

Of course, a telescope is only as good as its instrumentation. Therefore the revolution in telescope building must be matched by a revolution in instrument building. To fully exploit the capabilities of the 8-m telescopes requires a new generation of instrumentation. As a direct consequence of the increase in telescope aperture this implies an increase in the size of instrumentation. Instruments for 8-m telescopes are therefore likely to be larger than an equivalent instrument on a 4-m telescope. There are some key technological advances that have led to the ability to build better instruments. Examples are: new glass processing

technology, new types of glass, new high performance broad-band antireflection coatings, powerful optical design software, and large area CCDs.

The key performance drivers for new instrumentation can be summarised as follows:

- The performance of the telescope must not be degraded by the instrument,
- High throughput over a broad wavelength range,
- High spatial resolution to take full advantage of telescope image quality,
- Low emissivity so as not to compromise performance of IR optimised telescope designs.

Instruments may also be expected to perform over broader wavelength ranges than before, i.e. $0.3 - 1.8\mu$m and provide a wider range of observing modes.

A revolution in observing techniques has also arrived. Many of the 8-m telescopes plan to devote a considerable amount of the telescope time to queue scheduling (Puxley & Boroson, 1997). This means the observation being performed is specifically chosen from a database of observations to best match current conditions. This technique provides the most efficient use of telescope time. However, queue scheduling also requires that the instruments should have fast reconfiguration times, typically a matter of minutes to change from one mode, or instrument, to another.

The instrumentation requirements for 8-m telescopes are then somewhat different to that for 4-m telescopes in that they are expected to provide higher performance with a broader range of capabilities. Each 8-m telescope has an initial instrument package which is chosen to best suit the needs of the observing community. The aim of the instrument package on a general purpose telescope is to provide a wide coverage of the parameter space of wavelength and resolution (the observational phase space). The ultimate aim is to fill the resolution-wavelength space so that every possible combination is catered for. This parameter space may also be thought of as a cube if spatial resolution is included. The initial instrument complement of many of the 8-m telescopes is quite similar. High priority instruments are: Multi-object imaging spectrographs (MOS) for use in the visible to near infrared region, thermal infrared spectrographs, high resolution spectrographs and infrared imaging. Other types of instrument, such as interferometric capability, are of lower priority.

The initial instrument capabilities for the Gemini telescopes are similar to the categories already described. The Gemini instrument package will be provided by the following instruments: an infrared imager (NIRI), and infrared spectrometer (NIRS), a high resolution optical spectrograph (HROS), and a visible-near infrared multi-object spectrograph (GMOS). The Astronomical instrumentation group at the University of Durham is part of a collaboration to build the two Gemini multi-object spectrographs, the other collaborators being the Dominion Astrophysical Observatory, Canada, and the Royal Observatory Edinburgh. One of Durham's responsibilities is the dispersion elements for GMOS. Durham has also produced a conceptual design for an integral field unit for use with GMOS. Research into high resolution dispersion technology and integral field unit capability is described in this PhD thesis.

Smaller telescopes should not be forgotten. Various new 2-m to 4-m class telescopes are also being completed or are still under construction. The TNG, SOAR, the LJMT and SLOAN, are examples. For smaller telescopes to stay competitive in the era of large telescopes they have to provide novel instrumentation techniques filling niche areas of astronomy that are not catered for with the initial instrument capability of 8-m telescopes. Smaller telescopes also have the important role of providing test beds for new instrument development for use with 8-m telescopes. Therefore future instruments for 4-m telescopes might be expected to be even more advanced than 8-m instrumentation due to their need to remain competitive and the prototyping role that 4-m instrumentation will provide for new techniques.

A good example of a niche area of astronomy being filled by smaller telescopes is wide field CCD imaging and wide field multi-object spectroscopy. Wide field astronomy takes advantage of the etendue (the product of collecting area and field of view) provided by smaller telescopes. A number of 4-m class telescopes are being provided with survey modes, an example being 2dF at the AAT (Taylor *et al.*, 1997).

The Astronomical instrumentation group in Durham is very active in developing new astronomical techniques and much of this work is for instrumentation to improve the observing capabilities of 4-m telescopes. Therefore much of the work presented in this thesis, which was motivated by the technological advancement needed for GMOS, is also directly relevant for use with existing instrumentation on 4-m telescopes, possibly as an upgrade to enhance the performance of existing instrumentation.

1.2 Overview of optical spectroscopy

It was briefly discussed in the previous section that instrumentation for the 8-m class telescopes generally falls into four main categories: infrared imaging, infrared spectroscopy, low-medium resolution optical-near infrared spectroscopy and high resolution optical spectroscopy. A suite of instruments of this type provides the best coverage of the parameter space of wavelength and resolution as is necessary to cater for a wide range of observing requirements. These instruments are also of the highest scientific priority. As this thesis is concerned with developments in optical spectroscopy some of the instrumentation techniques in this area will be considered in more detail.

1.2.1 Low resolution spectroscopy

Astronomical spectroscopy is generally categorized in three areas: low, medium and high resolution spectroscopy. Low resolution spectroscopy, with resolutions of order a few hundred, is generally the regime of survey type instruments which require large wavelength coverage with low dispersion. This also allows the faintest magnitude limits to be reached. The use of higher dispersions spreads the limited flux over too many pixels leading to low signal to noise.

The majority of low resolution spectrographs are based on the focal reducer (FR) concept, i.e. a collimator, a dispersion element, and a camera. A collimator and camera is employed to demagnify the focal plane of the telescope, typically at Cassegrain or Nasmyth, to a scale which is appropriate for correct detector sampling. Focal reducers can therefore provide a large field of view, typically $\sim 10' \times 10'$, for both imaging and spectroscopy. The use of a collimator and camera automatically produces a useful collimated space into which a dispersion system, filters, polarisers, or an Etalon can be inserted. Focal reducers therefore provide both an imaging and a spectroscopic capability. Systems of this type are too numerous to mention but LDSS at the AAT, LDSS-2 at the WHT (Allington-Smith *et al.*, 1994), MOS/SIS at CFHT (Fevre *et al.*, 1994) and EFOSC at the ESO 3.6m (Dekker *et al.*, 1988) are perhaps some of the better known examples. LDSS-2 provides a field of view of $\sim$ 12 arcminute diameter, a wavelength coverage of 350-750nm and resolving powers of up to $\sim 1,000$. Similar performance is offered by the other instruments of this type. A common feature of

focal reducer type spectrographs is the ability to simultaneously observe a large number of objects ($\sim$ 25), through individual slitlets, or multislits, situated at the telescope focal plane. This can provide an enormous multiplex advantage over single slit spectrographs. The use of imaging provides a natural way to determine the positions of the objects to be observed. The images are then used to design the multislit masks and spectra can then be taken using the spectroscopic mode. To achieve high throughput, dispersion is normally provided by the use of a grism, which usually have peak efficiencies higher than that of similar dispersion gratings. The use of grisms does however have the disadvantage that the central wavelength on the detector cannot be tuned by tilting, as is the case with a grating.

Focal reducer technology has been extended for use with 8-m telescopes. The low resolution imaging spectrometer (LRIS) on the Keck telescope (Oke *et al*, 1995) is the first instrument of this type for an 8-m telescope. LRIS provides resolving powers in the range 500 to 5,000 with a wavelength coverage of $0.31 - 1.1\mu$m with a double beam design providing separate red and blue arms. Dispersion is achieved with a grating in the red and a grism in the blue. Another example of this type of instrument is FORS, the FOcal Reducer/low-dispersion Spectrograph for use on the ESO VLT (Seifert *et al.*, 1997). FORS provides a field of view of $\sim 7' \times 7'$, wavelength coverage from $0.33 - 1.1\mu$m, an image scale of 0.2" per pixel and spectral resolutions of up to 3,000 with the use of grisms. The MOS capability is provided via the use of 19 individually movable pairs of slitlets.

In moving from 4-m class telescopes to 8-m class telescopes there have been some changes in the basic parameters of the low dispersion spectrograph. The first is the extended wavelength coverage that is required. Achieving a similar field of view on an F/15 8-m telescope to that on an F/15 4-m telescope requires the collimator optics to double in size. The diameter of the collimated beam also approximately doubles in size. This implies the use of larger more expensive optical components. Aberration control also becomes more difficult as the diameter of the lenses increases. Therefore instrumentation for an 8-m telescope represents a significant step forward in spectrograph design and manufacture.

1.2.2 Medium resolution spectroscopy

Medium resolution spectroscopy on 4-m telescopes is generally the regime of the 'classical longslit' spectrograph. Light from the telescope passes through a slit which defines the

entrance to the spectrograph. The slit length is generally of order one arcminute and the width is adjusted to match the seeing conditions. Light from the slit is then collimated either with refractive or reflective optics (reflective optics are more common). Reflective optics have the advantage of being achromatic. The collimated beam is dispersed with a diffraction grating providing resolutions in the range $\sim 1,000 - 20,000$. The diffracted beam is then brought to a focus on the detector. Examples of this type of instrument are ISIS on the WHT the RGO spectrograph on the AAT. Medium resolution spectrographs are often the most used spectroscopic facility used on a telescope.

Despite being common for use with 4-m telescopes, longslit spectrographs are considered less important for use with 8-m telescopes. A reason for this might be their inefficiency either in number of objects observed (multiplex gain), their field of view, or use of the detector area. Typically only one spectrum is recorded at a time on the detector which might be considered as an inefficient use of the detector. The main advantage of longslit spectroscopy is the accurate sky subtraction that can be achieved with the use of a longslit. The merits and problems with longslit spectroscopy are discussed later, with relevance to integral field spectroscopy, in section 4.2.1.

Advances in technology have allowed the capabilities of a medium resolution longslit spectrograph and low dispersion multi-object spectroscopy to be merged into the same instrument package. GMOS is a good example of this providing the full range of resolutions offered previously by low and medium resolution spectrographs. The preference now is for maximum use of telescope and instrument capability and maximum observing efficiency. This implies observing many objects at a time through multislit masks and hence the move away from traditional longslit spectroscopy. Of course it is straight forward to implement longslit spectroscopy with a multi-object system simply by installing a longslit mask instead of a multislit mask.

1.2.3 High resolution spectroscopy

High resolution spectrographs are somewhat similar to medium resolution spectrographs in that they have a single entrance slit and gratings are used as the dispersing element. Medium resolution spectrographs generally use diffraction gratings in low orders of diffraction leading to moderate dispersion and resolution. High resolution is obtained by using echelle gratings

which operate at high order numbers and high angles of incidence. The relationships between resolution and angle of incidence etc are discussed in more detail in section 2.2. Echelle spectrographs typically reach resolving powers in the range 10,000 - 100,000 with reasonable slit widths ($\sim$ 1 arcsecond).

The use of high orders causes overlap in wavelength at the detector. This is because wavelengths diffracted in the different orders such that $n_1\lambda_1 = n_2\lambda_2 = ... = n_i\lambda_i$ occur at the same position on the detector. This is avoided by the use of cross dispersion to separate the different orders and wavelengths. Cross dispersion can be provided with either gratings, grisms or prisms. A disadvantage of the use of cross dispersion is that it severely limits the available slit length, to typically only a few arcseconds, if spatial overlap between the cross dispersed orders is to be avoided at the detector. However, cross dispersed echelle spectroscopy does represent an efficient use of detector area as the whole detector is required to capture all of the cross dispersed orders.

For stability reasons (echelle spectrographs are big instruments) high resolution echelle spectrographs are generally located at Nasmyth or Coude focus. This helps to minimise flexure and allows the instrument to be larger than at Cassegrain focus. Examples of echelle spectrographs in use on 4-m telescopes are the UCL coude echelle spectrograph (UCLES) at the AAT (Ryan & Fish, 1995) and the ESO multi-mode instrument (EMMI) at the NTT (Dekker *et al.*, 1986).

Most 8-m class telescopes plan to have a high resolution optical spectrograph. The High resolution echelle spectrometer (HIRES) is already in use on the Keck-I telescope (Epps & Vogt, 1993) with UVES planned for the VLT and HROS for Gemini. A review of high resolution spectrographs for large telescopes can be found in Pilachowski *et al* (1995). Of course the problems associated with building a low resolution spectrograph for use with an 8-m telescope also apply to high resolution spectrographs, i.e. the need for high image quality, larger optics, bigger spectrographs etc.

1.2.4 Increasing resolution

The consequence of increased telescope aperture on the resolution of the spectrograph has not yet been discussed. It can be shown (Wynne, 1989) that the spectral resolution, R,

of an astronomical spectrograph is related to the telescope aperture, D_{tel}, via the following equation:

$$R = \frac{m\rho\lambda W}{D_{tel}\chi} \tag{1.1}$$

where χ is the angular width of the slit projected onto the sky, W is the illuminated width of the grating, m is the diffraction order, ρ is the grating ruling density and λ is the wavelength. For a fixed grating size (or fixed collimated beam size) equation 1.1 shows that the spectral resolution is inversely proportional to the telescope aperture. This means unless the size of the grating can be increased by a factor of approximately two, for a spectrograph on an 8-m telescope, then there will be a reduction in resolution compared with the same spectrograph on a 4-m telescope. Therefore not only do the collimator optics have to increase in size but the dispersion optics also have to increase in size. This is a technical difficulty due to the current limitations on the sizes of dispersing elements, as described in section 2.3.1. There is, however, another solution to maintaining high resolution whilst the collimated beam size remains at a size similar to that with a 4-m telescope: the use of immersed gratings. An immersed grating consists of a prism optically coupled to a grating such that diffractions occurs within the prism. An immersed echelle is planned for use with HROS (Radley *et al.*, 1994) and immersed gratings are proposed as a way of obtaining high resolution with GMOS. An investigation of the properties of immersed gratings, in particular their use on 8-m telescopes as a way of increasing resolution, forms the basis for the first part of this PhD thesis. The motivation is to provide a way of maintaining the resolution of a spectrograph on an 8-m telescope at the level currently obtained with spectrographs on 4-m telescopes. The aim of using an immersed grating is to provide high resolution within the context of a multi-object and/or integral field spectrograph. Other techniques which achieve high resolution, such as using a cross dispersed echelle, are not readily compatible with multi-aperture spectroscopy.

1.3 Scientific motivation for this work

The previous section described the problem that the spectral resolution of a spectrograph on an 8-m telescope is reduced compared with the equivalent spectrograph on a 4-m telescope. It is important that spectrographs on 8-m telescopes can also achieve high resolution. The

provision of R=10^4 on 8-m multi-aperture spectrographs therefore requires the use of immersed gratings. Other techniques of producing high resolution, such as crossed dispersed echelles, are not compatible with use on a multi-aperture spectrograph. The use of large telescopes produces large collimated beam sizes forcing large dispersion optics to be used unless immersion is used to maintain reasonable beam sizes but keep high resolution.

The high spatial resolution expected to be obtained by 8-m telescopes means many previously unresolved objects can be expected to show structure. Clearly it is beneficial if this structural information can be retained when obtaining a spectrum of the object. If the object is simply observed with a long slit spectrograph then spatial information across the slit is lost. It was also mentioned earlier that longslit observations do not represent a particularly efficient use of detector area as very few spectra can be obtained. Longslit spectroscopy is even less efficient if the object being observed is an extended object as most of the light will be lost to the slit jaws. This also applies in conditions of poor seeing. It seems then that a spectroscopic observing mode which retains spatial information and provides an extended field of view would be useful for a variety of observations.

Preservation of spatial information and extended field of view can, of course, can be provided with the use of an integral field spectrograph. Integral field spectroscopy (IFS) provides a technique of observing the spectrum of a small two dimensional region whilst maintaining spatial information. IFS also represents a much more efficient use of detector area as the whole detector can be packed with information. IFS is a relatively new technique in astronomical spectroscopy and many of the current designs of integral field system are not best suited for use on 8-m telescopes, i.e. they have low throughput, or are not well suited to obtain high spatial resolution. There is much interest in having IFS as a normal observing mode on many 8-m spectrographs. The optimum design and construction of an integral field system for use with an 8-m provides the basis for the second half of this PhD thesis.

Integral field spectroscopy is important for use with 8-m telescopes due to the ability to preserve spatial information and the high efficiency of this mode of operation. IFS maximises the amount of information that can be obtained in a single exposure by making the best use of the limited detector area. IFS is particularly attractive in the infrared on large telescopes as many spectral features in high redshift galaxies will be shifted into the infrared. Adaptive optics also provides better image quality in the infrared. Spatial information should be

kept as galaxies even at high redshift show spatial structure as seen in the Hubble deep field images. The use of slits loses most spatial information. The large light grasp of 8-m telescopes also means it is possible to divide the image of faint objects into smaller pieces whilst still retaining good signal to noise. The excellent image quality of 8-m telescopes also allows information to be extracted on smaller spatial scales than before.

The value of 8-m telescope time means that new techniques such as high performance IFS should be developed on 4-m telescopes. This provides state of the art instrumentation for 4-m telescopes helping to maintain their competitiveness in an era of 8-m telescopes. Development of technology on smaller telescopes ensures that the best possible instrumentation can be provided for use on 8-m telescopes. A good example of this is the development of the SMIRFS-IFU for use with UKIRT described in the second part of this thesis. This instrument already provides large performance gains with CGS4 and UKIRT. The valuable experience gained from building this instrument will allow even higher performance to be achieved with future IFU designs for 8-m telescopes such as the GMOS-IFU.

A dual mode instrument which provides multi-aperture and integral field spectroscopic capabilities is particularly attractive. Multi-aperture instruments are well suited for adaptation for use as integral field spectrographs. It is therefore an obvious step to combine both modes (which represent most efficient use of telescope time via multiplex advantage) into a single instrument. Extension of the wavelength range of the instrument into the near-infrared is also attractive due to the relative ease of modifying an uncooled visible spectrograph for use in the near-infrared.

1.4 The Gemini multiobject spectrographs

The beginning of this introduction briefly described the capabilities of the new generation of 8-m class telescopes and the need for instrumentation to take full advantage of these capabilities. An example of one of this 'new breed' of instruments is the Gemini multiobject spectrograph (GMOS). As this PhD is primarily concerned with research and development for GMOS this instrument will be considered in more detail.

Two Gemini multiobject spectrographs are being constructed to equip both Gemini telescopes with a visible imaging and low-medium resolution multi-object spectroscopy capa-

Field of view	$5.5 \times 5.5\text{arcmin}^2$
Spectral resolution	$\lambda/\Delta\lambda \leq 10,000$ (0.25 arcsec slit)
Wavelength range	$0.36 - 1.1\mu$m (design capability to 1.8μm)
Image scale	0.08 arcsec/pixel
Detector	$3 \times (4096 \times 2048)$ CCD mosaic with 15μm pixels
Fore-optics	Atmospheric dispersion corrector integrated with field corrector
Main modes	– Multiaperture spectroscopy via masks – Longslit spectroscopy via masks – Integral field (2-D) spectroscopy – Direct imaging

Table 1.1: Summary of the proposed capabilities of GMOS.

bility. An instrument of this type is a high priority for the Gemini telescopes as it is the only instrument that will provide a visible light imaging capability. A detailed description of the capabilities of GMOS can be found in Allington-Smith *et al* (1996) and Davies *et al* (1997). A summary of the capabilities of the instrument is listed in table 1.1, adapted from Allington-Smith *et al* (1996). GMOS is a focal reducer type spectrograph incorporating all refractive optics. A diagram of the GMOS optics can be seen in figure 1.1. GMOS is perhaps slightly unusual in that the dispersion element is a grating rather than a grism. This does provide GMOS with the capability to achieve higher resolution than that available with grisms. Gratings also have the advantage of being able to adjust the central wavelength that is imaged on the detector to suit the observation. The optics are designed to preserve the excellent image quality expected to produced by the Gemini telescopes. This implies a very tight image quality specification on the GMOS optics of 50% encircled energy within 0.09 arcsec.

There are some important things to note from the GMOS specification. The first is the fine image scale (0.08 arcseconds per pixel) required to correctly sample the excellent images that are expected to be produced by the Gemini telescopes. Imaging is achieved by means of a fold mirror inserted in the collimated space instead of the grating. Also of note is the requirement to reach a spectral resolution of 10,000. There are a large number of scientific projects that benefit from high resolution as summarised in section 1.5. The main modes are imaging,

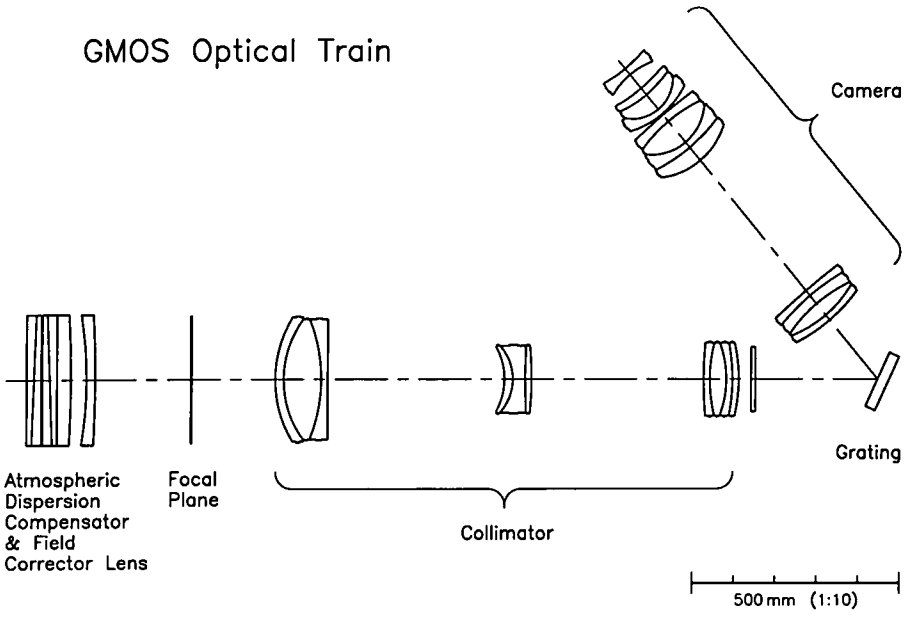

Figure 1.1: Diagram of the GMOS optical configuration.

longslit spectroscopy and multiaperture spectroscopy. Interchange between multiaperture masks and longslits is achieved by means of a mask changing mechanism situated near the telescope focus. The instrument should be capable of changing between observing modes quickly to match the current observing conditions. The requirement for an integral field spectroscopic capability, provided as one of the main observing modes of GMOS, should be noted. Of course the integral field spectroscopy capability should have the same high performance as the rest of the instrument, i.e. high throughput and high spatial resolution.

GMOS has also been designed with the intention of being used in the J and H-bands via the use of an infrared detector. This provides a very useful extension to the redshift range that the instrument can observe well known spectral lines of galaxies (wavelength range 3727-5007Å). Observations in the H-band allows galaxies up to about z=2 to be observed. Limiting the wavelength range to the H-band avoids the need for a complicated cooled instrument. It is therefore easier to implement a MOS mode in the J and H-bands.

The provision of a high resolution dispersing element for GMOS and an integral field unit are non-trivial issues. Much research and development is needed to find the best solution to both of these problems. The study of these two areas of increasing spectrograph performance forms the basis of the work presented in this PhD.

1.5 Key scientific motivations

Of course the type of instrument required for use with a telescope is ultimately determined by the science to be performed with that instrument. This section briefly describes the scientific programs that motivate the need to equip GMOS with a high resolution and integral field spectroscopic capability.

1.5.1 Medium-High resolution spectroscopy

The resolution of a spectrograph determines its ability to do two things: to detect small changes in wavelength, and the smallest difference in wavelength that still allows two separate spectral lines to be resolved. Some astronomical studies, such as studies of the interstellar medium, require high resolution to be able to accurately measure emission lines that are only separated by a very small difference in wavelength, and to measure the velocity width of the lines. The use of high resolution in studies of radial velocity is different. Here the ability to separate different wavelengths is less important and what is needed is the ability to measure a shift in the position of the spectrum caused by the doppler shift of the object. It is possible to measure a velocity to approximately 1/30th of a resolution element. A resolution of 10,000 therefore implies a radial velocity of 1kms^{-1} can be measured. In a review of the resolution needed for astronomical projects requiring radial velocity information, Suntzeff (1995) concludes R=10,000 is sufficient for most radial velocity studies. A resolution of up to approximately 10,000 is then very useful for most radial velocity work.

An example of a scientific project that will benefit from a resolution of 10,000 is the measurement of dark matter in low mass galactic systems. High precision radial velocity measurements of samples of giant stars in the Ursa Minor dwarf spheroidal galaxy imply a velocity dispersion of $7.5 \pm 1\text{kms}^{-1}$. A velocity dispersion such as this implies the gravitational potential is dominated by dark matter (Hargreaves *et al.*, 1994). These measurements were obtained with the ISIS longslit spectrograph at a resolution of $\sim 12,000$ to achieve a velocity precision of $\pm 2 - 3\text{kms}^{-1}$. GMOS will be able to observe fainter objects. Lower luminosity stars are more likely to be representative of the underlying stellar population and less prone to systematic atmospheric effects which could increase the velocity dispersion. The ability of GMOS to observe over a large area allows maps of the velocity dispersion to be obtained

as a function of radius. The large multiplex gain offered by GMOS means that the velocity distribution in dwarf spheroidal galaxies within the local group can be characterized in the equivalent of a single night. Grating improvements for GMOS were identified as a high priority upgrade by the first Gemini instrumentation workshop (Gillet *et al*, 1997) such that this type of observation could be performed.

1.5.2 Integral field spectroscopy

Examples of scientific projects include: the study of velocity fields, and star formation, in galaxies studied by the Hubble Space Telescope and to obtain accurate Tully-Fisher distances, determination of the ionisation source in active galaxies by examining the spatial variation of emission line ratios.

IFS also offers the ability to measure physical conditions in ionised gas, the distribution of star formation activity, stellar populations and the internal kinematics of galaxies of various types. With the spatial resolution provided by GMOS these techniques can be applied to galaxies over significant look back times thereby tracing evolution. Tully-Fisher distance determinations should also be possible to moderate redshifts. To match a wide range of objects also implies that the integral field unit should have the ability to adjust the sampling interval in the field of view. The sampling should also complement the image scale offered by the HST WFPC-2 to allow the study of galaxies observed by HST. Of course, the large field of view of an IFS also provides an image slicing capability in poor seeing conditions.

An integral field spectroscopy capability is a high priority requirement for many spectrographs on 8-m telescopes. The J and H-bands are particularly important as they allow observations of well studied galaxy emission lines (i.e. 3727–5007Å) at high redshifts. Study of these spectral features allows redshifts to be determined up to approximately z=2. IFS also provides the benefit of retaining spatial information as these objects may well be resolved by the high spatial resolution of 8-m telescopes. Limiting the use of the instrument to the J and H-bands avoids the need for cooling.

1.6 Structure of thesis

The motivation for the work in this PhD then is to provide GMOS with the capability of high spectral resolution and an integral field spectroscopy observing mode.

1.6.1 Immersed gratings

The work on providing high spectral resolution with GMOS is described first. Initial investigation in this area by Dr. Jeremy Allington-Smith (the GMOS deputy instrument scientist) concluded that the use of immersed gratings provides a suitable way of increasing the spectral resolution of GMOS. The first part of this thesis continues the investigation of the properties of immersed gratings as a way of achieving high resolution. The work on immersed gratings is organized as follows:

Chapter 2: The main purpose of the work presented in this chapter is to verify the theory of immersed gratings. The chapter begins by reviewing the theory of spectrograph performance and describes the factors that limit the performance. The various methods by which increased spectral resolution can be obtained, in particular for GMOS, are then reviewed. Immersed gratings are then investigated in more detail. Various publications relating to immersed gratings are reviewed leading to the conclusion that an experimental investigation of the properties of immersed gratings is essential to fully understand their properties.

The first step in the experimental investigation is a full derivation of the theory of immersed gratings. An experiment can then be built to test an immersed grating for comparison with the theory. The main performance parameters to measure are the resolution, dispersion, and angles of diffraction of the immersed grating. This chapter describes the construction of a small prototype immersed grating and the necessary apparatus to test it. The ultimate aim is to prove that immersed gratings can indeed provide high resolution.

Chapter 3: The purpose of the work in this chapter is to accurately measure the efficiency of an immersed grating in comparison with a non-immersed grating. This work is motivated by the current lack of understanding, particularly in the literature, of the

change in efficiency which occurs when a diffraction grating is immersed. The main aim, of course, is to determine if the efficiency of an immersed grating is lower or higher than an un-immersed grating, and if so by how much. This chapter begins by explaining some basic predictions of immersed grating efficiency performance. The experiment to accurately measure efficiency is described. The results of the efficiency measurements are then presented. Finally the production of immersed grating ghosts is investigated to ensure that ghosts do not present a problem.

1.6.2 Integral field spectroscopy

The second part of this PhD addresses the problem of providing an integral field capability for use with GMOS. Initial investigations of this problem led to the astronomical instrumentation group in Durham adopting the use of microlens-fibre based integral field unit technology. However, at that point, the technology had only been proposed and had yet to be prototyped. The second part of this thesis is concerned with the design, construction, and testing of a prototype IFU. The ultimate aim is to develop technology that can be used to construct an appropriate IFU for use with GMOS. The work on integral field spectroscopy is organized as follows:

Chapter 4: This chapter introduces the concept of integral field spectroscopy and reviews the various methods by which it can be performed. The advantages and disadvantages of each method are compared.

Chapter 5: This chapter begins by discussing the existing SMIRFS multi-object infrared fibre instrument. This instrument forms the backbone of the planned microlens-fibre based IFU prototype: the SMIRFS-IFU. The optical design of the SMIRFS-IFU (which was performed by Dr. Robert Content) is then described. This chapter concentrates on the various factors which limit the performance of an IFU, such as focal ratio degradation, and how they can be overcome. The design proposal for the GMOS-IFU is also presented.

Chapter 6: Perhaps the most important component in the construction of a microlens-fibre based IFU is the microlens array. Given that the SMIRFS-IFU was the first to be built

then there was a lot of work to be done to identify a suitable source of microlenses. The first part of this chapter is concerned with deciding what the appropriate characteristics of the microlens array should be. The main aim of the work in this chapter is to test microlens arrays, obtained from various manufacturers, and assess their suitability for use in integral field units. A considerable amount of experimental effort was invested in producing a method of accurately testing the microlenses. The experimental techniques are described in this chapter with the results of the microlens tests.

Chapter 7: This chapter describes the manufacturing techniques developed to construct the prototype SMIRFS-IFU. The aim of building the prototype is to learn about the capabilities (and limitations) of the techniques involved with the aim of improving future construction techniques. The construction techniques should also aim to provide the highest possible quality and performance. Most of the development work is in the construction of the integral field fibre bundle. Much of the design and construction was carried out by Dr. Roger Haynes. This chapter summarises that work and discusses the experimental techniques used to test the performance of the various components. The chapter also describes the procurement and testing of the high performance materials used in IFU construction. The main part of this chapter concerns accurately linking the fibre bundle with the microlens array. A number of optical devices were developed and constructed to allow this to be achieved.

Chapter 8: Following the successful construction of the SMIRFS-IFU it was commissioned at the United Kingdom Infrared telescope. This chapter describes the commissioning process. Observing with the prototype IFU provides valuable information about the performance of microlens-fibre based IFU technology on the telescope. It is difficult to simulate observing conditions in the laboratory environment. In particular the alignment of the instrument with the telescope and methods of providing adequate calibration were investigated. A number of optical 'on telescope' tests were also devised to thoroughly test the performance of the instrument. Indeed every possible trick was used to test the performance of the instrument. This chapter also describes observations of spectrophotometric standard stars which were made to accurately measure the throughput of the instrument. The measured efficiency is the compared with the predicted value to highlight problems in the manufacturing process which lead to

throughput loss.

Chapter 9: This chapter describes the scientific observations performed with the SMIRFS-IFU after the completion of the commissioning process. As IFS had never before been attempted with UKIRT and CGS4 some time had to be devoted to finding the optimal way of using the SMIRFS-IFU with the telescope, i.e. how to accurately point the telescope such that the object is within the field of view of the IFU. The ultimate purpose of any instrument is to do astronomy and this chapter also describes the results of observations of the active galaxy NGC7469 obtained during commissioning.

Chapter 10: The final chapter summarizes the work presented in this thesis. Conclusions are given and the prospects for future work also briefly described.

Chapter 2

Immersed gratings: theory and experiment

Abstract

The spectral resolution obtainable with an astronomical spectrograph on an 8-m telescope is theoretically predicted. It is shown that spectrograph constraints, in particular camera aperture, limit the highest spectral resolution obtainable with a spectrograph on an 8-m telescope to approximately half that with a 4-m telescope, for a constant collimated beam size. The use of immersed gratings is proposed as a method of achieving improvements in resolution without the need for major modifications to existing spectrograph designs. The use of immersed gratings can double the spectral resolution of a spectrograph and reduce the anamorphic beam factor. This is thought to make immersed gratings ideal for use on the Gemini multiobject spectrographs. A description of the properties of immersed gratings, with relevance to 8-m telescopes, is then given. The construction of a prototype immersed grating, and the subsequent experimental verification of the properties of immersed gratings, is also described.

2.1 Introduction

The introduction to this PhD described the scientific requirements of the Gemini multi-object spectrograph (GMOS). It was stressed that there is a significant need for GMOS to be able to reach a spectral resolution of $R = 10,000$. The various scientific projects that motivate the need for high resolution were also described. This chapter initially investigates the factors that limit the resolution of an astronomical spectrograph. The problem of achieving high resolution with GMOS is then described in more detail. Various methods by which spectral resolution can be increased are then investigated. It is found that the use

of *immersed gratings* (a grating optically coupled to a prism) provide the best method with which to improve spectral resolution. There have been numerous theoretical investigations of immersed gratings in the past which described their properties in great detail. However, there has been very little experimental investigation of their properties, or discussion of how to manufacture such a device. In particular it is important to know if immersed gratings possess any peculiar properties, that have been overlooked by the past theoretical investigations, that might limit their usefulness.

It was therefore decided to design and construct a prototype immersed grating. The construction phase should provide valuable information on how best to produce an immersed grating for use in an astronomical spectrograph, and highlight any possible manufacturing problems. The construction of a spectrograph is also described which can be used to test the performance of the immersed grating. The aim of the experiments described in this chapter are to verify the performance of immersed gratings given the considerable confusion that exists in the literature. The experimental investigation of the performance of the prototype immersed grating is described in the second half of this chapter.

2.2 Review of spectrograph performance theory

A schematic of a typical telescope and spectrograph configuration is shown in figure 2.1. The telescope forms an image of the sky on to a slit, of width s, which forms the entrance aperture to the spectrograph. The aperture of the telescope is denoted by D_{tel} and the focal length by f_{tel}. The diverging beam from the slit is then re-collimated by a collimator lens (usually a series of lens groups) of focal length f_{coll} and aperture D_{coll}. The spectrograph is matched to the telescope, such that the focal ratio of the telescope is equal to that of the collimator lens, to avoid any loss of light. A dispersion element is located in the collimated beam, usually at the pupil position. Commonly used dispersion systems are prisms, grisms and gratings. In the following discussion plane, classically-ruled, gratings are assumed, although the results are also relevant to grisms. The angle of incidence of the collimated beam with the grating surface is i and the angle of diffraction is θ. The diffracted beam is then imaged onto the surface of the detector, with the appropriate magnification, by means of a camera lens. Mechanical and optical constraints, i.e. to avoid vignetting, normally require that there

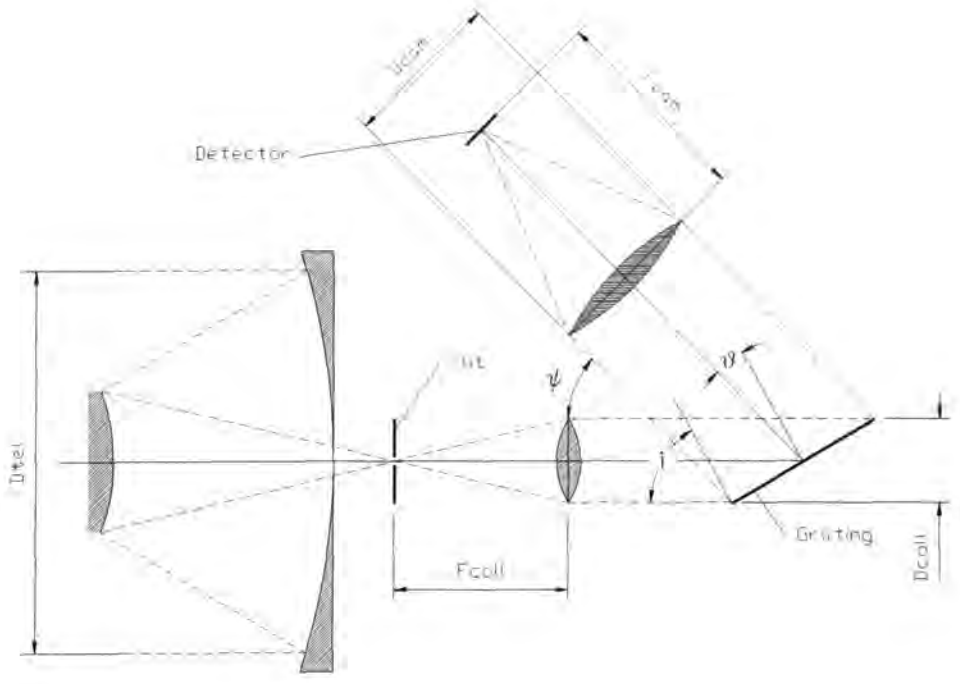

Figure 2.1: Schematic of the operation of a telescope and spectrograph.

is an angle, ψ, between the collimator and camera axes. The collimator to camera angle is related to the angles of incidence and diffraction via: $\psi = \theta - i$.

The angles of incidence and diffraction at the grating are related by the following equation, commonly known as the *grating equation*:

$$\frac{m\rho\lambda}{n_1} = \sin(i) + \sin(\theta) \tag{2.1}$$

where m is the order of diffraction, λ is the wavelength, ρ is the ruling density (number of grooves per metre) and n_1 is the refractive index of the incident medium. Normally a grating is used in air such that $n_1 = 1$. The grating equation can be differentiated to obtain the angular dispersion of the grating:

$$\left(\frac{d\lambda}{d\theta}\right) = \frac{n_1 \cos(\theta)}{m\rho} \tag{2.2}$$

The angular dispersion is then divided by the focal length of the camera to obtain the dispersion at the detector ($d\lambda/dx$), usually measured in nm/mm. The spectral resolution of the spectrograph is given by $R = \lambda/\Delta\lambda$ where $\Delta\lambda$ represents the projected width of the slit in wavelength units, i.e. $\Delta\lambda = \Delta x(d\lambda/dx)$. The projected slit width, Δx, can be calculated

from the magnification of the collimator/camera system together with the anamorphic effect of the grating as follows:

$$\Delta x = \Delta i \left(\frac{d\theta}{di}\right)\left(\frac{dx}{d\theta}\right) = \left(\frac{s}{f_{coll}}\right)\left(\frac{\cos(i)}{\cos(\theta)}\right) f_{cam}, \tag{2.3}$$

where Δi represents the angular width of the entrance slit given by s/f_{coll}. The resolution of the spectrograph can be found by combining equations 2.2 and 2.3 to give:

$$R = \left(\frac{\lambda}{\Delta\lambda}\right) = \lambda\left(\frac{dx}{d\lambda}\right)\frac{1}{\Delta x} = \frac{m\rho\lambda f_{coll}}{s\,\cos(i)} \tag{2.4}$$

This equation relates the spectral resolution to the parameters of the spectrograph. This equation shows that the highest resolution is obtained by using: high orders (as in echelles), high ruling densities, slow focal ratio collimators such that f_{coll} is large, narrow slit widths, or large angles of incidence such that $\cos(i)$ is small. Each one of these methods of increasing resolution will be discussed in more detail later. Equation 2.4 is more commonly written in terms of the telescope parameters, as in Wynne (1989), by substituting for f_{coll} and s, as follows:

$$R = \frac{m\rho\lambda W}{D_{tel}\chi} \tag{2.5}$$

where χ is the angular width of the slit projected onto the sky and W is the illuminated width of the grating. The slit width is usually determined by the seeing conditions during the observation and has to be large enough to avoid loss of light although not so large that resolution is seriously compromised. This equation is important as it highlights the difficulty with obtaining high resolution on large telescopes, that is the *resolution is inversely proportional to telescope aperture*, for fixed seeing and spectrograph parameters. If Littrow configuration is assumed, such that $m\rho\lambda = 2n_1\sin(i)$, then equation 2.5 becomes:

$$R = \frac{2mn_1 D_{coll}\tan(i)}{D_{tel}\chi} \tag{2.6}$$

as described in Dekker (1987). This equation can be thought of as expressing the resolution in terms of the optical path difference between the two edges of the grating (the optical path depth), $D_{coll}\tan(i)$, divided by the optical path difference across the telescope aperture, $D_{tel}\chi$. This implies that high resolution requires a grating with a large optical path depth, or a telescope with a small optical path depth i.e. a narrow slit width.

It is worth emphasising that equations 2.4, 2.5 and 2.6 are all exactly equivalent although each expresses the resolution in a slightly different way. Equation 2.4 is useful in the laboratory environment as the resolution is expressed in terms of the spectrograph parameters

only. Astronomers may prefer to use equation 2.5 which relates the resolution to the collimated beam size and the telescope parameters. The various different forms for expressing the resolution of a grating may be a cause for confusion.

2.2.1 GMOS resolution requirements

As an example of the difficulty of achieving high resolution with a telescope of large aperture the case of the Gemini multiobject spectrograph will be considered.

The scientific specification (GMOS, 1995) for GMOS is to reach a slit width resolving power product (SWRP) of 2,500 over the full design wavelength range of 0.4–1.1μm. This means that with a 0.25 arcsecond slit a spectral resolution of R=10,000 is required to meet the SWRP requirement. However, this limits observers who wish to obtain resolutions of up to 10,000 to using a narrow slit which, in non-optimal seeing conditions, will severely limit the flux. Ultimately this leads to a reduction in telescope efficiency, something that should be avoided with 8-m telescopes. A 0.5 arcsecond slit is better matched to the average seeing at Mauna Kea and should therefore ensure higher throughput. In the report of the first Gemini instrument workshop (Gillet *et al*, 1997) it was recommended that GMOS be upgraded to a spectral resolution of 25,000, i.e. a SWRP of order 5,000 via "grating improvements". This upgrade is regarded by the Gemini science committee with a high priority. The problem to be addressed then is: *how to reach spectral resolving powers of 10,000 with a 0.5 arcsecond slit width.* Of course an SWRP of 5,000 also implies a resolution of 25,000 with a 0.2 arcsecond slit width but, slit widths this small will require the use of adaptive optics. It should be noted that extending the resolution of GMOS to the region around 25,000 fills the resolution gap that exists between GMOS and the High Resolution optical spectrograph (HROS) which has a lowest resolution of $\sim 60,000$ with a 0.5 arcsecond slit.

High resolution is used in conjunction with the stability of GMOS provided by the active and passive flexure control, to provide accurate radial velocity measurements. R=10^4 allows radial velocity to be determined to a precision of 1-2kms^{-1}.

The GMOS instrument is assumed to have the following parameters[1]: a collimated beam size, D_{coll}, of 100mm, a collimator focal length of f_{coll} = 1600mm and a camera focal length

[1]This was the design at the time when this research was carried out, but the optical design has changed slightly since then.

of f_{cam} = 500mm. A scale drawing of the GMOS optical layout is shown in figure 1.1, (Davies *et al.*, 1997). The angle between the collimator and camera axes is 45°. A 0.5 arcsecond slit measures 310μm at the focal plane of the Gemini telescope and is mapped to $\sim$ 6.5 pixels by the magnification of the instrument. Note that although GMOS is used here as an example the following arguments can be applied to any spectrograph. Substituting these parameters into equation 2.4, assuming a wavelength of 850nm (the wavelength required to measure the Calcium triplet in studies of dwarf spheroidal galaxies), R=10^4 requires that $m\rho/\cos(i) > 2.3 \times 10^6$. This is equivalent to saying, using equation 2.6, an optical path difference between the two edges of the grating of 100mm is required to achieve R=10^4. An example of a configuration that fulfils this inequality is a 1300g/mm grating operating in first order at an angle of incidence of 59° producing a resolution of 11000. A disadvantage of operating the grating at large angles of incidence is that the beam size on the grating, given by $W = D_{coll}/\cos(i)$, can become very large and eventually exceed the manufactured size of available gratings. In this example W = 194mm which is still an acceptable length of grating. The losses produced by overfilling the grating may be acceptable in certain circumstances allowing modest increases in resolution to be obtained. Overfilling the grating leads to a loss of light but, surprisingly, the resolution increases. The explanation for this is overfilling the grating corresponds to viewing a smaller area of the telescope primary mirror, equivalent to using a smaller telescope, and hence there is no loss in resolution.

There is, however, another more serious disadvantage preventing the use of a grating in this configuration. The width of the diffracted beam, in the direction of dispersion, is broadened by the *anamorphic factor*, AF, of the grating. It can be seen in figure 2.1 that the diffracted beam is broadened on leaving the grating. The anamorphic expansion of the collimated beam is given by the following equation:

$$AF = \frac{D_{cam}}{D_{coll}} = \frac{\cos(\theta)}{\cos(i)} \tag{2.7}$$

The anamorphic effect of the grating causes the output beam to become elliptical in shape whereas the input beam has a circular cross section. For the above example the anamorphic factor is 1.88, this means the camera aperture has to be 188mm wide to accept the diffracted beam. The design of GMOS, as shown in figure 1.1, can only accommodate a maximum anamorphic factor of 1.4 causing a large fraction of the diffracted beam to be vignetted by the camera aperture. It is clear from the optical diagram of GMOS that a collimator to

camera angle of 45° allows very little space for a large camera aperture. The parameter space of ruling density, diffraction order and angle of incidence can be explored to find alternative solutions. For example: the ruling density of the grating can be reduced if higher grating orders are used, i.e. a 600 grooves per mm grating in second order. However this does not produce any decrease in the anamorphic factor. The use of high orders with long wavelengths often means no solution can be found which simultaneously satisfies the grating equation and the collimator to camera angle.

If the limiting AF is incorporated into the prediction for the maximum resolution obtainable with a 0.5 arcsecond slit then the result is a maximum spectral resolution of 5,182. This produces a SWRP of 2,591 which is much lower than the goal of 5,000. It is then the maximum beam dilation that is the severe limitation to the highest resolutions that can be achieved with this type of spectrograph configuration. Note that if the camera aperture can be enlarged to accommodate larger beam sizes then the limiting resolution can also be increased. This is difficult to achieve, however, as it would require modifications to the optical design. It should also be noted that obtaining suitable large astronomical gratings with high ruling densities is non-trivial. The maximum ruling densities available for standard ruled gratings are in the range 1,200-2,400 grooves/mm although they may not be available with a suitable size. The Milton-Roy catalogue shows the maximum size of high density ruled grating available is only 102mm square which is too small for most spectrograph designs.

It is clear then that achieving a slit width resolving power product of 5000 is non-trivial task using conventional grating technology. In summary the following factors contribute to limit the maximum obtainable resolution:

- The grating equation and $\psi = \theta - i$ cannot be satisfied for high ruling densities or long wavelengths,
- The required grating size becomes very large, large gratings are expensive and currently only available in widths up to 200 mm and light will be lost if smaller gratings are used,
- The anamorphic factor exceeds the limit set by the camera optics so that light is lost at the edges of the camera. It is the anamorphic factor that most seriously limits the highest obtainable resolution.

2.3 Methods of increasing resolution

The previous section described the limitations imposed on spectral resolution by the size and geometry of the spectrograph. This section discusses the various techniques by which the spectral resolution can be increased, with particular emphasis on increasing the resolution of spectrographs for use with 8-m telescopes, although the techniques described are applicable with telescopes of any aperture.

2.3.1 Increased grating size

It is clear from equation 2.5 that an increase in resolution is obtainable by increasing the illuminated width of the grating W. Alternatively, this can be thought of as increasing the focal length of the collimator, as in equation 2.4, thereby reducing the angle subtended by the slit. Increasing the width of the grating is also equivalent to increasing the optical path depth, equation 2.6. Achieving high resolution by means of larger echelles or gratings does not just increase the size of the echelle. The entire spectrograph optics also have to be scaled up to suit. This implies larger lenses or mirrors and the associated increase in cost, weight and complexity of providing mechanical support. There is also the problem maintaining flexure at an acceptable and controllable level. A spectrograph, such as ISIS, which obtains a resolution of $R = 10^4$ on a 4-m telescope would therefore have to be approximately doubled in size on an 8-m telescope to retain a resolution of $R = 10^4$.

This 'big is best' approach has been adopted for a number of medium–high resolution spectrograph projects for various telescopes. However, the maximum size of ruled gratings available is limited by the size of ruling engines used to manufacture them. Gratings with high ruling densities are also limited in size by diamond wear[2]. The upper limit to the size of ruled gratings is currently around 400mm. It is unlikely that larger ruling engines will be constructed due to: cost, inability to produce uniform coatings, and diamond wear (Hoose *et al.*, 1995). Large gratings must therefore be constructed by using a number of smaller gratings to form a mosaic.

The High resolution echelle spectrograph (HIRES) on the Keck 10-m telescope (Epps & Vogt,

[2]A specially shaped diamond tool is used to manufacture ruled gratings, see Hutley (1982).

1993) uses a mosaic of three R2 echelles[3] mounted simultaneously on a single granite backing substrate. The total size of the echelle mosaic is 31 × 122cm, as illustrated in Pilachowski (1995), illuminated with a 31cm diameter beam. The need for an enormous baseplate and accompanying mountings makes the entire assembly large and heavy. The individual grating mounts also have to be adjusted to maintain the alignment of the gratings. It is interesting that Keck has a segmented mirror and segmented gratings. Clearly this is a technique which is not best suited to the space and weight constraints of the Cassegrain focus and can only be adopted at Nasmyth, or a similar focal platform with suitable load bearing capabilities.

2.3.2 Increased angles of incidence

Increasing the spectral resolution by means of an increase in the illuminated length of grating can also be achieved by using the grating at larger angles of incidence. This is the technique adopted by some designs of echelle spectrograph where the angle of incidence has been increased from 63.5° to 80°, i.e. an R4 echelle is used instead of an R2 echelle. Whilst this may help to maintain the size of the spectrograph optics at a more manageable level it does require the use of large echelles.

This approach has been adopted for use with the VLT UV-Visual Echelle Spectrograph (UVES) instrument as described in Dekker & D'Odorico (1992). The beam size in UVES is 200mm and the large angle of incidence with an R4 requires the use of an echelle 800mm in length implying the use of an echelle mosaic. However, a different approach to that of HIRES has been adopted for mosaic production. UVES will use a mosaic of two echelles which have been replicated onto the same substrate effectively producing one large echelle with only a small gap between the replications. Even with replication the individual echelles are still large at 22 × 42cm. It is possible with this method to produce phased mosaics, i.e. there is no wavefront error between the separate replications. This technique also avoids the optical mounts required in the HIRES design and is therefore thought to require less maintenance. A prototype of this type of mosaic technology has already been constructed (Hoose *et al.*, 1995) for use on ESO's EMMI instrument. The results of astronomical tests are described in Dekker *et al.* (1994).

[3]R2 refers to the tangent of the blaze angle which in this case is 63.4°.

2.3.3 Increased ruling densities

Resolution can be increased by using gratings with high ruling densities, i.e. by increasing ρ in equation 2.4. However to satisfy the grating equation they have to operate with large angles of incidence which leads back to the problem of large anamorphic factors. With very high ruling densities, and long wavelengths, there may not even be a solution to the grating equation. However, high ruling density gratings may be useful in the blue spectral region $\lambda \sim 400$nm (Pasquini *et al.*, 1994).

Gratings with ruling densities greater than 1200g/mm are generally of the holographic type, i.e. the rulings are produced by a holographic recording process. Ruled gratings with high ruling densities are generally not available in the sizes necessary for astronomical instruments due to limitations of diamond wear. Holographic gratings are easier to produce with large sizes and high ruling densities and have the advantage of producing less ghosts and scattered light leading to higher spectral purity. The disadvantage of using holographic gratings is the difficulty in the production of a blazed facet, and hence high efficiency. This problem is worse for holographic gratings with low ruling densities as high ruling density gratings operate in a regime where only the first and zeroth diffraction orders propagate. As only two orders propagate, reasonable efficiency can be achieved as no light is lost to the other orders. The high resolution, 3000g/mm, holographic grating in use on EMMI (Pasquini *et al.*, 1994) provides a peak efficiency of $\sim 50\%$. It is often the lower efficiency of holographic gratings, in comparison with conventional blazed gratings, that makes them inadequate for use in astronomical applications.

2.3.4 Volume phase holographic gratings

It was mentioned earlier that the GSC had recommended the upgrade of GMOS resolution to 25,000. The same report also noted that: 'grating efficiency is a major limitation to GMOS throughput'. This implies that technologies which allow grating efficiency to be improved should also be investigated. A relatively recent development is that of *Volume Phase Holographic gratings* (VPH). Unlike conventional ruled gratings, diffraction with a VPH grating occurs in a thin layer of transmissive material with a modulated refractive index. This is Bragg diffraction and can produce high efficiency over a range of wavelengths

and diffraction orders (Barden *et al.*, 1998) by tilting the grating, i.e. the grating is tunable. Theoretical efficiency of 100% is claimed, with high ruling densities (up to 6000g/mm), and low dependance of efficiency with polarization. Published data in Barden *et al.* (1998) shows VPH gratings to have higher efficiency than equivalent ruled gratings.

The grating structure is holographically recorded in dichromated gelatin. The gelatin allows the interferometric fringes to be converted to a refractive index variation which produces the phase grating. VPH gratings can be used in both transmission and reflection via appropriate orientation of the fringe pattern with respect to the incoming beam. Holographic grating production is known for its ability to produce high ruling densities with large grating sizes both of which help to achieve high resolution.

The application of VPH grating technology to astronomical spectroscopy is still in the early stage of development. However, the potential advantages of high efficiency, large gratings, high ruling densities, and the ability to tune the grating clearly make this an area to be watched with keen interest. A VPH grating is planned for use with the upgraded version of LDSS at the AAT.

2.3.5 The GMOS solution

The 'big is best' approach then seems to be the preferred option for achieving high resolution with Nasmyth (or Coude) spectrographs on 8-m telescopes. The Gemini telescopes however, have the restriction that all instruments must be mounted at the Cassegrain focus. This produces various size and weight restrictions and introduces strict flexure tolerances. This clearly precludes the use of extremely large optics in Gemini instrumentation. The HIRES echelle would not even fit into the space envelope of a Gemini instrument!

The GMOS requirement is to increase resolution without any increase in the size of the grating or the spectrograph optics. It was described in section 2.2.1 that the limiting factor was mainly the large anamorphic factor produced by the use of a grating with a high ruling density at large angles of incidence. It was also limited by the inability to satisfy the grating equation with long wavelengths. A large optical path depth is required but without the use of a large grating. The solution then is to reduce the anamorphic factor and the size of grating, alter the grating equation so that it can be satisfied, and still have high resolution. All

this can be made possible by utilising the anamorphic properties and high refractive indices of prisms. The collimated beam passes through a suitably chosen prism which is optically coupled to the surface of the grating. This produces what is known as an *Immersed Grating* as illustrated in figure 2.2. The properties of these devices, in particular their application to GMOS, are discussed in detail in the remainder of this chapter.

It should be noted that the use of immersed gratings, as a means of obtaining higher resolution, is also being investigated for use in the Gemini High resolution optical spectrograph. HROS developments are discussed briefly in section 2.4.1.

2.4 Immersed grating review

The previous section described methods by which the resolution of a spectrograph, in particular GMOS, can be improved. Most techniques cannot be considered due to the limitations imposed by the spectrograph, therefore the use of immersed gratings is proposed as a solution, as also proposed for HROS. This section reviews some of the previous work on immersed gratings and their application to astronomy.

2.4.1 Immersed gratings for the visible

It has been known for some time that placing the grating in a medium of index n produces an increase in Resolution. Longhurst (1973, p270) states: "the resolving power is proportional to the index of the medium in which it is mounted", a Littrow configuration is assumed. Dekker (1987) explores this idea further in the context of an astronomical spectrograph. Dekker finds the relation that: "the resolving power of an astronomical spectrograph is equal to the depth of the grating divided by the depth of the incoming wavefront". This statement is expressed in equation 2.6. Immersing the grating within a high index material then provides a way of increasing the grating depth. Anamorphic immersion gratings, where the prism face is inclined at an angle to the incident beam, providing an even greater increase in resolution by allowing increased lengths of grating to be illuminated.

The possibility of using an immersed echelle was investigated by ESO (Dekker, 1987) for use with the ESO multi-mode instrument (EMMI) to provide increased resolution at red

wavelengths. Dekker proposed to use an anamorphic echelle in EMMI (Dekker *et al.*, 1986) to allow the 120mm collimated beam to illuminate the full length of a 408mm echelle, thus producing a large increase in grating depth. This idea was abandoned with an R4 echelle mosaic, in air, being used instead. The reasons for choosing an R4 echelle in preference to the immersed R2 echelle are unknown although they are possibly related to the lower efficiency obtained upon immersion. This decrease in efficiency was measured in the experiment described in Dekker (1992) .

A more detailed study of the properties of immersed gratings, in general, was carried out by Charles G. Wynne and is described in five publications (Wynne 1989, 1990a, 1990b, 1991, 1992). In the first paper (Wynne, 1989) Wynne disagrees with the concept that increased resolution is a direct consequence of immersion, as discussed in section 2.5. Instead Wynne concludes that an immersed grating is equivalent to a grating in air with a larger blaze angle. Confusion arises because Dekker gives the resolution as equation 2.6, in terms of grating depth and refractive index, whereas Wynne gives the resolution as equation 2.5, in terms of wavelength and illuminated grating width. In fact these two equations are equivalent as shown in section 2.2. It is true, however, that a gain in resolution can be achieved by using an immersed grating with the grating in air, i.e. there is an air space between the prism and the grating. The increase in resolution in this case arises from the anamorphic properties of the prism increasing the illuminated length of grating.

In the second paper (Wynne, 1990a) Wynne discusses the gains in spectrograph efficiency that can be achieved by using prisms with gratings to change the anamorphic factor of the dispersion system. This then leads to more efficient use of the available camera aperture with an increase in the prism angle reducing the beam dilation. Wynne (1990b) describes the use of immersed gratings to allow the grating equation to be satisfied with longer wavelengths and finer gratings, or higher orders, than is possible without immersion. Wynne (1991) proposes that immersed gratings can be used to double spectral resolution. Finally, Wynne (1992) discusses the possibility of using immersed gratings in tandem, i.e. achieving higher dispersion, and hence resolution, via using immersed gratings in series. In this way tandem immersed gratings can be used to achieve resolutions as high as those normally associated with echelles.

It is important to note that while the references cited so far describe the theoretical advan-

tages of immersed gratings none actually presented any experimental evidence, except for the measurement of efficiency in Dekker's work.

One of the few groups to be actively pursuing the use of immersion in an astronomical spectrograph is the Optical science laboratory in London. Immersion is the chosen approach for the Gemini High Resolution Optical Spectrograph (HROS), to allow high resolution to be achieved in the limited space available. HROS (Walker *et al.*, 1994) uses an immersed echelle to achieve high resolution whilst the beam diameter remains only a modest 160mm (half the size of that with HIRES). The gain in SWRP of the immersed echelle is 1.46 compared with the same echelle in air. A detailed description of the benefits of using an immersed echelle with HROS can be found in Szumski (1995). The immersing prism also has an inclined face which forms the first element of a chain of cross dispersing prisms. In fact HROS proposes to have the highest resolution of any of the 8-m high resolution spectrographs described in the paper by Pilachowski (Pilachowski *et al.*, 1995) which reviews the designs of many of the proposed high-resolution spectrographs for 8-m class telescopes. The reason that high spectral resolution can be obtained with Gemini instrumentation is partly due to the high specification on imaging performance allowing narrower slits to be used than is the case with other 8-m class telescopes.

2.4.2 Immersed gratings for the Infrared

The discussion has so far concentrated on the use of immersed gratings in the visible, 0.3-1.1μm. From equation 2.6 the gain in resolution that can be achieved is proportional to the refractive index of the immersing medium. For common glasses that transmit in the visible this limits the refractive index to the range $\sim 1.5 - 1.9$. In the infrared region, $1.1 - 5\mu$m, it is possible to obtain transmissive materials with much higher refractive indices. Examples are Silicon $n = 3.4$ and Germanium $n = 4$. Therefore the potential gains from immersed gratings in the Infrared are much greater.

The development of near-infrared immersed gratings for use in ESO instrumentation is described in Wiedemann & Jennings (1993) and Wiedemann (1994). The potential gains in the infrared are: very high resolutions, and the ability to reduce the overall size of the spectrograph optics. A prototype immersed grating was manufactured for ESO by anisotropic chemical etching of a Silicon prism. The grating is etched directly into the prism avoiding

interfacing problems between grating and prism. Interfacing the grating to the prism is expected to be more difficult in the infrared as the optical cement must be both a good index match to the prism and have high infrared transmission. Experimental results are presented which confirm operation as an immersed grating. Strong ghosts, due to grating imperfections, and considerable scattered light were measured. A more serious problem was the measured efficiency was three times lower than expected.

The construction and evaluation of an infrared immersed echelle, with a ruling density of 40g/mm, is also described in Graf *et al.* (1994) for use at $\sim 10\mu$m. The grating was also manufactured directly in Silicon using anisotropic etching techniques. Graf also notes that etching can produce echelles with larger groove spacings than can be obtained by conventional ruling techniques, although the Spectronics catalogue has echelles available with ruling densities as low as $\sim$ 20g/mm. This is an advantage for high resolution IR instruments where the wavelength approaches the size of conventional rulings.

It should be noted that a monolithic infrared immersed grating can also be adapted for use as in infrared grism. The only difference is the grating is not reflection coated thus allowing the collimated beam to exit through the grating. The construction of an infrared grism, utilising anisotropic etching of Silicon, for use with ESO's Thermal Infrared Multimode Instrument (TIMMI) is described in Kaufl (1994).

2.5 Immersed grating theory

This section describes the theoretical performance predictions for a telescope spectrograph configuration containing an immersed grating. The results are compared with those for an un-immersed grating derived previously in section 2.2. The relevance of immersed gratings to increasing resolution with GMOS is then discussed. Finally the immersed gratings proposed for use with GMOS are discussed.

2.5.1 Formulae relating to immersed gratings

An optical diagram of an immersed grating can be seen in figure 2.2. In the diagram angles are defined as positive if measured anticlockwise from the normal to the surface to the

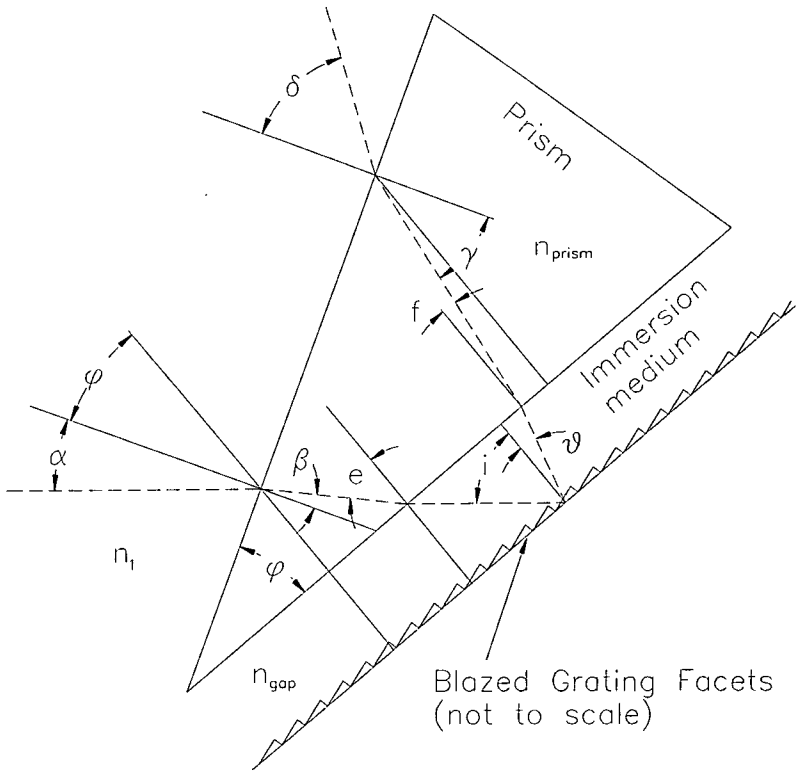

Figure 2.2: Schematic of an immersed grating. Normals to surfaces are shown with a solid line. The ray path is shown with a dashed line. Positive angles are measured anticlockwise from the normal to the ray. The angles are labelled as described in the text.

incident ray. Collimated light from the collimator lens is incident on a prism of refractive index n_{prism} at an angle α. The refractive index of the incident medium, normally air, is n_1. The prism is optically coupled to the grating via a medium of refractive index n_{gap}. Diffraction now occurs within this medium so that in the grating equation (equation 2.1) the refractive index must be included. Collimation is not disturbed by the prism. After passing through the immersing layer the diffracted beam then leaves the prism at an angle δ. The collimator to camera angle is now given by $\psi = \delta - \alpha$. The calculation of dispersion and resolution is similar to that shown in section 2.2 but now the anamorphic magnification at each prism interface has to be included. The angular dispersion of the grating $d\lambda/d\theta$ is modified by the immersion medium-prism interface and the prism-air interface such that the angular dispersion of the immersed grating is given by:

$$\left(\frac{d\lambda}{d\delta}\right) = \frac{n_1 \cos(f)\cos(\delta)}{m\rho\cos(\gamma)} \tag{2.8}$$

where the angles f, δ and γ are as defined in figure 2.2. The angles δ and γ are related via Snell's law:

$$n_{prism}\sin(\gamma) = n_1 \sin(\delta) \tag{2.9}$$

and similarly for angles α and β. Note also γ is related to f via $\gamma = f - \phi$.

As before dividing the angular dispersion by the focal length of the camera gives the dispersion scale at the detector ($d\lambda/dx$). This equation can be directly compared with the equation for the angular dispersion of an un-immersed grating given in equation 2.2. It can be seen that the dispersion is now related to the angles of refraction within the prism rather than the angle of diffraction. Therefore the refractive (anamorphic) properties of the immersing prism can be used to increase the available dispersion.

The projected slit width, Δx, now has to include the anamorphic magnification produced at each refractive interface and is given by:

$$\Delta x = \left(\frac{s}{f_{coll}}\right)\left(\frac{\cos(\alpha)}{\cos(\beta)}\frac{\cos(e)}{\cos(f)}\frac{\cos(\gamma)}{\cos(\delta)}\right) f_{cam} \tag{2.10}$$

with the angles α, e and β as illustrated in figure 2.2. The resolution can now be obtained, in terms of the spectrograph properties, by combining equations 2.8 and 2.10 to get:

$$R = \left(\frac{\lambda}{\Delta\lambda}\right) = \lambda\left(\frac{dx}{d\lambda}\right)\frac{1}{\Delta x} = \frac{m\rho\lambda f_{coll}\cos(\beta)}{s\cos(\alpha)\cos(e)} \tag{2.11}$$

The equation for the resolution of an immersed grating is then directly comparable with that for an un-immersed grating, equation 2.4. It is interesting to note that the refractive index of the prism, or the immersing medium, does not appear in equations 2.8, 2.10 or 2.11. The refractive index is, however, included implicitly because it determines the angles of diffraction and refraction.

The immersing layer is assumed to be plane-parallel and therefore does not produce any anamorphic effect[4]. However, the immersing medium can be crucial to the operation of an immersed grating. The wavelength at which diffraction occurs within the immersing layer is modified by the refractive index of the medium such that λ reduces to λ/n_{gap}. This important property allows longer wavelengths, or equivalently higher ruling density gratings, to be used than would be possible if the grating were un-immersed. This reduction in wavelength also makes it possible to observe the higher grating orders with the number of observable orders increasing in proportion to n_{gap}. In short: immersion allows $m\rho\lambda$ to be increased and hence resolution.

In the un-immersed case the length of grating, W, required to intercept the input beam is

[4]The immersing layer does produce a small beam displacement, but with a thin immersing layer this effect will be negligible

simply $W = D_{coll}/\cos(i)$. In the immersed case this becomes:

$$W = \frac{D_{coll}}{\cos(e)} \frac{\cos(\beta)}{\cos(\alpha)} \tag{2.12}$$

Again it can be seen that refraction within the prism can be used to advantage to reduce, or increase, the illuminated length of grating. By substituting equation 2.12 into equation 2.11 the formula for resolution reduces to that given in already equation 2.5. This shows that if the same ruling density, diffraction order, wavelength and illuminated width of grating are used with an immersed grating as with an un-immersed grating then an equal resolution will be obtained. The advantage with using immersed gratings is not necessarily a direct increase in resolution in proportion to the refractive index of the immersing medium. Instead the advantage comes from the prisms ability to reduce the anamorphic factor enabling higher resolutions to be obtained without overfilling the camera aperture.

The anamorphic factor is now becomes:

$$A.F. = \frac{D_{cam}}{D_{coll}} = \frac{\cos(\delta)}{\cos(\gamma)} \frac{\cos(f)}{\cos(e)} \frac{\cos(\beta)}{\cos(\alpha)} \tag{2.13}$$

which should be compared with the anamorphic factor of an un-immersed grating, equation 2.7. All equations relating to immersed gratings reduce to the equivalent formulae for an un-immersed grating if $n_1 = n_{prism} = n_{gap} = 1$.

The reduction in anamorphic factor available does also mean that higher resolution can be obtained, for a fixed anamorphic factor, with an immersed grating. The increase in resolution comes from the ability to use an increased length of grating without the associated increase in AF producing an *anamorphic immersed grating.*

2.5.2 Analysis of immersed grating properties

The equations presented in the previous section allow the performance of a spectrograph containing an immersed grating to be predicted. The main difficulty in solving the equations is finding a suitable configuration of prism angle, refractive index, angle of incidence and angle of diffraction that satisfies the restrictions imposed by the spectrograph, i.e. fixed collimator to camera angle and anamorphic factor. In order to find a solution and predict the properties of an immersed grating quickly, a number of computer programmes were written. These programmes allow a solution to the equations to be found quickly and provide

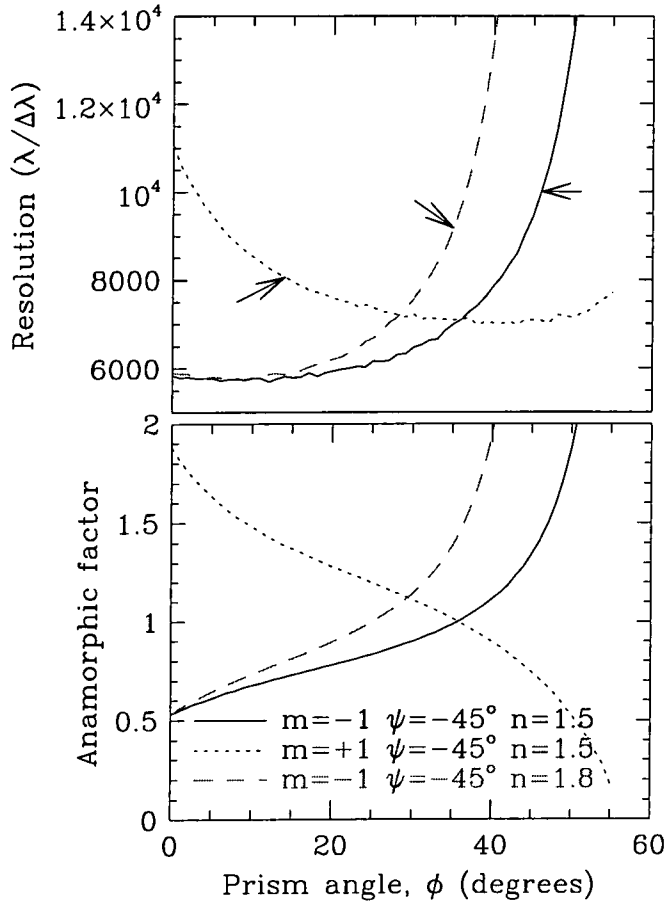

Figure 2.3: Plot to show resolution (upper plot) and the corresponding anamorphic factor (lower plot) versus prism angle for an immersed grating with the parameters shown in the legend and 1300g/mm. The arrows shown in the upper plot mark the resolution at which the anamorphic factor exceeds the limit of 1.4. Note that the use of a high refractive index prism, n_{prism} = 1.8, allows smaller prism angles to be used to produce the same resolution.

appropriate output such as predictions of resolution etc. The theoretical predictions of the performance of the prototype immersed grating, described in section 2.6, were calculated using the developed computer software.

It is difficult to understand the advantages of immersed gratings from the formulae presented in the previous section. The advantages are perhaps best illustrated by returning to the problem of achieving a SWRP of 5000 with GMOS as described section 2.2.1. The basic problem was to obtain a spectral resolving power of $R = 10^4$ with a 0.5 arcsecond slit at a wavelength of 850nm. It was shown that a resolution of 11,000 could be achieved by using a 1300g/mm grating inclined at an angle of 59° to the incident beam. This solution was, however, found to be extremely unsatisfactory due the large anamorphic factor produced, implying vignetting losses at the camera.

The application of immersed gratings to this problem will now be considered. A plot of the resolution obtained with the 1300g/mm grating versus increasing apex angle of the immersing prism is shown in figure 2.3. The plot shows two configurations for a prism with

refractive index of 1.5 corresponding to diffraction in either positive or negative first order. Note the arrows in the upper plot which indicate the resolution at which the anamorphic factor exceeds the GMOS limit of 1.4. The plot also shows resolution versus prism angle for a prism with refractive index of 1.8 used in negative first order.

It can be seen in the upper plot of figure 2.3 that a resolution of 10,000 can be achieved in negative first order with a prism angle of 46° and a prism refractive index of 1.5. The lower plot shows the corresponding anamorphic factor which is 1.4. A resolution of 10,000 is slightly smaller than the value of 11,000 obtained in the un-immersed case but there is a large reduction in the anamorphic factor. This shows that immersed gratings clearly provide a way of reducing the anamorphic factor whilst allowing high resolutions to be obtained.

Figure 2.3 (upper plot) also shows that if the prism angle is increased beyond 46° then the resolution also increases accordingly. However, as the prism angle is increased the anamorphic factor (figure 2.3 lower plot) also increases beyond the limiting value of 1.4. A prism angle of 48°, with negative first order diffraction, is needed to match the un-immersed grating resolution of 11,000. At this resolution the immersed grating produces an anamorphic factor of 1.6 which exceeds the limit, but it is still considerably lower than the anamorphic factor that is produced without the use of immersion. When the resolution in the immersed and un-immersed cases is equal then the illuminated width of the grating, W, can be shown to be the same in both cases. This shows that, for the same grating ruling density, higher resolution in the immersed case than the un-immersed case is obtained when the illuminated width of the grating is larger. Immersion therefore allows increased lengths of grating to be used than is the case without immersion, whilst the anamorphic factor remains within the limits of the spectrograph. The converse is also true: for a given resolution the use of immersion allows the illuminated length of grating to be smaller than in the un-immersed case. This implies smaller spectrographs can be constructed by using immersed gratings.

The effect of increasing the refractive index of the prism can also be seen in figure 2.3. Increasing the refractive index of the immersing prism from 1.5 to 1.8 allows a smaller prism angle to be used to reach the same resolution. The plot shows that a resolution of 10,000 requires a 46° prism with $n = 1.5$ but the prism angle reduces to 37° with $n = 1.8$. However there is a small penalty in that the anamorphic factor with the high index prism is larger, at 1.54, than the value of 1.4 obtained with the prism of lower refractive index. The main

benefit of using a high index prism comes from the ability to reach higher ruling densities at longer wavelengths, than is possible without immersion, due to the reduction of wavelength within the immersing medium.

In summary the use of an immersed grating provides the following benefits:

- More efficient use of camera aperture via reduced anamorphic factors and hence reduced vignetting,
- Anamorphic properties of the prism allow increased lengths of grating to be used without increasing the anamorphic factor,
- For fixed ρ and m immersion allows longer wavelengths to be used,
- Ability to use higher diffraction orders,
- Possibility of using smaller diffraction gratings.

2.5.3 Other advantages of immersion

The discussion so far has mainly concentrated on the ability of an immersed grating to provide higher resolution with the GMOS spectrograph. It should be emphasised that this is not the only benefit that can be produced by the use of immersed gratings. Another view is that for a given resolution the use of immersion allows the design of a more compact spectrograph. The collimated beam size and the camera aperture can be reduced leading to cost savings, smaller size and possibly lower aberrations. A more compact design is a major advantage in infrared systems where the entire spectrograph optics are required to be located within the tight confines of a cryostat. The potential gains in spectrograph efficiency, by matching the anamorphic factors of all gratings to the camera aperture, has already been suggested in Wynne (1990a).

2.5.4 Immersed grating proposal for GMOS

The results of the theoretical investigation of the properties of immersed gratings, presented in the previous section, indicates that they can be satisfactorily used to increase the SWRP of GMOS from the present limit of $\sim 2,500$ to $\sim 5,000$. A study of possible designs of

ρ	ξ	ϕ	λ_b	R_b
2400 g/mm	21.0°	30.0°	444nm	6852
1800 g/mm	26.7°	30.0°	724nm	9212
1200 g/mm	17.5°	30.0°	724nm	5268

Table 2.1: List of the proposed (Allington-Smith & Lee, 1995) immersed gratings for use with GMOS. The blaze angle is denoted by ξ and the blaze wavelength by λ_b. The resolution which is obtained at blaze is listed under R_b.

immersed grating for GMOS was performed (Allington-Smith & Lee, 1995). This study looked for suitable designs of immersed grating to increase the spectral resolution available with GMOS. The report identified the immersed grating configurations listed in table 2.1 as providing a good complement to the un-immersed gratings already proposed. Of course, the aim of any complement of diffraction gratings available for use with a spectrograph is to try and fill the parameter space of resolution and wavelength. The astronomer then has a choice of a broad range of observing possibilities, hopefully to suit any observing programme.

A plot of resolution versus wavelength for the immersed grating configurations listed in table 2.1 is shown in figure 2.4. The immersed gratings are shown in close hatch in the upper half of the plot. The horizontal width of the hatched regions in figure 2.4 represents the wavelength coverage on the GMOS detector. The blaze wavelength of each grating is indicated by a black circle. The immersed gratings can be identified with reference back to table 2.1. The plot clearly shows the gain in resolution, of up to a factor of $\sim$ 2.3, that can be achieved via the use of immersed gratings. The immersed grating plots are terminated when the maximum anamorphic factor of 1.4 is exceeded. The bottom half of figure 2.4 (plotted with broad hatching) shows the range of resolutions available with un-immersed gratings. The plots stop abruptly at R=5,000 as this is where the limiting anamorphic factor is exceeded, as discussed in section 2.2.1. Regions of cross hatching in the curves for immersed gratings correspond to the possible production of a ghost image at the detector by direct reflection of the collimated beam from the front surface of the prism. This region is therefore not recommended for use if ghosting is to be avoided. The production and prevention of ghosts is described in more detail in section 3.6.

The triangle, circle, and star symbols shown in figure 2.4 represent the resolution and wavelength coverage required to complete certain *key science projects* (GMOS OCD, 1995). The

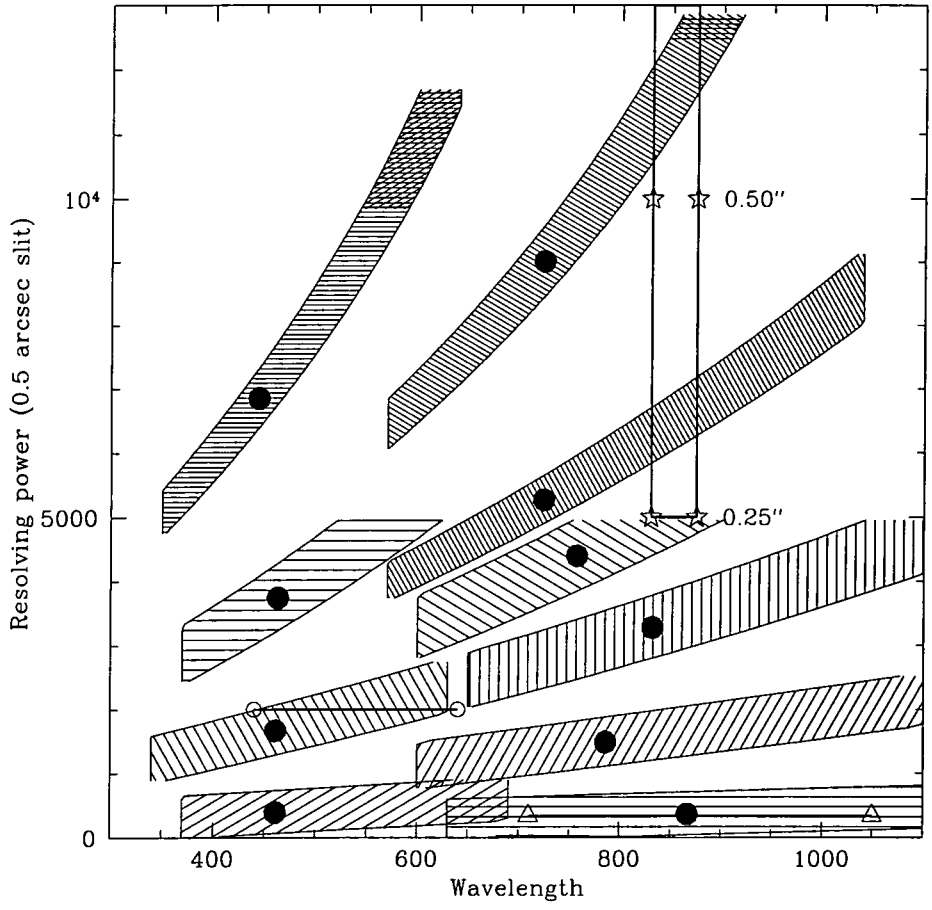

Figure 2.4: Plot of resolution versus wavelength for a variety of diffraction gratings proposed for use in GMOS. This plot is reproduced from Allington-Smith & Lee (1995) where a detailed discussion of its content can be found. Immersed gratings are indicated with close hatching and un-immersed gratings with broad hatching. The blaze wavelengths of the gratings are indicated by circles. It is clear that immersed gratings achieve more than double the resolution of un-immersed gratings. The width of the hatched regions represents the wavelength range present on the detector. The curves are terminated when the anamorphic factor exceeds 1.4 or the predicted efficiency falls below certain limits.

triangles indicate the resolution, $R = 340$, and broad wavelength coverage, 720-1060nm, required to observe the redshift of galaxy clusters at redshift $z = 1$. The circles indicate the resolution and wavelength range required to study the brightest cluster galaxies at $z = 0.2$. Finally, the stars indicate the resolution and wavelength coverage required for highly accurate ($< 2\text{kms}^{-1}$) dynamical studies of e.g. stars in dwarf spheroidal galaxies. The required resolution of 10^4 requires the use of a 0.25 arcsecond slit with an un-immersed grating. The slit width can be increased to over 0.5 arcseconds if an immersed grating is used providing a large gain in throughput during non-optimum seeing conditions.

Clearly then the addition of immersed gratings to GMOS would increase the already wide range of resolution and wavelength coverage available with GMOS. It would also provide astronomers with the capability to perform high resolution spectroscopy over the wide field of view offered by GMOS.

Of course the advantages that immersed gratings provide for GMOS may also be of benefit to other astronomical spectrographs. The increase in resolution available could be used to double the resolution of spectrographs on 4-m telescopes. They would then providing resolutions of order $R = 20,000$ and upwards. Immersed gratings therefore provide a method of filling the 'resolution gap' that exists between grating spectrographs and echelle spectrographs in the region $R \sim 15,000$.

2.6 Prototype immersed grating

The prototype immersed grating was constructed from a 1200 g/mm Milton-Roy[5] diffraction grating with a blaze angle of 21°. The grating was immersed with a 30° BK7 prism. The prototype immersed grating is also similar in design to one of the immersed gratings proposed for use with GMOS, table 2.1. The construction of the immersed grating is described in more detail in section 2.7.2. This design of immersed grating was chosen to produce the largest change in properties of the grating with immersion whilst being straightforward, and cheap, to construct. An appreciable change in properties with immersion is required to allow the performance of the prototype immersed grating to be accurately verified experimentally.

There are various different ways in which the immersed grating can be assembled. Each

[5]Milton-Roy has now become Spectronics.

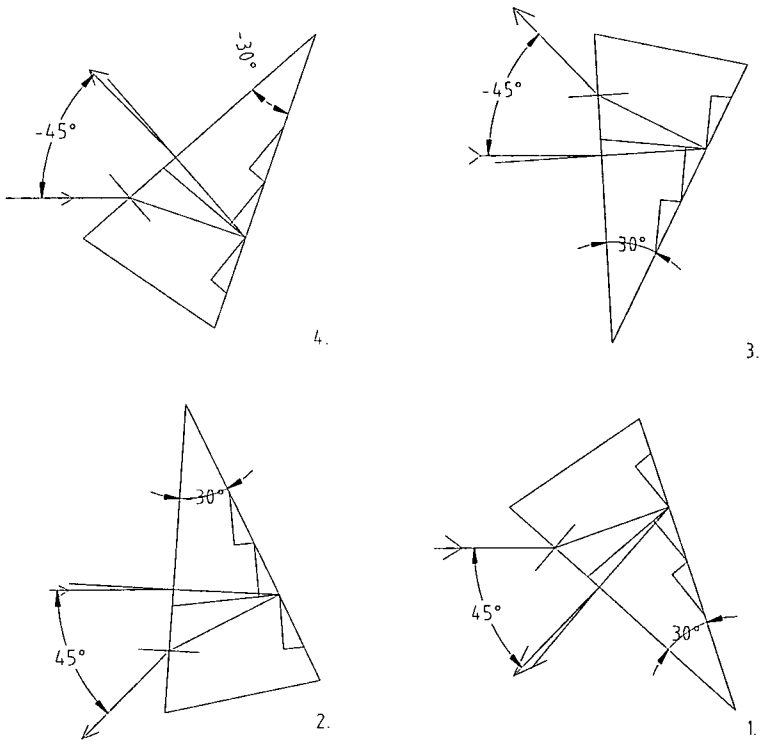

Figure 2.5: Diagram of the four possible configurations of immersed grating. The parameters of each configuration are listed in table 2.2.

ref no.	Order	ψ	ϕ	α	δ	Resolution	Illumination
1.	+1	45	30	-49	-3.7	1865	case-b
—	−1	45	30		no solution		—
—	+1	45	-30		no solution		—
2.	−1	45	-30	3.7	48.9	1596	case-a
3.	+1	-45	30	-3.9	-48.7	1596	case-a
—	−1	-45	30		no solution		—
—	+1	-45	-30		no solution		—
4.	−1	-45	-30	48.7	3.7	1865	case-b
un-imm	+1	-45	0	-45	0	2000	case-a
un-imm	−1	-45	0	0	-45	1415	case-b

Table 2.2: The immersed grating configurations possible for all combinations of order, prism angle and collimator to camera angle. The configurations labelled with a reference number are illustrated in figure 2.5. The resolution predicted is that obtained with the test spectrograph described in section 2.8.1.

configuration represents a different combination of ψ, ϕ and m with the grating being illuminated slightly differently in each case. The four possible configurations for the prototype immersed grating are illustrated in figure 2.5. The prototype can therefore be constructed and used in any of these four configurations. Note that each configuration is labelled 1,2,3 or 4 for future reference. The theoretical predictions for the performance of the immersed grating configurations shown in figure 2.5 are listed in table 2.2. The performance of the prototype was predicted using ray tracing software developed specifically to design and predict the properties of immersed gratings. The performance of the grating in the un-immersed case is also listed in table 2.2 for comparison. It can be seen that some combinations of ψ, ϕ and m do not produce a realisable configuration. Configurations 1 and 4 are equivalent in performance with one being the mirror image of the other, i.e. a rotation of 180° about the collimator axis. The same applies to configurations 2 and 3. Configurations 1 and 4 correspond to case-b illumination conditions, as described in section 3.2.1, with configurations 2 and 3 corresponding to case-a illumination. Case-a illumination can be thought of as blaze to collimator and is generally the preferred orientation in astronomical spectrographs for un-immersed gratings as it produces higher resolution.

Note that with an un-immersed grating the highest resolution is always achieved in the case-a illumination configuration. Figures 2.1 and 3.1 illustrate a grating used with case-a illumination. This type of illumination is achieved with a large angle of incidence between the input beam and the grating normal. This illuminates the maximum length of grating and produces high resolution. It is also often the configuration which produces the highest efficiency, as described in section 3.2.1. A plot of resolution versus wavelength for the prototype grating prior to immersion can be seen in the upper plot of figure 2.6. The resolution shown is that predicted with use on the 'test spectrograph' which was used to test the performance of the grating, as described in section 2.8.1. It can be seen the case-a illumination curve always has a higher resolution than that with case-b. It can also be seen that case-a illumination soon exceeds the limiting anamorphic factor for GMOS of $AF = 1.4$. A plot of anamorphic factor versus wavelength for the prototype grating configurations is shown in the lower half of figure 2.6.

A property of immersed gratings is they exhibit a 'cross-over' in resolution where the highest resolution swaps from being in case-a illumination to case-b illumination. This cross over

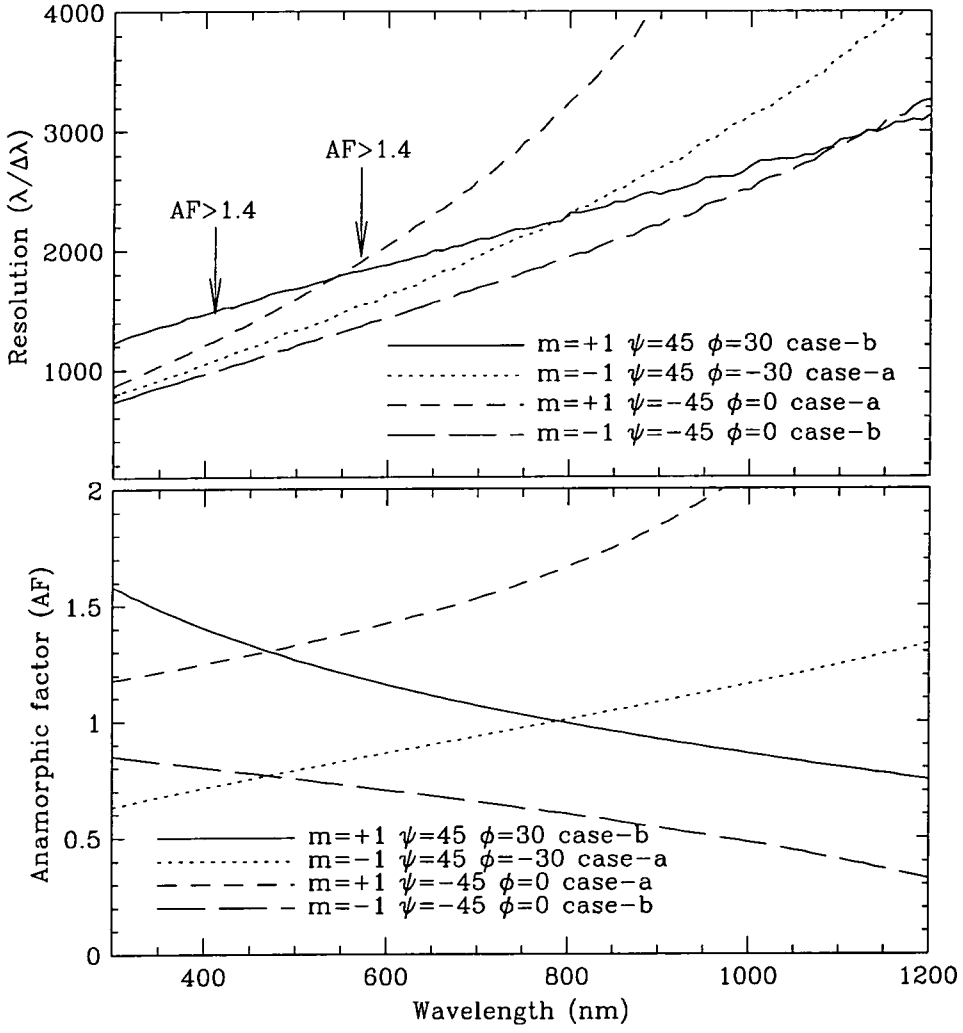

Figure 2.6: Plot of resolution versus wavelength (upper plot) and anamorphic factor versus wavelength (lower plot) for the prototype immersed grating in configurations 1 and 2 as illustrated in figure 2.5. The resolution, and anamorphic factor, of the un-immersed grating is also shown for comparison. The points at which the anamorphic factor exceeds 1.4 are indicated with arrows. Note the cross over point in the two curves of immersed grating resolution versus wavelength occurs when $AF = 1.0$.

point can be clearly seen in figure 2.6, at approximately 810nm, where the resolution for the two configurations of immersed grating is equal. Equal resolution also implies that the anamorphic factor of the two configurations is the same, i.e. equal to unity, and the corresponding 'cross-over' in anamorphic factor can be seen in the lower half of figure 2.6. This interesting property of immersed gratings means that you get *two useful gratings for the price of one.* Changing between the two immersed grating configurations simply requires that the immersed grating is rotated through 180° about a normal to the grating surface, i.e. the immersed grating is placed in the spectrograph upside down. Because of this novel feature the family of immersed grating efficiency curves, for the proposed GMOS upgrade, presented in figure 2.4 is in fact incorrect. Each immersed grating should have two curves for resolution versus wavelength. The curves of resolution versus wavelength for the proposed GMOS immersed gratings, in both case-a and case-b illumination, are plotted in figure 2.7 which is directly comparable with figure 2.4. The case-b configuration provides higher resolution blueward of the cross-over point and case-a illumination (case-a is plotted in figure 2.4) provides higher resolution redward of the cross-over point. The configuration with the highest resolution also provides the largest wavelength coverage and has less oversampling at the detector. However, un-immersed gratings always provide the highest resolution, and better wavelength coverage, in case-a illumination. This means that the two configurations of immersed grating provide a better coverage of the resolution-wavelength parameter space than an un-immersed grating. This is thought to be a useful property of immersed gratings that has been previously overlooked. It means that the parameter space of resolution and wavelength can be even more densely filled than is shown in figure 2.4 leading to an increased choice of grating configurations for use when observing.

2.7 Construction of an immersed grating

In this section the techniques used to construct the prototype immersed grating are described. The more advanced techniques that might be used to construct an immersed grating for use in an astronomical spectrograph are also discussed.

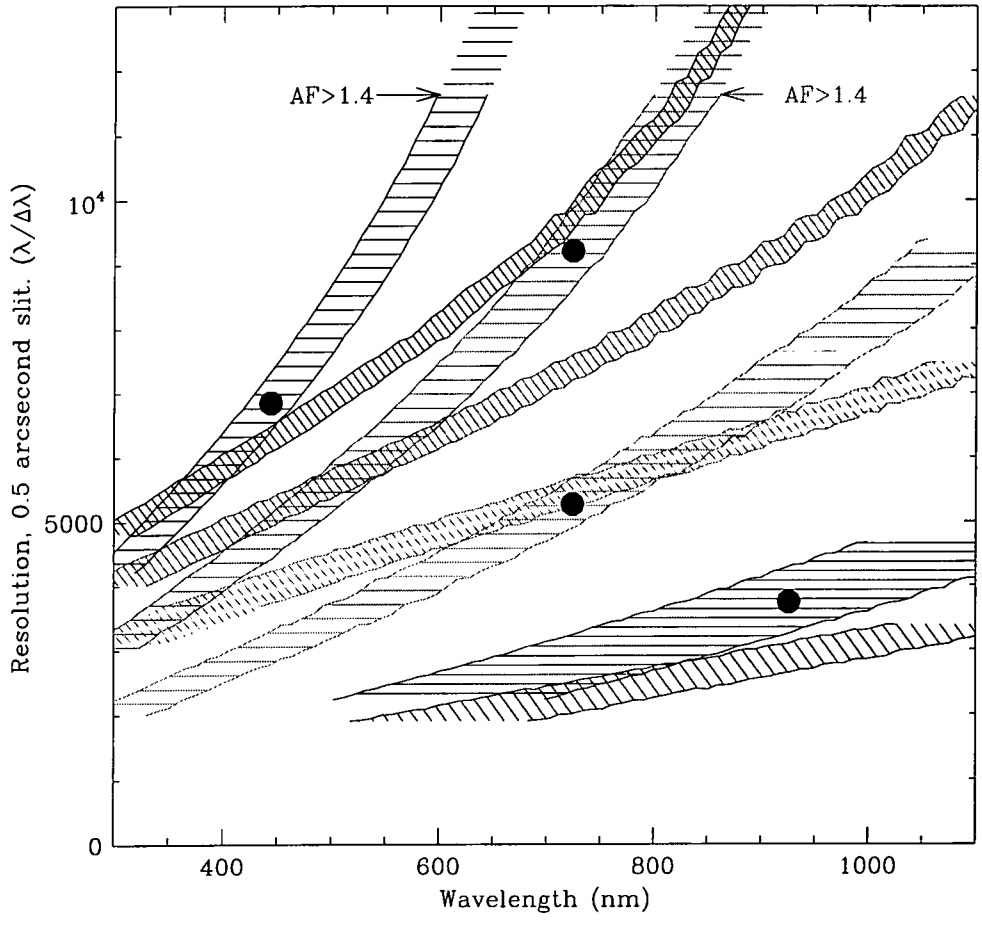

Figure 2.7: Plot of resolution versus wavelength for the three immersed gratings proposed for use with GMOS. The width of the curves represents the wavelength range that is visible on the detector. The black circles indicate the resolution at the blaze wavelength. The curves shown in horizontal hatch are the same as those already shown in figure 2.4 and are for case-a illumination. The gratings can be identified from table 2.1. Also shown, with diagonal hatching, are the curves for case-b illumination. Below the wavelength of the cross-over point in resolution the case-b configuration provides higher resolution. The lower plot, blaze at 924nm $R = 3744$, is for an un-immersed grating. For an un-immersed grating there is no cross-over in resolution and hence case-b always has lower resolution than case-a.

2.7.1 Manufacture of an astronomical immersed grating

There are various proposed methods by which an immersed grating can be produced. The main requirement is that the immersion process should not damage the surface of the grating in any way.

One possibility is to directly replicate the grating onto the back surface of the prism, in a manner analogous to the production of a grism. The back surface of the replicated grating then needs to be silvered in order to reflect the incident light. An immersed grating can therefore be thought of as a reflecting grism. In this way the grating is permanently fixed to the prism. This does however require that the grating be replicated in a substance which is optically transparent and possesses a good index match with the immersing prism. It is also necessary that the thermal expansion properties of the prism material and the replication resin match to avoid mechanical distortions of the grating with changing temperature.

Another possibility is to attach a prism directly to a standard reflection grating. This can be done by means of an appropriate optical coupling fluid or optical adhesive. The coupling fluids or adhesive can be chosen to match the refractive index of the immersing prism. Gluing the prism to the grating is preferable to oiling as the glue forms a permanent bond. If oil is used then there is the possibility that the fluid can flow from the prism/grating interface with time. This would require the fluid to constantly be replenished. It may be difficult to obtain optical coupling oils, or cements, which satisfy the requirements of index matching and high transmission over a broad wavelength range. This problem is worse for echelles than gratings as echelles are used over the entire wavelength range of the instrument. For a large astronomical device there is expected to be some difficulty in locating the prism onto the surface of the grating without damaging either component. It may also be difficult to avoid the production of bubbles in the immersing layer.

The technique adopted for the production of the immersed echelle for HROS (Radley *et al.*, 1994) is to first glue a glass substrate to the echelle surface. Additional prisms are then added to the glass substrate to build up the immersed echelle.

Immersed gratings/echelles for use in the infrared may be manufactured by direct ruling of soft infrared transmitting materials such as KRS5. Certain infrared transmitting materials can also be chemically etched to produce a blazed diffraction grating structure, as described

in Wiedemann & Jennings (1993).

The requirements of the prism, which can have a large volume in some cases, are quite demanding. The prism glass needs to have high homogeneity to reduce wavefront distortions due to refractive index variations. Low bubble and exclusion content is also required to reduce the production of scattered light. The prism refractive index may also need to be a good match to that of available replication resins, if the grating is to be replicated directly onto the prism substrate, as is the case for grisms.

The high resolution and dispersions of immersed gratings also implies a requirement for extra stability in their mounting arrangements. Flexure that may be tolerated with a low dispersion grating, i.e. a shift of 0.2 pixels per hour, may be too large with an immersed grating due to the much higher dispersion. Gratings need to be mounted such that: they remain flat (they are not distorted) and do not degrade the wavefront, and they remain stable, i.e. do not flex during and observation. Precise adjustment of the tilt will also be required for high resolution gratings. As the wavelength within the immersing medium is reduced this implies an increased tolerance on the surface flatness of the grating to avoid the production of wavefront distortions. $\lambda/4$ surface flatness in air reduces to $\lambda/4n$ within the immersing medium.

The main problem to be addressed is: how to attach the prism to the grating surface? Clearly there is still much development to be done to find a satisfactory way producing a large immersed grating for use in an astronomical instrument.

2.7.2 Manufacture of the prototype immersed grating

For the production of the prototype immersed grating it was decided to couple the prism to the grating by means of an optical coupling fluid. This technique was also used in the production of a prototype immersed echelle for use in HROS (Radley *et al.*, 1994). The oil has the advantage that it remains liquid thus allowing the prism to be removed from the grating after tests have been performed. The oil chosen, thanks to the advice of Francisco Diego was Glycerol (Diego, 1994). Glycerol has a refractive index of approximately 1.5 which is a good match with many common glass types. It is also soluble in Water and Ethanol allowing it to be readily washed from the grating and prism surfaces. The properties of

Glycerol are discussed in more detail in section 2.7.2.

The grating chosen for the prototype was a Milton-Roy (now Spectronics) 1200 grooves per mm grating with a blaze angle of $\eta = 21°$ (this grating was available in the optics laboratory). To keep the cost to a minimum a suitable prism was selected from the SPIERS-ROBERTSON range of optical components. The prism chosen was BK7 glass and has an angle of $\phi = 30°$. This combination of prism and grating is similar to one of the immersed gratings proposed for the GMOS upgrade, as described in section 2.5.4.

Immersing the prism to the grating

Before the prism was immersed to the grating surface some tests were performed on the grating surface to discover what effect, if any, the Glycerol would have. For example it is known that a grating surface can be removed by washing with warm water as the replicating resin is dissolved. A small amount of Glycerol was applied to the corner of a spare 600 grooves per mm Milton-Roy grating to observe the effect of the Glycerol on the grating surface. It was found the Glycerol could readily be removed by flushing the grating surface with distilled water. After the water droplets had dried some residue was seen to remain on the grating surface, however, the grating surface was found to be undamaged by the washing process. The residue is thought to be trapped within the grating rulings. This residue is likely to be due to impurities in the distilled water and the Glycerol implying that very high purity chemicals should be used for the immersing process.

To attach the prism to the grating, the grating was first mounted in place on the optical mount. The grating mount was then fixed flat on the optical bench with the grating surface facing vertically upwards ready for the prism to be applied. A thick layer of Glycerol was then applied to the centre of the prism face which is intended for immersing with the grating. Extreme care must be taken in the application of the Glycerol layer to the prism to avoid the production of bubbles. Even tiny bubbles can spread to a large area under the action of surface tension. The layer of Glycerol applied to the prism surface measured approximately 30mm by 30mm. After the Glycerol has been allowed to settle the prism was turned upside down and gently placed onto the grating surface. This has to be done quickly otherwise the Glycerol will begin to run from the prism. Fortunately the extremely high viscosity of Glycerol prevents it from forming drips quickly. The thickness of the Glycerol layer is

sufficient to allow the prism to 'float' on the surface of the grating avoiding damage to the delicate rulings. The prism is able to slide about, on the supporting layer of Glycerol, allowing it to be correctly positioned on the grating. Clearly extreme care (and a steady hand) is needed when the prism is placed onto the grating surface.

With the grating flat on the bench the action of gravity is enough to cause the excess glycerol to run from the prism-grating interface. Surface tension (capillary action) eventually produces a uniform thin layer of glycerol. The excess glycerol is allowed to run away from the grating via the grooves cut into the grating mount. A photograph of the immersed grating can be seen in figure 2.10.

Properties of Glycerol

Glycerol is an organic compound, chemical formula: $HO - CH_2 - CH(OH) - CH_2 - OH$. The refractive index[6] of Glycerol, at a temperature of 20°C, is n_D=1.474. This is a good index match to the BK7 glass of the prism (n_D=1.517). Glycerol is water soluble and soluble in other organic liquids (i.e. Ethanol) so it can be easily washed from the grating surface. Glycerol is hygroscopic but this property was not thought be a problem for the production of the prototype immersed grating. The high viscosity of Glycerol, 1490cps, provides high surface tension ensuring that the liquid does not readily run from the prism-grating interface. Glycerol is also cheap and readily available from laboratory chemical suppliers.

The absorption spectrum of glycerol was measured using a Perkin-Elmer UV/VIS/NIR Lambda 19 atomic absorption spectrophotometer. This is a dual beam spectrometer[7] which measures the atomic absorption spectra of a sample placed in the test beam. A small quantity of Glycerol was placed into the sample holder and the absorption spectrum was measured. The dual-beam operation of the instrument measures the absorption coefficient to an accuracy of 10^{-5} absorptance units. The total thickness of the Glycerol sample measured was 10mm, as defined by the sample holder. The absorption spectrum of Glycerol can be seen in figure 2.8.

The absorption spectrum of Glycerol is relatively featureless over the region 400–900nm,

[6]Glycerol data obtained from (Weast, 1978).

[7]full details of this instrument can be found at the Perkin-Elmer www site:
http://www.perkin-elmer.com:80/uv/l900.html

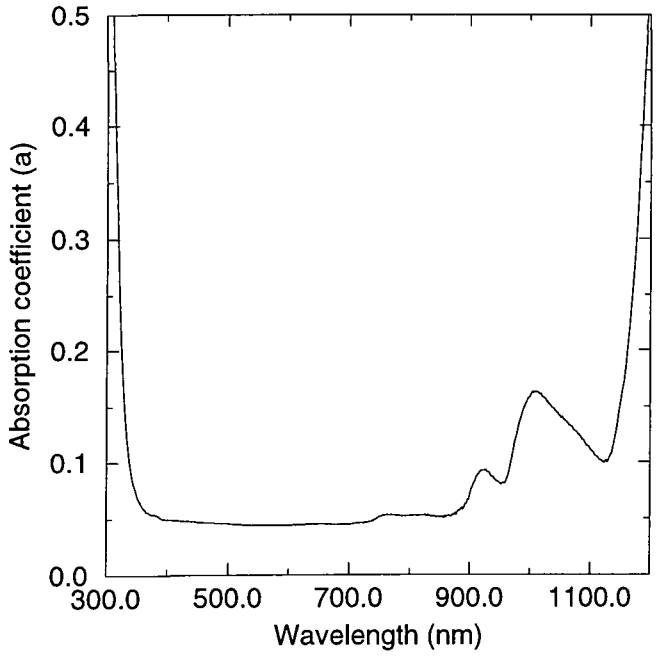

Figure 2.8: Absorption spectrum of a 10mm thick sample of Glycerol. The ordinate is shown as the absorption coefficient, a. The absorption coefficient is related to the transmission of the sample via $a = -\log_e t$, where t is the transmission. The error in the measurement of the absorption coefficient is 0.01%.

with absorption features redward of 900nm. As the thickness of Glycerol present in the immersing layer is likely to be small, the absorption spectrum is not expected to affect the measurement of grating efficiency at a level that is detectable.

It should be noted that Glycerol was initially thought to be a relatively chemically inert substance which would not affect the grating surface. However, after a period of approximately 3 months, a slight dis-colouration of the grating surface within the immersing layer was found to appear and bubbles had formed. Further tests showed that glycerol reacts with Aluminium to produce a white crystalline substance resembling salt. The bubbles are thought to be due to Hydrogen or Oxygen gas released from the Glycerol. This is thought to be due to oxidation of the Aluminium by the Glycerol, which is a very mild acid. A ruled grating surface presents a large surface area at which chemical reactions can occur. Whilst this does not present a serious problem for the prototype immersed grating it does prevent Glycerol from use with an IG intended for astronomical use.

Removal of prism from grating

In section 2.6 it was described that there a number of alternative configurations in which the immersed grating can operate. To test all possible configurations it is therefore necessary to be able to remove the prism from the grating surface and re-apply the prism in an alternative configuration. These configurations are illustrated in figure 2.5. As the Glycerol remains

liquid it is possible to slide the prism over the grating surface on the immersing layer of glycerol. Additional Glycerol is applied to the region where the prism is to be moved to in order to replenish the Glycerol layer. In this way the prism can be removed from the grating without damaging the grating surface. The mating surfaces of the prism and the grating can then be washed, with distilled water, prior to reapplication of the prism. This technique is not, however, recommended for use with Astronomical instruments due to the high probability of damaging the grating surface.

2.8 Experimental verification of immersed grating theory

A number of papers, discussed in section 2.4, have described the theory of immersed gratings. There was some confusion in the literature over which theory correctly predicted immersed grating performance. There has also been very little experimental work to verify the theoretical predictions. Whilst there is no reason to doubt that the theory is correct, there may be some subtle effects that have been overlooked. The aim of this experiment then is to check the theory of immersed gratings via testing of the prototype immersed grating. This section discusses the measurement of resolution and dispersion for the prototype immersed grating. The measurement of grating efficiency and the analysis of ghosts is described in the next chapter.

The theoretical predictions for the performance of the prototype immersed grating were presented in section 2.6 and listed in table 2.2. To test the theoretical predictions of immersed grating performance a small spectrograph was constructed on an optical bench in the laboratory. The 'test spectrograph' is described in detail in the next section.

2.8.1 Description of the test spectrograph

An optical diagram of the test spectrograph can be seen in figure 2.9. A photograph of the test spectrograph can also be seen in appendix A, figure A.1.

To measure the dispersion of the immersed grating it is necessary to illuminate the grating with a number of known monochromatic wavelengths. The spectrum produced by the grating

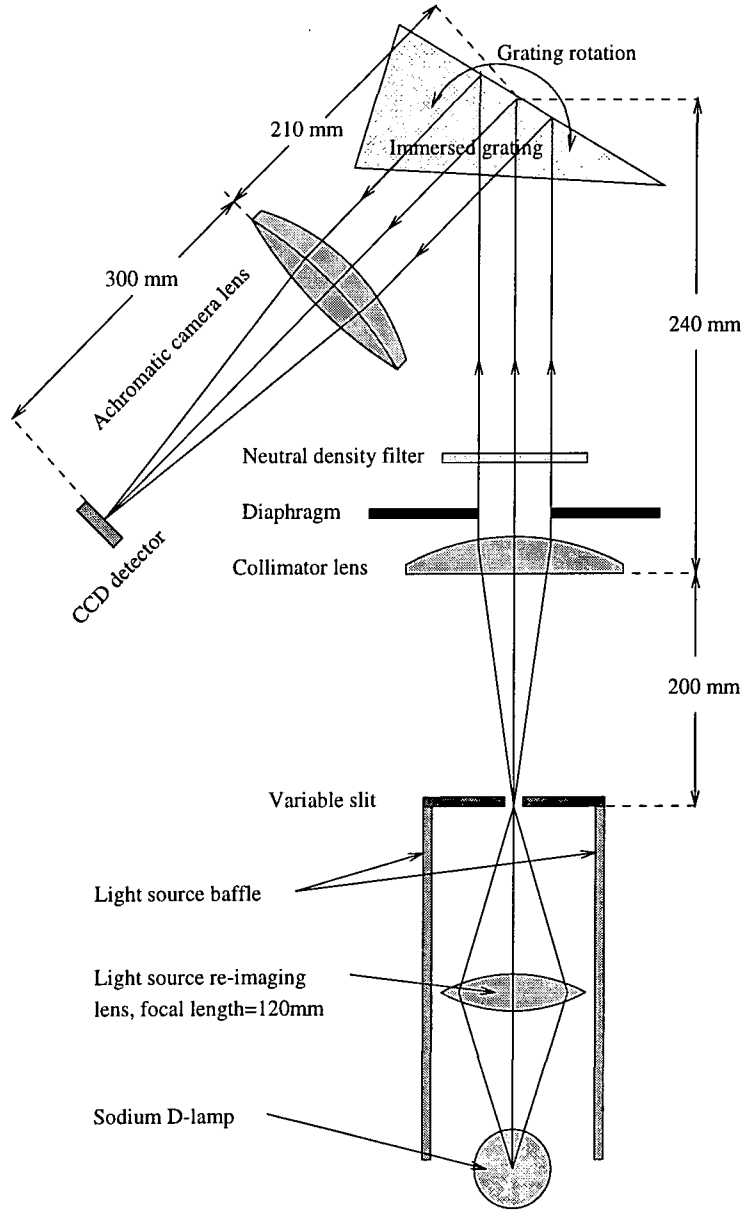

Figure 2.9: Schematic to show the optical components in the immersed grating test spectrograph.

is then recorded using a CCD camera. From the CCD image it is then possible to measure the dispersion of the system from the distance between the different spectral features. A Sodium D lamp was found to be a suitable light source for this purpose. The Sodium lamp produces a bright yellow doublet (known as the Fraunhofer D-lines) with wavelengths $\lambda_{D1} = 588.995$nm and $\lambda_{D2} = 589.592$nm. A spectral resolution of R=987 is therefore required in order to resolve the doublet, which also provides a test of immersed grating resolution.

A 14W Sodium gas discharge lamp was used as the light source in the test spectrograph. The gas mixture in the lamp is such that both Sodium D lines are produced with approximately equal intensity[8]. This avoids problems associated with measuring the spectral resolution from lines of differing intensity.

The light source is reimaged onto the entrance slit to the spectrograph via a lens, as shown in figure 2.9. The lens is positioned to uniformly illuminate the spectrograph slit. The entire light source optical assembly is baffled to prevent stray and scattered light from entering the spectrograph. The entrance slit width can be varied by means of an adjustment screw. The slit width was set to the required value of 100μm by means of a feeler gauge. After adjustment the slit width was checked to be approximately correct with a travelling microscope. Errors in the slit width, which defines the spectral resolution, were estimated to be 5%.

The light from the slit is collimated using a 200mm focal length plano-convex lens (note that the plane side faces towards the slit to reduce spherical aberration). A variable diaphragm is placed in the collimated beam immediately following the collimator lens to restrict the beam size to 10mm. This helps to reduce the aberrations of the lenses and produces a beam of appropriate size with which to illuminate the immersed portion of the grating. Increasing the beam size only changes the performance of the spectrograph by increasing the optical aberrations. The beam size has no effect on the spectral resolution of the system. Neutral density filters can also be placed in the collimated beam to reduce the intensity (the light source is not variable) of the beam in order to avoid saturation of the detector.

The collimated beam is then incident on the diffraction grating which is to be tested. The grating assembly is discussed in section 2.8.2. The diffracted beam is reimaged onto the detector by means of a 300mm focal length achromatic camera lens. There is an angle of 45° between the collimator and camera axes. This simulates conditions in an astronomical

[8]Note that the atomic transition probabilities predict that λ_{D1} will have an intensity twice that of λ_{D2}.

spectrograph and also provides enough space between the collimator and camera apertures to avoid vignetting. The camera lens is mounted on a purpose built mount which locates to the optical bench an an angle of 45° with respect to the collimator axis. Both the collimator lens and the CCD camera are mounted on travelling stages to allow accurate focusing.

2.8.2 Immersed grating mount

The immersed grating needs to be mounted such that both the grating and the prism are adequately supported. It is especially important that the prism cannot move whilst immersed to the grating as this could damage the grating surface. The mount also needs to be able to be fixed to a rotation stage to allow the grating angle to be adjusted. The method by which the immersed grating was mounted can be seen in the photograph shown in figure 2.10. The immersed grating mount consists of a flat base plate with an upright. The grating is attached to the upright using optical coupling fluid. The surface tension between the back of the grating substrate and the support upright is sufficient to locate the grating firmly in place. However as the coupling fluid remains liquid it is also straight forward to remove the grating after use. Mounting in this way does not damage the surface of the grating. There are grooves machined in the mount base plate to allow excess coupling fluid to flow away (these can be seen in figure 2.10).

The immersed grating mounting structure can be fixed onto a rotation stage by means of four screws. The mount is also devised such that the grating surface is positioned at the centre of rotation of the rotating stage. A Daedel motorised rotation stage was used to control the grating movement. The rotation stage is controlled by means of a computer and associated drive electronics. The rotation stage can be positioned to an accuracy of one thousandth of a degree. This allows accurate measurement of the angles at which diffraction takes place with the immersed grating. It is also straightforward to quickly rotate the grating to a new angle by means of the computer drive software.

2.8.3 Calibration of COHU CCD camera

To accurately measure the dispersion and resolution of the prototype immersed grating it is necessary to record an image of the spectrum. To do this a COHU 6700 series CCD

Figure 2.10: Photograph of the immersed grating taken during manufacture. Note the glycerol layer, seen at the top right corner of the prism, has yet to fully expand to the full area of the prism. The immersed grating is seen positioned on the grating mount.

camera was used. The COHU CCD is a TV frame rate device which produces an analogue output. To digitally record the image the CCD is linked to a PC via a frame-grabber card. The frame-grabber card digitises the analogue output of the CCD producing an 8-bit image which is 512×512 pixels in size. The COHU CCD camera was specifically chosen for its' linear response and the ability to operate the camera without automatic gain control. Non-linear response and automatic gain control are common features of TV frame rate CCD cameras which make them unsuitable for recording scientific images. The output from the CCD camera can also viewed on a television monitor during the experiment.

The response characteristics of the CCD camera and frame-grabber combination were determined from exposures of a standard light source taken through various neutral density filters. The detector was found to be linear up to approximately 220 counts after which the response became non-linear. During the experiments care was taken to ensure that the intensity level on the detector was kept within the range over which the detector response is linear. Images taken with the frame-grabber are stored in binary format. The images were analysed using the astronomical data reduction package IRAF. The images can be converted from binary format into IRAF format by means of the *irafil* package.

In order to accurately measure distances on the CCD image it is necessary to know the size

of the pixels. The combination of CCD camera and frame-grabber produces an effective pixel size which is not the same as that of the detector. The effective pixel size was measured by scanning an image across the detector, in steps of 1mm, and measuring the displacement between the successive images. The effective pixel size was found to be $12.35 \pm 0.20\mu$m in the x direction (the long axis of the detector) and $8.35 \pm 0.20\mu$m in the y direction.

2.9 Immersed grating test results

The previous section described the design and construction of a spectrograph with which to test the prototype immersed grating. The motivation for testing a prototype immersed grating is to check that the theory is correct given the confusion that presently exists in the literature. Clearly it is helpful to have direct experimental verification of the immersed grating theory so that it can be used with confidence. This section describes the results of a series of optical tests conducted on the prototype immersed grating. The grating was also tested prior to immersion to confirm the accuracy of the test equipment. The tests consisted of the measurement of resolution, dispersion and angle of diffraction. The results of these tests can then be directly compared with the theoretical predictions previously described in section 2.6.

2.9.1 Spectrograph test with un-immersed grating

The first part of the experimental investigation of immersed grating performance was to verify the performance of the test spectrograph. This was done by measuring the resolution and dispersion produced by the 1200g/mm grating prior to immersion. Images of the Sodium spectrum were taken with the grating in various configurations, as listed in table 2.3. An example of the image produced by the system can be seen in figure 2.11 and the corresponding intensity profile in figure 2.12. Note that these figures show images taken with an immersed grating but the spectrum looks similar with an un-immersed grating.

The centroid of the two spectral lines can be found, to an accuracy of approximately 0.1 pixels, by using Astronomical data reduction software, such as IRAF. From the distance between the two spectral lines the dispersion of the test spectrograph can be found via equation 2.8. The projected slit width (the image width) can be found by measuring the

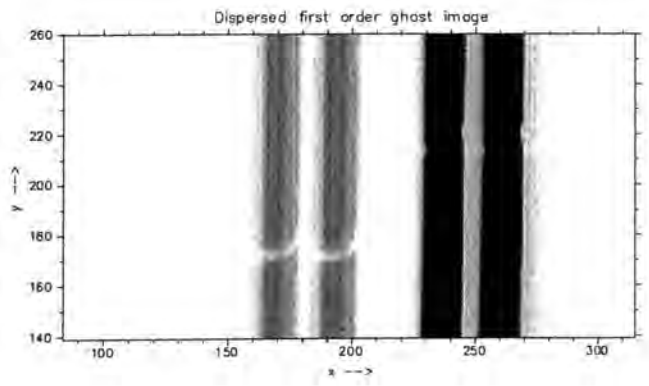

Figure 2.11: Image of the first order dispersed Sodium D-lines spectrum, taken with the test spectrograph and the immersed grating. A ghost image, produced by reflection from the back surface of the prism, can be seen as the fainter lines at x=180.

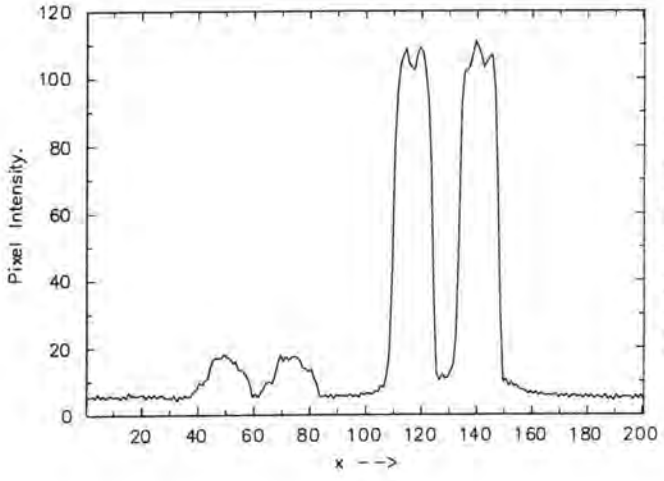

Figure 2.12: Intensity cross section of the image shown in figure 2.11. The dispersion can be found from the distance between the two Sodium D-lines. The resolution can be found from the FWHM of the spectral line profile.

	Angle α°		Image width (μm)		Dispersion (nm/mm)		Resolution $\lambda/\Delta\lambda$	
order	theory	expt	theory	expt	theory	expt	theory	expt
$m = 0$	22.5	22.525	150	148.1	–	–	–	–
$m = -1$	0	0	212.7	209.8	1.962	1.963	1415	1431
$m = +1$	45	45.059	106.7	100.3	2.778	2.768	2000	2123
$m = 0$	22.5	22.527	150	156.7	–	–	–	–
$m = -1$	0	0	212.7	216.9	1.962	1.971	1415	1378
$m = +1$	45	45.055	106.7	104.9	2.778	2.78	2000	2020

Table 2.3: Summary of theoretical predictions and measured performance for the 1200g/mm un-immersed grating with the test spectrograph. The $m = +1$ configuration corresponds to case-a illumination and has higher resolution. Theoretical predictions are listed under the columns headed 'theory' and experimental results under the columns headed 'expt'. The image width is the width of the re-imaged slit.

FWHM of the spectral lines. The accuracy with which the FWHM can be measured is limited somewhat by the software function that is used to approximate the image profile. The accuracy in the measurement of FWHM was estimated to be approximately 0.2 pixels. From the image width, and dispersion, the resolution of the system can be found via equation 2.11. Note that the resolution criteria adopted here is the *Sparrow criteria* (Hutley, 1982) which states that two adjacent wavelengths are just resolved when their respective images of the entrance slit just touch. The Sparrow criteria therefore assumes that the widths of the slits are such that the effects of diffraction and aberrations can be neglected (i.e. no broadening of the image), which is certainly the case with the test spectrograph. The Rayleigh criteria is not used as the images are not diffraction limited.

The measurement of angles of diffraction can determined from the encoders on the motorised rotating stage. The rotating stage encoder is set to zero at the position at which the $m = -1$ spectrum is centred on the detector. This acts as a reference angle from which other angles of diffraction can be measured. The spectrum can be centred on the detector to an accuracy of $\sim 0.02°$ (0.1mm at the detector) simply by observation of the spectral image on the TV monitor. Once the required spectrum is centred on the detector the position of the motorised rotating stage can then be found from the drive software.

The results of the measurements on the un-immersed grating are summarised in table 2.3. Theoretical predictions are listed under columns labelled 'theory' and experimental results under columns labelled 'expt'. The first thing to notice is the small difference between the predicted and measured angles of diffraction. It was found that the optical mount which defines the collimator to camera axis actually produces a collimator to camera angle of $\phi = 45.06°$ and this accounts for the observed difference in angles. This small change in collimator to camera angle has a negligible effect on the other theoretical predictions. In all cases there is some disagreement between the measured image width and the theoretically predicted value. This disagreement is attributed to the errors in setting the slit width, discussed in section 2.8.1, errors in the position of the spectrograph lenses, and measurement errors on the CCD image. The theoretical predictions and measured values of dispersion agree to within 0.5%. Finally, the theoretically predicted values of resolution and the measured values again show some disagreement. The difference between the two values is found to be correlated to the errors in the measured slit width. Therefore if the measured image width is 5% smaller

than the theoretical prediction, then the resolution will be 5% higher.

In conclusion the grating and test spectrograph were found to perform as predicted by the theoretical calculations. The accuracy of the results is mainly limited by the input slit width.

2.9.2 Immersed grating test results

In the first test of immersed grating performance the immersing prism was placed in front of the 1200g/mm grating with an air gap remaining between the prism and the grating surface. This produces an immersed grating with $n_{gap} = 1.0$. The Sodium spectrum produced in this configuration is shown in figures 2.11 and 2.12. It should be noted that the figures show two spectra, the fainter of the two is a ghost image. The ghost image is produced by reflection from the back surface of the prism, which is not antireflection coated. If the prism was in perfect alignment with the grating surface the ghost image would coincide exactly with the primary image. For the purposes of the performance test the prism was deliberately misaligned by approximately 0.1° to avoid problems with the ghost image blurring the measured PSF. A more thorough discussion of the production of ghost images with immersed gratings is given in section 3.6.

The theoretical predictions of immersed grating performance and the experimental results are listed in table 2.4. The small differences between measured and predicted angles is due to the problem described in the previous section. The measured image width is found to be consistently bigger than the theoretically predicted value. This is thought to be due to the limitation on the accuracy with which the input slit width could be set.

The difference between the measured and theoretical values for dispersion in the un-immersed case was $\sim$ 0.5%, but with immersion this increases to $\sim$ 4.0%. In all cases the measured dispersion is higher, i.e. less nanometres per mm, than the theoretically predicted value. The additional dispersion is due to the dispersion of the prism increasing the total dispersion of the system. This effect has already been described in Wynne (1989). The dispersion of the prism was not included in the theoretical calculation. The measured increase in dispersion is consistent with the calculated additional dispersion due to the BK7 prism of 3.7%, within the experimental errors. The additional dispersion of the prism produces a small increase in the resolution of the system. This may be a useful gain for an astronomical

			Angle $\alpha°$		Image width (μm)		Dispersion (nm/mm)		Resolution $\lambda/\Delta\lambda$	
n_{prism}	n_{gap}	order	theory	expt	theory	expt	theory	expt	theory	expt
1.517	1.0	m=-1*	3.8	3.786	175.2	176.5	2.109	2.041	1596	1636
1.517	1.0	m=+1*	48.8	48.85	128.4	133.3	2.46	2.372	1865	1865
1.517	1.0	m=-1*	3.8	3.81	175.2	178.1	2.109	2.030	1596	1630
1.517	1.0	m=+1*	48.8	48.82	128.4	131.9	2.46	2.376	1865	1880
1.517	1.473	m=+3	-3.7	-3.67	327.7	330.7	0.354	0.35	5074	5096
1.517	1.473	m=+2	24.4	24.43	196.9	200.9	0.97	0.954	3087	3075
1.517	1.473	m=+1	48.8	48.8	128.4	133.3	2.46	2.372	1865	1865
1.517	1.473	m=0	76.4	76.5	49.5	62.93	–	–	–	–
1.517	1.473	m=-1	3.8	–	175.2	181.2	2.109	2.031	1596	1602
1.517	1.473	m=-2	-20.6	-20.614	114.3	119.7	1.275	1.253	4046	3929
1.517	1.473	m=-3	-48.6	-48.66	68.4	97.49	0.78	0.771	11044	7843

Table 2.4: Experimental results taken with the immersed grating and the test spectrograph. The results shown with an asterisk were taken with an air gap between the prism and the grating.

immersed grating, particularly if high dispersion glasses can be used, such as Schott SF6. The effect of additional dispersion by the prism makes the measured resolution higher than the theoretically predicted value, however, this gain is somewhat offset by the increased image width which reduces the resolution slightly. The dispersion of the prism also implies that the zero order diffraction from the grating will be dispersed slightly.

Finally the prism was immersed with the grating, using the procedure described in section 2.7.2, and subsequently tested. As diffraction now takes place inside the Glycerol this allows access to the higher grating orders. This cannot be achieved without immersion, i.e. with an air gap, as either the grating equation cannot be satisfied or total internal reflection traps the beam inside the prism. The measured performance of the immersed grating at diffraction orders m=0, 1, 2, and 3 is listed in table 2.4.

The large difference between the theoretical and measured image widths for the $m = 0$ and $m = -3$ cases is due to the optical aberrations of the spectrograph broadening the slit image. These orders require the use of high angles of incidence at the prism surface producing a large anamorphic effect. This broadens the output beam considerably, and produces a displacement of the output beam, thus illuminating the spectrograph camera

under different conditions. Vignetting of the broadened beam by the camera, and the prism, will also contribute to increasing the measured image width, as vignetting will lower the actual anamorphic factor and lead to a broader image. This increased image width also has the effect of significantly degrading the resolution performance.

Note that there is no difference in the performance of the immersed grating, in first order, with or without immersion to the prism. This implies that the immersing layer has no effect on the resolution or dispersion of the system. The high resolutions that are produced in second and third orders can only be obtained by the use of immersion. This, of course, is a direct illustration of the performance gains available via the use of immersed gratings. Without the use of immersion the second and third orders do not propagate.

The results of the experimental tests indicate that the immersed grating does perform as predicted by the theory described in section 2.5. No significant deviations from the theory were observed within the limits imposed by the experimental errors. The difference between the measured and predicted dispersion can be accounted for by including the effect of prism dispersion in the theoretical calculations. The increased dispersion, produced by the prism, is a gain rather than a limitation to the performance of the immersed grating.

2.10 Summary & Conclusions

In the first part of this chapter the performance of an astronomical spectrograph was predicted theoretically. The performance of the Gemini multiobject spectrograph was then considered in more detail. It was found that a resolution of 10,000 can only be obtained with GMOS by using a 0.25 arcsecond slit. This limits high resolution observations to narrow slits unless a way of increasing spectral resolution can be found. The problem is the limiting spectral resolution is inversely proportional to the telescope aperture. Therefore a spectrograph on an 8-m telescope has half the resolution of the equivalent spectrograph on a 4-m telescope.

As a solution to this problem the use of immersed gratings was investigated. Immersed gratings provide a techinique of roughly doubling spectral resolution. The benefits that can be obtained by the use of immersed gratings are summarised as follows:

- Diffraction within a medium of refractive index n allows longer wavelengths, higher ruling densities, and higher diffraction orders to be used.
- The anamorphic properties of the prism reduce the size of camera aperture that is required for a given resolution.
- The anamorphic properties of the prism also allow the illuminated length of grating to be increased.

The net effect of these properties is to produce an increase in spectral resolution. This provides a way of increasing the resolution of spectrographs on 8-m telescopes back to the level obtainable on 4-m telescopes. It also allows smaller spectrographs to be constructed in the infrared where the gains available with high index materials are even greater. It was also noted that an immersed grating can be used in both case-a and case-b illumination conditions providing better coverage of the resolution wavelength parameter space than with an un-immersed grating.

A literature review was also presented summarising the properties of immersed gratings. However, it was noted from the literature review that an experimental verification of immersed grating performance had not yet been carried out. In order to verify the optical performance of an immersed grating, and to look for any unforeseen problems, a prototype immersed grating was constructed and tested. Manufacture of the prototype immersed grating was achieved by coupling a BK7 prism to a 1200g/mm grating with an index matching oil. Glycerol was chosen due to its ability to be readily removed after immersion. Whilst suitable for the laboratory prototype it is likely that oil cannot be used in the environment of an astronomical spectrograph. Manufacturing techniques for immersed gratings are therefore identified as an area which requires further investigation before use in astronomical instrumentation. The theoretical performance of the prototype immersed grating was predicted using ray tracing software developed by the author.

A test spectrograph was constructed in the laboratory to allow accurate measurements of the prototype immersed grating performance. Theoretical predictions of the immersed grating performance were then tested directly on the test spectrograph. The tests showed that the immersed grating performed as expected with the measured resolution, angles of diffraction, and projected slit widths agreeing, within experimental errors, to the theoretical predictions.

A small discrepancy between the predicted dispersion and the measured dispersion was found. This was caused because the theoretical prediction did not include the dispersion of the prism. A slight improvement in dispersion, and hence resolution, can be therefore be produced by using prisms made with high dispersion materials.

The experimental results prove that immersion gratings are feasible and do indeed produce the claimed benefits. This work is then at a stage where it is ready to be applied to the production of an immersed grating for use in an astronomical spectrograph. This work shows that immersed gratings offer the capability of providing a high resolution upgrade to the GMOS instrument, allowing resolutions of up to 25,000 to be obtained.

Chapter 3

Immersed gratings: Efficiency

Abstract

This chapter presents measured efficiency curves for the prototype immersed grating described in the previous chapter. Theoretical predictions of immersed grating efficiency, and the position of passoff anomalies, are also described. It is found that the peak blaze efficiency of the prototype immersed grating is $\sim 15\%$ lower than that measured with the un-immersed grating. The blaze peak is also shifted to longer wavelengths because of the refractive index of the prism. The loss in efficiency is attributed to two main loss mechanisms: air-glass reflection losses at $\sim 8\%$, and metal-dielectric losses (the reduction in reflectivity of an immersed metal surface) accounting for the remaining loss. This chapter presents conclusive evidence for the measurement of metal-dielectric losses which have been overlooked in previous published work. Finally the production and measurement of ghosts is discussed. The integrated intensity of the brightest ghost was found to be $\sim 2\%$ of the parent line. Ghosts are therefore not thought to be a cause for concern given they can be eliminated by use of antireflection coatings.

A grating can lead to a blur,
When it's lines cause some ghosts to occur.
I showed wriggles and bumps,
And then also some lumps,
But reviewers have yet to concur.
(Anon.)

3.1 Introduction

A number of papers described in the literature review of section 2.4 discussed the possibility of using an immersed grating to achieve high resolution. The theoretical predictions of the optical performance of an immersed grating have now been verified experimentally, as described section 2.9.2. Therefore the optical performance of an immersed grating can be accurately predicted using the theory presented in section 2.5. Another important aspect of the performance of any dispersion system is its efficiency. That is the ratio of the amount of light in the useful diffracted beam to that incident on the grating. To date only a small number of authors have presented preliminary data on measurements of immersed grating efficiency: Radley *et al.* (1994) , Dekker (1992), and Wiedemann & Jennings (1993). Rather worryingly both Dekker and Wiedemann find unexplained efficiency losses occur when the grating is immersed. Perhaps the reason then that immersed gratings have not been pursued for use in instruments is the worry that the efficiency is compromised with immersion. It is therefore crucial that a detailed study of the efficiency loss mechanisms with immersed gratings is performed. Only Radley claims that the efficiency is not significantly affected by immersion, although it will be shown later that this result was a misunderstanding. The aim of the work described in this chapter is to predict, measure, and understand the behaviour of grating efficiency with immersion. A full experimental investigation is especially important given the confusion in the published literature.

This chapter describes the construction of laboratory apparatus, and the series of experiments performed on the prototype immersed grating, to characterise its efficiency and investigate in detail any loss mechanisms. The aim of these experiments is to fully understand the changes in efficiency which occur with immersion. Theoretical predictions of immersed grating behaviour are also presented for comparison with the measured results. A number of efficiency loss mechanisms were measured and these are described in detail. This chapter also describes the measurement of ghost images that are produced by multiple reflections within the immersing prism.

3.2 Theoretical predictions of grating efficiency

Before the experimental results of immersed grating efficiency can be fully understood it is necessary to have some prior knowledge of what performance, and changes in performance, are to be expected. This section describes the theoretical prediction of grating efficiency characteristics and the prediction of the occurrence of Rayleigh passoff anomalies.

3.2.1 Scalar theory

The efficiency of a diffraction grating, for configurations which satisfy certain assumptions, can be predicted from scalar theory. The major assumption of scalar theory is that geometrical optics can be used to predict to behaviour of the incident and diffracted light. This also assumes that the behaviour of the grating is independent of the polarization of the incident light. The assumptions made in assuming scalar theory therefore limit its use to the region where the inequality $\lambda/\sigma < 0.2$ is satisfied, where σ is the groove length. Scalar theory is therefore particularly useful for predicting the efficiency of echelle gratings where λ/σ is quite small (< 0.02).

The prediction of diffraction grating efficiency, using scalar theory, proceeds as follows. Many of the angles used in the following equations are shown in figure 3.1. The intensity of the diffracted beam, I, is given by the following formula, adapted from James & Sternberg (1969):

$$I = I_0 \left(\frac{\sin^2 N\gamma'}{\sin^2 \gamma'} \right) \left(\frac{\sin^2 \gamma}{\gamma^2} \right) \tag{3.1}$$

where I_0 represents an intensity normalisation factor, γ' is the phase difference between the centres of radiation from adjacent slits and γ is the phase difference between the rays coming from the centre and edge of one slit. N represents the total number of grooves. As N increases so does the theoretical resolving power of the grating. The intensity envelope of the diffracted beam is defined by the diffraction pattern for a single slit multiplied by the diffraction pattern for multiple slits. The sinc function represents a single slit diffraction pattern, and the periodic function represents the multi-slit diffraction pattern.

The first phase term, γ', is given by:

$$\gamma' = \frac{k\sigma}{2}(\sin i + \sin \theta) \tag{3.2}$$

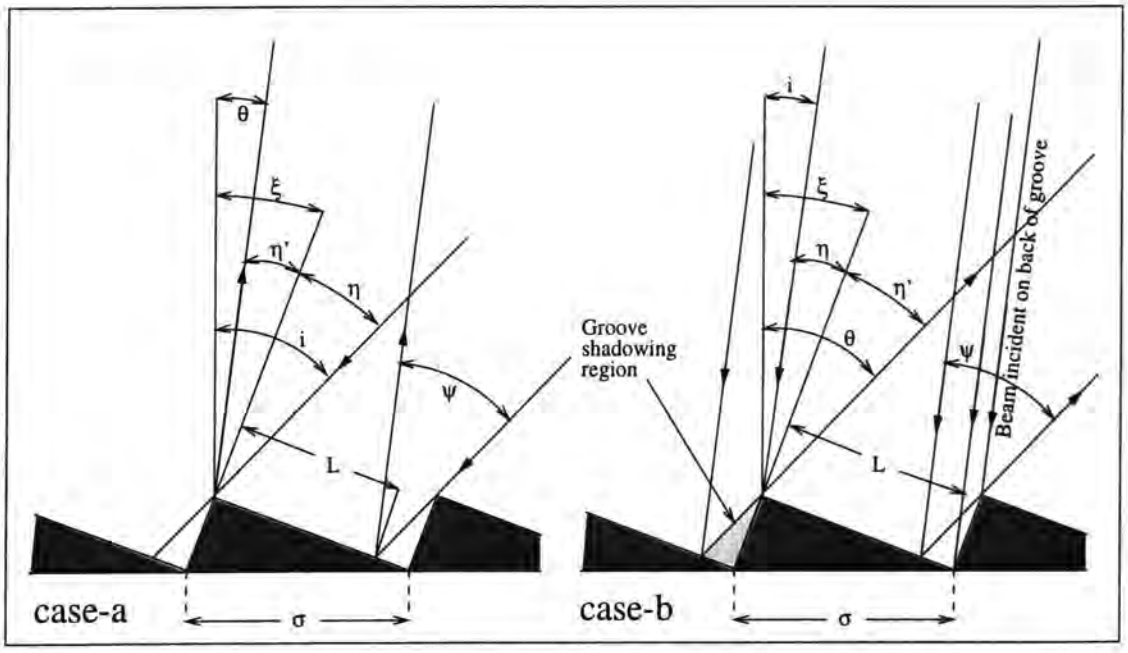

Figure 3.1: Illustration of case-a and case-b illumination types at the diffraction grating surface. With case-b illumination a small fraction of the input beam is incident on the back surface of the facet, and a portion of the diffracted beam is shadowed by the groove profile. Case-a corresponds to $i > \xi$ and case-b corresponds to $i < \xi$. The various angles are labelled as follows: i is the angle of incidence, θ is the angle of diffraction, ξ is the blaze angle all measured with respect to the normal to the grating, ψ is the angle between the camera and collimator axes, η is the angle between the incident ray and the facet normal, and η' is the angle between the diffracted beam and the facet normal. L is the illuminated length of the facet and σ is the groove spacing.

where σ is the groove length (the grating spacing), $k = 2\pi/\lambda$, and i and θ are the angles of incidence and diffraction respectively measured with respect to the grating normal. The condition for a maximum in intensity in equation 3.1 is $\gamma' = \pm n\pi$, where n is an integer. When this condition is satisfied equation 3.2 reduces to the more familiar grating equation, equation 2.1.

The second phase term, γ, is given by:

$$\gamma = \frac{kL}{2}(\sin\eta + \sin\eta') \tag{3.3}$$

where k is as before, L represents the illuminated width of the grating facet, η is the angle between the facet normal and the incident beam (see figure 3.1), and η' is the angle between the facet normal and the diffracted beam. The illuminated length of the facet is given by;

$$L = \sigma\cos\xi - \sigma\sin\xi\tan\eta \tag{3.4}$$

Equations 3.1–3.4 can be solved to find the intensity I in each diffraction order that propagates. The efficiency of the diffraction grating in a given order is then given by the ratio of the intensity in that order to the summed intensities over all orders (Schroeder & Hilliard, 1980). The illuminated width of the facet, L, is important because it varies depending on the angle of incidence of the input beam. Two configurations[1] of groove illumination are possible: generally referred to as case-a, where the angle of incidence is greater than the blaze angle, and conversely with case-b (Szumski, 1995). The illuminated length of groove is different in each case. Figure 3.1 illustrates examples of case-a and case-b illumination conditions. With case-b illumination a fraction of the incident beam illuminates the back surface of the grating facet and is lost[2]. Also a small portion of the diffracted beam is vignetted by the groove producing *groove shadowing*. These two effects combine to produce a reduction in efficiency for case-b illumination. In case-a illumination all of the incident beam is diffracted and no groove shadowing occurs although the illuminated length of groove may be smaller. Experimental observations of the reduction in efficiency with case-b illumination are presented in Schroeder & Hilliard (1980). In Astronomical spectrographs case-a illumination is therefore the preferred choice.

[1]Strictly speaking three configurations are possible if the configuration where the incident and diffracted beams are out of the plane of the grating is included.

[2]With geometrical optics it should undergo corner cube reflection, however, reflection at this angle doesn't necessarily obey the grating equation.

3.2.2 Change in blaze wavelength

A grating is said to be blazed if the diffracted light has a maximum in efficiency for some diffracted wavelength. The blaze condition occurs when the sinc function in equation 3.1 reaches a maximum. This occurs when equation 3.3 is equal to zero implying $\eta = \eta'$ i.e. the incident and diffracted beams undergo normal reflection from the grating facet. This is equivalent to saying the light from the centre and edge of the facet is in phase. Combining equations 3.3 and 3.4 and substituting for η and η' produces the following equation relating the blaze wavelength, λ_b, to the blaze angle and the angle between the collimator and camera axes;

$$\frac{m\rho\lambda_b}{n} = 2\sin(\xi)\cos\left(\frac{\psi}{2}\right) \tag{3.5}$$

where the variables are as already described in section 3.2.1. From this equation it is straightforward to predict the behaviour of the blaze wavelength with changing spectrograph configurations. If the collimator to camera angle is increased then there is a corresponding decrease in the blaze wavelength according to the $\cos(\psi/2)$ term. The longest blaze wavelength occurs with a Littrow configuration and *departure from Littrow reduces the blaze wavelength.* The measured change in blaze wavelength with departure from Littrow for a grating, as predicted by the theory presented, is described in section 3.4.1. The equations presented can also be used to predict that the blaze peak efficiency is reduced when the angle ψ is increased, as shown in Szumski (1995). It is important to note that departure from Littrow conditions also changes the wavelengths at which anomalies occur, as discussed in section 3.2.4.

3.2.3 Failure of scalar theory

The scalar theory of diffraction grating efficiency produces reasonable results for the region $\lambda/\sigma < 0.2$. However this method has some serious limitations: it does not take account of the reflectivity of the grating surface, and the theory becomes increasingly unreliable for $\lambda/\sigma > 0.2$. In the region $\lambda/\sigma > 0.2$ polarization effects also become important. Scalar theory does not include any treatment of polarization. The efficiency curves for the two polarizations split with the P-plane efficiency profile resembling the the scalar case. The S-plane profile shows significant structure. These effects are due to the interaction of the electromagnetic wave with the metallic surface of the grating and can only be explained with

a full electromagnetic wave solution. The electromagnetic treatment involves the solution of the boundary value problem at the grating surface and is a complex mathematical and computational problem. The electromagnetic solution is beyond the scope of this work. More details on the electromagnetic treatment of diffraction grating efficiency can be found in: Maystre *et al.* (1980), Loewen *et al.* (1977), and Hutley (1982).

Scalar theory also violates the *reciprocity theorem.* The reciprocity theorem states that the efficiency has the same value in case-a and case-b and equivalently the efficiency in zero order does not change when the grating is rotated by 180° about an axis which is perpendicular to the plane on which it has been ruled. The violation of reciprocity theorem by scalar theory can be explained as the scalar theory presented does not include the width of the diffracted image in the calculation of efficiency. It is simply assumed that efficiency can be calculated from the ratio of peak intensities. If the change in image size is included, as in described in Bottema (1981), then this accounts for the efficiency difference between case-a and case-b illumination. In case-b the diffracted beam has a lower amplitude but this is compensated for by the increased width of the image[3] such that the total integrated intensity in the image is the same. Case-a illumination produces higher resolution-luminosity product and is generally preferred for use in Astronomical spectrographs.

It is therefore a general rule that as the wavelength approaches the grating spacing electromagnetic theory has to be used. The limitation of scalar theory to the regime where $\lambda/\sigma < 0.2$ means that it can only be used to make qualitative predictions for the performance of the prototype immersed grating such as: approximate position of blaze wavelength, change in blaze wavelength with increasing collimator to camera angle, and wavelength at which passoff anomalies occur. The scalar theory described will be used to make these predictions during the rest of this chapter. The prediction of polarization effects requires electromagnetic theory and is beyond the scope of this work.

3.2.4 Anomalies

The scalar theory presented above is inadequate to accurately predict the efficiency of a diffraction grating. It can, however, be used to predict the wavelength at which anomalies

[3]In case-b illumination the projected image of the slit is broadened due to the anamorphic properties of the grating, i.e. conservation of etendue.

occur, as described in the following section.

An anomaly is simply a sharp discontinuity in a grating efficiency curve, examples of which are labelled in the measured efficiency curves shown in figure 3.4. Anomalies occur in two distinct types: *Rayleigh passoff anomalies* and *resonance anomalies.* Rayleigh anomalies occur when the angle of diffraction is 90° and the diffraction order skims the grating surface, i.e. the order is said to 'passoff' the grating surface. The position of Rayleigh passoff anomalies is not affected by the grating surface material, it only depends on wavelength and diffraction geometry. Other anomalies can be classified as resonance phenomena and are due to energy absorption by the surface of the grating. The periodic groove structure is capable of coupling between the incident electromagnetic field and the electrons in the surface. These anomalies are then critically dependent on the surface structure and conductivity. Resonance anomalies are frequency dependent and may not be influenced by the immersing medium.

This section concentrates on the variation of Rayleigh passoff anomalies with immersion as the position of passoff anomalies can be predicted using scalar theory. The prediction of resonance anomalies again requires a full electromagnetic solution and is not presented here. A full description of the various types of anomaly can be found in Hutley (1982, chapter 6). Anomalies which are particularly strong are a nuisance as not only do they cause a reduction in efficiency but their signature may be introduced into astronomical spectra. For example, the un-immersed Littrow grating anomaly at 555nm (section 3.4.5) can be clearly seen as a dark band across a white light spectrum, taken with the efficiency spectrograph. The presence of anomalies may make accurate flux calibration difficult and, in extreme cases, may even be confused with spectral features.

The wavelengths at which passoff anomalies occur, for various configurations of collimator to camera angle and prism angle, are listed in table 3.1. Note that in the Littrow configuration that two diffraction orders leave the grating surface (they 'passoff') at the same wavelength. As the collimator to camera angle departs from Littrow the anomalies split and occur at different wavelengths. Therefore there are fewer anomalies in Littrow configuration. The wavelength of anomalies with the immersed grating is identical with that for the un-immersed grating if the wavelength is corrected for the refractive index of the immersing medium. For example, the immersed m=-2 passoff anomaly at 492nm is equivalent to the un-immersed m=-2 passoff anomaly at 334nm as 492/1.473=334. The position of anomalies was predicted

		Diffraction order (m) and passoff wavelength						
ψ	ϕ	$m=-3$	$m=-2$	$m=-1$	m=0	m=1	m=2	m=3
0°	0°	239nm	334nm	556nm*	—	—	556nm*	334nm
8°	0°	255nm	357nm	593nm	—	—	518nm	310nm
28°	0°	296nm	413nm	678nm	—	—	425nm	254nm
45°	0°	328nm	455nm*	744nm	—	—	348nm	205nm
0°	30°	352nm	492nm	819nm*	—	—	819nm*	491nm
45°	30°	432nm	608nm*	1012nm	—	—	624nm*	381nm

Table 3.1: Table of wavelengths at which diffraction occurs, for various diffraction orders, along the grating surface causing S-plane Rayleigh passoff anomalies. Note that the wavelength at which anomalies occur changes with increasing collimator to camera angles. The wavelengths marked * indicate the anomaly was observed in the grating efficiency curves described in section 3.4.

using an adapted version of the optical ray tracing software described in section 2.6. Note that the immersed grating anomaly at $\sim$ 615nm is expected to be particularly strong because it consists of two anomalies which have converged to the same wavelength. The merging of two anomalies in this way is quite common as the collimator to camera angle is varied. In summary: *Rayleigh passoff anomalies are only dependent on* $\lambda/\sigma n$, and their position can therefore be predicted using scalar theory.

The design flexibility with immersed gratings, to change the prism angle and refractive index, allows the wavelength at which anomalies occur to be changed. This feature may be useful in avoiding the production of anomalies at important wavelengths for astronomical study.

3.3 Experimental measurement of grating efficiency

This section describes the experimental apparatus developed to accurately measure the efficiency of the prototype immersed grating. A detailed description is given of how the experiment was performed. The data analysis, and sources of experimental error are also discussed.

3.3.1 Spectrograph to measure efficiency

The optical arrangement used to measure the efficiency of the prototype immersed grating is a modification of the test spectrograph already described in section 2.8.1. An optical diagram of the efficiency spectrograph can be seen in figure 3.2. The experimental apparatus is based on a similar experiment (Johnston *et al.*, 1986) used to measure the efficiency of the Anglo-Australian Observatories' diffraction gratings.

The Sodium lamp used in the test spectrograph has been replaced with a current stabalized Tungsten filament lamp. A stable power supply is used to provide constant current (or Voltage) to the lamp. A constant current supply is necessary to achieve a constant level of illumination during the time period of the efficiency experiment. Errors in the measurement of efficiency will be introduced if the lamp output varies considerably between measurement of the grating beam flux and the reference beam flux. The output of the lamp was found to be constant at the 0.5% level over a time period of 10 minutes. Note the lamp output was also found to be repeatable on a day to day basis providing the current is set to the same value as before.

In order to measure the efficiency of the immersed grating at different wavelengths a variable monochromatic light source is needed. This was provided by means of an Oriel 77250 1/8m grating monochromator. The light source illuminates the monochromator input slit via a small condenser lens. The bandwidth of the monochromator is defined by the width of the output slit. For the efficiency experiment a bandwidth of 5nm FWHM (note the monochromator output is a triangle function) was selected by using a slit width of 0.75mm. The output slit was constructed from Boots razor blades! The monochromator slit width has to be large enough to provide adequate flux whilst being narrow enough that the bandwidth doesn't disguise narrow features present in the grating efficiency curve. The wavelength which the monochromator produces can be set to an accuracy of less than 1nm.

An order sorting filter was placed at the input slit of the monochromator to avoid contamination from the second order spectrum. A neutral density filter was also placed in the diverging beam after the monochromator to allow adjustment of the intensity without the need to adjust the stable light source. Frequent adjustment of the light source may cause stability problems. The diverging output beam from the monochromator is collimated using

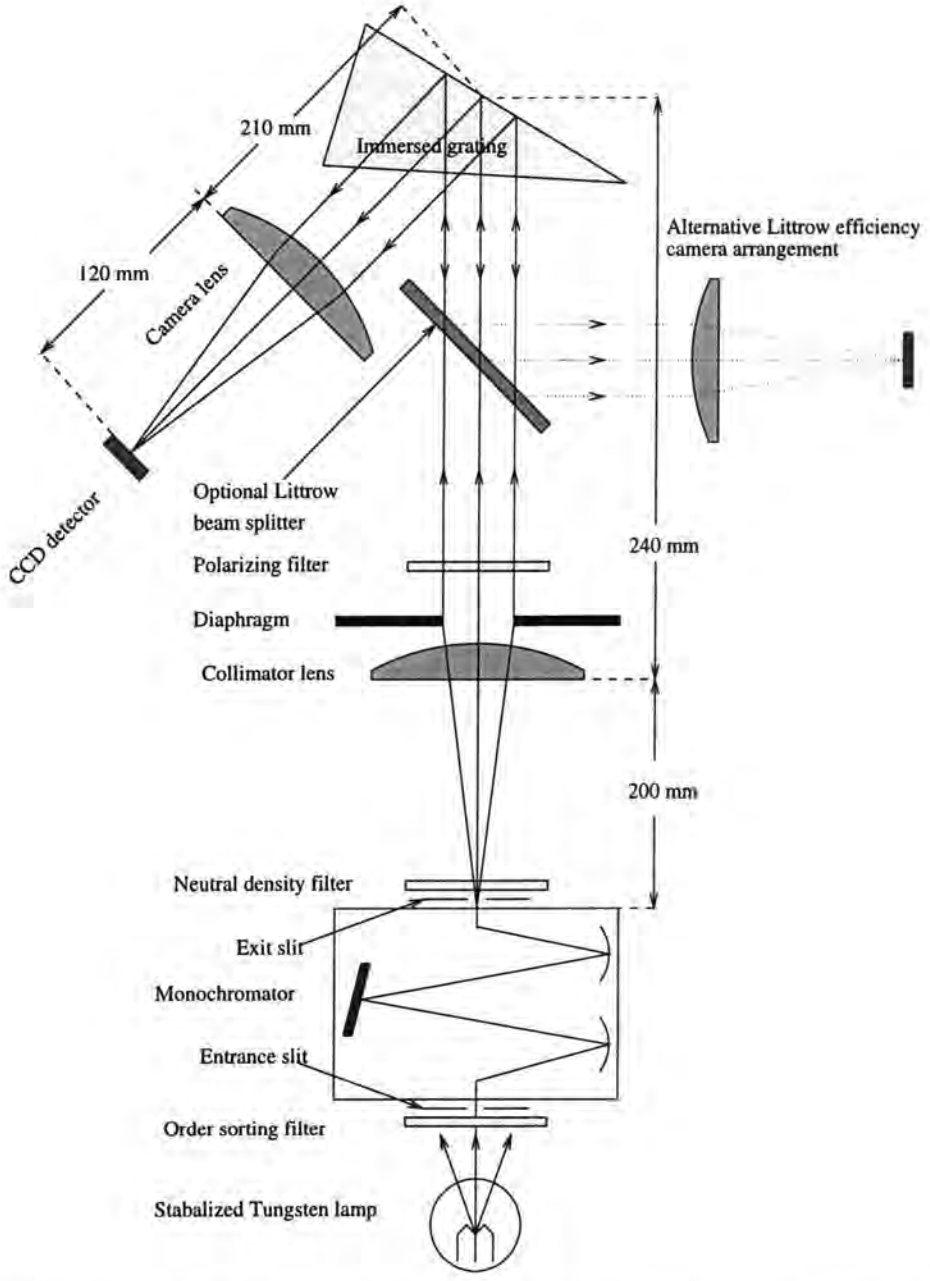

Figure 3.2: Schematic of the spectrograph used to measure the efficiency of the prototype immersed grating. Note the two alternative camera arrangements. The immersed grating can be quickly replaced with a mirror to allow efficiency measurements relative to the mirror to be made.

a 200mm focal length plano-convex lens. As with the test spectrograph, a diaphragm is used to limit the beam size to 10mm in order to reduce aberrations.

A linear polarizing filter is placed in the collimated beam to produce linearly polarized light. This allows light which is polarized at any angle with respect to the grating rulings to be produced. A Polaroid[4] HN32 polarizing film was used over the wavelength range 400–750nm. Redward of 750nm the HN32 looses its polarizing properties. In the range 750–1000nm an HR polarizing film was used. Light polarized at 45° with respect to the grating rulings is used to represent un-polarized light.

The linearly polarized beam is then incident on the immersed grating where diffraction occurs. The dispersed beam is then imaged onto the CCD detector by a 120mm focal length plano-convex lens. A short focal length camera is needed to reimage the broad monochromator slit onto the detector at a suitable magnification. The grating efficiency can be measured with either $\psi = 0°$, Littrow configuration, or $\psi = 45°$ between the collimator and camera axes. The Littrow configuration is achieved by inserting a beam splitter into the collimated beam to reflect the dispersed beam onto the camera arrangement, as illustrated in figure 3.2. The extra reflection by the beam splitter in the Littrow arrangement does not affect the measurement of efficiency, although a brighter light source is needed to compensate for the additional reflection losses.

3.3.2 Efficiency measurement procedure

The efficiency of the immersed grating is measured in comparison with a reference mirror. The flux in the diffracted beam from the grating is first measured. The grating is then replaced with the reference mirror and the flux in the reflected beam is measured. The ratio of the two measurements provides the *relative efficiency* of the diffraction grating, the measurement being relative to the reflectivity of the mirror. The *absolute efficiency* can be found by correcting the relative efficiency ratio for the reflectivity of the reference mirror.

The experimental procedure is as follows: first the monochromator is set to the appropriate wavelength and the grating stage is rotated to the correct angle such that the dispersed

[4]More information on the Polaroid range of linear polarizing films, including data sheets, can be found at: http://www.polaroid.com/products/oem/polarizers/products/lin-polar.html

image is present in the centre of the detector. Errors due to variations in pixel response[5] across the detector are minimised by always illuminating the same portion of the detector. The appropriate order sorting filter, typically a GG455 or GG495 Schott glass filter, is placed before the monochromator to avoid second order contamination. Then adjustments are made to the focus of the collimator and camera lenses to correct for chromatic aberration. The maximum intensity in the CCD image is then checked to ensure it is within the linear range of the detector. The COHU CCD detector and frame grabber, described in section 2.8.3, were used for the measurement of grating efficiency. The beam intensity is adjusted accordingly, to ensure that the detector operates within its linear range, by means of neutral density filters or variation of the power supply. The dispersed image produced by the grating can then be digitally recorded. The grating assembly is then removed and the reference mirror is inserted in place producing a reflected image of the monochromator slit on the CCD camera. After alignment a reference mirror exposure is taken for comparison with the grating exposure. The procedure is then repeated for different wavelengths. Efficiency measurements were limited to within the wavelength range 400–1000nm by the intensity of the light source and the quantum efficiency of the CCD.

3.3.3 Data analysis

The images are analysed using IRAF astronomical data reduction software. An efficiency measurement image would look similar to that shown in figure 3.14 except that the ghost image would not be present, only the 'primary' image would appear. The background level in the exposure is estimated from the region surrounding the slit image, in a manner similar to astronomical photometry, avoiding the need for separate background exposures. The background level is partly due to the contribution from dark current of the detector and a contribution from stray light within the laboratory. Following background subtraction of the images the relative efficiency of the immersed grating can be found by taking the ratio of the total integrated counts in the grating exposure to the total integrated counts in the reference mirror exposure.

The absolute grating efficiency can then be found by correcting the relative efficiency for the reflectivity of the reference mirror. The measured reflectivity of the laboratory reference

[5]The pixel response was found to vary by 1% across the detector.

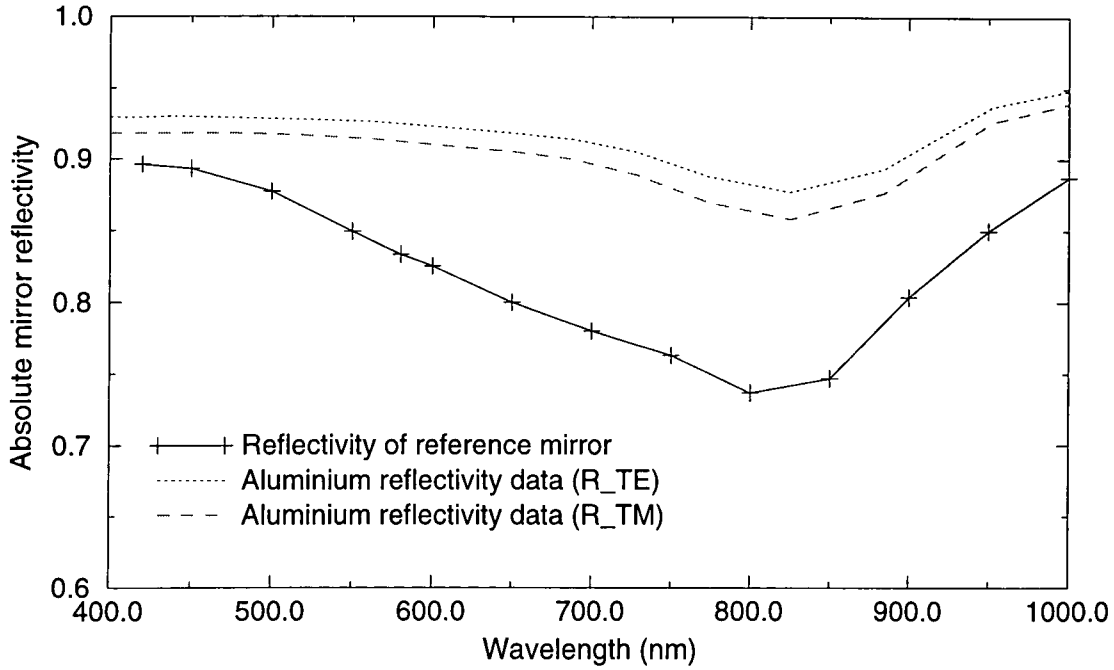

Figure 3.3: Plot of the reflectivity of the reference mirror used in the measurement of grating efficiency. Errors are indicated by the size of the symbols. The mirror reflectivity was measured with $\psi = 45°$. Also shown is the theoretical reflectivity data for a freshly deposited Aluminium surface, in both transverse electric, labelled R_TE, and transverse magnetic, labelled R_TM, polarizations, data taken from Shiles (1980). Note the difference in reflectivity between the two polarization states. The reflectivity for unpolarized light is the average of the two.

mirror is shown in figure 3.3. The reflectivity of the reference mirror was measured using a modified version of the efficiency spectrograph. The camera assembly was mounted on a rotating arm to allow the collimator to camera angle to be varied anywhere in the range $20° - 180°$. The reflected beam from the reference mirror was measured with $\psi = 45°$. The mirror is then removed and the intensity of the direct beam is measured with $\psi = 180°$, i.e. the 'straight through' position.

The reflectivity of the mirror was measured with 45° polarized light only as the measured difference in reflectivity between S and P-plane polarizations was less than 1% and can therefore be ignored. The error in the measurement of the reflectivity of the reference mirror is indicated by the size of the symbols plotted in figure 3.3, i.e. approximately $\pm 0.5\%$. Note that the reference mirror used has a particularly low reflectivity, however this does not affect the accuracy of the efficiency measurements. The low reflectivity may be due to

a degradation of the surface coating. A freshly coated mirror would be expected to have a reflectivity closer to the theoretical prediction, also shown in figure 3.3. Definitions of transverse electric and transverse magnetic polarizations can be found in optics texts such as Pedrotti & Pedrotti (1993).

3.3.4 Errors in the measurement of efficiency

There are two main sources of errors in the measurement of efficiency: light source intensity variations, and background subtraction errors. As discussed in section 3.3.1 the light source variations are less than 0.5%. Errors are also introduced in the data reduction process if the contribution from background light is incorrectly estimated from the dispersed image. This produces an uncertainty of approximately 0.5% in the integrated intensity for both the grating and reference mirror exposures. The uncertainty in the measurement of absolute grating efficiency is therefore approximately 1%. The accuracy of the results was confirmed by the excellent agreement of efficiency measurements taken many days apart.

3.4 Efficiency results

In this section the results of the experiment to measure the efficiency of the prototype immersed grating are presented. The results are discussed and compared with the theoretical predictions of section 3.2. This section also contains some discussion of *Rayleigh passoff anomalies* which can be seen in the measured grating efficiency curves. Anomalies were described in more detail earlier in section 3.2.4.

3.4.1 Comparison of immersed and un-immersed grating efficiency

The efficiency of the immersed grating was measured using the procedure described in section 3.3.2. In the first experiment the efficiency of the immersed grating was measured with a collimator to camera angle of 45° , with case-a illumination conditions and with 45° polarized light. This configuration was used to simulate conditions in an astronomical spectrograph. The efficiency of the un-immersed portion of the grating was also measured, in the same configuration, for comparison. The measured efficiency curves are presented in figure 3.4.

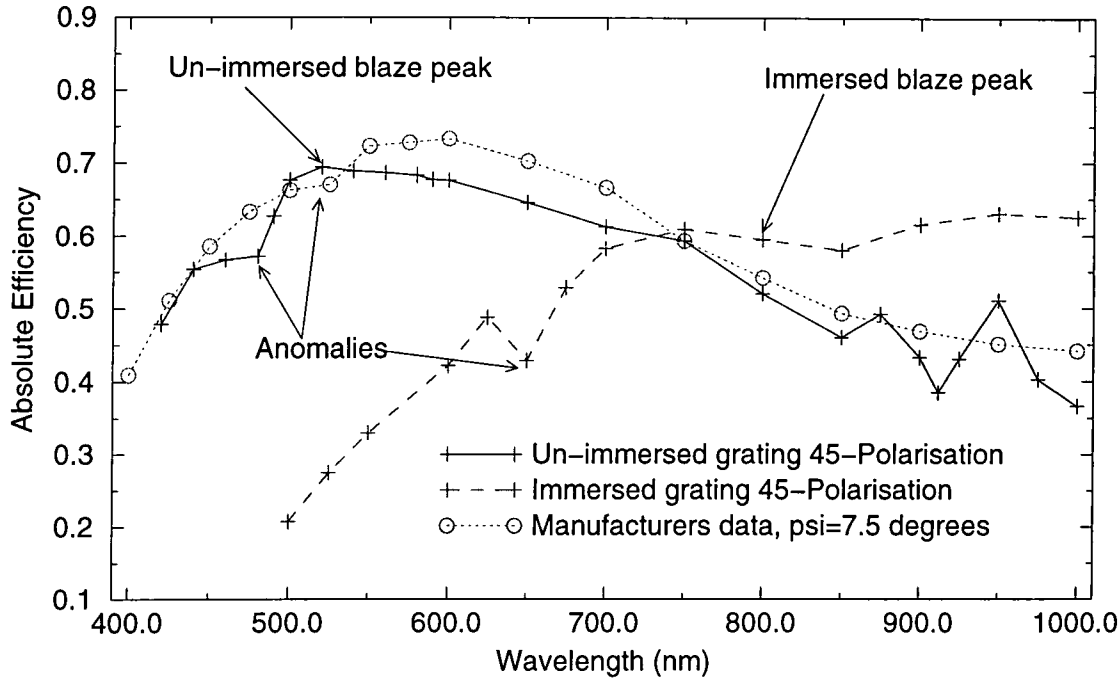

Figure 3.4: Plot of absolute efficiency curves for the immersed grating and the un-immersed grating taken with $\psi = 45°$. Also shown for comparison is the efficiency curve from the manufacturers data sheet, taken with $\psi = 7.5°$.

The size of the symbols used in all subsequent efficiency plots indicates the magnitude of the experimental errors. Note that in some cases the absolute efficiency curves are shown i.e. the efficiency has been corrected for the reflectivity of the reference mirror. The reflectivity of the reference mirror is shown in figure 3.3.

Also shown in figure 3.4 is the efficiency curve taken from the manufacturers (Milton-Roy) data sheet. The manufacturers data was obtained with a collimator to camera angle of 7.5 degrees. The manufacturers data exhibits a blaze peak at approximately 600nm. This is in good agreement with the blaze wavelength of 596nm predicted using scalar theory described in section 3.2.1, equation 3.5. The blaze peak with $\psi = 45°$ shifts to shorter wavelengths and occurs at approximately 530nm. This is in reasonable agreement with the predicted value from scalar theory of 552nm. This demonstrates that the position of the blaze wavelength can only be estimated using the scalar theory, more accurate predictions of grating performance requiring a full electromagnetic solution.

The peak efficiency in the $\psi = 45°$ configuration is reduced by $\sim 5\%$ compared with the peak efficiency in the $\psi = 7.5°$ configuration. It is well known (Loewen *et al.*, 1977) that

the blaze efficiency is reduced as the collimator to camera angle is increased. Similar results for a 1200g/mm grating are presented in Johnston *et al.* (1986). Scalar theory can be used to predict this decrease in efficiency when the theory is applicable. As the collimator to camera angle is reduced towards a Littrow configuration case-a and case-b illumination conditions become increasingly similar. In Littrow there are no groove shadowing losses, the illuminated length of groove also reaches a maximum, and the efficiency can be expected to be higher. The position of passoff anomalies also changes, it shifts to shorter wavelengths as the collimator to camera angle is increased. Passoff anomalies occur when one or more diffraction orders is diffracted along the grating surface, i.e. $\theta = 90°$. As this diffraction order no longer propagates the energy previously contained within that order is redistributed among the other orders leading to discontinuities in the efficiency at that wavelength. Anomalies were described in more detail in section 3.2.4.

The cause of the structure in the un-immersed grating efficiency curve in the region 850–1000nm is unknown. It may be in some way related to the performance of the infrared polarizer. However, the data sheet for the infrared polarizer shows no marked variation in polarization capability in this wavelength range. Similar behaviour can be seen in the 1200g/mm grating efficiency curves presented in Johnston *et al.* (1986) indicating that this is a common feature of 1200g/mm gratings.

The immersed grating exhibits a blaze peak which occurs at approximately 800nm. The position of the blaze peak is determined by the wavelength within the immersing medium. A blaze wavelength of 800nm is therefore equivalent to a blaze wavelength in air of $\sim 540nm$ i.e. $800/n_{gap}$. Unfortunately the immersed blaze peak coincides with the Aluminium absorption feature at $\sim 800nm$ somewhat disguising the shape of the blaze peak. The position of the blaze peak can be seen more clearly in figure 3.6. As the position of anomalies is also wavelength dependent they too change position, by a factor of approximately the refractive index of the immersing medium, upon immersion. It should be noted that the shift in the position of the blaze peak only occurs if the prism is immersed to the grating. The prototype immersed grating can also be used with an air gap between the prism and the grating surface in which case there would be no shift in the blaze peak.

The major result of the immersed grating efficiency measurement is that *the blaze efficiency is reduced with immersion.* Figure 3.4 shows that the immersed blaze efficiency is approximately

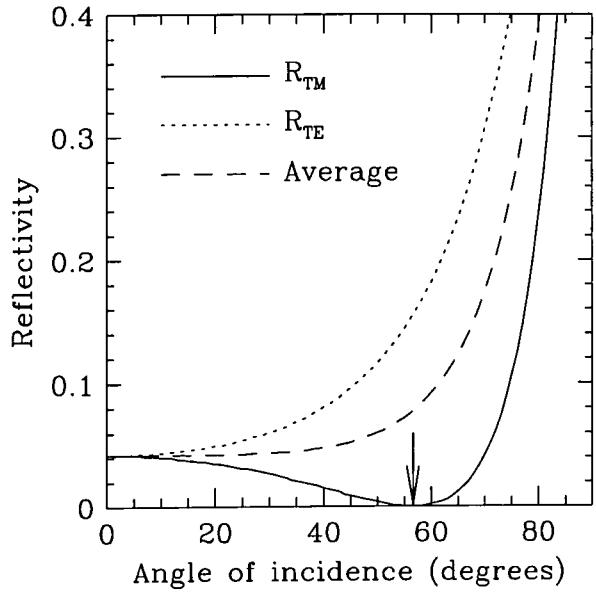

Figure 3.5: Plot of reflectivity of an air-glass surface. The glass has a refractive index of 1.5. Reflectivity curves for TE, TM and unpolarized (labelled average) light are shown. The position of Brewster's angle is marked with an arrow.

15% lower than with the un-immersed grating. This reduction in efficiency is partly due to Fresnel's reflection losses at the uncoated surface of the immersing prism. Air-glass losses account for a reduction in efficiency of $\sim 4\%$ per air-glass interface, as shown in figure 3.5. Air-glass reflection losses can be avoided by the use of suitable antireflection coatings and these are discussed in more detail in appendix A.1. Absorption losses in the BK7 glass prism and the immersing layer of Glycerol account for less than 0.1% of the total loss. The small difference in refractive index between the Glycerol and the BK7 prism produces reflection losses of 0.04%. The remaining loss is attributed to the reduction in reflectivity of a metal surface when it is immersed. These *metal-dielectric losses* are a cause of confusion in previous published measurements of immersed grating efficiency (Radley *et al.*, 1994). Due to their importance a separate investigation of metal-dielectric losses was performed, as described in section 3.5. The efficiency data presented here and efficiency loss mechanisms present with immersed gratings are discussed in more detail in section 3.4.5.

Note that a shift in blaze wavelength will occur even if the immersing medium is a plane parallel piece of glass rather than a prism. This effect was first described in the original immersed grating experiment (Hulthen & Neuhaus, 1954). The ability of an immersed grating to tune the blaze wavelength via appropriate choice of the immersing medium may be a useful property. In this way the blaze wavelength can be optimised to suit a particular astronomical application. This gives more choice of blaze wavelengths than is available with

un-immersed gratings which can only be obtained with certain blaze angles. Taking this idea further an immersed grating in oil can be imagined. By using oils of different refractive indices, and allowing the oil to be changed, a grating with a variable blaze wavelength could be produced. This would have the advantage of the highest possible efficiency for any wavelength of observation.

3.4.2 Comparison of case-a with case-b efficiency

A plot of both case-a and case-b relative efficiency curves, for immersed and un-immersed grating configurations and 45° polarized light, is shown in figure 3.6. It is clear from the plot that there is no difference, within the experimental uncertainties, between the efficiency measured with case-a illumination and case-b illumination. This indicates that the effect of groove shadowing, if any, is at a level of less than 1%. This result also demonstrates that the grating can be used with either a blaze to collimator configuration, or a blaze to camera configuration, without any loss in efficiency. Note that the relative efficiency curves, which are independent of the reflectivity of the Aluminium grating coating, show the position of blaze peaks more clearly than the absolute efficiency curve shown in figure 3.4. By displaying relative efficiency curves the immersed blaze peak is not disguised by the Aluminium absorption feature at 800nm. It should be noted that grating manufacturers often provide relative efficiency curves, which can mislead the reader into thinking the efficiency is higher than is actually the case.

Note the two data points obtained in second order[6] with the immersed grating are also shown. Second order is only available at these wavelengths with the use of immersion. The second order efficiency would be expected to peak at approximately 400nm. It would be an interesting exercise for the future to measure the efficiency of immersed grating in the different orders. The efficiency in the higher orders is important as one of the advantages of using immersed gratings is that they allow higher orders to be used, resulting in higher spectral resolutions. Second order measurements could not performed with the current design of efficiency spectrograph due to limitations of the equipment.

It should be stressed that obtaining the same efficiency with case-a and case-b illumination is

[6]The second order measurements were originally mistaken for first order measurements until the dispersion indicated that they were in fact second order.

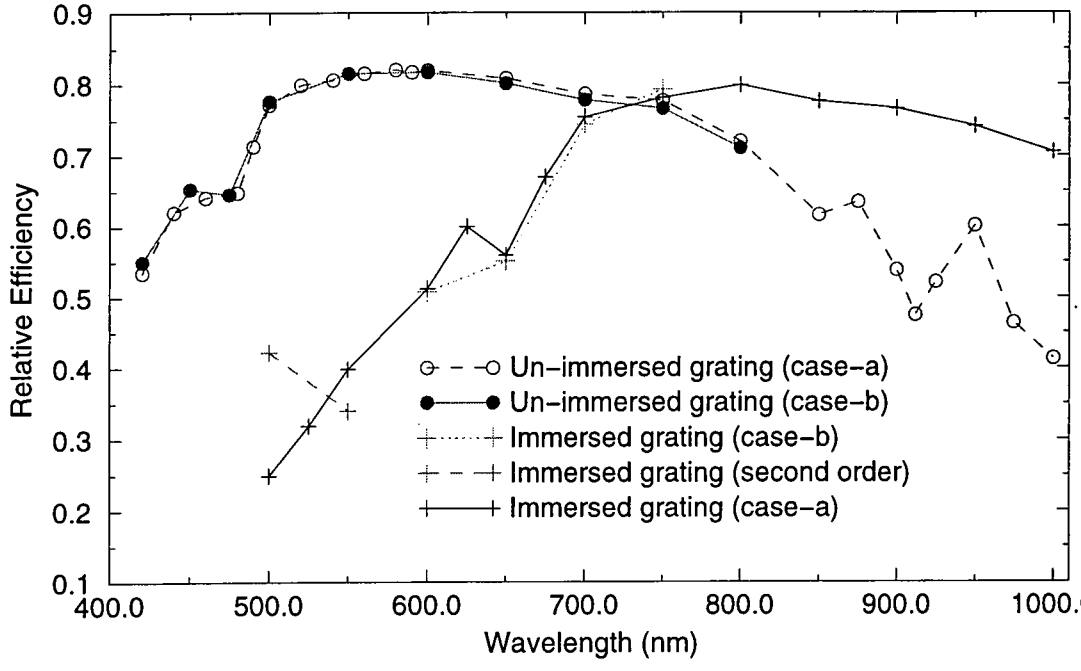

Figure 3.6: Comparison of case-a and case-b efficiencies for the immersed and un-immersed grating configurations and 45° polarized light. Both case-a and case-b show the same efficiency within the experimental errors. The second order efficiency for the immersed grating is also shown.

a very important result for immersed gratings. With an un-immersed grating the maximum resolution is always obtained with case-a illumination, which is the preferred illumination type. However, with an immersed grating there is a cross over point at which the best achievable resolution swaps from being with case-a illumination to case-b. This 'cross over' in resolution can be seen in figure 2.6. Therefore it may be necessary to use an immersed grating with both case-a and case-b illumination conditions depending on the wavelength and resolution of interest. Clearly it is advantage then if the efficiency is unaffected by loss mechanisms such as groove shadowing.

3.4.3 Behaviour of efficiency with polarization

The behaviour of the immersed grating efficiency with linearly polarized light was also measured, as shown in figure 3.7. Efficiency curves for both Littrow and $\psi = 45°$ spectrograph configurations are shown. The two linear polarization types are P-plane polarization and S-plane polarization. P-plane polarized light has the electric vector parallel with the grating rulings and S-plane polarized light has the electric vector perpendicular to the grating rulings. Care has to be taken with definitions of linear polarization as authors in the field of gratings can use different definitions to those used in, for example, the prediction of Fresnel's reflection losses. This can lead to some confusion!

It is interesting that neither of the polarized light efficiency curves exhibit a blaze peak which occurs at the blaze wavelength predicted by equation 3.5. It is the P-plane polarization that is expected to be most closely predicted by the scalar theory. There are some important features to notice in the polarized light efficiency curves. Firstly the P-plane polarization does not exhibit any anomalies, anomalies are only seen with S-plane polarization. The position of the S-plane passoff anomaly changes, from $\sim$ 800nm to $\sim$ 650nm, with increasing collimator to camera angle. Secondly the S-plane efficiency continues to increase, after the P-plane efficiency has started to decrease, reaching $\sim$ 90% relative efficiency. This produces a potentially useful broad peak in efficiency. Gratings with blaze angles in the region of 21 degrees are well known for their wide S-plane high efficiency performance, as shown in Loewen *et al.* (1977). Of course it would be interesting to find out over what wavelength range high efficiency can be achieved. This would require extending the range of the efficiency measurement into the near infrared.

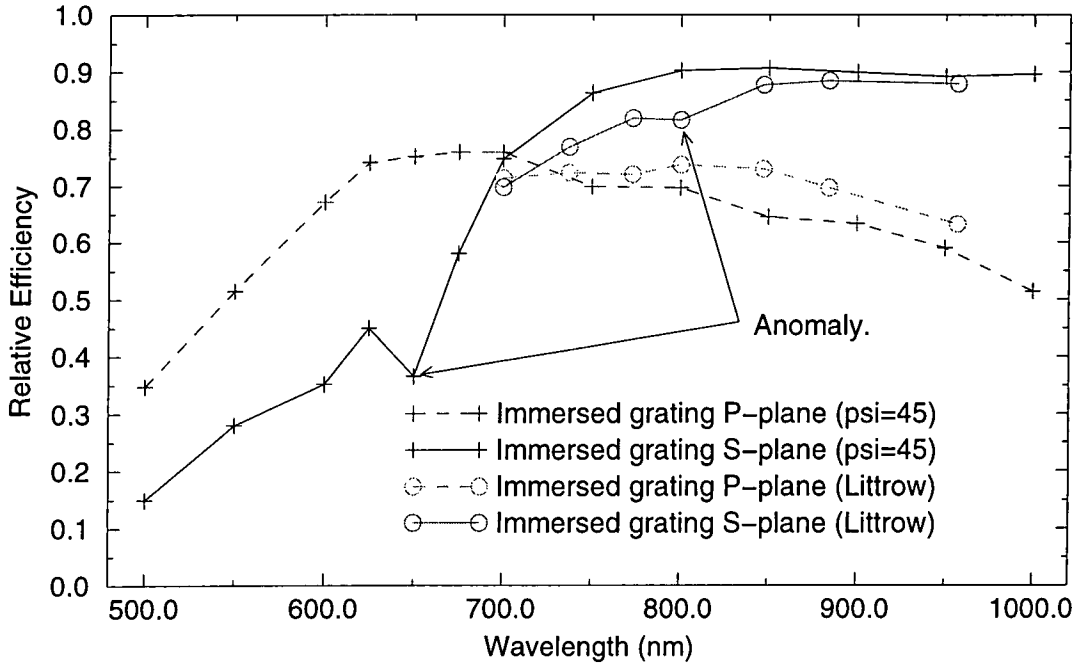

Figure 3.7: Plot of relative efficiency for the immersed grating in both S-plane and P-plane polarizations. The efficiency curves corresponding to $\psi = 45°$ and Littrow ($\psi = 0°$) are shown. Note the shift in position of the S-plane anomaly, from $\sim$ 800nm to $\sim$ 650nm, with changing collimator to camera angle and the change in the P-plane blaze peak.

The grating used to manufacture the prototype immersed grating has a blaze angle of $\xi = 21°$. It therefore belongs to a category of gratings called *special low anomaly gratings*, as described in Loewen *et al.* (1977). This means that the strong Rayleigh passoff anomalies occur in the blaze direction (the wavelength at which the $m = -1, +2$ anomaly occurs is also the blaze wavelength) and their effect is suppressed. The reason for this is unknown. A disadvantage of gratings with this blaze angle is they possess the lowest P-plane efficiencies. Departure from Littrow causes the anomalies to split, as summarised in table 3.1, and they grow in strength. It can be seen in figure 3.7 that the S-plane anomaly at 650nm, with $\psi = 45°$, is more marked than that at 800nm in Littrow. It is perhaps unfortunate that a 'special low anomaly' grating was used for the prototype immersed grating. More information on the effect of immersion on anomalies may have been obtained by using a grating type which exhibits stronger anomalies.

3.4.4 Comparison with electromagnetic theory

Figure 3.8 presents a comparison of the measured un-immersed grating efficiency curve, $\psi = 45°$ case-a illumination, with a theoretically predicted efficiency curve. The theoretical prediction was obtained using the 'PC Grate' software produced by the Optometrics group (Ferguson, 1996). The PC grate software performs a rigorous electromagnetic periodic boundary value solution to Maxwell's equations at the grating surface. The software also allows the finite conductivity of the grating surface to be included in the calculation. The theoretical prediction shows good agreement, to within a few percent, with the experimental data in the region 400-800nm. There is a discrepancy in the depth of the m=2 anomaly at $\sim 475nm$ (anomalies are described in more detail in section 3.2.4). This may be due to inadequate sampling of the region surrounding the anomaly causing the feature to appear less intense. There is also some disagreement in the region $\lambda > 800$nm. As mentioned in section 3.4.1 the cause of the structure in the efficiency curve is unknown. A possible cause may be contamination on the grating surface altering the surface conductivity in this wavelength region. The generally good agreement between the PC grate software predictions and the experimental results indicate that the software would be a useful tool in any future investigation of diffraction grating efficiency curves. In particular it may be useful in deciding which is the best choice of grating for an instrument as the efficiency for that instrumental

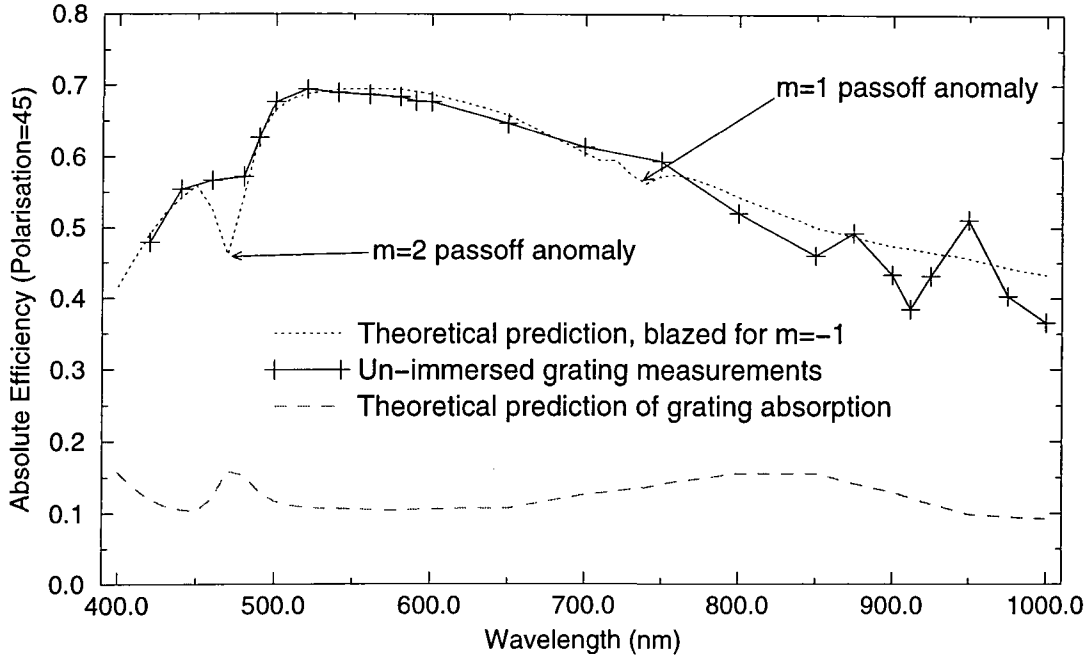

Figure 3.8: Comparison of the theoretically predicted grating efficiency with the experimental data. The theoretical predictions were obtained from (Ferguson, 1996) using finite conductivity theory. The absorption of the grating surface is also shown. Note that the absorption peaks in the region corresponding to the passoff anomaly at $\lambda \sim 475$nm i.e. energy is coupled into the grating surface.

configuration can be predicted in advance. This may avoid the purchase of a grating that turns out to be non-optimal.

The output of the PC grate software also includes the efficiency in the other diffraction orders and the absorption by the grating surface. The total contribution of the diffraction orders and surface absorption is required to equal 100% by the principle of conservation of energy. The surface absorption is also plotted in figure 3.8. The broad increase in absorption centred at $\sim$ 825nm causes the slight reduction in reflectivity of Aluminium in this region, as seen in figure 3.3. However, the absorption feature at $\sim$ 475nm is also of note as it ccincides with the passoff anomaly. This illustrates the property that at a passoff anomaly energy can be coupled into the grating surface leading to a corresponding reduction in the grating efficiency. This electromagnetic coupling of the diffracted wave (diffracted at 90° to the grating surface) in general only occurs with S-plane polarized light. It will be described later, section 3.5, that immersing a metal surface leads to a reduction in reflectivity. This

can also be thought of as an increase in absorption. This possibly indicates that absorption features associated with passoff anomalies may become more pronounced with immersion. There is an indication in figure 3.4 that the immersed grating anomaly, at $\sim 650nm$, is stronger than the un-immersed anomaly at $\sim 480nm$. Clearly more measurements in the region of anomalies are needed, and theoretical predictions of efficiency, to fully understand the subtle absorption effects which occur with immersion.

3.4.5 Littrow efficiency curves

It is difficult to directly compare the efficiency of the immersed grating with that of the un-immersed grating when the collimator to camera angle is 45°. This is because ψ within the immersing medium is reduced by refraction. It has already been described, in section 3.4.1, that the shape of the efficiency curve (the blaze profile), and the peak efficiency, depends critically on the angle ψ. Immersion reduces the collimator to camera angle from $\psi = 45°$ in air to $\psi \sim 28°$ within the prism. The increase in peak efficiency due to this reduction in collimator to camera angle is estimated at approximately 5% (Loewen *et al.*, 1977). Note that this is simply an estimate from published efficiency curves as an accurate prediction of the behaviour of efficiency with ψ is beyond the scope of this work. Therefore to keep ψ constant and allow direct comparison of efficiencies, in the same part of the blaze profile, it is necessary to use the Littrow configuration. The collimator to camera angle, which is 0°, is then the same in both immersed and un-immersed cases regardless of whether or not diffraction occurs within an immersing medium. This experiment required a modification to the efficiency test spectrograph, by the incorporation of a beam splitter, as described in section 3.3.1. The resulting Littrow efficiency curves are shown in figure 3.9.

The efficiency of the immersed grating, at a given immersed wavelength, can be directly compared with the efficiency of the un-immersed grating at the equivalent wavelength in air i.e. the immersed efficiency at 700nm is equivalent to the un-immersed efficiency at $700/n_{gap} = 475$nm. To allow this comparison to be made the immersed efficiency curve has also been plotted in figure 3.9 with this shift in wavelength applied. The ratio of the immersed to un-immersed grating efficiencies is also plotted. In the Littrow configuration the position of the m=(2,-1) passoff anomaly is the same in both immersed and un-immersed cases, unlike the previous case when $\psi = 45°$. In Littrow the S-plane m=(2,-1) passoff

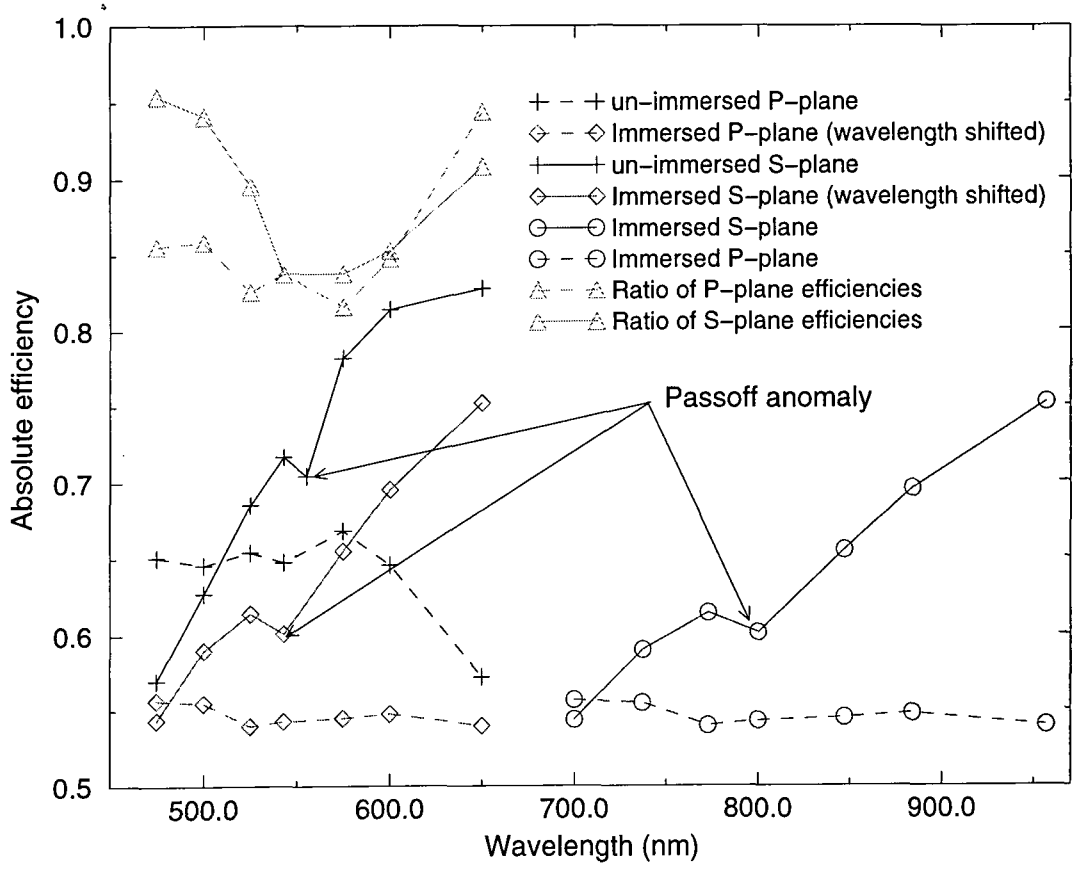

Figure 3.9: Plot of absolute efficiency curves obtained in the Littrow configuration for both the immersed and un-immersed grating. Curves for both S and P-plane polarizations are shown. The immersed grating efficiency curves have also been shifted in wavelength, by dividing by the refractive index of the immersing medium, for direct comparison with the un-immersed grating data. The ratio of the immersed efficiency to the un-immersed efficiency is also shown. Note that the position of the S-plane immersed and un-immersed anomalies coincides in the Littrow configuration.

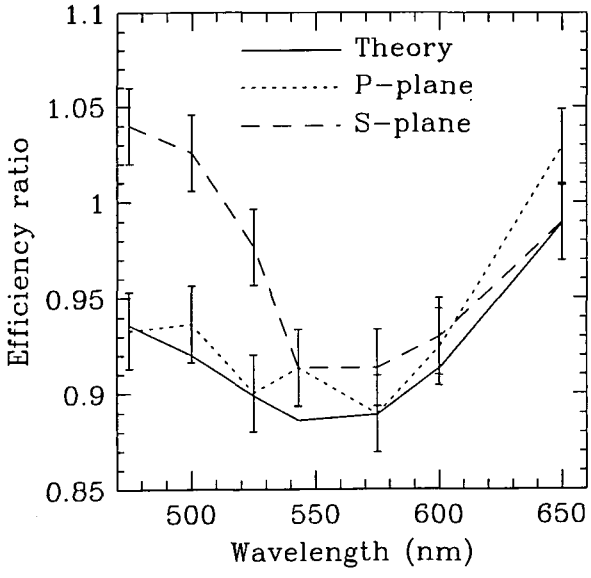

Figure 3.10: Plot to show the ratio of immersed to un-immersed grating absolute efficiency curves in Littrow configuration (adapted from figure 3.9). The ratio has been corrected to remove the effect of air-glass losses at the prism surface. Also shown is the theoretical prediction obtained from the change in reflectivity of an immersed Aluminium surface.

anomaly is no stronger with immersion than without, otherwise a deviation on the plotted curve of efficiency ratio would have been observed. This is in contrast to the previous result for $\psi = 45°$. It is still clear, however, that there is a reduction in the efficiency of the immersed grating.

As the same part of the blaze profile is being used in both the immersed and un-immersed configurations the efficiencies are now directly comparable. The ratio of efficiencies shows that the absolute efficiency with immersion is $\sim 5-20\%$ lower than in the un-immersed case. It must be remembered that some of this loss is due to reflection losses at the surface of the prism, which amount to a total loss of approximately 9% in the Littrow configuration. Figure 3.10 shows the ratio of efficiencies corrected to remove the effect of Fresnel's reflection losses. It can now be seen that for some wavelengths the absolute efficiency of the immersed grating is actually higher. If it is assumed that complex electromagnetic effects can be ignored then the ratio of efficiencies, in Littrow, is simply related to the ratio of reflectivity of the metal surface at the two wavelengths being compared. This assumes that the reflectivity of the grating facet is the same as that of bulk Aluminium. The resulting ratio of reflectivity of an immersed Aluminium surface compared with an un-immersed surface is also plotted in figure 3.10. This curve was predicted using the theory presented in section 3.5 and the data for the reflectivity of Aluminium from Hunter (1985b). It can be seen that the P-plane efficiency ratio is reasonably well fit by the theoretical prediction. This might be expected as it is P-plane behaviour that is most closely predicted by scalar theory. However the S-plane

efficiency ratio is higher than expected from the theory.

Clearly the assumption that complex electromagnetic interactions can be ignored is risky, especially as the wavelength is only a factor of two smaller than the groove size. This result does indicate though that the reduction in efficiency of an immersed grating can be related, in P-plane polarization, to the drop in efficiency of an immersed metal surface. The S-plane ratio shows an improvement in efficiency for a small portion of the blaze profile. This indicates then that for certain conditions *it may be possible to achieve higher efficiencies with immersion.* The cause of this is unknown but it does indicate that to fully understand the change in grating efficiency with immersion a full electromagnetic solution is required.

3.4.6 Comparison with other published results

A prototype immersed echelle has been manufactured at the Optical science laboratory (Radley *et al.*, 1994) for use in the Gemini high resolution optical spectrograph: HROS (Walker *et al.*, 1994). The prototype immersed echelle consisted of a 79g/mm R2 echelle immersed to a 63.5° Fused Silica prism. The prism angle is chosen to match the blaze angle of the echelle. Glycerol is used as the immersing medium. Fused Silica is used in HROS to achieve high transmission in the ultraviolet, a very important science requirement for high resolution studies of stars. The efficiency measurement was performed with un-polarized white light, simultaneously integrating the blaze profile over a range of echelle orders. A collimator to camera angle of 12° was employed. The final result showed that the blaze peak efficiency was reduced by $7\% \pm 3\%$ with immersion. Their conclusion was that "there is no evidence for any metal-dielectric loss" with the immersed echelle, conflicting with measurements presented in section 3.4.1.

The statement that there are no metal-dielectric losses is thought to be slightly misleading. The collimator to camera angle seen by the echelle, within the immersing medium, will be less than that in air. It has already been described in section 3.4.1 that the efficiency of a grating increases as the collimator to camera angle is decreased towards a Littrow configuration. It is therefore believed that the increase in efficiency due to the smaller collimator to camera angle within the prism balances the metal-dielectric loss.

Efficiency measurements on a prototype immersed echelle are also described in Dekker (1992).

The prototype consisted of a 31.6 g/mm R2 echelle immersed to a BK7 prism. The efficiency of the immersed echelle was found to be 8–10% lower than the un-immersed echelle after the effects of reflection losses had been removed. The reason for this loss is not described but is most probably due to metal-dielectric losses. It is interesting to note that Dekker abandoned the concept of an immersed echelle in favour of an echelle mosaic. Dekker also mentions some work by Paul Schechter on immersed gratings for use at Las Campanas but no reference to this work could be found. This does show that there has been interest in immersed gratings for many years and it is perhaps surprising that none are in regular (known) use on telescopes.

3.4.7 Interesting consequences of electromagnetic theory

The light diffracted by a diffraction grating is distributed between the various diffraction orders. It therefore follows that if the number of diffraction orders which propagates is kept to a minimum then the efficiency in the order of interest will be increased. This can be achieved in a Littrow configuration if $\lambda/\sigma n > 2/3$. When this condition is satisfied only the first and zeroth orders can propagate and no light is lost into other orders. This region will also be free from anomalies, section 3.2.4, as passoff anomalies can no longer occur as all other orders having already left the grating.

It was described in section 3.2.3 that case-a and case-b types of illumination have the same efficiency as a consequence of reciprocity theorem. It can also be shown via reciprocity theorem (Maystre *et al.*, 1980) that for a grating operating in Littrow configuration which satisfies the condition $\lambda/\sigma n > 2/3$, which has a blaze angle greater than 19.5°, and for S-plane polarized light, that 100% efficiency can be achieved in the first order. This implies that the efficiency in the zeroth order reduces to zero. As the only order then propagating is the first order it will possess an efficiency that is limited only by the reflectivity of the grating surface. As there is no change in efficiency between case-a and case-b illumination this means the grating can be rotated by 180°, about an axis perpendicular to the plane of the grating surface, and the efficiency remains constant. This corresponds to the case where the back of the groove is illuminated rather than the blazed facet. This configuration may occur in an astronomical spectrograph if the grating is accidentally inserted upside down.

An experiment was performed to verify this interesting theoretical prediction. The efficiency

of the un-immersed grating was measured, with S-plane polarized light, in the Littrow configuration at a wavelength of 600nm, such that $\lambda/\sigma = 0.72$. The efficiency was measured with angles of incidence $\alpha = \pm 21°$, with $\alpha = +21°$ corresponding to blaze and $\alpha = -21°$ corresponding to illuminating the back of the grooves, equivalent to rotating the grating by 180°. The relative efficiency measured in the normal blaze configuration was 98% reducing to 48% in the back of groove configuration. Note that an efficiency of 98% implies that the only losses are due to the reflectivity of the grating surface. This is the highest possible efficiency that can be obtained with a diffraction grating. It was noted that the image quality with back of groove illumination was much worse than in the normal blaze configuration. Clearly this does not verify the prediction of reciprocity theorem but it does demonstrate the high efficiency that can be achieved with a diffraction grating via appropriate illumination conditions. The lower efficiency measured for case-b may simply be because the back of the grooves are uncoated.

The zeroth order was also observed by eye, as the polarization of the input beam was rotated, and was indeed found to disappear for S-plane polarized light. It seems quite incredible that the mirror reflection from the grating surface can be made to vanish! This means that all the incident light is diffracted into the first order producing the highest efficiency possible.

A diffraction grating with high efficiency, as described, may be of considerable benefit in reducing losses within an astronomical spectrograph. Diffraction grating efficiencies typically peak at $\sim 70\%$ and represent a considerably loss to the throughput of a spectrograph. Clearly then if the grating efficiency can be increased this represents a useful increase in throughput for the spectrograph.

It is well known that polarized light entering a prism at Brewster's angle does not suffer from any reflection losses, as shown in figure 3.5. This polarization is also that which displays the highest possible diffraction efficiency, discussed above. As the prism has to operate at high angles of incidence, Brewster's angle is typically $\sim 60°$, this produces a large anamorphic effect leading to an increase in the spectral resolution. This leads to the possibility of constructing a high resolution, high efficiency spectrograph, which operates with S-plane polarized light. This would involve splitting the input beam into the two polarization states by means of some optical device, such as a polarizing beam splitter or Woolaston prism. The P-plane polarized light then has to be rotated by 90°, by means of a waveplate or similar

device, to produce S-plane polarized light. The input beam to the spectrograph then consists solely of S-plane polarized light which will be diffracted with high efficiency. Of course the gain in efficiency has to over compensate for the losses in the polarizing beam splitting fore-optics. This type of instrument would probably be best suited to dual beam operation, i.e. as a spectropolarimeter, as the two polarization states can be measured independently. This would make an interesting instrument design project for further investigation. The concept of using immersing prisms at Brewster's angle, in a similar fashion, is also described in Dekker (1987).

3.5 Metal-dielectric losses

The lower efficiency of an immersed grating, described in section 3.4.1, was attributed to two main loss mechanisms: Fresnel's reflection losses at the prism surface and metal-dielectric loss at the interface between the immersing medium and the grating surface. Reflection losses at an air-glass surface are well known, however, it is less well known that the same Fresnel's equations used to predict reflection losses also predict a loss at a metal-dielectric interface. The modification to the derivation of Fresnel's equation (Jenkins & White, 1976, p524) is to represent the refractive index of the metal, n_c, by a complex number, as follows:

$$n_c = n_R + in_I \tag{3.6}$$

where n_R is the real refractive index and n_I is the imaginary[7] refractive index of the material. The real refractive index behaves as an ordinary refractive index, determining the wave speed in the material. The imaginary refractive index behaves as an extinction coefficient, determining the rate of absorption in the material (Pedrotti & Pedrotti, 1993). The variation of n_R and n_I with wavelength, for an Aluminium surface, and the corresponding reflectivity, can be seen in figure A.2. The reflectivity of Aluminium is frequency dependent, therefore the change in wavelength within the immersing medium does not affect the reflectivity of the metal surface. Metals with a high conductivity (high n_I) generally have high reflectivities. The transverse magnetic reflectivity, $R_{||}$, of a metallic surface has a minimum in reflectance at the *principle angle*, in a similar fashion to Brewster's angle with dielectrics.

[7]The imaginary refractive index may also be given the symbol κ in some optics texts.

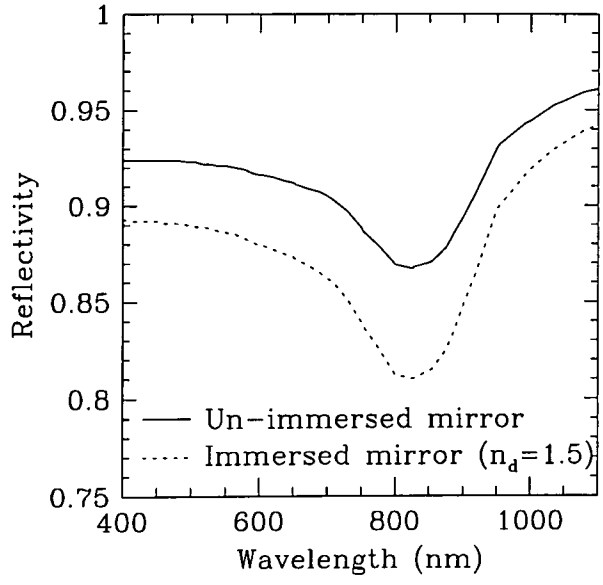

Figure 3.11: Plot of the reflectivity of an Aluminium surface versus wavelength for unpolarized light. The angle between the incident and reflected beams is 45°. Two curves are shown, the curve with higher reflectivity is for front surface reflection, and the lower curve is when the surface is immersed in a medium of refractive index equal to 1.5.

The reflectivity of an immersed metal surface can be found using the following equations:

$$R_{\perp} = \frac{(n_p \cos\theta_i - n_R)^2 + n_I^2}{(n_p \cos\theta_i + n_R)^2 + n_I^2} \tag{3.7}$$

$$R_{\parallel} = \frac{(n_R \cos\theta_i - n_p)^2 + n_I^2 \cos^2\theta_i}{(n_R \cos\theta_i + n_p)^2 + n_I^2 \cos^2\theta_i} \tag{3.8}$$

where n_p is the refractive index of the incident medium and θ_i is the angle of incidence. Note that in the derivation of these formulae the assumption was made that the transmitted wave in the metal propagates normal to the surface. Therefore these formulae become less accurate if the complex refractive index of the metal is small. A full derivation of the equations predicting the reflectivity of an immersed metal surface can be found most introductory optics texts (Fowles, 1989; Pedrotti & Pedrotti, 1993). For normal incidence, $\theta_i = 0°$, equations 3.7 and 3.8 can be simplified leading to the following formula for reflectivity of an immersed metal surface:

$$R = \frac{(n_p - n_R)^2 + n_I^2}{(n_p + n_R)^2 + n_I^2} \tag{3.9}$$

As an example; the reduction in reflectivity of an Aluminium mirror, upon immersion within a medium of refractive index 1.5, is shown in figure 3.11. The reduction in reflectivity is generally around 4% although this will depend critically on the actual properties of the immersed metal surface. Metal-dielectric losses increase with the refractive index of the immersing medium. In the case when $n_I = 0$ (a perfect dielectric) equation 3.9 reduces the well known formula for Fresnel's reflection from a glass surface.

The effect of metal-dielectric losses upon immersing a mirror was tested, independently of the immersed grating experiment, by immersing a front surface mirror to a microscope slide. The test was done at 580nm with S-plane polarized light and an angle of incidence of 22.5°. The reflectivity of the mirror was found to drop by $\sim$ 7% with immersion. This result cannot be theoretically predicted, for comparison, as the complex refractive index of the mirror coating is unknown. The plot of reflectivity versus wavelength for the reference mirror shown in figure 3.3 showed that there is considerable variation between the theoretical reflectivity of an Aluminium mirror and the measured reflectivity. Therefore it is difficult to know precisely the properties of the mirror which was immersed. The observed 7% drop is, however, similar to the reduction in reflectivity expected for an Aluminium surface predicted using published refractive index data (Hunter, 1985b) as shown in figure 3.11. Note that the complex refractive index of a metallic surface can be determined by *ellipsometry* (Hunter, 1985a; Hilton & Hilton, 1973). Similarly predictions for the metal-dielectric loss of a grating surface would require accurate knowledge of the complex refractive index of the grating coating. Prediction of the metal-dielectric loss at the grating surface would also require a full electromagnetic solution, for the same reasons as already described in section 3.2.3. The Fresnel's equations cannot be applied to a grating facet as the angles of incidence and reflection are not equal except at blaze. The equations presented do, however, allow an estimate of the metal-dielectric losses that might be expected with an immersed metal surface.

3.5.1 Prevention of metal-dielectric losses

It may be possible to prevent metal-dielectric losses by coating the metallic grating surface with a suitable multilayer dielectric coating prior to immersion. A full description of this technique is described in Clapham & Raine (1969). Following the derivation of Clapham & Raine the absorption, A, of an immersed metal surface is given by $A = 1 - R$. Rearranging equation 3.9 for A gives:

$$A = 1 - R = \frac{4 n_p n_R}{(n_p + n_R)^2 + n_I^2} \tag{3.10}$$

As n_I is usually very large the absorption is therefore approximately proportional to n_p. This means the highest possible reflectivity is achieved with the metal in air ($n_p = 1$). To

retain high reflectivity with immersion implies there should be a gradation[8] of the refractive index of the immersing medium towards $n_p = 1$ at the metal surface. This can be achieved by using a suitable multilayer coating on the grating surface. However, one of the principle advantages of an immersed grating is that diffraction should occur within a medium of high index, implying unavoidable metal-dielectric losses. It is unknown how a multilayer coating would affect the diffraction properties i.e. can a thin dielectric film, significantly less a wavelength thick, be regarded as an immersing medium in which diffraction occurs? This clearly comes back to the case where scalar theory is inadequate and a full electromagnetic solution is required to predict performance. It is also unknown whether a complicated dielectric coating could even be applied to the grating surface.

Although immersing the grating surface initially leads to a reduction in reflectivity the immersing medium also protects the grating surface from any contamination. A reduction in the efficiency of an un-immersed grating is expected to occur with time as the surface becomes contaminated and oxidised. This cannot happen with an immersed grating unless the immersing medium reacts in some way with the grating surface. The surface of a grating is also difficult to clean due to it's fragility meaning it is difficult to remove any contaminants. The surface of the prism, however, can be readily cleaned. Immersion is therefore expected to preserve the reflectivity of the grating surface. This characteristic might be particularly useful when gratings are used in extreme conditions which might damage the surface, i.e. in vacuum ultraviolet experiments.

3.6 Ghost images

The dispersion element in an astronomical spectrograph is placed in a collimated beam, usually at the pupil plane. The addition of a prism in the collimated beam introduces an extra air-glass surface. Reflections from any additional air-glass surfaces may then be focussed onto the camera to form *ghost images.* Ghost images are more likely to occur in the collimated beam, as the collimated beam is always brought to focus by the camera. Note the ghosts referred to in this section are due to reflections within the optical system and are not *grating ghosts*[9], which are due to grating ruling defects, as described in Hutley (1982).

[8]This can be thought of an antireflection coating working in reverse.

[9]Such as Rowland ghosts, close to the diffracted order, and Lyman ghosts, between orders.

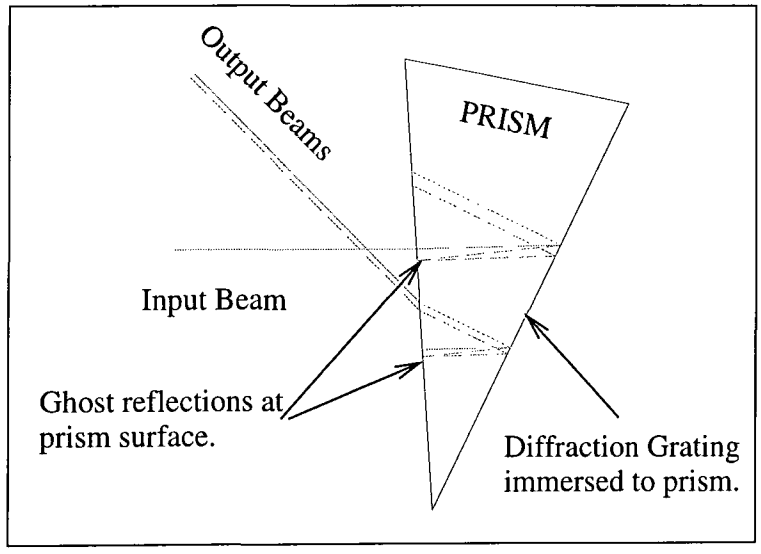

Figure 3.12: Schematic of the production of an immersed grating ghost. The configuration shown is for the prototype immersed grating operating at a wavelength of 589nm. A ghost occurs at 617nm due to second order diffraction, followed by reflection from the prism surface, followed by first order diffraction.

The probability of producing a ghost image also increases with an immersed grating because of the additional diffraction orders which can propagate within the immersing medium. In particular ghosts can occur if the angle of diffraction is the same as the prism angle producing normal reflection from the prism surface back to the grating.

An example of the production of a ghost within the immersed grating is shown schematically in figure 3.12. In the example shown, light, at a wavelength of 617nm, enters the immersed grating and is diffracted in first order towards the camera. Second order diffraction also occurs in a direction back towards the incident beam. The second order beam is then reflected from the front surface of the prism back towards the grating. Finally first order diffraction directs the beam towards the camera to the same position as the parent beam.

Other configurations of prism ghost are also possible, over a wide range of wavelengths and diffraction orders. Table 3.2 summarises the properties of some ghosts produced with the prototype immersed grating at 589nm. The ghosts listed will occur in the same position on the detector as the wavelength of interest (589nm). It can be seen from table 3.2 that ghosts occur in 'families' where the sum of the diffraction orders involved is 2,3 or 4. Each family produces ghosts which occur at similar wavelengths. The example shown in figure 3.12 is from the family where the orders sum to produce $\Sigma m = 3$. Ghosts which occur with $\Sigma m = 4$ will occur at twice the wavelength of $\Sigma m = 2$ ghosts. In some cases the ghosts are produced with high diffraction orders leading to very large dispersions, the surface brightness of these ghosts is therefore likely to be low. The intensity of ghosts is also reduced somewhat by vignetting. The optical path of the ghost within the prism produces beam displacement

Ghost family	First pass	Second pass	Ghost wavelength	Dispersion	Slit width
m=1	—	—	589nm	5.26nm/mm	70.1μm
$\Sigma m = 2$	m=1	m=1	904nm	3.05nm/mm	51.0μm
$\Sigma m = 2$	m=2	m=0	840nm	1.30nm/mm	141.3μm
$\Sigma m = 3$	m=1	m=2	557nm	2.12nm/mm	33.7μm
$\Sigma m = 3$	m=2	m=1	617nm	1.72nm/mm	71.6μm
$\Sigma m = 3$	m=3	m=0	560nm	0.87nm/mm	141.3μm
$\Sigma m = 3$	m=4	m=-1	458nm	0.23nm/mm	423.4μm
$\Sigma m = 4$	m=1	m=3	395nm	1.57nm/mm	25.7μm
$\Sigma m = 4$	m=2	m=2	452nm	1.53nm/mm	51.0μm
$\Sigma m = 4$	m=3	m=1	459nm	1.14nm/mm	84.2μm
$\Sigma m = 4$	m=4	m=0	420nm	0.65nm/mm	141.3μm

Table 3.2: Table of ghost wavelengths for the immersed grating configuration with a central wavelength of 589nm. The ghost is diffracted in the order listed under 'first pass', then reflects from the surface of the prism and is diffracted again in the order listed under 'second pass'. The resulting dispersions and output slit widths, for an input slit width of 100μm, are also listed.

offsetting the ghost beam from the centre of the camera axis leading to vignetting. Many ghosts can be avoided completely by the use of suitable bandpass or order sorting filters to limit the wavelength range incident on the grating. Many ghosts incident on the prism surface at large angles will undergo total internal reflection and become trapped within the prism. Whilst these ghosts do not reach the detector they may contribute to an increase in the total intensity of stray or diffuse background light.

Every wavelength of observation has an associated set of ghosts. A plot of the predicted wavelength, λ_g, of various immersed grating ghosts versus the central wavelength, λ_c, is shown in figure 3.13. The *central wavelength* is the wavelength of interest on the detector. Also shown in figure 3.13 is the line corresponding to $\lambda_g = \lambda_c$. Ghosts which occur on this line in the diagram are unavoidable. These ghosts belong to the family of ghosts which is very difficult to avoid, in this case $\Sigma m = 3$.

The production of ghosts isn't confined to the immersed grating. Reflections from the CCD detector surface and the slit jaws can also produce in focus ghosts. Reflections from the detector surface can be quite intense if the detector isn't antireflection coated, as is the case

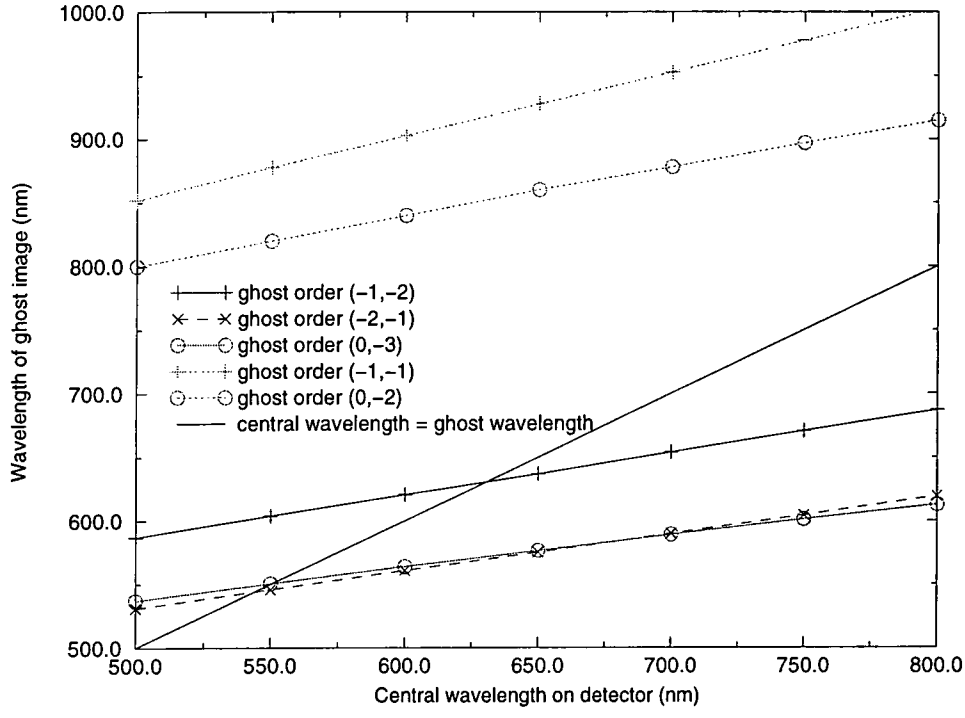

Figure 3.13: Graph of central wavelength versus wavelength at which an air-glass surface prism ghost will appear. For example with a central wavelength of 600nm ghosts will occur at: 561nm, 564nm, 621nm, 840nm, and 903nm caused by the various grating orders listed in the legend.

in the experiment described below. The high refractive index of Silicon produces Fresnel's reflection of $\sim 30\%$ unless the detector is antireflection coated. Out of focus ghosts can also be produced, e.g. by reflections from lens surfaces, contributing to an increase in instrumental background light present on the detector.

3.6.1 Experimental investigation of ghosts

The presence of ghosts on the detector may be a problem for some astronomical observing programmes. An example of where in-focus ghosts might be particularly problematic is in emission line studies. If a bright emission line also produces an in focus ghost this may be confused as another emission line unless the observer knows where to expect ghosts and with what intensity. In order to determine the intensity of ghost images caused by the prototype immersed grating an experimental investigation was performed. The efficiency spectrograph was used, as described in section 3.3.1, with the exception that the COHU CCD camera was replaced. As the ghost images are likely to be of low intensity compared with the parent line a detector with lower noise and higher dynamic range is preferable. Instead an Astromed CCD camera, containing an EEV PC8607/B CCD detector, was used. The detector is cooled to 130K with liquid Nitrogen giving much lower noise than the room temperature COHU CCD. The dynamic range is also considerably better, 16 bits, compared with the 8 bits provided by the frame-grabber.

To detect ghosts it was decided to simulate the operation of the immersed grating within a spectrograph. The grating was positioned such that the wavelength of interest, corresponding to the central wavelength of an observation, was centred on the detector. The monochromator was then scanned in wavelength, whilst the grating remained fixed, to look for ghost images produced at wavelengths around the central wavelength. Care was taken during the measurement of immersed grating ghosts to avoid the production of ghosts elsewhere in the optical path. Otherwise confusion might result between the different ghost images on the detector. It is possible to measure the integrated intensity of ghost images where the parent image is also present of the detector, i.e. where $\lambda_g = \lambda_c$ in figure 3.13.

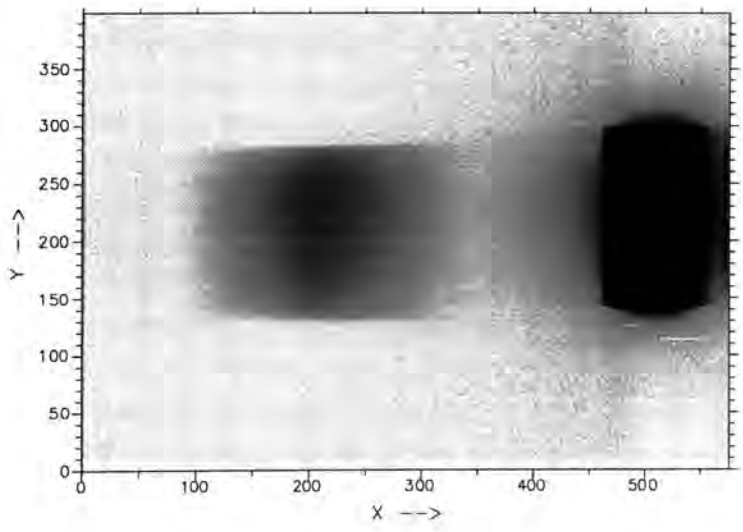

Figure 3.14: Image of an immersed grating ghost, at 617nm, caused by first order diffraction, then Fresnel's reflection within the immersing prism, and finally second order diffraction. The ghost is the faint dispersed image. The 'parent' image is the black area (black due to scaling) to the right of the image. The integrated ghost intensity is less than 1% of that of the parent in unpolarized light.

This allows direct comparison of the ghost image and parent image intensity without complications due to changes in wavelength or grating angle. An example of a ghost observation is shown in figure 3.14.

The image shows the ghost produced by the optical path illustrated in figure 3.12. By taking the ratio of the integrated intensity in the ghost image to the integrated intensity in the parent image, after background subtraction, the relative amount of energy in the ghost with respect to the parent can be found. Results for the relative efficiencies of various ghosts are listed in table 3.3. From the image in figure 3.14 a number of features are apparent. The ghost image is very dispersed (ghost dispersions are listed in table 3.2) with respect to the parent. This helps to lower the peak intensity with respect to the parent peak intensity. There is also a slight offset of the ghost position from the parent along the Y axis. This is attributed to a slight misalignment between the plane of the prism surface and the grating surface. The peak intensity of the ghost is 0.34% of the parent image. Due to the low intensity of the ghosts with respect to the parent image, and their diffuse nature, the accuracy in measuring the relative ghost intensity is $\sim \pm 5\%$.

The intensity of a ghost image is difficult to predict due to the lack of knowledge regarding the distribution of light in the different diffraction orders. Ghost production also occurs at many different angles of incidence and diffraction at the grating surface making intensity prediction even more difficult. Therefore a comparison of measured relative ghost intensity

λ_g	order	Σm	R_{TM}	R_{TE}	$\epsilon_g(TM)$	$\epsilon_g(TE)$
617	(-1,-2)	-3	0.043	0.043	0.012	0.0060
558	(-2,-1)	-3	0.000	0.125	–	0.0134
562	(0,-3)	-3	0.005	0.120	–	0.0060
600*	(-1,-2)	-3	R_{CCD}	R_{CCD}	0.0362	0.0147

Table 3.3: Measured intensities of ghosts, with respect to the parent image, for various immersed grating ghosts. The reflectivity of the prism surface for the ghost reflection is listed under R_{TM} and R_{TE} for the two polarization states. Note that in some cases the ghost intensity is too low to measure due to the low reflectivity of the prism surface. Ghost intensities for the two polarization states are listed under $\epsilon_g(TM)$ and $\epsilon_g(TE)$. * indicates a CCD detector reflection ghost not a prism ghost. R_{CCD} is the reflectivity of the CCD at 600nm, estimated at $\sim 30\%$.

with theoretical predictions is not presented. Ghosts which are formed in zeroth, first and second orders are likely to have the highest surface brightness as their dispersion is lower than with higher order ghosts. It can be seen in table 3.3 that Fresnel's reflection from the prism reduces to nearly zero, in transverse magnetic polarization, for certain ghosts. This often means ghosts can only be seen in transverse electric polarization. Note that by far the brightest ghost is that due to Fresnel's reflection from the uncoated surface of the CCD detector. The other ghost families were also checked, to confirm their existence and position, but the relative intensities were not measured. An example of a $\Sigma m = 2$ ghost, at 835nm, can be seen in figure A.3. The wavelengths of predicted ghosts and actual ghosts were found to agree to within 10nm. Slight differences might be expected as the dispersion of the Glycerol was not included in the calculation. Therefore the position of ghosts can be predicted with high accuracy even if the intensities cannot.

The GMOS specification document (GMOS, 1995) states that: "no single localised parasitic image shall have a surface brightness exceeding 2% of the field illumination for any 100nm bandpass in the design range (assuming a typical CCD and dewar)". Even without antireflection coatings the immersed grating fulfils the GMOS specification for maximum ghost intensity, although this result may change for a different configuration of immersed grating than the prototype. This implies already that ghost images are not a major disadvantage which would prevent the use of an immersed grating.

Of course the intensity of ghosts, caused by the air-glass reflection at the surface of the

prism, can be dramatically reduced if the prism is antireflection coated. High performance antireflection coatings that may be suitable for use with immersed gratings are described in appendix A.1. Ghosts can also be deflected away from the camera axis by tilting the input face of the prism with respect to the camera axis. Unfortunately this introduces a small amount of cross dispersion into the system. This is, of course, not a problem if the immersing prism is also the first prism in a cross dispersion system, as is the case with HROS (Radley *et al.*, 1994). Ghosts which are not caused by the immersed grating, i.e. slit ghosts, can be removed by adjustments of the spectrograph optical design and adequate ghosting analysis should be included in any optical design.

It is beyond the scope of this work to exhaustively predict ghosts for every possible configuration of immersed grating. The exact number and intensity of ghosts depends on the exact immersed grating configuration. An immersed grating for use on a telescope will have to be designed carefully, possibly with small adjustments made to the prism angles, to avoid the production of strong ghosts. The observer should also be aware of any ghosts which may occur for the particular observing setup being used. However the conclusion of the above analysis is that *immersed grating ghosts are not a major cause for concern*, especially with antireflection coated optics.

3.6.2 Scattered light

Although an investigation of the scattered light properties of immersed gratings was not performed it is worth briefly mentioning as scattered light was detected with the ghost experiment described above. Ideally all the light from a diffraction grating should be confined to the diffraction orders. Grating surfaces are usually not perfect and a small amount of scattered light can be produced between the diffraction orders, i.e. not confined to discrete angles. This scattered light is caused by defects in the grating rulings and contamination on the surface. More information on scattered light and its measurement can be found in Hutley (1982) and Verrill (1978). An example of the band of scattered light, present in the plane of dispersion of the grating, can be seen in figure A.3. It is also quite straight-forward to qualitatively observe scattered light by eye. Gratings often have defects where a ruling has not been successful and these can easily be seen by eye over a wide range of angles i.e. they produce scattered light. A typical image of a grating surface, viewed in scattered light,

can be seen in Hutley (1982, p150). Dust and contamination on the grating surface also act as scattering centres and can be seen readily be eye. As an immersed grating surface is protected from contamination by the prism it is possible that scattered light will be less intense with immersed gratings.

3.7 Summary & Conclusions

This chapter described in detail the experimental investigation of the change in efficiency which occurs when a grating is immersed. Theoretical predictions of grating efficiency via scalar theory were found to be inadequate although they can be used to predict some simple features, such as: position of anomalies, and change in blaze wavelength with increasing collimator to camera angle. Theoretical prediction of grating efficiency actually requires a full electromagnetic solution at the grating surface and is beyond the scope of this work. It was found that the change in grating efficiency with immersion can be explained by simple loss mechanisms, discussed below, without the need for additional electromagnetic loss mechanisms which could only be predicted via electromagnetic theory.

The main result was; *the efficiency of a grating was found to be reduced, by* $\sim 15\%$*, when immersed to a prism.* This reduction in efficiency was attributed to two main causes:

- air-glass reflection losses at the uncoated surface of the prism,
- metal-dielectric losses due to the lower reflectivity of of an immersed metal surface.

Fresnel's reflection losses can be minimised by the use of suitable AR coatings. Fresnel's reflection losses are well known but metal-dielectric losses are less well known. The theory for their prediction was presented together with experimental proof of their effect on an immersed mirror surface. The metal-dielectric losses are, however, difficult to avoid, but this is not a particular cause for concern. This is because the metal-dielectric loss is somewhat offset by a gain in efficiency due to the production of a smaller collimator to camera angle, by refraction, within the prism. The collimator to camera angle reduces from $\psi = 45°$ in air to approximately $\psi = 28°$ within the prism. This produces an efficiency gain of $\sim 5\%$ at the blaze peak. The ratio of immersed to unimmersed grating efficiency in P-plane polarization

was shown to be consistent with that expected from metal-dielectric losses. The S-plane ratio however showed the immersed grating to be more efficient than expected leading to conclusion that efficiency gains may be possible. It may also be possible to reduce metal-dielectric losses by use of a multilayer dielectric coating applied to the grating surface. This is topic for future investigation because it requires the use of electromagnetic theory and was beyond the scope of the present work. Although efficiency losses may have contributed to the rejection of immersed gratings, for use in past projects, this work finds that efficiency losses are not a major cause for concern. Indeed with more research into the subtle interaction between the immersing medium and the grating surface *efficiency gains* may even be possible.

Some other consequences of immersion were also measured. The blaze wavelength was found to shift with immersion, by a factor approximately equal to the refractive index of the immersing medium. The blaze peak also becomes broader. Immersion also allows access to higher grating orders than are available without immersion. No difference was found in efficiency between case-a and case-b illumination conditions indicating that groove shadowing effects can be ignored. This is an important result as immersed gratings can be used with both case-a and case-b illumination, unlike un-immersed gratings which are only used with case-a. The immersed grating exhibits the usual characteristics of efficiency with polarized light. The efficiency in S-plane polarized light exhibiting anomalies and a higher peak efficiency than P-plane polarized light. The high S-plane efficiencies available, coupled with the use of the prism at Brewsters angle, leads to the possibility of constructing a high efficiency spectropolarimeter.

The position of Rayleigh passoff anomalies can be accurately predicted for immersed gratings providing a correction is made for the wavelength within the immersed medium. There is no evidence for any substantial change in the behaviour of Rayleigh passoff anomalies with immersion. The comparison of the immersed grating efficiency performance with the results of other authors indicates that the only significant loss mechanism, that was previously not fully understood, is due to metal-dielectric losses. There are no other unpredictable mechanisms operating which lower the efficiency of the immersed grating.

The additional air-glass surface present in the collimated space with an immersed grating can lead to the production of various in-focus ghosts. A common cause of ghosts within the prism is multiple reflections between the prism surface, which is uncoated, and the grating.

An experimental investigation of these ghosts found them to be faint and dispersed, with a peak intensity less than 0.4% of the parent image. This is within the specification for the production of ghosts with the GMOS. The production of ghosts is therefore not thought to be a serious disadvantage preventing the use of immersed gratings. The intensity of ghosts can be reduced dramatically if the prism is antireflection coated.

Air-glass reflection losses are, of course, straightforward to minimise by use of antireflection coatings. Antireflection coatings for use with immersed gratings are complicated by the need to operate at large angles of incidence. A preliminary investigation of Silica sol-gel coatings for use with immersed gratings (described in appendix A.1) indicated high performance (low reflectivity) but this was found to degrade slightly with time. Good AR coatings are also crucial to reducing the intensity of in-focus ghosts as in-focus ghosts are caused by multiple reflections between the prism surface and the grating.

The general conclusion then is that there aren't any serious disadvantages to be overcome which would prevent the use of immersed gratings. Any small loss mechanisms are more than offset by the potential gains that immersion has to offer. In most cases careful design can in fact eliminate most efficiency loss mechanisms.

The only thing left to do now is build one!

Chapter 4

Introduction to integral field spectroscopy

Abstract

Integral field spectroscopy (IFS) is a technique which simultaneously captures both imaging and spectral information of an object. This chapter introduces the concept of IFS and describes the various techniques by which it can be achieved. Comparison of the various techniques leads to the conclusion that a combination of microlens and fibre based integral field unit (IFU) technology provides the best technique with which to construct an IFU for the Gemini multi-object spectrograph. Microlens-fibre based IFUs planned for construction by the Astronomical instrumentation group in Durham, in particular the GMOS-IFU, are then described in more detail.

4.1 Introduction to integral field spectroscopy

The two most commonly used observing modes are imaging and longslit spectroscopy. However, a limitation to these standard astronomical observing techniques is that they only capture information in two dimensions. Imaging captures information in two spatial dimensions: right ascension and declination (x and y) with only very limited spectral information. Spectroscopy captures information in one spatial dimension, along the slit, and the spectral dimension, across the detector. Imaging is ideal for astronomical applications, such as photometry, where spectroscopic information is not required. Limited spectroscopic information can be obtained, of course, by the use of bandpass filters. Longslit spectroscopy is best suited to the observation of point sources, such that the majority of the flux from the object enters the slit. If, however, the observer wishes to capture both imaging information and

spectroscopic information then the standard techniques of imaging and spectroscopy have to be adapted provide information in the extra dimension. Clearly multi-dimensional observing represents a saving in telescope time for particular applications.

The capture of both imaging and spectroscopic information simultaneously is now generally referred to as *Integral Field Spectroscopy* or IFS. The device which reformats the three dimensional information from the sky to fit onto a two dimensional detector is known as an *Integral Field Unit* or IFU. In general integral field spectroscopy can be thought of as a technique which maximises the amount of information which is packed onto the available detector area.

An illustration of the scientific potential of IFS is shown in figure 4.1. The example illustrated is the proposed field of view of the GMOS-IFU overlaid on various objects of astronomical interest in the galaxy cluster Abell 2218. It is clear that a wealth of information about each target will be obtained from the integral field data cube. The design of the GMOS-IFU is optimised to full advantage of the high image quality expected to be produced by Gemini.

4.2 Techniques of integral field spectroscopy

The advantages of integral field spectroscopy are obvious. Over the last ten years a large number of different types of integral field instrument have been proposed and built. Integral field spectroscopy systems generally fall into two categories depending on whether the primary observing mode of the instrument is imaging or spectroscopy. Fabry-Perot spectrometers (FPS) and Fourier transform spectrometers (FTS) are examples of 'imaging' instruments. Both FPS and FTS instruments build up the third dimension by scanning. Instruments which form a spectrum (spectroscopic systems) and build up the third dimension by clever reformatting of information at the detector are generally referred to as Integral field spectrographs (Monnet, 1994).

The spectroscopic integral field units constructed (or proposed) can be further divided into three main categories: microlens systems, fibre systems and image slicers. Each of these is illustrated in schematically in figure 4.2. In the following sections a description of each type of system is given summarizing the advantages and disadvantages associated with each. The more traditional methods of obtaining three dimensional information are also discussed

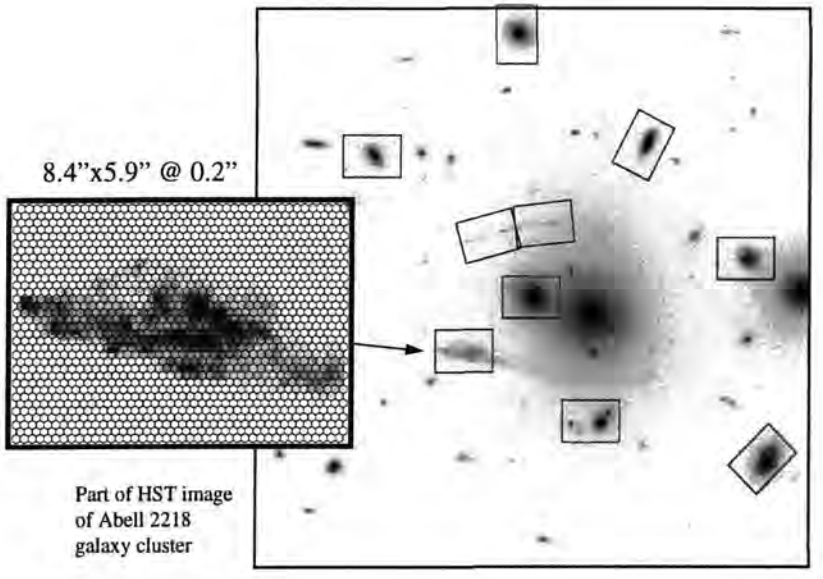

Figure 4.1: High spatial resolution Hubble space telescope image of the galaxy cluster Abell 2218. The image contains various gravitationally lensed objects which are ideal candidates for study with a high spatial resolution IFU such as that proposed for use with GMOS. Overlaid on the image are boxes representing the field of view of the IFU shown to the left of the picture. The IFU field shown is that proposed for the GMOS-IFU (Allington-Smith *et al.*, 1997a). The image is reproduced courtesy of Dr. Ray Sharples, private communication.

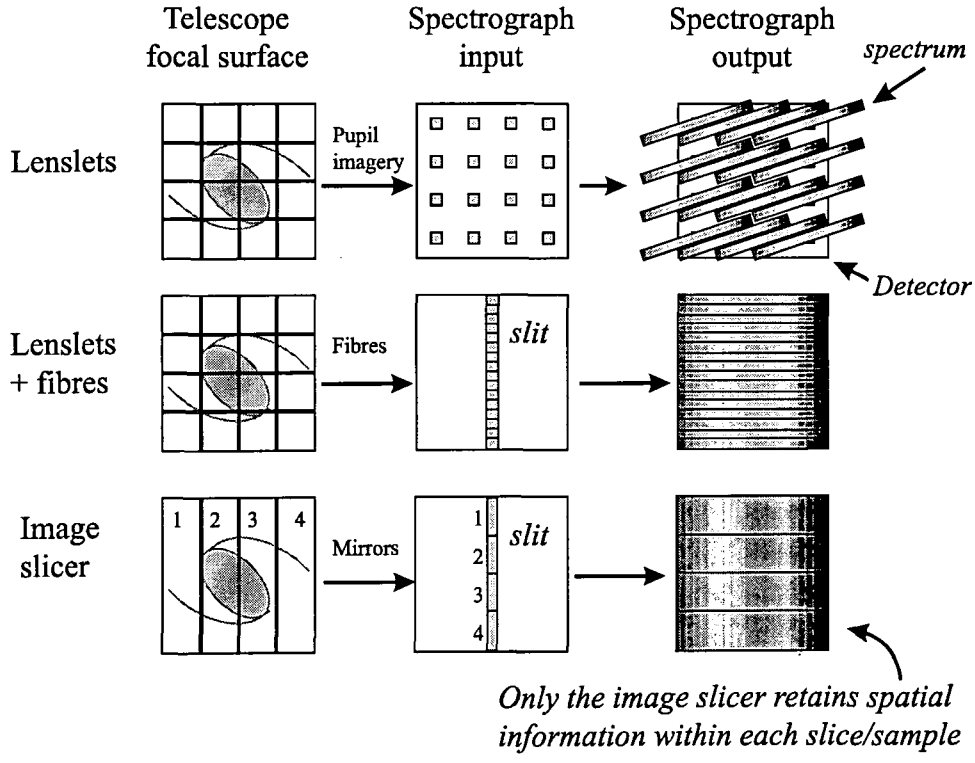

Figure 4.2: Schematic demonstrating the operational principle of the different types of integral field unit.

for comparison. A number of useful papers and review articles discussing all types of three dimensional spectroscopy, and their scientific uses, can be found in Comte & Marcelin (1994).

4.2.1 Longslit Spectrometers

A longslit spectrograph provides spatial information along the slit and spectral information. In order to measure the other spatial dimension the longslit has to be scanned across the object. An exposure is taken at one position, the telescope is then offset by the appropriate amount (typically the width of the slit) and another exposure is taken. This is clearly a time consuming process. Often the object of interest will only occupy a small fraction of the available slit length with the rest being devoted to sky. While this provides excellent background subtraction capabilities (this is still one of the principal advantages of longslit spectrographs) it is not a particularly efficient use of detector area.

An example of this type of observational technique is described in Dubath & Meylan (1994) where a kinematical map of the core of the globular cluster M15 has been measured. In order

to build up a velocity map of the core of the globular cluster five separate longslit exposures were taken with steps of one arcsecond (the width of the slit) between each exposure. This requires very accurate spatial registration between the different slit positions to avoid the introduction of systematic effects because of slit positioning errors. The need to take exposures over a long time frame may also introduce calibration problems due to atmospheric transmission changes and variable slit jaw losses due to seeing variations. Clearly these problems can be avoided if spectra of the required field of view can be obtained simultaneously leading to a considerable saving in observing time.

4.2.2 Scanning Fabry-Perot Spectrometers

A Fabry-Perot spectrometer system typically consists of a focal reducer type system with a collimator, camera and a collimated beam space. The Fabry-Perot Etalon is situated in the collimated space and produces a monochromatic image, i.e. it can be thought of as a narrow band interference filter. The spacing between the etalon plates and the order of interference determines the wavelength that is transmitted. To obtain spectroscopic information it is necessary to scan the etalon through the required wavelength range by increasing the etalon spacing. An image is taken at each scan position and a three dimensional data cube can be built up. Therefore coverage of a large spectral range would be a time consuming process with a scanning Fabry-Perot. Therefore the data cube produced by a FPS is generally of limited wavelength range. Examples of systems of this type are Taurus at the Anglo-Australian Observatory (Taylor & Atherton, 1980) and HIFI at the University of Hawaii 2.2m (Bland & Tully, 1989).

The advantage of a Fabry-Perot comes from the large field of view obtained in a single exposure. Another advantage of an etalon over more conventional spectroscopic techniques is very high spectral resolution can be obtained i.e. the bandpass of the etalon is very narrow, typically $\sim 10\mathring{A}$, providing a spectral resolutions in excess of $R \sim 1000$. Fabry-Perot systems are therefore best suited to observing spatially extended emission line objects where high spectral resolution is required. Examples of astronomical object that are particularly suited for observation with a Fabry-Perot IFS system are: extended gaseous nebulae, emission line galaxies, planetary nebulae searches, and imaging of faint emission features.

4.2.3 Imaging Fourier transform spectrometers

In its simplest form a Fourier transform spectrometer consists of a Michelson interferometer with the addition of a collimator and camera lens (Longhurst, 1973, p161). The source is therefore reimaged onto the detector via the collimator and camera lenses. An imaging fourier transform spectrometer (Maillard, 1994) uses a 2D detector, such as a CCD, at the focal plane of the camera. Interference is produced between the two mirrors of the interferometer and is recorded at the focal plane. The optical path difference between the mirrors is adjusted by scanning one of the interferometer mirrors. A disadvantage of the Michelson layout of interferometer is that 50% of the incident light is lost. However, a theoretical throughput of 100% can be achieved with use of more elaborate optical layouts (Bohlender, 1994). This means (in theory) that every incident photon reaches the detector.

The intensity of the emergent radiation is measured as a function of optical path difference, by scanning the mirror, producing the *interferogram.* The spectral distribution of the source, the *spectrogram*, can then be found from the fourier transform of the interferogram. Each pixel on the detector produces an interferogram of the corresponding area of sky. Therefore the spectral distribution for every pixel on the detector can be found from the interferogram. Imaging fourier transform spectroscopy therefore provides a spectrum for every pixel on the detector, and with large detectors, a large field of view. As an image is taken at each position of the scanning mirror a broad band image of the source is automatically produced, i.e. the entire spectrum is present in the output of an FTS. FTS offers the ability to choose the spectral resolution over a wide range (Bland-Hawthorn, 1994).

It seems then that FTS offers the ultimate in IFS, high throughput, large field of view, and high resolution, i.e. a large multiplex advantage. However the construction of an imaging FTS is difficult due to the required tolerances that must be achieved with the alignment of the mirrors. There is also the disadvantage that many exposures have to be taken, over a long period of time, to build up the interferogram. The exposures may therefore be subject to changes in atmospheric conditions which occur during the observations, and guiding errors.

The problem of maintaining the alignment of the interferometer is less critical as the wavelength is increased and this has led to the use of FTS mostly in the infrared region. Possibly the only FTS in use for astronomical spectroscopy is the CFHT Fourier Transform Spec-

trometer (Bohlender, 1994; Simmons *et al.*, 1997). This system provides Imaging-FTS over the J, H, and K-bands with a radial velocity resolution of up to $500ms^{-1}$.

4.2.4 Microlens Integral Field Spectrometers

A schematic of this type of system is shown at the top of figure 4.2. In a microlens based integral field system a microlens array is situated at the focal plane of the telescope or at the focal plane of a suitable telecentric enlarger system. Each microlens produces an image of the telescope pupil which acts as the as the entrance 'slit' to a traditional focal reducer type spectrograph. The major advantage of using microlens arrays at the focal plane is they provide contiguous spatial coverage without the loss of fill factor associated with fibre bundles. This system also has high throughput as only one optical component, the microlens array, is required to reformat the image into individual spectra.

One of the first examples of this type of instrument is TIGER (Bacon *et al.*, 1995) and this type of instrument is now often called a 'TIGER type' system after the precursor. Other systems in use are the Optically Adaptive System for Imaging Spectroscopy (OASIS) on the CFHT (Bacon, 1994) and the Kyoto University 3D spectrograph (Ohtani *et al.*, 1994). The Kyoto spectrograph design offers the useful feature of simultaneous object and background observations via the use of a special preoptics system. A TIGER type system, known as SAURON, is also currently being built for use with the William Herschel telescope (Bacon, 1996). Note that optical tests on the microlens array planned for use with SAURON were done as part of this thesis and are described in section 6.5. Tiger type systems can also be adapted for use in the thermal infrared (Herbst, 1998) as it is relatively straightforward to cool the microlens array to cryogenic temperatures. This may be an advantage over other types of IFU that incorporate fibres, as the performance of fibres at cryogenic temperatures is often thought to be a high risk area.

The field of view and the number of spatial elements is determined by the size and number of lenses in the microlens array. The spatial sampling can be adjusted by appropriate choice of enlarger optics situated before the microlens array. Microlens IFUs therefore provide a large field of view but at the expense of limited spectral coverage. The microlens array also has to be rotated slightly with respect to the detector rows and columns to avoid overlap between adjacent spectra.

The use of a TIGER type integral field spectrograph can also be combined with the use of a scanning Fabry-Perot etalon. This produces a hybrid TIGER type system with the advantage high spectral resolution given by the etalon. An example of a system of this type is PYTHEAS (Georgelin & Comte, 1994) which is a modification to the TIGER instrument with a Fabry-Perot etalon placed in the beam prior to the microlens array.

4.2.5 Fibre systems

The ability of optical fibres to transfer light from one place to another, as used so successfully in multi-object fibre systems, makes them an obvious choice for use in integral field spectroscopy. Integral field spectrographs incorporating optical fibres are often referred to as 'ARGUS' type IFUs. The large number of existing multi-object fibre spectrographs also makes fibre based IFUs an obvious choice in order to match existing instrumentation. Perhaps the first fibre based IFU is that described in Vanderriest (1980). A large number of fibre based IFUs have since been constructed. There have been various fibre based IFU systems in use on the WHT: HEXAFLEX (Arribas *et al.*, 1991) has two 61 fibre bundles each providing a different sampling interval, 2D-FIS (125 fibres with separate background field) provides an IFU capability when used in conjunction with the ISIS spectrograph (Garcia *et al.*, 1994), and Integral (175 fibres) can be used with the WYFFOS spectrograph (Arribas *et al.*, 1998). The WIYN and the KPNO 4-m telescope has Densepak, an array of 49 fibres. The CFHT provides an ARGUS mode, of 594 fibres, with the MOS spectrograph (Vanderriest *et al.*, 1994). There are also numerous other projects not mentioned here.

In a fibre based IFU the input image is formed directly onto a two dimensional array of optical fibres. The fibre bundle can be situated at the telescope focal plane, or the telescope focal plane can be reimaged onto the fibre bundle via a telecentric enlarger system. The two dimensional input fibre bundle is then reformatted to form the one dimensional entrance slit to a spectrograph. This process is indicated schematically in the middle diagram of figure 4.2. The input image is sampled by the the optical fibre core with the core diameter determining the spatial resolution. The minimum distance between the fibre cores is limited by the fibre buffer diameter and it is this which determines the spatial sampling. Typically small core closely packed fibre bundles are used for high spatial resolution astronomical applications and larger core well spaced fibre bundles for applications which require a larger field of view

without the fine spatial resolution. Sampling the field of view with fibres clearly does not provide contigous spatial coverage nor a high fill factor. Light is lost to the areas between the optical fibres. The fill factor obtained with a fibre bundle is typically $\sim$ 70% depending on the core/buffer ratio used. A general rule of thumb is that the cladding thickness should be ten times the longest wavelength which is required to propagate within the fibre, i.e. 10μm cladding for operation at 1μm. This may limit the fill factor to lower than 70%. This loss in fill factor is a major disadvantage of fibre based IFUs. Contiguous spatial coverage can only be re-gained by means of a complex dither pattern on the sky. The loss in fill factor will always be limited by the requirement of a minimum cladding diameter for correct operation of the optical fibre. The field of view is ultimately limited by the number of fibres that can be accommodated along the spectrograph slit or the detector.

Optical fibres also have the disadvantages associated with focal ratio degradation (FRD) which is equivalent to a non-preservation of etendue. FRD causes either a loss of spectral resolution or throughput or both. The effects of FRD are decreased if the fibre is operated at fast focal ratios, typically around F/5. This often requires the use of magnification optics in front of the fibre bundle to convert the telescope focal ratio to one that is more suitable for propagation in fibres. At the output slit magnification optics may also be needed to efficiently couple the fibre output focal ratio into the spectrograph. Fibre based IFUs are therefore particularly well suited for use in conjuction with multi-object based fibre systems which have spectrographs specifically designed for use with fibres.

Fibre based IFUs have generally been used in the optical region, however, their use is not restricted to the optical only. The technique has also been used for infrared observations, a bundle of 61 fibres, ISIS-IR, was used on the 2m Pic du Midi telescope (Cuby *et al.*, 1993) and a prototype IR-densepak (25 ZrF_4 fibres) on the KPNO 4-m (Levin *et al.*, 1993). The extension of the technique to the near infrared, J and H-bands, is quite straightforward as thermal emission is not yet the dominant source of background and standard Silica fibres maintain good transmission. The use of fibre IFUs in the thermal infrared is likely to be more difficult requiring the use of cold optics, cold baffles, and possibly cooled fibres. Another difficulty is Silica fibre has high attenuation redward of the H-band requiring the use of either: very short lengths of Silica fibre to reduce losses, or other types of fibre material such as Zirconium Fluoride or Chalcogenide fibres types (Haynes, 1995). With the new generation

of IR optimised 8-m telescopes there is however likely to be a scientific need for extending IFS capabilities into the infrared. Fibre based IFUs for use in the IR is therefore likely to be an area of much future research considering their popularity (see below) in the optical.

Despite the disadvantages fibre based IFUs are popular as they are relatively cheap, straight forward to manufacture (using existing fibre techniques developed for multi-object systems), and easily adaptable to existing multi-object fibre systems. Long lengths of optical fibre also provide flexibilty in where the spectrograph is mounted in relation to the telescope. In many cases the fibre fed spectrograph is mounted on the dome floor adjacent to the telescope. This reduces the complexity and cost of the spectrograph as no flexure is experienced in the stable environment away from the telescope. It may also be possible to pack bare fibres closer together on the spectrograph slit than is the case with the lens-fibre based systems described in section 4.3. The element to element slit spacing isn't limited by the size of the output microlens associated with each fibre therefore more spatial elements may be available on the slit.

4.2.6 Image slicer systems

The principle of an image slicer is shown in the final diagram in figure 4.2. In an image slicer[1] type system mirrors are used to reformat the telescope focal plane into a slit. The focal plane of the telescope is sampled by a series of mirrors which can be thought of as separate longslits. Each slit-mirror is slightly inclined in order to direct the light to a further set of mirrors which reformat the small slits into one longslit which feeds a spectrograph. An example of this type of device is the 3D instrument described in Weitzel *et al.* (1996). In the 3D system the telescope focal plane is sampled by 16 mirror slices, each measuring 8 × 0.4mm. The 16 slices are reformatted by the combining mirror to form a 'staircase' (i.e. there is a small offset in the spectral direction between each slice) type spectrograph slit which is 128mm long. This then feeds a conventional collimator-grism-camera type spectrograph.

An advantage of image slicer systems is they preserve spatial information along the slit just as in a longslit spectrograph. This means that throughput losses due diffraction broadening along the slit length are also reduced. The width of the slit projected onto the sky determines

[1]The traditional use of image slicers as it the entrance to longslit spectrographs to provide higher spectral resolution as described in Diego (1993).

the spatial sampling across the slicer with spatial sampling along the slit being determined by the detector pixels. The width of the slit also determines the spectral resolution of the instrument. Another advantage is that there are no FRD losses i.e. mirrors preserve etendue.

For correct operation the optical path length of each image slice must be the same. Therefore the slicing mirrors have to be arranged to provide optical path length compensation. The position of input and exit pupils must also be preserved. This is rather difficult to achieve without incurring some loss due to defocus across the slice or vignetting because the pupil position is incorrect. This is also means that accurate optical alignment of the slicing mirrors is crucial. Alignment of a large number of very thin mirrors is thought to be a major manufacturing difficulty with slicer type systems.

In its simplest form the image slicer only contains two slicing mirrors, and with gold coatings, this minimises light loss and thermal emission. The efficiency of the slicer is reduced by the defocus aberrations of the tilted mirrors and by diffraction at the narrow slits. The fill factor of an image slicer is limited only by the ability to pack the slicing mirrors as closely as possible with a minimum dead space. The published throughput of the slicer in 3D is 90%. The image slicer system therefore has an advantage of high efficiency. As the system only contains mirrors it is also thought to be straightforward to cool to cryogenic temperatures, thus allowing it to be used in the thermal infrared region, as in the proposed Gemini Near InraRed Spectrograph (GNIRS) image slicer (Content, 1997b). The 3D slicer is operated at ambient temperature. It is unknown whether fibre type systems would survive the thermal cycling process associated with operation in a cryogenic environment.

A disadvantage of image slicers is the manufacturing difficulty involved in producing the thin slicing mirrors. The sampling is limited by the size of the thinnest mirror which can be produced which was 0.4mm in the case of 3D. The FOV is also limited by the maximum slit size that can be accepted by the spectrograph. Scaling the 3D instrument to accommodate a 1024 square array would require a total slit of $\sim$ 400mm. This makes the spectrograph very large and expensive to construct, not to mention the difficulty of controlling aberrations with such a large length of slit.

It is also more difficult to build image slicers to match existing spectrographs. A new design of image slicer has been proposed, the advanced image slicer (AIS), as described in Content (1997), which overcomes many of the optical difficulties with image slicers by the

use of curved mirrors. Advanced image slicers are being proposed for use in various IR spectrographs. The GNIRS image slicer has already been mentioned. The UKIRT imager spectrometer, UIST (Ramsay-Howat *et al.*, 1998), being built at the Royal Observatory Edinburgh also proposes to provide an integral field capability via the use of an AIS (Content, 1998a). The compact design of the AIS and high performance make it a possible choice for use in the instrument capability of the New generation space telescope (Content, 1998b).

4.2.7 Summary

Various different methods of integral field spectroscopy have been described. Each method is best suited to a particular scientific requirement. The choice of the best design for an integral field unit is therefore determined by the science which is to be achieved. In Durham the science drivers are imaging and spectroscopy of high redshift faint galaxies. This requires an integral field unit with high spatial sampling to be able to resolve features in the galaxy, but over only a limited field of view. The ability to use the integral field unit on existing instrumentation is also a priority.

There are some advantages to IFS that are applicable to all types of IFU design. Target acquisition is easier with an IFU than with a narrow slit due to the large field of view of the IFU. The exact location of the IFU field with respect to the sky can be found after the observation has taken place from the reconstructed image. The large field of view of the IFU also captures all of the light from a compact source so there are no slit losses. This is particularly useful in non-optimum seeing conditions where much of the light in the seeing disk would be lost to a long slit. The absence of a slit also minimises systematic effects, such as velocity offsets, due to incorrect positioning of the source on the slit. IFUs also offer the capability to achieve higher spectral resolution than a slit because of their action as image slicers. Again throughput may be higher as very narrow slits are not required. There are also no losses with IFUs due to atmospheric dispersion, again this is due to the large field of view being able to gather all of the light. The effects of atmospheric dispersion on the data cube can be removed within software.

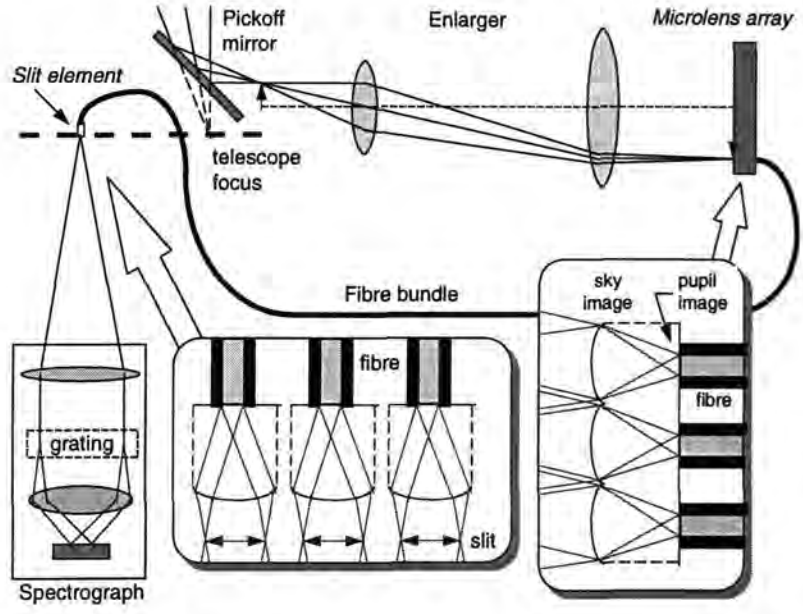

Figure 4.3: Schematic of the operation of a fibre-microlens integral field unit. The system shown is the GMOS-IFU (the output slit is in the same plane as the telescope focus) but the principle applies to any microlens-fibre based IFU.

4.3 Microlens and fibre systems

The design adopted for the construction of integral field units by the Astronomical Instrumentation Group in Durham is to combine the use of both microlenses and fibre bundles. This technique takes advantage of the gains available with microlenses and fibres. A schematic of the proposed system can be seen in figure 4.3. The figure shows a general IFU which incorporates a magnification system to enlarge the image produced by the telescope. Light from the telescope is directed through the enlarger system by means of a pickoff mirror. The enlarger system consists of a magnification lens, which produces an enlarged image of the telescope focal plane at the microlens array, and a field lens which ensures the pupil is at infinity i.e. the rays are telecentric.

The sampling in the telescope focal plane (or the focal plane of the enlarger optics) is determined by the size of each microlens. The use of contiguous hexagonal, or square, microlenses provides $\sim$ 100% fill factor which is unavailable with bare fibre bundles. Each microlens reimages the telescope pupil onto an optical fibre which is optically coupled to

each lens. The focal ratio entering the fibre, determined by the microlens, can be chosen to provide the best FRD performance within the fibre. The optical fibres provide an efficient way of reformatting the two dimensional input field into a one dimensional slit. This gives the maximum packing of information onto the detector. Microlenses are also used at the output slit to reimage the fibre core onto the spectrograph pupil, i.e., they convert the output focal ratio of the fibre to one which matches the focal ratio of the spectrograph.

The combination of microlenses and fibres provides an efficient versatile system. The ability of the microlenses to convert the focal ratio of the telescope to one which is optimum for transmission in fibres, and then do the reverse at the output, is very important. This means a microlens-fibre system can be built which matches virtually any telescope to any spectrograph. This allows an IFU to be built which can provide an IFS capability on existing long/multi-slit spectrographs which were not designed for use with optical fibres. The SMIRFS-IFU is an example of this providing IFS on an F/36 telescope and spectrograph, a focal ratio which is highly non-optimal for use with fibres.

Clearly if a dedicated fibre spectrograph is available then this technique becomes easier to realize as microlenses are no longer required at the output slit, the fibre spectrograph already being matched to the focal ratio of the fibre. An example of an instrument of this type is SPIRAL described in Parry *et al.* (1997). The advantages of using microlens-fibre IFUs at the input still remains however.

The difficulty in this technique is the technological development required to find suitable microlens arrays and methods for accurately coupling the microlens arrays with the optical fibre bundle. Much of this research and development is described in chapters 6 and 7. The SMIRFS-IFU was envisaged as a prototype instrument to develop the necessary technology and techniques with which to build more ambitious IFUs.

4.3.1 Other microlens-fibre IFU projects

Microlens-fibre based integral field units are also being developed for use with a number of other astronomical spectrographs. The SPIRAL instrument intended for use on the Anglo-Australian Telescope (Parry *et al.*, 1997) is only a prototype with 37 spatial elements. A phase-B version of this instrument is also planned with $\sim$ 500 spatial elements. An advantage

of the SPIRAL type of instrument is the use of reasonably large microlenses, approximately 4mm in diameter, which allows for straightforward alignment of the fibres with the microlens focii. It will be seen later in this PhD that aligning the fibres accurately with the microlenses presents a significant technological obstacle. The use of large microlenses also reduces the effects of non-telecentricity across the fibre face, a problem discussed in section 5.3.5.

Similar technology to that used in SPIRAL is being used for the IFU in another instrument: the Cambridge OH suppression instrument COHSI (Piche *et al.*, 1997). This instrument provides a travelling infrared IFU capability which can be taken to virtually any telescope. COHSI also incorporates an OH suppression capability via 'hardware masking', i.e. the infrared OH emission lines are masked at the focal plane of a high resolution spectrograph.

There are also some fibre-lenslet IFUs proposed for use with the new generation of 8-m telescopes. The Visible multi-object spectrograph (VIMOS) has plans for an ambitious IFU with $\sim 6,400$ spatial elements (Fevre *et al.*, 1998) utilising arrays of crossed cylindrical microlenses.

A new technique is being developed for ESO by the Max Planck Institute in Garching, Germany, which also incorporates the use of both optical fibres and microlenses. The major difference in this case is the microlenses are actually formed directly from the end of the fibre. In this instrument SINFONI (Tecza, 1997), which is planned for use on the VLT, individual hexagonal microlenses are formed onto the input end of the optical fibres using a special manufacturing technique. The end of the optical fibre is melted to form a tear-drop shape to which additional glass is added. The tear-drop is then polished to form a lenslet directly on the end of the fibre. SINFONI will provide 1000 spatial elements over the spectral range $1 - 2.5\mu$m. As Silica fibres are used in the near-infrared this requires that the fibres are short to avoid absorption losses. This technique of forming microlenses directly onto the optical fibres is potentially very useful as it avoids the need for complex optomechanical hardware to align microlenses with fibres, as described in section 7.3.1. Clearly this is an area of significant technological development that should be watched with keen interest in case these devices become commercially available.

Chapter 5

SMIRFS-IFU overview

Abstract

In this chapter the optical design of the SMIRFS integral field unit, for use in the J and H-bands at UKIRT, is described. The final design was for a system with 72 hexagonally close packed microlenses, with a sampling of 0.6 arcseconds, producing a total field of view of 6×4 arcseconds^2. Optical fibres are used to reformat the 2D input field to a 1D slit which feeds the CGS4 spectrograph. The optical principles leading to the chosen design are discussed as well as the methods by which optimal performance can be achieved. A brief discussion of optimum sampling and image reconstruction is also given. Finally the proposed design of the GMOS-IFU is described.

5.1 Introduction

In the previous chapter an overview of the various techniques of integral field spectroscopy was presented. After reviewing the advantages and disadvantages of each technique it was decided to combine the advantages of both microlens based IFUs and fibre based IFUs producing a hybrid fibre-lenslet design. This was then chosen as the design of IFU for future investigation by the Astronomical instrumentation group in Durham. The motivation for this work is the need to provide a high performance integral field capability for the Gemini multiobject spectrographs. The GMOS-IFU has to convert the focal ratio of the Gemini telescope to one suitable for use in optical fibres. The IFU also has to convert the output focal ratio from the optical fibres back to that of the spectrograph. High throughput is also a high priority. These requirements led to the use of lenslet-fibre based IFU technology as the obvious choice.

Before embarking on the ambitious GMOS-IFU project it was clear that a large number of technical difficulties had to be overcome. It was therefore decided to design and construct a modest prototype lenslet-fibre IFU system. This prototype IFU was conceived as the addition of an integral field capability to the existing Durham SMIRFS instrument. The design and construction of the prototype would act as a technology demonstrator to prove the concept of lenslet-fibre based IFUs. This chapter initially describes the existing SMIRFS instrument. The optical design of the SMIRFS-IFU, dictated by the need to match existing instrumentation, is then described in detail. The various factors which contribute to degrade the performance of the IFU, and the means of avoiding them, are also discussed. A brief discussion of sampling and image reconstruction with integral field spectroscopy is then presented. Finally the future projects, proposed for construction in Durham, are described and the concept for the GMOS-IFU is presented.

5.2 SMIRFS instrument overview

The SMIRFS-IFU described in this chapter is an upgrade to the existing SMIRFS instrument. SMIRFS is the *Spectroscopic Multiple InfraRed Fibre System* designed and built by the Astronomical Instrumentation Group in Durham. A full description of SMIRFS can be found in Haynes (1995) and Haynes *et al.* (1998a, 1998b).

SMIRFS is an infrared multiple object fibre system which allows up to 14 objects to be observed simultaneously. The system was designed for use on the United Kingdom InfraRed Telescope (UKIRT) with the CGS4 spectrograph in the J, H and K-bands. The main components of SMIRFS are as follows:

- The fibre bundles.
- The field plate unit (FPU).
- The slit projection unit (SPU).
- The guide fibre unit (GFU).

There are two fibre bundles: an ultra-low OH^- Fused silica fibre bundle for use in J and H-bands and a Zirconium Fluoride fibre bundle for use in the K-band. The size of the fibre

cores is 4.5 arcseconds (400 microns). The F/36 beam from UKIRT is coupled into the fibres by means of a small Calcium Fluoride lens positioned in front of each fibre. This converts the F/36 telescope beam to F/5 which is more suitable for propagation in fibres. The fibres can be positioned anywhere within a 12 arcminute diameter field of view with a minimum separation of $\sim$ 13 arcseconds. Typically $\sim$ 10 fibres are allocated to objects with the remainder used for background subtraction. There are also microlenses at the fibre output to convert the fibre focal ratio back to approximately F/36. The fibres are reformatted into a slit which is reimaged into the CGS4 spectrograph by means of the SPU. The K-band slit has an Aluminium mirror mask in front of it to reduce thermal emission from the fibre slit. The reflective mask prevents thermal emission, from the brass structure supporting the fibres, from entering the spectrograph. This mask was fitted as part of an upgrade to the original SMIRFS instrument. In the original design there was no masking at the output slit leading to a problem with thermal emission from the slit.

The fibres are held in position at the focal plane of UKIRT by means of the *field plate unit* (FPU). This is a mechanical interface which locates the field plate onto the telescope instrument support structure. The field plate is a 2mm brass plug-plate with holes drilled in it corresponding to the positions of the objects to be observed. The fibres are then located in the field plate. The field plate unit has a rotation mechanism for correct alignment of the fibres with the objects.

The *slit projection unit* is a device which reimages the SMIRFS output slit onto the cold slit of CGS4. An optical diagram of the SPU, adapted for use with the SMIRFS-IFU, can be seen in figure 5.1. Direct access to the CGS4 slit is impossible due to mechanical and thermal constraints. The SPU optics consist of a 408mm focal length Gold coated spherical mirror and a flat Aluminium mirror. The spherical mirror reimages the fibre slit onto the CGS4 cold slit and the Aluminium mirror provides a fold in the system. The optics of the SPU operate at 3° off-axis in order to avoid vignetting of the beam by the fold mirror. The mirrors are located on kinematic mounts and fixed inside a light tight box which locates onto CGS4. The SMIRFS output slit has to be curved to match the spherical focal plane produced by the SPU spherical mirror.

The final component to SMIRFS is the *guide fibre unit.* Three guide fibres can be located in the science field to aid field acquisition and guiding. The guide fibres consist of small

bundles of seven fibres packed into a hexagon. The guide fibres are fed to the GFU which reimages the fibres onto an autoguider camera. The autoguider can then be observed in the telescope control room to allow field acquisition by the telescope operator.

The SMIRFS multi-object system has been used successfully on a number of observing runs to observe globular clusters in the galactic plane (Haynes *et al.*, 1998a). It is particularly suited to this due to the density of objects in globular clusters being well matched the number of fibres, and the low extinction of infrared wavelengths allowing observations at low galactic latitudes. The performance of SMIRFS is also described in a commissioning note; Allington-Smith *et al.* (1997b).

5.3 Optical design of SMIRFS-IFU

The optical design of the SMIRFS-IFU was done at the University of Durham Astronomical Instrumentation Group by Robert Content. The design is described here for completeness. The design principles are also discussed as they are directly applicable to the design of future integral field units.

The SMIRFS-IFU was proposed as an upgrade to the existing SMIRFS multi-fibre instrument (Haynes, 1995) re-using many of the parts of SMIRFS which were described in the previous section. The SMIRFS-IFU is designed for use directly at the F/36 focus of UKIRT. Spectroscopic capability is provided by the CGS4 spectrograph, which also operates at F/36. The SMIRFS-IFU therefore has to be designed to operate with an F/36 input and output beam whilst reducing the effect of FRD losses within the optical fibres. A schematic of the operating principles of a lenslet-fibre based IFU is shown in figure 4.3.

The SMIRFS-IFU was also designed with a specific scientific programme in mind. Good spatial resolution and the ability to observe in the J and H-bands make the instrument ideal for kinematical mapping, and the study of emission line ratios, in compact active galactic nuclei. The scientific capabilities of the SMIRFS-IFU are described in more detail in chapters 1 and 9.

5.3.1 Limitations imposed by CGS4

The CGS4 spectrograph is described in Ramsay-Howat (1994) and Wright (1993). CGS4 is a cryogenically cooled longslit spectrograph located at the F/36 Cassegrain focus of UKIRT. Various combinations of dispersion, resolution and slit width are provided by the instrument through the use on interchangeable slits/gratings located on various wheels. Two cameras are available: the 'long camera' with a focal length of 300mm and the 'short camera' with a focal length of 150mm. The cameras and gratings are changed every semester (a complicated process which requires the instrument to be thermally cycled and dismantled). The SMIRFS-IFU was scheduled to be completed when CGS4 was in the 'short camera' mode. The use of the CGS4 short camera imposes various limitations on the design of the SMIRFS-IFU. Because of vignetting inside CGS4 the short camera is limited to operation with only 72 pixels of the 256 $\times$ 256 InSb detector. Each pixel corresponds to 1.22 arcseconds at the slit (slit length is 58.1mm). Therefore the maximum number spatial elements that can be obtained with the SMIRFS-IFU, with one fibre per pixel sampling, is 72. With one fibre per pixel sampling the IFU output PSF is undersampled in the spatial direction. This is not thought to be a disadvantage and is discussed in more detail in section 5.4. The SMIRFS-IFU can also be used in future with the 'long camera' which provides 1 fibre per 2 pixels sampling and is therefore more optimum.

As CGS4 is cryogenically cooled it is impossible to gain access to the slit as it is contained within the cryogenic vacuum vessel. This means that the SMIRFS-IFU output slit cannot simply be placed at the position of the CGS4 slit when using the SMIRFS-IFU. There is also only a limited space available for additional optics in front of CGS4 due to space constraints on the telescope. To overcome this the SMIRFS-IFU output slit is reimaged onto the CGS4 slit by a series of mirrors. A diagram of this optical system, referred to as the *slit projection unit* or SPU is shown in figure 5.1. The mirrors are housed in a container which is placed in a position in front of CGS4 normally occupied by the CGS4 calibration unit. This reimaging system imposes some limitations on the optical design of the SMIRFS-IFU as described in section 5.3.3

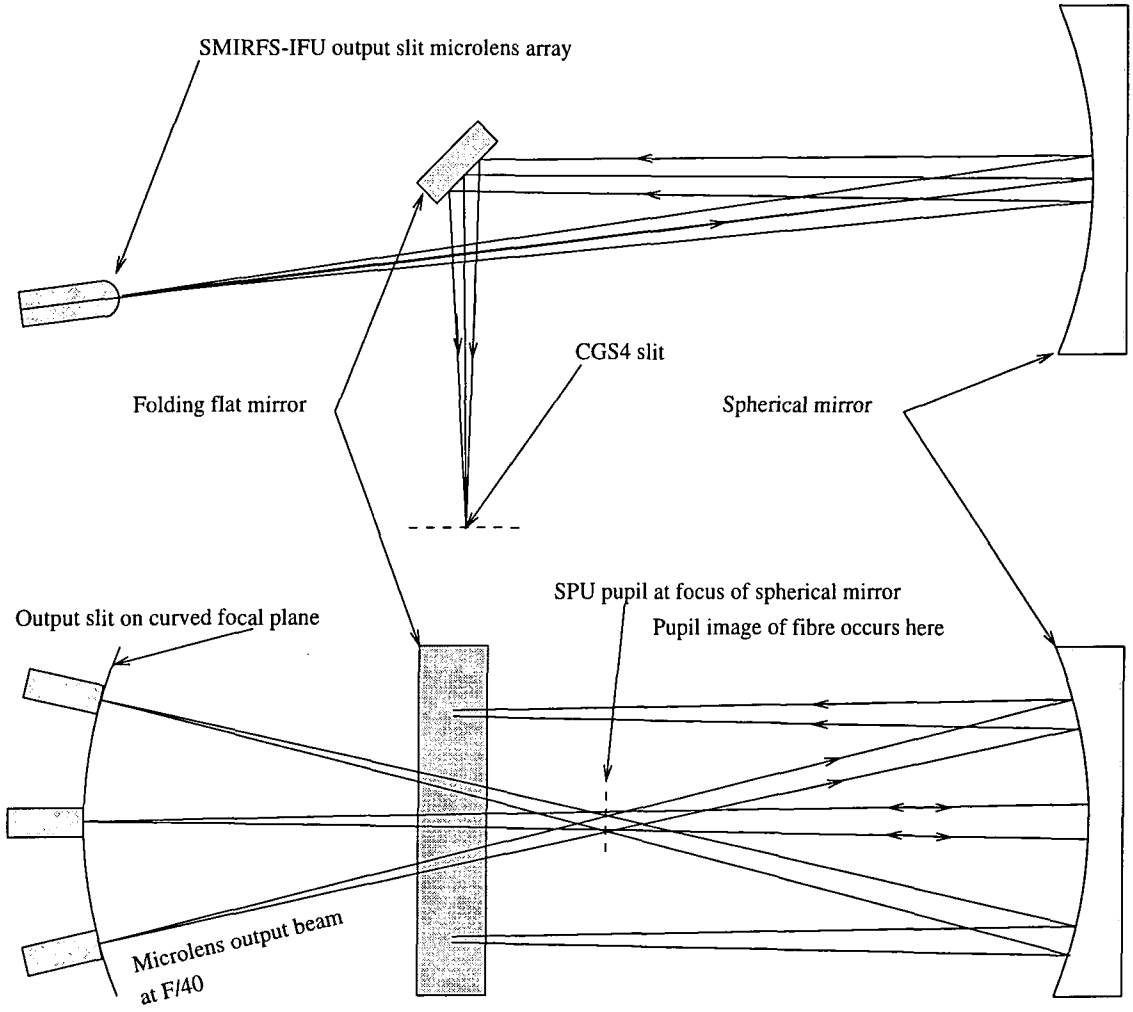

Figure 5.1: Optical diagram (plan and side view) of the SMIRFS-IFU output slit and slit projection unit. Each output slit block is individually pointed at the SPU pupil, which occurs where the fibre is reimaged by the microlens. The output slit blocks are also situated on a curved focal plane to reduce the aberrations of the spherical mirror. The folding mirror directs the beam into CGS4.

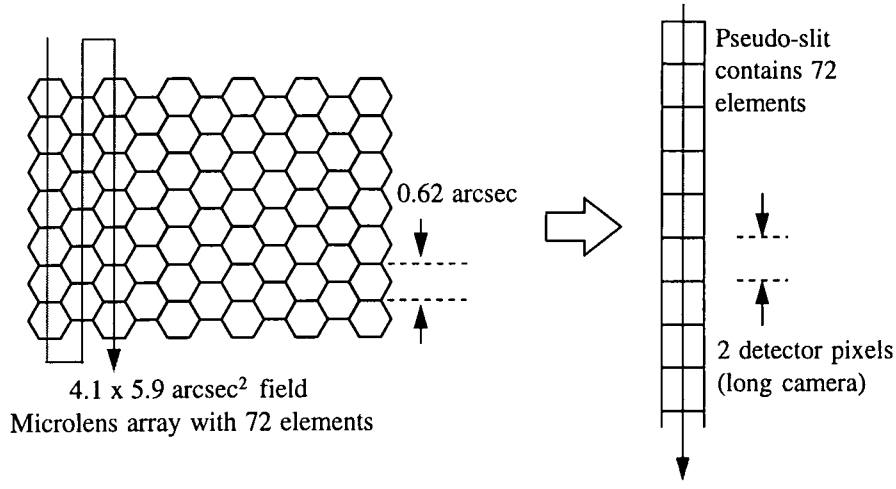

Figure 5.2: Diagram illustrating how the SMIRFS-IFU input field is reformatted at the output slit. Adjacent spatial elements at the input are also adjacent on the output slit. Note the reversal of the field to slit mapping direction at the end of each row on the input field.

5.3.2 Design of input microlens fibre feed

The plate scale at the F/36 Cassegrain focus of UKIRT is 1.53 arcseconds per mm. The median seeing provided by UKIRT is $\sim 1 - 1.2$ arseconds[1]. To correctly sample the seeing disk (Nyquist sampling) the IFU sampling needs to be ~ 0.6 arcseconds corresponding to microlenses measuring 0.39mm. Note that with the SMIRFS-IFU the microlenses are located directly at the focal plane of the telescope. In other IFUs being designed an enlarger stage is located before the microlens array to magnify the telescope focal plane. There is a trade-off between adequate sampling at the input and field of view. Clearly the seeing disk is oversampled at the expense of limiting the total field of view. The field of view is even more restricted by the limitation imposed by CGS4 of 72 spatial elements. A sampling of 0.62 arcseconds (0.406mm) was chosen as this closely matches the diameter of a standard size gauge tube. This is a manufacturing constraint and is described in more detail in section 7.3.2. The final design of the SMIRFS-IFU input field can be seen in figure 5.2. An aspect ratio of ~ 1.4 was chosen to match the aspect ratio of a variety of astronomical objects, although another aspect ratio could have been chosen.

Hexagonal microlenses were chosen for use at the input as the hexagonal shape provides the

[1]Prior to the installation of the UKIRT tip/tilt secondary.

best approximation to a circle. This minimises the effect of what the author calls *Geometric FRD* which is an effective broadening of the input focal ratio due to the geometric shape of the microlens. Geometric FRD is caused because there is a 17% difference between the inside and outside diameters of a hexagon. If, for example, the inside diameter of the hexagon defines an F/10 beam then the corners of the hexagon will produce an F/8.5 beam. This can be thought of as an additional focal ratio degradation as the spectrograph has to accommodate the F/8.5 beam if throughput losses are to be avoided. With F/10 hexagonal lenses, measured from the inside diameter, only 91% of the light is contained within F/10. The effect of geometric FRD is much worse with square (or rectangular) lenses where the difference between the focal ratio defined by the inside diameter and the corners is much greater. In extreme cases losses due to geometric FRD would mean the sampling element on the sky isn't actually a hexagon but a circular aperture defined by the FRD cone. This change in sampling pattern may cause systematic effects in the image reconstruction process. Of course the major advantage of hexagonal input microlenses is they provide close to 100% fill factor (as would square lenses).

The input microlenses are designed to reimage the telescope exit pupil, which is the UKIRT secondary mirror, onto core of the optical fibre. The sampling is determined by the size of the lens. The diameter of the fibre is determined by the focal ratio at which the fibre is to operate. The fibre core diameter, Φ, can be found from the following equation:

$$\Phi = \alpha D_{tel} F_{fibre} \tag{5.1}$$

where α is the required sampling interval (in radians) on the sky, D_{tel} is the diameter of the telescope primary mirror and F_{fibre} is the focal ratio at which the fibre is to operate.

It was decided that the SMIRFS-IFU fibres would accept an input focal ratio of F/13. This requires that the fibre core is 150μm in diameter for a sampling interval of 0.62 arcseconds. Also 150μm core fibres are readily available as a standard product from Polymicro technologies thus avoiding the need for custom fibre to be made. The input microlenses were designed to produce a pupil image which is 151.1μm in diameter so as to slightly overfill the optical fibre. The fibre then acts as a baffle and prevents thermal emission from the telescope support structure, and the sky surrounding the secondary, from entering the fibre. The dominant source of background in the J and H-bands is night sky emission so the amount of sky background entering the fibre has to be kept to a minimum.

The input microlenses were designed to provide the best image quality at the edge of the fibre cores in the H-band. Image quality is important at the edge of the fibre as this is where losses would occur if the pupil image was blurred. Lower image quality can be tolerated at the centre of the fibre core. The microlens manufacturer (Adaptive Optics Associates) provides a specification on focal length at 632.8nm so care has to be taken to allow for the chromatic aberration of the microlenses in the optical design. The dispersion of the microlens material produces approximately a 4% change in focal length between 0.633μm and 1.65μm as described is section 6.3.3.

5.3.3 Design of output microlens fibre slit

There are certain optical requirements imposed on the SMIRFS-IFU output slit by the need to work with the SMIRFS slit projection unit and CGS4. The slit projection unit (SPU) reimages the SMIRFS-IFU output slit onto the CGS4 slit, at unit magnification, by means of a spherical mirror (radius of curvature is 408mm). As the CGS4 slit is flat in order to achieve best image quality with the SPU spherical mirror requires that the SMIRFS-IFU output slit focal plane be curved. The optimum radius if curvature of the SMIRFS-IFU output slit is then approximately half the radius of curvature, $\sim$ 204mm, of the spherical mirror. The SPU also has to provide an exit pupil which is at infinity for correct imaging inside CGS4. This means the fibre pupils all have to be reimaged at the entrance pupil of the spherical mirror. This is illustrated in the optical diagram shown in figure 5.1. The entrance pupil of the spherical mirror is located at the focus, approximately 200mm from the mirror surface.

Square microlenses were chosen for use at the SMIRFS-IFU output slit. The geometry of square lenses is a perfect match to the slit geometry. Square lenses also capture the maximum amount of light from the FRD cone produced by the fibre. The lens size is determined by the plate scale at the CGS4 slit with one pixel on the detector corresponding to 0.793mm at the slit (1.22 arcseconds). Due to the difficulty of preparing a curved fibre slit, and the troublesome task of obtaining microlenses located on a curved substrate, the curved slit was approximated by 12 slit blocks. This is illustrated in the mechanical drawing shown in figure 7.3. Each slit block contains six square microlenses. The optimum position of each slit block on the curved focal plane was determined by ray tracing. Each slit block is positioned at

the correct angle such that the projected image of the fibre is located at the pupil of the spherical mirror.

The focal length of the output microlens was chosen to provide an ~F/40 output beam. This will then slightly underfill the CGS4 pupil (the grating) and should reduce vignetting inside CGS4. It also helps to compensate for diffraction broadening caused by the IFU which would otherwise lead to overfilling of the spectrograph pupil. The design of output microlenses was optimised to provide the best quality pupil image formed by three microlenses of the group of six. The other three are not needed in the optimisation as their pupil image is the same due to symmetry. In this way the optimum lens design is found for the output microlens array as a whole rather than the optimum for one lens. The focal ratio of the output microlenses is F/7.5. This is approximately the focal ratio that will be produced by the optical fibre due to focal ratio degradation of the F/13 input beam. The effective slit width of the SMIRFS-IFU output slit is defined by the size of the exit pupil which is located just in front of each output microlens. The maximum size the exit pupil can reach occurs when the FRD cone from the fibre completely fills the microlens aperture and is the same size as the output microlens. If the FRD cone from the fibre underfills the microlens aperture, however, a smaller pupil image will be produced. Underfilling of the output microlens aperture will lead to a small increase in the spectral resolution that can obtained. The gain in resolution available from fibres with low FRD characteristics is a property of microlens-fibre systems only, and provides a small advantage. The disadvantage, of course, is the spectral PSF is variable with FRD, and may require accurate calibration. Underfilling also means that no light is lost due to vignetting by the output microlens.

It should be noted that FRD is equivalent to a loss of information in the optical system, or alternatively it can be thought of as non-conservation of etendue. Either spectral resolution, spatial resolution, or throughput (or a combination) is degraded due to FRD.

The projected image of the fibre produced by each output microlens occurs approximately 200mm from the lens and is 5mm in size. It is necessary that all the fibre images produced by one slit block overlap, to avoid vignetting inside CGS4. To achieve this the spacing of the fibres, 0.817mm, is made slightly larger than the spacing of the output microlenses, 0.793mm. The small angle introduced by the difference in spacing between the microlenses and the fibres is enough to cause the fibre images to be located in the correct position at the

SPU spherical mirror entrance pupil.

5.3.4 Design trade-offs

The design of an integral field unit involves a subtle trade off between spectral resolution, spatial resolution and throughput. For example, the SMIRFS-IFU could have been designed such that the focal ratio within the fibres is F/5. Equation 5.1 can then be used to predict that the core diameter of the fibre is reduced to $\sim 60\mu$m. The output microlenses then become F/3 instead of F/7.5. Losses due to FRD are decreased and the spectral resolution is increased as it is unlikely that the F/5 input beam would degrade to F/3 overfilling the output microlens aperture i.e. the effective slit width is smaller. However there will be losses due to the increased difficulty of coupling the pupil image into the smaller fibre at the input. Throughput losses due to positioning errors increase as the fibre size decreases. There is a limit to this coupling efficiency determined by the positioning error budget discussed in section 7.3.2. The effect of aberrations with the input microlens will also cause increased losses with smaller fibres. Diffraction by the fibre core at the output will have an increased effect (diffraction can be thought of as an additional source of FRD). If the fibres are made oversized to accommodate the positioning errors and optical aberrations then there will be increased sky background. This increase in sky background is only a concern on infrared telescopes where there is no baffling in order to keep thermal emission to a minimum. In the visible there is adequate baffling on the telescope and the fibre core size can be increased to accommodate positioning errors without any risk of background contamination.

The performance of an integral field unit can be characterised in terms of a figure of merit. A simple figure of merit would be the product of number of spatial elements, number of spectral elements and throughput. The figure of merit, Q, can be represented by an equation of the following form:

$$Q = T^{\alpha} N_{spatial}^{\beta} N_{spectral}^{\gamma} \tag{5.2}$$

where T is the transmission, $N_{spatial}$ is the number of spatial elements and $N_{spectral}$ is the number of spectral resolution elements. The choice of exponents varies according to the application but could simply be $(\alpha, \beta, \gamma) = (1, 1, 1)$. This figure of merit can also be thought of as an observing efficiency, an IFU with a higher figure of merit producing a larger data

cube. The maximum figure of merit that can be achieved with an IFU is generally limited by the available detector area. In general optimising the performance of an integral field unit for, say, the maximum number of spatial elements will limit the other factors in the figure of merit, i.e. packing a large number of spatial elements onto the detector limits the spectral range that can be achieved. The general point is that integral field spectroscopy operates in a regime with a maximum figure of merit. Changing one factor in the figure of merit therefore causes corresponding changes in the other factors. Another example is with a fibre based IFU, if the fibre core size is increased to gather more light, at the expense of spatial resolution, the spectral resolution will also decrease because of the increased size of fibre core. Designing an integral field unit is therefore a subtle process in which the best design can only be achieved by careful balancing of the factors in the figure of merit and optimising for the particular factor that best suits the scientific requirements.

5.3.5 Secondary focal ratio degradation

Geometric focal ratio degradation caused by the shape of the microlens has already been described. There is however another source of focal ratio degradation in microlens fibre systems which has been termed 'secondary focal ratio degradation'. It should be noted that although these effects are called FRD they do not occur inside the optical fibre but they produce the same overall effect as additional FRD. Secondary FRD (Parry *et al.*, 1997) is caused because the microlens is of order the same size as the optical fibre. This is illustrated in figure 5.3.

The input focal ratio to the fibre, from figure 5.3, is given by $F_{fibre} = t/2h$. Secondary FRD is caused because the beam at the edge of the fibre is faster than at the fibre centre because of the size of the fibre i.e. the pupil image formed at the fibre is not telecentric across the face of the fibre. The focal ratio at the edge of the fibre is $F_{sec} = t/2(h + d)$. In the case of the SMIRFS-IFU with $h = 0.206\mu$m, $d = 0.075\mu$m and t=5.35mm then $F_{fibre} = 13$ and $F_{sec} = 9.5$. When the effect of geometrical FRD is included in the calculation as well the fastest beam entering the fibre is F/8.5. Secondary FRD is worse when the fibre is large compared with the size of the lens. It is necessary to include the effects of secondary FRD and geometrical FRD when calculating the optimum focal ratio at which the fibre should operate. Geometric and secondary FRD generally mean the microlens has to be made slower

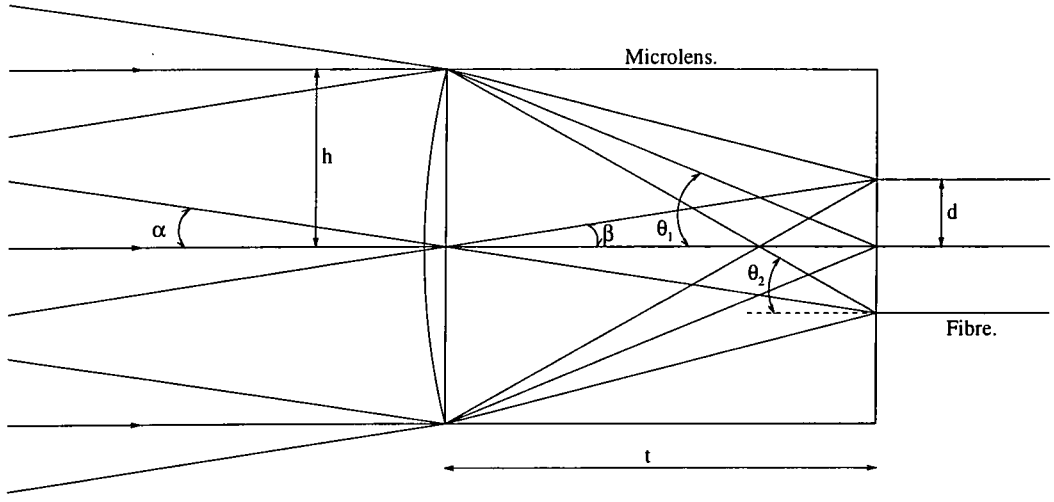

Figure 5.3: Schematic of pupil imaging onto an optical fibre by a microlens. h is the radius of the microlens, d is the radius of the fibre core, t is the focal length of the microlens. The input focal ratio is denoted by the angle α. The input focal ratio to the fibre is denoted by θ_1, with the focal ratio due to secondary FRD given by θ_2.

(i.e. F/13 to F/15) such that the losses are compensated. The influence of secondary FRD becomes less important if microlenses which are considerably larger, by a factor of ten or so, than the fibre core are used. A system which takes advantage of this by using lenses which are 4mm in size is SPIRAL (Parry *et al.*, 1997) virtually eliminating losses due to secondary FRD. Note that this effect is termed "non-telecentricity across the fibre face" in Parry *et al.* (1997).

5.3.6 SMIRFS-IFU technical specification

The preceding sections described the optical design of the SMIRFS-IFU and some of the factors which influenced the choice of design. The final design of the SMIRFS-IFU is summarised in table 5.1. It should be noted that the focal ratios specified in table 5.1 are only approximate due to the combined effects of geometric FRD, secondary FRD and actual FRD. It can be seen for instance that the input focal ratio of F/13 is predicted to be broadened to ~F/8 at the output.

Number of spatial elements		72
Spatial sampling	α	0.6"
Total field of view		6" × 4"
Input microlens pitch		412μm
Input microlens focal length (in air)		5.35mm
Optical fibre core diameter	Φ	150μm
Fibre input focal ratio	F_{fibre}	~F/13
Fibre output focal ratio		~F/8
Output microlens pitch		793μm
Output microlens focal length (in air)		5.95mm
Focal ratio of projected beam into CGS4		~F/40

Table 5.1: Technical specification of the SMIRFS-IFU as manufactured. The symbols are those used in equation 5.1.

5.4 Sampling and reformatting

In order to maximise the field of view available with the SMIRFS-IFU a sampling of 1 fibre per pixel was used at the detector. This is contrary to the general rule (Nyquist sampling) that the fibre image should be sampled by two pixels per FWHM. It is also generally the case in fibre spectrographs that there are gaps in between each fibre/spectrum to avoid cross talk between adjacent fibres. However cross talk between fibres can be tolerated with integral field spectroscopy if neighbouring elements on the slit are also adjacent on the sky, as illustrated in figure 5.2. The IFU input field can then be thought of as a series of adjacent longslits on the sky which are reformatted to a series of longslits at the spectrograph slit. Correct sampling is provided by the IFU spatial elements rather than the detector pixels. The spectra should be packed closely together such that the distribution of light on the detector is similar to that which would have been obtained from a longslit sampling the sky directly.

A general rule for IFS is that optimum sampling is achieved when the FWHM of the input image is sampled by two slit elements. It is important to realise that optimum sampling of the science field is achieved by the IFU input and not the detector. Therefore the sampling of the IFU output further downstream, i.e. at the detector, is less critical. This sampling strategy achieves the most efficient use of the available detector area. The sampling process,

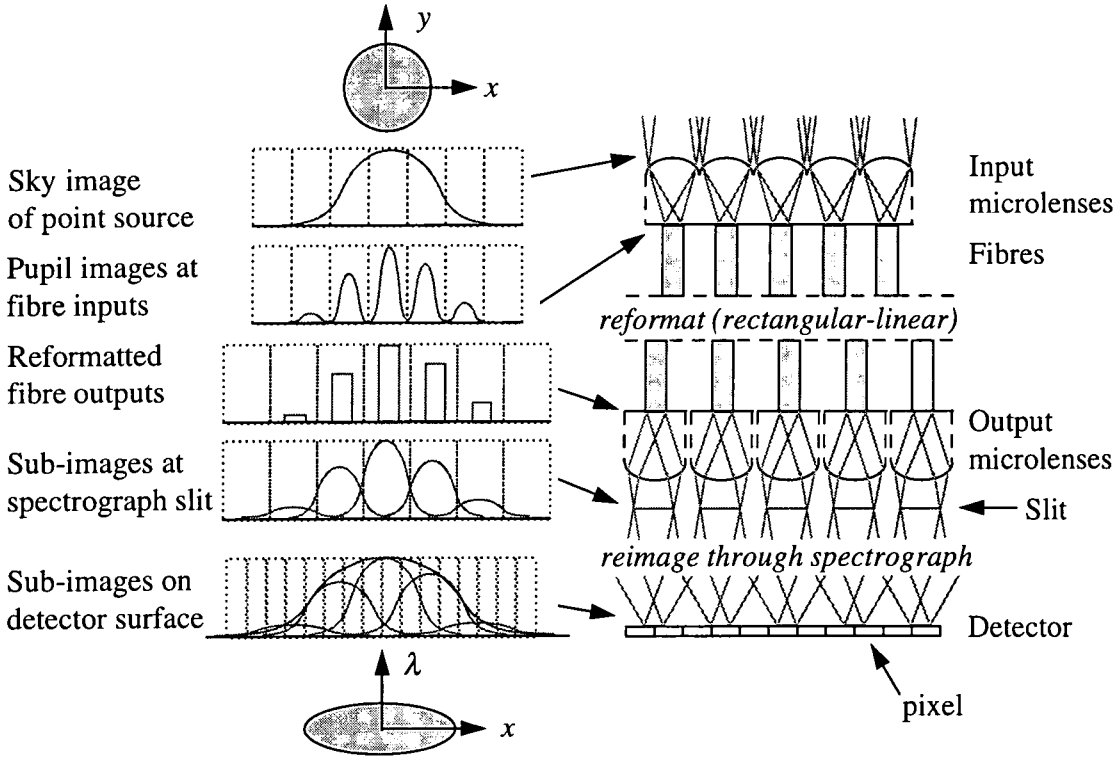

Figure 5.4: Schematic of the detection process in integral field spectroscopy. Adjacent elements at the input are mapped to adjacent spectra at the detector. In this way cross talk between elements can be tolerated producing a blurring of the reconstructed PSF in the spatial direction.

from science field to detector, is illustrated schematically by the diagram shown in figure 5.4. The 'detection process' and optimum sampling strategy is described in more detail in Allington-Smith (1996) and Allington-Smith & Content (1998). The detection process can be summarised as follows, with reference to figure 5.4:

- The spatial profile of the source is sampled by the IFU spatial elements.
- Each microlens forms a pupil image onto the fibre core.
- The fibre scrambles the pupil image producing a modified output pupil illumination function (approximately a 'top hat' function).
- The fibre output is reimaged onto the spectrograph slit with a slight broadening due to optical aberrations.
- The spectrograph slit is reimaged onto the detector where each element of the slit forms an image slightly broadened by aberrations.

Note that the fibre receives both radial and azimuthal image information at the input. However scrambling within the fibre will cause this imaging information to be lost. Fibre scrambling is usually complete azimuthally, but only partial radially. This means that a spot of light imaged onto the fibre core will be seen as a ring of light on the fibre core at the output (viewing the fibre core is the near-field pattern) due to azimuthal scrambling. The projected image of the fibre core, the far-field pattern, will show a thin ring and not a top hat like illumination pattern as some radial information is usually preserved, except in cases of extreme FRD. Incomplete radial scrambling by fibres can be a disadvantage in some cases, such as high spectral resolution work (Casse & Vieira, 1997), as it means the detected PSF varies with changes in seeing.

The effects of optical aberrations, FRD, and diffraction cause the detected spatial profile to be broader than that at the input to the IFU. Some broadening of the PSF may also be caused by the sampling pattern of the detector. There is then a broadening of the reconstructed IFU image in the spatial direction due to overlap between adjacent spatial elements on the detector. This is equivalent to a broadening of the reconstructed image in the 'slit' direction. This broadening does not occur in the other spatial dimension on the IFU

as the fibre PSF is correctly sampled in the spectral direction i.e. there is no cross talk across the IFU, only along the pseudo-slits. This broadening was measured for the SMIRFS-IFU from a reconstructed image of a standard star as described in section 8.5.4. The degradation in spatial resolution due to all of the above effects has, in general, only a small effect.

Some degradation in the accuracy of the image reconstruction may also be caused by the fibre flat-field. Each fibre will have a slightly different transmission to that of its neighbours due to manufacturing problems. The fibre to fibre throughput variation therefore introduces artificial gradients in intensity between adjacent lenses. Unless the effect of fibre to fibre throughput variation is removed, via flat-fielding observations, these variations will imprint themselves on the reconstructed image.

The correct configuration to provide optimal sampling has to be individually modelled for each design of IFU. There may be limitations which prevent optimal sampling from being realised, such as minimum separation of the fibres at the output slit. In some designs of IFU where separate background fields are provided then gaps will be needed between background spectra and object spectra to avoid cross talk. Unfilled areas on the detector may also be needed to allow spectrograph scattered light to be estimated. In general it is the available detector area which limits the field of view of an IFU. It is therefore crucial to maximise the use of the available detector area with correct sampling whenever possible.

5.5 Relevance to future projects

It has already been said that the SMIRFS-IFU is only a technology demonstrator for more ambitious IFU projects. The next project following the SMIRFS-IFU is the Thousand Element Integral Field Unit (TEIFU) for use with the University of Durham Electra adaptive optics system (Buscher *et al.*, 1995) on the William Herschel Telescope. TEIFU will feed the WYFFOS fibre spectrograph (Worswick *et al.*, 1995). TEIFU is described in more detail in Haynes *et al.* (1998a,1998b). TEIFU provides approximately 1000 spatial elements with a sampling of 0.12, 0.25 and 0.5 arcseconds. The spatial scale being chosen by use of different magnification optics. Fine sampling is required to match the high image quality provided by the Electra adaptive optics system. As with SMIRFS hexagonal microlenses are used at the input to reimage the telescope pupil onto the fibre core. The fibres are oversized

compared with the pupil image in order to reduce losses due to positioning errors. Fibres can be oversized on the WHT without risk of increasing the background light as the WHT is a baffled telescope. The fibres will operate at F/5.6. Conversion back to F/8 required by the WYFFOS spectrograph is done by means of microlens at the output slit in a similar fashion to SMIRFS-IFU. Each fibre reimages to one pixel on the detector. Clearly this instrument is a major step forward from SMIRFS-IFU due to the massive increase in the number of fibres and the smaller components required.

The optical design of TEIFU is made slightly more complicated by the addition of magnification fore optics (this also applies to the design of the GMOS-IFU). The fore optics are required to reimage the focal plane of the telescope onto the microlens array, at an appropriate magnification, to determine the spatial sampling and allow reasonable sizes of microlenses to be used (i.e. greater than 250μm). The fore optics must not degrade the quality of the adaptive optics corrected image or lower throughput. Care must also be taken to avoid chromatic effects, such as changes in magnification with wavelength, otherwise a blurring of the projected pupil image at the fibre may result.

5.5.1 The GMOS integral field unit

The ultimate aim of the microlens fibre development programme is to provide an IFU capability for the Gemini multi objects spectrograph (GMOS). This system is more complicated because of the high image quality specifications required to match the expected performance of the Gemini telescopes. The instrument also needs to be robust and easy to use as it will be a common user instrument, unlike the SMIRFS-IFU or TEIFU. The entrance plane and the exit plane of the IFU must also coincide, as shown in figures 4.3, so that the GMOS-IFU can be inserted into the optical path as a 'black box'. No focus adjustment or mechanical changes to the GMOS optics are therefore required, i.e. the spectrograph operates in IFU mode just as if it were looking at a normal multiaperture mask. The GMOS-IFU must therefore be located in the space normally occupied by a focal plane mask. This imposes severe size and weight constraints. Despite the difficulties a design for the GMOS-IFU has been proposed as shown in figure 5.5.

The method of operation of the GMOS-IFU is illustrated schematically in figure 4.3 and is somewhat similar to that of both SMIRFS-IFU and TEIFU. Light from the telescope is

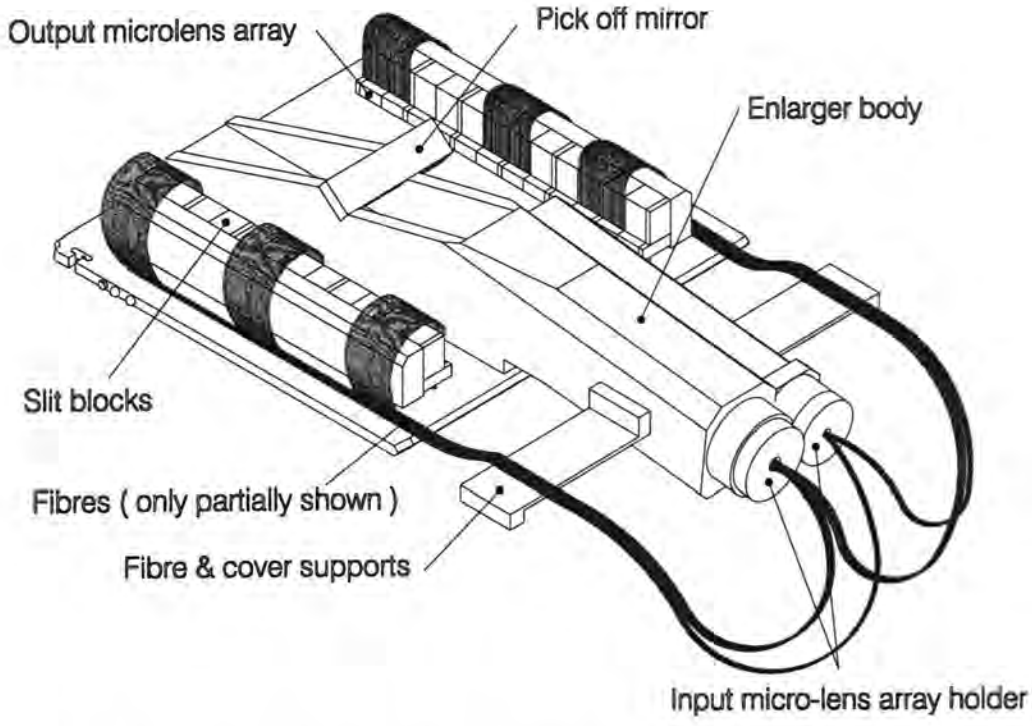

Figure 5.5: Mechanical drawing of the proposed design of integral field unit for the Gemini multiple object spectrograph. The GMOS-IFU is severely space constrained by the requirement to fit within the mask changing apparatus. A schematic of the operation of this IFU can be seen in figure 4.3.

fed into a telecentric enlarger system by a pickoff mirror. The enlarger system produces an enlarged image of the telescope focal plane at the microlens array. Various spatial sampling scales can be chosen by the use of different magnification optics. This provides the GMOS-IFU with great versatility in being able to match a wide variety of scientific targets. As with SMIRFS-IFU the microlens array is used to feed a fibre bundle at the optimum focal ratio to minimise losses due to focal ratio degradation. Fibres provide a neat way to direct the light back to the telescope focal plane where the output slit is located. Microlenses are also used at the output slit to convert the output focal ratio from the fibre back to that required by the GMOS. Another novel feature of the GMOS-IFU is the provision of a separate background IFU. This means both the object and an un-connected background field, to allow precise background subtraction, can be observed simultaneously. A discussion of the advantages of this technique can be found in Allington-Smith *et al.* (1997a). However, it does mean the additional complication of building two IFUs within the small space envelope. The background field is a factor of ten smaller than the object field. The proposed design of GMOS-IFU that achieves all this within the space envelope defined by the multiaperture mask changer is shown in figure 5.5.

The major difficulties in constructing the GMOS-IFU are mainly to do with achieving high throughput and high image quality. To achieve high throughput requires accurate knowledge of how to predict the performance of the microlenses and fibre bundle. The theoretical performance can then be accurately predicted to allow the optimum design to be found. Much of the work in this thesis is concerned with performance measurement techniques applied to the components used in integral field spectroscopy, in particular the microlens arrays. High throughput also implies tight mechanical tolerances in manufacturing the mechanical components such as the tube array. The techniques developed to meet these demanding tolerances are also discussed in this thesis.

High image quality is needed to maintain the superb image quality expected to be produced by the Gemini telescopes. This requires fine sampling of the telescope focal plane implying small fibres and miniaturisation of the components, i.e. small diameter microlenses and micro-tubes. The baseline scientific requirement is for IFU sampling of 0.2 arcseconds, with $\sim$ 2000 spatial elements, covering a field of view of 50arcsec^2. This sampling implies a fibre core size of 40μm. Simply handling a small diameter fibre is difficult enough without the

added difficulty of inserting 1000 into an array of tiny tubes! Preserving high image quality requires high performance magnification lenses and microlenses. Testing the image quality of microlenses for use in IFS forms a major part of this thesis.

5.5.2 Multi-object integral field spectroscopy?

In the future it is quite likely there will be a scientific requirement for IFUs to perform multi-object spectroscopy. The objects will be sampled by mini-IFUs instead of the single fibres or multi-slits currently used. Multi-object spectroscopy is recommended as a major observing mode for the proposed prime focus fibre instrument on the Subaru telescope (Allington-Smith, 1997). This technique will then provide all the advantages of integral field spectroscopy over a wide range of targets, distributed within a field. Another major advantage, of course, is the multiplex gain associated with multi-object observing. This requires miniaturisation of the microlens-fibre IFU package so that many of them can be accommodated in the telescope focal plane with the minimum amount of dead space between adjacent mini-IFUs. This is clearly an area for future research and development.

5.6 Summary & Conclusions

The introduction to this chapter discussed the need for a prototype lenslet-fibre based IFU to act as a technology demonstrator for future, more ambitious, IFU projects. It was decided then to build a modest IFU as an upgrade to the existing SMIRFS multifibre instrument. The capabilities of the SMIRFS instrument were then described. A detailed description of the optical design of the SMIRFS-IFU was then given. The capabilities of the SMIRFS-IFU are somewhat limited by the need to be used with the CGS4 spectrograph which only has a slit length of only 72 pixels. Despite this disadvantage a design is presented that makes full use of the available detector area by employing a mapping of one IFU spatial element per pixel. Each IFU spatial element measures 0.6 arcseconds in size at the focal plane of UKIRT providing optimum sampling of the seeing disk expected with UKIRT. The input consists of an array of 72 hexagonally close packed microlenses providing a total field of view of 6×4 arcseconds with an aspect ratio of 1.4.

The input microlenses feed the optical fibres at approximately F/13. This focal ratio was chosen after careful consideration of the effects of focal ratio degradation. The fibres are made slightly smaller than the size of the pupil image formed by the input microlenses in order to reduce the amount of thermal background that enters the fibre. The output focal ratio from the fibre, predicted to be approximately F/8, is then converted back to a focal ratio suitable for use within the CGS4 spectrograph by means of another set of microlenses. The output microlenses have to be situated on a curved focal plane due to the imaging requirements of the slit projection unit. To achieve this the output slit is therefore broken up into 12 blocks of 6 lenses to approximate the required curvature.

The careful balance of design parameters necessary to optimise the throughput of an IFU is also described. For instance the fibres can be used with a faster focal ratio than F/13 (F/5 is optimal for reducing FRD) but this requires the use of smaller core diameters. The losses due to fibre positioning and imaging aberrations then become more severe than if larger fibres had been used. A figure of merit is presented which represents the observing efficiency of the IFU. In general altering one factor in the design of the IFU will influence other factors and may lower the figure of merit. The additional effects of the small size of the microlenses on the focal ratio degradation are also described. Ideally lenses which are considerably larger then the fibre core diameter should be used.

Optimal sampling strategy and image reconstruction with an IFU is also discussed. The general rule of thumb is that the input FWHM should be sampled by two slit elements. The reconstructed image is expected to be broadened slightly, in the spatial dimension, due to crosstalk between adjacent elements at the IFU slit. This is, of course, a consequence of maximising the figure of merit by packing one fibre per pixel onto the detector.

Finally future designs of IFU being developed in Durham, particularly the concept for the GMOS-IFU, are described. The overall conclusion is that lenslet-fibre based IFUs provide an excellent solution to the problem of achieving high throughput and high spatial resolution in integral field spectroscopy. The use of both microlenses and optical fibres allows a wide range of design options such that an IFU can be designed for use on virtually any telescope or spectrograph.

Chapter 6

Microlenses for integral field spectroscopy

Abstract

This chapter describes the procurement and characterization of the microlens arrays intended for use in the integral field units already described. The microlens performance requirements are discussed followed by a description of the available types of microlens. Microlens samples were obtained from Adaptive Optics Associates (AOA) and the National Physical laboratory (NPL) for testing. The performance tests and experimental apparatus are described. After analysis of the test results microlenses from AOA were chosen for use due to their superior performance. This chapter also presents the results of further tests carried out on various AOA microlens arrays. In general the image quality is good but with lower encircled energy performance than expected due to scattered light losses.

6.1 Introduction.

The microlens arrays are crucial components in the integral field units described in the previous chapter. They provide an efficient way of coupling light into an optical fibre at the correct focal ratio to minimise losses due to focal ratio degradation. They also efficiently couple the light from the fibre into the spectrograph. This cannot be done efficiently with bare fibre bundles alone unless a dedicated fibre spectrograph is used. The advantages provided by microlens arrays can be summarized as follows:

- Higher fill factor than with bare fibre bundles.

- Continuous spatial sampling over the field of view.
- Conversion of input focal ratio to one that is suitable for propagation in optical fibres minimising losses associated with focal ratio degradation.
- Conversion of focal ratio back to one that is suitable for the spectrograph.

The gains that can be achieved with microlens arrays are only worthwhile if the microlenses themselves do not degrade the performance of the instrument. A thorough investigation of the availability and performance of commercial microlens arrays is therefore required to find microlenses suitable for use in IFS. This chapter describes the investigation of the properties of various microlens arrays. Some of the results given in this chapter, especially those regarding the microlenses intended for use with TEIFU and eventually GMOS-IFU, have been published in the following paper (Lee *et al.*, 1998).

6.1.1 Microlens requirements

Microlens arrays have many characteristics, such as focal length, aperture etc, each one of which can be optimised to give the best performance by appropriate choice of manufacturing methods. Some manufacturing methods are best suited to produce characteristics that are of little use in the application to integral field spectroscopy such as: large focal ratios (F/20 and above), lens pitch less than 100μm and afocal[1] properties. The microlenses typically used in IFS can also be quite large in comparison with the requirements of other applications, such as those discussed in section 6.1.2. This is a restriction that precludes the use of certain manufacturing methods which are best suited to producing small microlenses.

Integral field spectroscopy places stringent requirements on the quality of the microlens arrays. The main requirements for microlens arrays to be used in integral field spectroscopy applications, in particular lens-fibre based systems, are described in the following sections.

Lens pitch

The pitch is the separation between the optical axes of each microlens. This means the lens spacing and the distance between the point spread functions (PSF) should be the same. The

[1] where the lens shape is the superposition of two lens profiles and produces two focal lengths. This property is commonly used in the optoelectronics industry.

pitch is determined by several instrument design factors such as: spectrograph constraints, the required sampling on the sky and the diameter of the microtubes used to house the fibres. The correct pitch needs to be maintained over the entire microlens array and needs to exactly match the pitch of the input fibre bundle.

Fill factor

The fill factor of a microlens array is the ratio of the active area of a lens within an array to the dead space between the lenses. Ideally microlens arrays with fill factors as close to 100% as possible are required to avoid loss of light from the input field. Hexagonally close packed microlenses are generally used at the input to the fibre bundle as the hexagonal shape produces less 'geometric FRD' than square or rectangular lenses. Geometric FRD is the range in focal ratio produced because of the difference between the inside and outside diameters of a hexagon. Conversely it can be an advantage for the microlenses used at the output slit to be square or rectangular as they then couple the maximum amount of light from the fibre FRD cone into the spectrograph.

Focal length

The thickness of the microlens substrate is chosen such that the pupil image occurs at the back surface of the substrate ensuring efficient coupling of light into the optical fibres. It is necessary for the focal length of the lenses to remain constant over the array as variations in focal length will cause a change in the size and position of the pupil image and a corresponding drop in the amount of light which enters the fibre. As an example a 2% increase in the focal length of the SMIRFS-IFU input microlens array causes the pupil image to increase in size also by approximately 2%. The pupil image is then bigger than the optical fibre causing a 4% light loss due to vignetting.

Image quality

Ideally diffraction limited imaging is required with aberrations kept to a minimum. In some applications this will require microlenses with an aspheric profile to be produced to reduce the effect of aberrations caused by a spherical surface. Image quality basically determines

the ability to get the light down the fibre. Poor image quality causes the pupil image formed by the microlens to be blurred leading to a loss of coupling efficiency with the fibre. In some cases it may be possible to oversize the optical fibre to accept a certain degradation in image quality, however, this can then lead to an increase in the sky background that is admitted to the fibre. If the fibre is the field stop then oversizing the fibre can allow additional background light to enter the optical system. Optical telescopes will have baffling so oversizing the fibre at the input will not increase the amount of background light. Infrared telescopes do not have baffling so oversized fibres will allow additional background light and thermal emission to enter the fibre.

Poor image quality at the output microlens again causes the pupil image to be blurred leading to loss of light inside the spectrograph and the mixing of light from one microlens into the spectrum formed by the adjacent microlens, i.e. cross talk between the IFU elements. A blurring of the PSF at the output also increases the effective slit size thus reducing the spectral resolution of the system and reducing the number of elements that will fit along the slit.

Scattered light

This is listed separately to image quality as it is possible for microlenses to produce very good quality images but with an overall background of scattered light, as described in section 6.3.5. Light scattered at the surface of the microlens is lost to the optical system except for the small fraction that enters the optical fibre or spectrograph slit.

Absolute throughput

This is the ratio of the amount of light incident at the lens surface to the amount of light that is detected at the focus of the lens within a defined aperture. This aperture can be defined as that of the optical fibre. The absolute throughput performance will be affected by absorption losses in the lens material and substrate, reflection losses and the scattered light performance. Absolute throughput can be maximized by use of lens materials that have good transmission at the operational wavelength. This is not always possible as some manufacturing techniques limit the choice of materials. It is also desirable to have broad

band antireflection coatings but again the microlens material, such as epoxy, cannot always be coated successfully or without risk of damaging the lens surface.

6.1.2 Types of microlens

It was briefly mentioned in the previous section that microlens arrays come in a wide variety of shapes and sizes but not all are useful for integral field spectroscopy. This section describes the various different types of microlens that are commonly available with emphasis on those which are useful for use in astronomical instruments. For each type of microlens the manufacturing techniques used are also discussed.

Two dimensional arrays of many very small lenses, known as microlens arrays, have a growing variety of applications. The largest use of microlens arrays is in the optoelectronics industries where microlenses are used in: high speed optical data transmission between computers, collimation of laser diode arrays, and laser beam steering, to name but a few of the numerous applications. They are also used in imaging applications such as integral photography, efficiency enhancement of detector arrays, optical processing, and medical endoscopes. A full review of the uses of microlens arrays can be found in Hutley (1991). The traditional use of microlens arrays in astronomy has been in wavefront sensor technology. Microlens arrays are used as the pupil segmentation and focusing element in a Shack-Hartmann wavefront sensors as typically used in adaptive optics systems. Wavefront sensors generally use microlens arrays with small apertures and large focal ratios to provide the correct pupil sampling and enough optical 'leverage' to detect small deviations from a flat wavefront.

Microlens arrays can be categorised into three types depending on the way in which they form an image. There are *fully refractive* microlenses, which are basically scaled down macro-lenses, *diffractive* microlenses, which can also be thought of as Fresnel zone plates, and *graded-index* microlenses. Diffractive microlenses are commonly used in the telecommunications industry where they are required to work with monochromatic light only, generally at infrared laser wavelengths. Their limitation to be used with monochromatic light (diffractive lenses suffer severe chromatic aberration), as well as the aberrations associated with forming an image via Fresnel diffraction, precludes their use in Astronomical instrumentation. Graded index lenses (GRIN) have the disadvantage that they cannot be produced with 100% fill factors. Achieving high fill factors requires the lenses to be packed together which

destroys the index gradients and leads to significant cross talk between adjacent lenses and loss of image quality. They also produce severe chromatic aberration (due to dispersion) and are best used with quasi-monochromatic light. GRIN lenses have, however, been used successfully in high resolution (i.e. small wavelength range) single object spectroscopy (Avila & D'Odorico, 1993) where they are used to couple light from the telescope focal plane into an optical fibre. Integral field systems are therefore limited to the use of fully refractive microlenses as they can be used over a broad range of wavelengths, can be obtained with high fill factors and have superior image quality.

Refractive microlenses can be produced via a variety of manufacturing techniques. The most widely used manufacturing techniques are based on the LIGA process (Ruther *et al.*, 1997). In the LIGA process a uniform layer of photoresist material is applied to a glass substrate. The photoresist layer is then exposed to collimated X-ray radiation through a photolithographic mask. The patterns in the lithographic mask define areas of exposed and un-exposed photoresist. The areas of exposed photoresist can then be removed by dissolving with the appropriate chemical leaving behind areas of un-exposed photoresist. In this way both diffractive and refractive microlens profiles can be produced in photoresist material. After production of photoresist microlenses on glass substrates a variety of etching techniques can then be used to transfer the lens profile into the substrate such as electron beam etching and reactive ion etching. The original microlens array can also be replicated to produce many copies in a manner analogous to the replication of diffraction gratings. The LIGA process cannot produce microlens arrays of any size and shape due to certain limitations imposed by the resist layer, lithographic technology and the etching process. Photoresist microlenses are typically limited to numerical apertures (NA) from 0.15 to 0.4 and diameters from 20μm to 800μm.

A problem with etching techniques is the chemical plasmas can produce roughness on the microlens surface. Also microlenses with large sag heights become progressively more expensive to manufacture due the increased etching times required. Typical etch rates are of order tens of nanometres per minute. As an example etching a 1mm diameter F/5 lens, with a sag height of order 90μm, would require 3 days in the etching plant to produce the desired lens profile. This is a severe limitation to the sag heights of lenses that can be produced due to the enormous running costs of etching plants. The typical limitations on etched glass lenses

are: numerical apertures from 0.05 to 0.2 and diameters from 20μm to 500μm

The LIGA process, although common, is not the only manufacturing technique available and some companies have developed proprietary techniques for producing microlenses. A few of these techniques are described in the next section.

6.1.3 Microlens suppliers

Due to the large variety of applications for microlens arrays there are a correspondingly large number of manufacturers and suppliers. A thorough investigation of these suppliers was carried out before lenses suitable for use in the integral field instrumentation projects could be chosen. In this section a brief summary of the microlenses available from the manufacturers contacted is given along with relevant details of manufacturing techniques not described in section 6.1.2.

LIMO. Lissotschenko Mikrooptik produces cylindrical microlenses directly in a variety of glass substrates using a proprietary manufacturing technique. The profile of the required cylindrical microlens is first micro-machined into steel producing a master. The profile of the master is then transferred into the glass substrate using an ultrasonic abrasion technique. Arrays of microlenses are made by combining two cylindrical arrays in a crossed formation thus producing a lens of square or rectangular aperture. Hexagonal lenses cannot be produced at a reasonable cost. It should be noted that LIMO can produce both aspheric and hyperbolic cylindrical lens profiles which dramatically reduces the aberrations caused by imaging with crossed cylindrical lenses.

Adaptive Optics Associates (AOA). This company can supply microlenses with the pitch controlled to submicron accuracy over large substrates. The arrays are also available in any geometrical pattern with high fill factors. Aspheric designs are not possible as they have no control over the conic constant. The active array needs a surrounding one lens margin to define the correct shape to the lens. The exact manufacturing technique is proprietary and is not described to customers.

Hughes Danbury. This company produces individual glass microlenses and arrays. There is a severe limitation that 200 microns is the maximum microlens aperture that can be supplied with their manufacturing technique. The manufacturing technique used is unknown.

Teledyne Brown. This company manufactures refractive microlens arrays using a lithographic process. However the manufacturing process only allowed the microlens radius of curvature to be achieved on a "best effort basis" with an error of 5%. The manufacturing technique is also limited to producing circular lenses which are separated from adjacent lenses by a strip of chrome reducing the fill factor that can be obtained. Other limitations were a maximum array size of 3 inches and substrate thickness of 0.6mm.

National Physical Laboratory (NPL). A microlens array test sample was obtained from this company the full details of which are described in detail in appendix B.1.

Out of the many microlens manufacturers listed only two were chosen for further investigation: the National Physical Laboratory and Adaptive optics associates. The other manufacturers were rejected on the grounds of excessive cost, delivery schedules or inability to produce the required microlenses with adequate specification. More details of the lenses obtained from NPL and AOA can be found in appendix B.1 and section 6.3 respectively.

6.1.4 Optical properties of refractive microlenses

A microlens is usually constructed as a small plano-convex lens. Microlenses generally have only one surface with optical power due the to difficulty of manufacturing a micro-optical element with more than one curved surface. The microlens can be illuminated in two ways depending on whether the plane or the convex surface is facing the incident beam. The two types of illumination possible are shown schematically in figure 6.1. If the input beam is incident on the convex surface of the microlens such that the focus is produced in glass (or in air if the substrate thickness is less than the focal length) then this is defined as Type-I illumination, this is shown in the upper plot in figure 6.1. Type-II illumination is defined when the input beam is incident on the plane lens surface producing a focus in air .

With spherical lenses Type-I illumination has superior image quality due the production of smaller amounts of spherical aberration. The imaging properties produced by Type-I and II illumination are different and are briefly discussed below.

The *paraxial* focal length (Longhurst, 1973, p14) of a lens consisting of a single spherical surface as shown in figure 6.1 is given by equations 6.1 and 6.2

$$\mathrm{f_g} = \frac{n_l(\lambda)R}{n_l(\lambda) - 1} \qquad (\mathrm{Type - I\ illumination}) \tag{6.1}$$

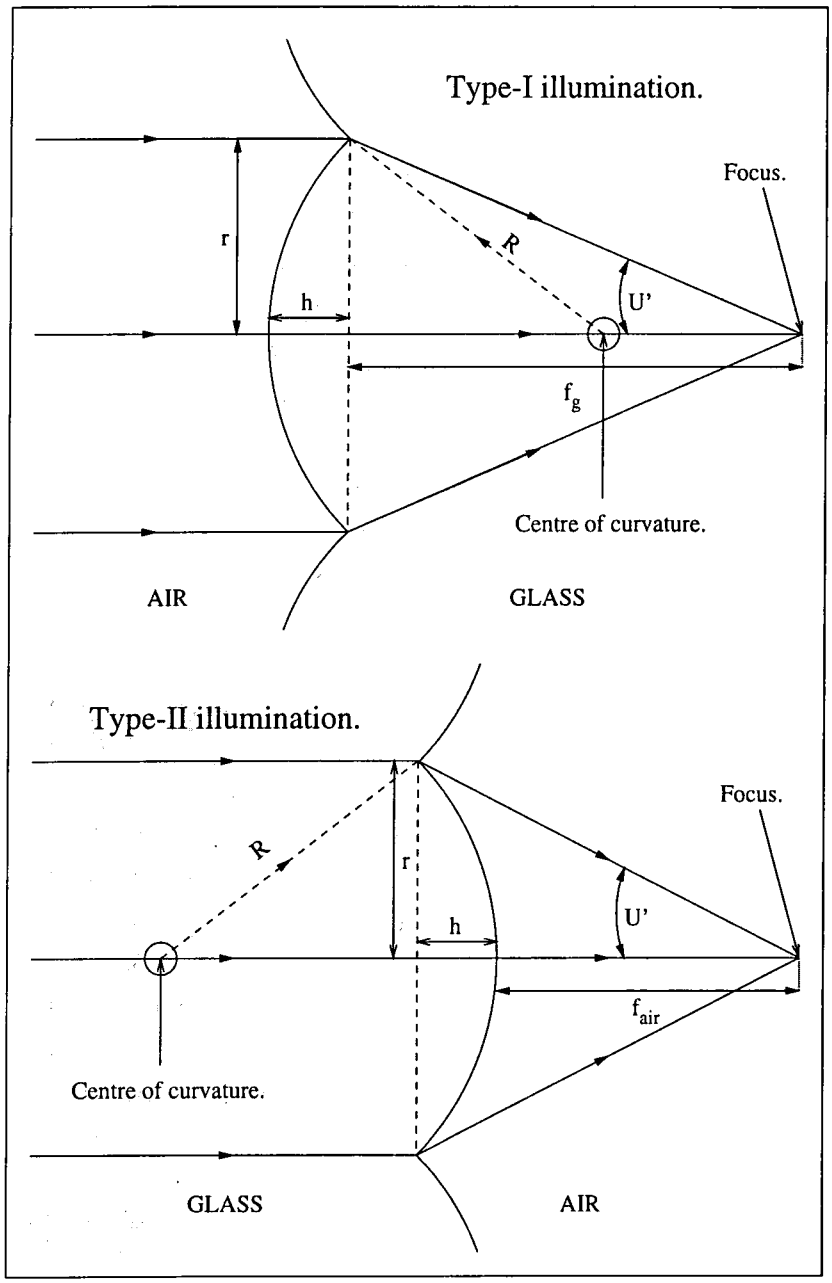

Figure 6.1: The parameters describing a single surface microlens. The lens is shown in both Type-I illumination, with the focus in glass, and Type-II illumination, with the focus in air. R is the radius of curvature of the lens surface, r is the radius of the lens aperture, h is the sag height, U' is the angle formed between the optical axis and the marginal ray , f_g and f_{air} denote the paraxial focal lengths in glass and air respectively.

$$f_{air} = \frac{R}{n_l(\lambda) - 1} \qquad \text{(Type - II illumination)} \tag{6.2}$$

where R is the radius of curvature of the lens surface, n_l is the refractive index of the lens material and λ is the wavelength. f_{air} and f_g are the focal lengths in air and glass respectively. These equations assume the lens material has the same refractive index as the substrate, which is not necessarily the case i.e. if the microlens consists of an epoxy lens on a glass substrate. If the refractive index of the substrate, n_s, is greater than that of the microlens material then the focal length in glass is decreased and vice versa. The focal length in air is only dependent on the refractive index of the lens material. The height of the surface undulation, h, (also known as the sag height) of a lens with an aperture of radius r is given by the following equation:

$$h = R - (R^2 - r^2)^{\frac{1}{2}} \tag{6.3}$$

The sag height is a useful parameter to know as it is quite often the limiting factor in the manufacture of microlenses. Note that for a hexagonal microlens there is an inner microlens radius, r_i, which determines the spacing between lenses, and an outer microlens radius, r_o, which is the distance to the corners of the hexagon.

If the microlenses are of simple spherical shape the image formed will exhibit the aberrations associated with imaging by a spherical surface. Microlenses used in IFS are used on axis, the off axis angle is typically less than 1°, so off axis aberrations such as coma and astigmatism can be ignored. The dominant aberration is then *spherical aberration.* The effect spherical aberration (S.A.) has on image formation by a plano-convex is illustrated in figure 6.2. It can be seen that the paraxial rays are brought to a focus at a point P which is displaced from the point M at which the marginal rays come to a focus. The distance MP between the marginal focus and the paraxial focus is the *longitudinal aberration* and provides a measure of the amount of S.A. present in the lens. The longitudinal aberration of a microlens illuminated with Type-I illumination is approximately four times less than that produced with Type-II illumination. Microlenses are therefore normally used with type-I illumination to improve their image quality.

In the presence of S. A. there are various definitions of focus. The geometrical spot size reaches a minimum at point Z, indicated in figure 6.2, known as the circle of least confusion (Longhurst, 1973, p383). The position at which the diffraction spot size is minimum (Maha-

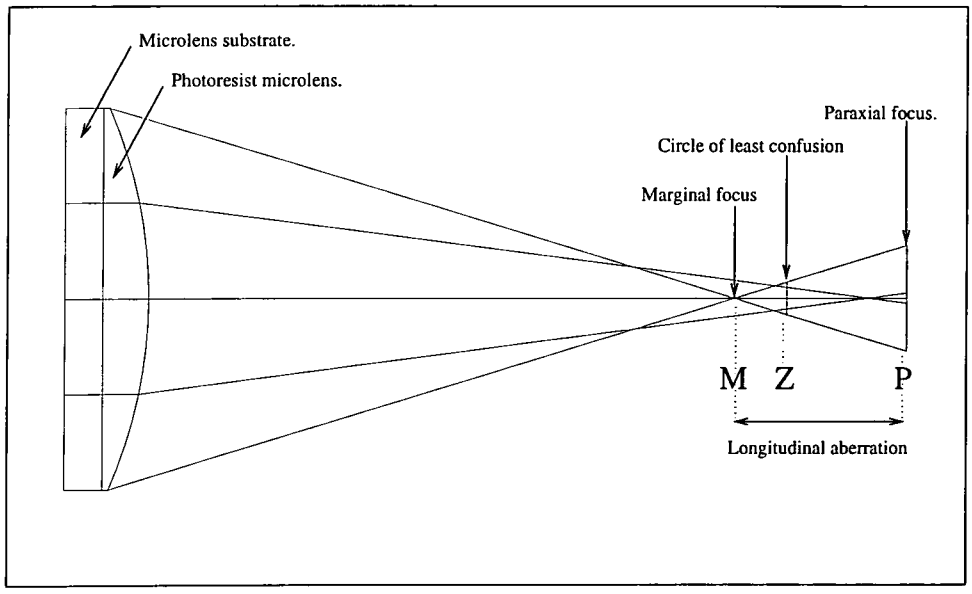

Figure 6.2: Zemax optical ray trace of the NPL microlens with type-II illumination illustrating the effect of spherical aberration. The marginal focus, M, paraxial focus, P, and circle of least confusion, Z, are shown. The NPL microlens consists of photoresist on a glass substrate.

jan, 1991, p76) is found to occur midway between the marginal and paraxial focii. This focus also has the property that the axial irradiance reaches a maximum at this point. This focus is then called the position of *maximum central intensity* or the MCI focus (Mahajan, 1991, p74) . The MCI focus is readily found experimentally as it is simply the focus position at which the brightest core to the PSF is observed. Either side of the MCI focus the intensity falls off symmetrically, provided the Fresnel number of the lens N, given by $N = r^2/\lambda f_g$, is greater than about 5. It is usually the case with microlenses that they are diffraction limited, i.e. the best focus is the MCI focus. The position of best focus will change, however, as the spot size due to aberrations starts to become dominant over the diffraction spot size.

The *depth of focus* of a microlens (Longhurst, 1973, p331) is the maximum movement away from the ideal image plane which can be made without causing any observable (by eye) deterioration of the image. The Rayleigh quarter wave limit for depth of focus, dl', can be calculated from equation 6.4

$$dl' = \frac{\pm\lambda}{8n_2 sin^2\left(\frac{U'}{2}\right)} \tag{6.4}$$

where λ is the wavelength of observation ,n_2 is the refractive index of the image space and U' is the angle formed between the optical axis and the marginal ray. The higher the focal ratio

of the lens the larger the depth of focus becomes. The depth of focus limits the accuracy with which the focus of a microlens can be determined, unless accurate measurement techniques are used as described in section 6.3.3.

Theoretical predictions of the performance of the microlenses described later in this chapter were done using the Zemax optical ray tracing software. This software has the ability to generate ray diagrams, (as shown in figure 6.2) point spread functions, encircled energy (EE) plots, and predict spot radii. The theoretical azimuthal encircled energy plots which are shown later in this chapter were all produced using Zemax. In the microlens tests azimuthally averaged PSFs were also measured but Zemax can only produce one dimensional[2] PSF cross sections. The production of azimuthally averaged PSFs with Zemax involved calculating the PSF cross section at a given rotation of the microlens aperture, then changing the rotation of the lens by a small amount, and re-calculating the PSF (note this process is only necessary for non-radially symmetric microlens shapes). The PSF cross sections were then summed with the appropriate weights to calculate the azimuthally averaged PSF for comparison with the measured PSF.

6.1.5 Summary of microlenses tested

In total six different microlenses arrays were obtained, one array from the National Physical Laboratory and five arrays from Adaptive Optics Associates. The optical specifications of these microlenses are summarized in table 6.1. The results of tests on the NPL lenses, which are manufactured using a different technique to the AOA lenses, are described in appendix B.1. Extensive tests were carried out on all AOA microlens arrays except for the rectangular lens array intended for use with the TEIFU output slit. As the AOA microlenses are all manufactured in the same way the results are directly comparable. The lens diameter, D_l, listed in table 6.1 is the inside diameter of the microlens and should be multiplied by the appropriate factor, for that lens geometry, to calculate the outside diameter. Similarly the tabulated values of sag height and focal ratio were also calculated using the inside lens diameter. The inside radius of the lens is denoted by r_i and the outside radius by r_o. For a hexagonal lens $r_o = 2r_i/\sqrt{3}$ and for a square lens $r_o = \sqrt{2}r_i$ The theoretical Airy radius, R_A^T,

[2]When this work was done the version of zemax being used did not provide 2D PSF analysis, but more recent versions do provide this capability.

	shape	Diameter $D_l = 2r_i$(mm)	Focus f_{air}(mm)	Radius R(mm)	sag h(μm)	Focal ratio	NA	R_A^T (μm)
NPL	circ	0.495	0.85	0.51	64	F/1.7	0.290	1.0
SMIRFS-in	hex	0.412	5.35	2.70	10	F/13	0.038	8.6
SMIRFS-out	squ	0.793	5.95	3.14	25	F/7.5	0.066	4.3
TEIFU-in	hex	0.305	1.46	0.73	16	F/4.8	0.104	2.8
TEIFU-out	orth	0.14 × 0.2	0.43	0.22	24*	F/3.06*	0.228	-
SAURON	hex	1.7	4.45	2.34	160	F/2.62	0.190	1.3

Table 6.1: Summary of microlens specifications. Parameters: r_i, f_{air}, R, and h are as described in section 6.1.4. The theoretical Airy radius, R_A^T, is calculated at λ=543nm. * indicates the focal ratio is different in X and Y due to the rectangular shape of the lens. The SMIRFS-IFU, TEIFU and SAURON microlenses were all manufactured by AOA.

was determined from the azimuthally averaged PSFs, at a wavelength of 543nm, calculated using the procedure described in section 6.1.4.

6.2 Microlens test experiment

Section 6.1.1 described the various requirements a microlens array has to fulfil for use in an integral field spectrograph. In summary the features of most interest for microlens arrays used in integral field spectroscopy are: pitch, fill factor, focal length, image quality, and efficiency of the array. Some other lens properties, such as shape of wavefront, lens surface quality, and modulation transfer function, whilst interesting are less useful in this context and difficult to measure. The microlens tests devised therefore concentrated on measurement of the features of most interest.

In order to check the microlens requirements a series of optical tests were devised. In principle the techniques used in the testing of microlenses are no different to those used in testing normal lenses. However, the small size of the microlenses often means that standard lens testing equipment cannot be used. It is also necessary to measure features of the whole array rather than just one lens.

The following section describes the purpose built experimental apparatus that was developed to test microlens arrays. A full description of microlens test procedures can also be found in Hutley *et al.* (1991).

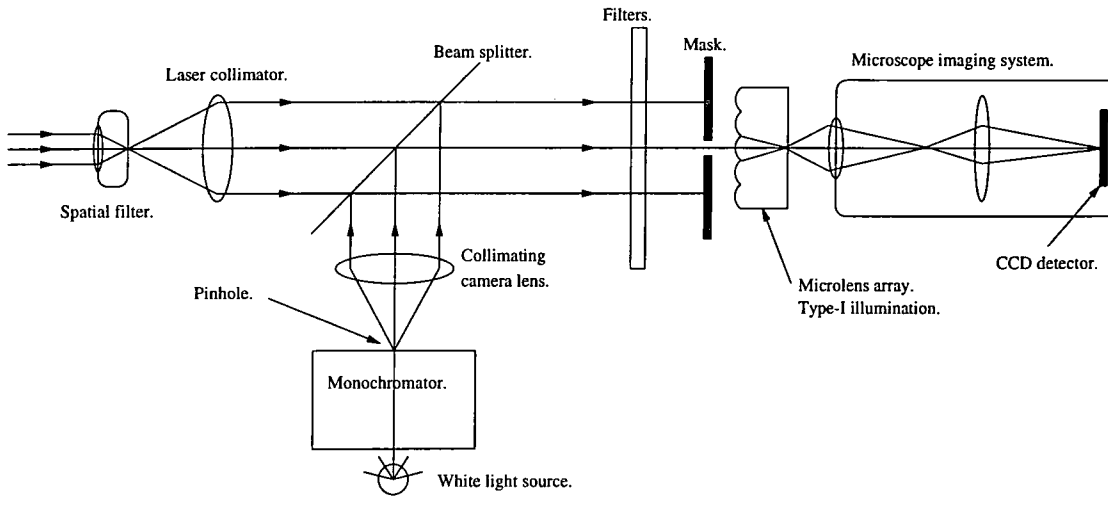

Figure 6.3: Schematic of the microlens test experiment setup.

6.2.1 Test apparatus

A diagram of the apparatus used to test microlenses can be seen in figure 6.3. The main component of the apparatus is an Olympus microscope. The microscope is fitted with an accurate X-Y-Z travelling stage which can be used to measure distances such as focal length (Z axis) and lens pitch. In addition to the binocular eyepiece the microscope can be fitted with a CCD camera or a 35mm camera body. This allows images of the microlens surface to be taken from which the fill factor can be found. The microscope is also used to reimage the microlens Point Spread Function (PSF) onto the CCD detector. A selection of microscope objectives with different magnifications is available to match the size of the PSF to the sampling and field of view of the detector for detailed analysis of the PSF. The field of view with low magnification is also large enough to allow imaging of many PSFs simultaneously. The CCD camera and field of view is described in section 6.2.3.

To illuminate the microlens under test either a laser, a white light source, or both can be used. The appropriate light source is selected by means of a beam splitter. The laser used in the experiment was a green, λ = 543nm, 1mW Helium-Neon laser with a beam size of $\sim$ 1mm. The laser beam first passes through a spatial filter to produce a clean diverging F/4 beam. The spatial filter removes diffraction noise, caused by dust particles, from the profile of the laser beam. The F/4 beam is then collimated using a purpose built collimation lens. The final laser beam is 12mm in diameter and is collimated to $\lambda/4$ wavefront accuracy. The larger diameter beam produced by the laser collimator provides more uniform illumination

over the area of the microlens compared with the small beam direct from the laser. The laser beam was accurately collimated by using a lateral shearing interferometer. The laser beam was used to illuminate the microlens array for the measurements of the PSF. An alternative collimated white light source was also provided to allow imaging of the lens surface.

A monochromator was used to provide a monochromatic light source for the measurement of the refractive index of the microlens epoxy. A pinhole was placed behind the monochromator to provide an approximation to a point source with which to illuminate the microlens array. The pinhole acts as a point source if the image of the pinhole formed by the microlens and microscope combined is of order the same size as the diffraction pattern or below the resolution limit of the microscope. The monochromatic light was collimated using an F/1.2 50mm Pentax camera lens. Illumination for the monochromator was provided by a voltage stabalized Tungsten lamp.

Assorted filters can placed just in front of the microlens array if required. Band pass filters were used to block second order contamination from the monochromator. Neutral density filters were also placed in the laser beam to reduce the amount of light incident on the microlens to avoid saturation of the detector. This is necessary as there is no control of the brightness of the laser as there is with the white light source.

An improvement to the scattered and stray light performance of the system was made by the addition of a large pinhole aperture just in front of the microlens array such that the lens was illuminated through the pinhole. The pinhole diameter was chosen to just overfill the microlens thus minimising the amount of stray light entering the lens and reducing the amount of light entering the lenses surrounding the test lens. The whole microscope assembly was enclosed within a light tight cover. Experiments were always performed in the darkness available within the optics laboratory.

The optical axis of the microlens array was aligned precisely with the input laser beam by an auto-collimation method. Light reflected from the flat area of substrate surrounding the microlens array was aligned precisely with the input laser beam until fringes could be observed indicating the misalignment of the microlens axis with the incident laser beam was less than 0.1°.

6.2.2 Laser intensity variation.

The variation in intensity of the laser beam was measured on numerous occasions each time a series of exposures were taken over a period of time. The variation in integrated light of the measured PSF was typically 5% for ten exposures taken over a period of ten minutes with the central peak intensity of the PSF showing a variation of 10%. The variation of laser intensity with time could not be shown to follow any regular or predictable pattern. The source of the intensity variation is unknown but is consistent with manufacturers specifications[3]. Variations in intensity do not affect the measurement of microlens PSFs, or encircled energy curves, as these are always normalised in order to remove the effect of integrated intensity variations. These variations do however prevent absolute throughput measurements from being made. The accuracy of absolute throughput measurements is critically dependent on the power output from the light source being stable and reproducible. The white light source was known to be stable, from the experiments already described in section 3.3.1, but was found to be insufficiently bright to adequately illuminate the microlens. These experimental difficulties prevented the absolute throughput of the test microlens arrays from being measured. This is unfortunate as absolute throughput measurements would have determined accurately any light loss mechanisms present with the microlenses.

6.2.3 Microscope & CCD calibration.

For the measurement of microlens PSFs two different types of CCD imaging system were used. The performance of these detectors is described in the following sections along with the calibration of the microscope-detector combination. The detector characteristics are summarized in table 6.2 and the microscope characteristics in table 6.3. The procedure for determining the microlens PSF and encircled energy from the reduced data is also described.

COHU CCD + frame grabber.

The first detector system consisted of a TV frame rate CCD camera linked to a PC frame grabber card for data capture. The frame grabber converts the analogue output from the CCD camera into an 8-bit 512 × 512 digital image. There are various limitations to this

[3]manufacturers specification is: power stability after 20 minutes ±5%

CCD	No. of pixels	pixel size	chip area	Dynamic range	integration time	temp
COHU	512×512	$12.35 \times 8.35\mu$m	6.3×4.3mm	8-bit	0.02s	ambient
ST6	375×242	$23 \times 27\mu$m	8.6×6.5mm	16-bit	0.01-1000s	$-20°$C

Table 6.2: Characteristics of the CCD detectors used to measure microlens PSFs.

system. The dynamic range of the frame grabber is limited and the detection process is noisy as the chip operates at ambient temperature. Also the integration time is fixed at the TV frame rate with no capability of changing it, this severely limits this cameras usefulness for imaging faint sources. The advantage of the COHU CCD system is the finer spatial sampling, provided by the small pixels, compared with the second type of CCD system used. Note the COHU CCD was also used in the experiments on immersed gratings and more details on the calibration of this detector can be found in section 2.8.3.

SBIG ST6 CCD

To improve the capabilities of the microlens test experiment the CCD detector was upgraded to an ST6 imaging system from the Santa Barbera Instrument Group[4] (SBIG). This is an astronomical CCD system with the advantages of a larger detector area, thermo-electric cooling, variable exposure times and much greater dynamic range. The main problem with the ST6 camera is the appearance of blooming (bleeding along columns of the CCD chip) which occurs when the illumination level is high, i.e. full well is reached in less than one second. Blooming is particularly bad when short exposures of bright sources are taken. The effect of blooming was reduced by operating the CCD with the anti-blooming electronics switched on and by using long exposure times.

The ST6 dark exposures show a slope in counts increasing along the columns of the detector according to increasing readout time. There is no gradient along the rows of the detector. There are also a large number of hot and cold pixels. The effect of the dark count gradient and bad pixels is reduced by the camera automatically taking an accompanying dark frame, an image with zero seconds exposure time, with each exposure. The dark frame is automatically subtracted from the accompanying image thus removing these 'cosmetic' effects. The dark

[4]Full details of SBIG CCD devices can be found at http://www.sbig.com

count was found to reduce by approximately a factor of 5 with cooling by 20°C. The detector was operated at −20°C with the temperature kept stable by the ST6 hardware.

Exposure sequence

A typical exposure sequence for the measurement of microlens PSFs consisted of N background exposures, N PSF images and a further N background exposures. The number, N, of exposures taken was typically ten. A dark frame is automatically taken with each exposure by the CCD hardware. The background exposures were taken to eliminate any stray light present in the laboratory that may contaminate the microlens PSF images. The exposures were always taken in high resolution mode (no pixel binning) and with low noise readout. The readout time for the full chip is one minute. The CCD camera can be programmed to take each exposure automatically eliminating the need for the user to be present in the laboratory. The co-added background exposures typically had an average intensity level of 100 ± 0.3counts which is the same as the bias level added automatically by the ST6 hardware. This means the background light entering the experiment was minimal.

Data reduction

The background exposures were first combined using the *imcombine* package in IRAF. Cosmic rays and deviant pixels were removed by combining the images with a cosmic ray rejection algorithm. The co-added background exposures bracketing the PSF observation generally had a small intensity offset of ± 0.1counts. The PSF images were then background subtracted and combined using *imcombine* as before. The CCD bias level is removed as a consequence of subtraction of the averaged background frame.

The image is also magnified to correct for difference in pixel scale between the detector rows and columns. The ST6 pixels are rectangular which causes a scale change and the COHU CCD has a scale change due to the sampling of the frame grabber. The pixel scale is discussed in the next section. After the CCD exposures have been reduced the PSF and encircled energy can be calculated. This was done using the IRAF package *pprofile*[5]. This task computes the centroid of the PSF using a standard IRAF centroiding algorithm and

[5]pprofile is part of the package stsdas.hst_calib.ctools

then calculates the azimuthally averaged intensity profile and encircled energy with respect to the centroid. The intensity profile produced is normalised by dividing by the peak intensity. The encircled energy is also normalised by dividing by a user specified value. The value used in the normalisation is not critical as the encircled energy can easily be renormalised with another value at a later stage by other software.

Microscope plate scale

The conversion from units of pixels on the detector to micrometres can only be done accurately with knowledge of the plate scale of the microscope. The plate scale needs to be known to measure the size of microlens PSFs and to measure the actual size of the microlens. The pixel scale of the CCD cameras was calibrated by taking an image of a reticule (i.e. a calibrated millimeter scale). The combination of COHU CCD camera and the frame grabber produces an image 512 by 512 pixels but the plate scale in the x and y directions is different due to the sampling by the frame grabber. The reticule was photographed separately in both the x and y directions, using the appropriate microscope objective, to calibrate the two CCD axes independently. The results obtained with various microscope objectives are listed in table 6.3. There are two sources of error associated with calibrating the CCD pixel scale: defocus of the reticule image and centroiding errors on the image itself. A 30μm defocus of the reticule image was found to produce an error in the measured plate scale of 0.05%. The focus can normally be set more precisely than $\pm$30μm. Centroiding errors on the reticule image led to a $\pm$0.2% error in the measured plate scale. The ST6 detector plate scale was also separately calibrated in the x and y directions due to the detector pixels being rectangular. The reticule scale was checked using a travelling microscope and found to be accurately sized.

6.3 TEIFU microlenses

The first microlens array to be tested was a sample array supplied by Adaptive Optics Associates. This array is intended for use as the input microlens array with the IFU for the William Herschel Telescope and Electra adaptive optics system. This instrument is known as the Thousand Element Integral Field Unit or TEIFU (Haynes *et al.*, 1998c). The

CCD	Objective magnification	NA	X scale μm/pixel	Y scale μm/pixel	Field of view μm$\times\mu$m	Resolution $\delta(\mu$m)
COHU + FG	$\times$100	1.25	0.1225	0.0834	63 $\times$ 43	0.26
COHU + FG	$\times$10	0.30	1.2245	0.8357	627 $\times$ 428	1.1
ST6	$\times$20	0.72	1.163	-		0.72
ST6	$\times$10	0.30	2.341	2.747	878 $\times$ 665	1.1
ST6	$\times$3	0.12	7.273	8.548	2727 $\times$ 2069	

Table 6.3: CCD image plate scales for assorted magnifications. COHU + FG indicates the COHU CCD camera with the frame grabber. Microscope objectives used were Olympus $\times$10, 20 ,40 ,100 and 3. The limiting resolution of the microscope, δ, is given by $\delta = 0.61\lambda$/N.A. where N.A. is the numerical aperture of the microscope objective and λ is 543nm.

specification for the lenses is given in table 6.1. AOA microlenses were chosen for further investigation because they are available in any shape (square, hexagonal, etc), have high fill factors, can be produced in large arrays, any pitch can be specified, and there is no limitation on the numerical aperture.

6.3.1 Description of microlenses.

The TEIFU input array test sample consisted of a small array of approximately 80 microlenses placed on a microscope slide. The microlenses are manufactured in a thin layer of UV curing epoxy which has been deposited on to a glass substrate, which in this case is a microscope slide. For microlens arrays to be incorporated into IFS systems the substrate would be carefully chosen such that the microlens focus occurs at the back surface of the substrate.

The manufacturing method used by AOA is proprietary technique about which little is known. However, what is known is that lenses are produced using a master. The master is replicated in the UV curing epoxy to produce the microlenses. The microlens shape is micro-machined in a soft metal using a computerised machine tool. It is unknown whether the master consists of just one microlens which is then replicated many times to produce an array or if the whole array is first produced in the master.

It should be noted that AOA microlens arrays have to be made oversized. For example if an array of 5 $\times$ 5 lenses is required then the actual array has to consist of 7 $\times$ 7 lenses. The

5×5 lenses in the centre of the array are the active lenses and have the correct shape but are surrounded by a layer of unused lenses. It is a requirement of the manufacturing technique that there are 'spare' lenses surrounding the active array. These spare lenses do not have the correct shape. A lens only possesses the correctly specified shape if it is completely surrounded by other lenses. These 'spare' lenses can be seen in the microphotograph of the SMIRFS-IFU output microlens, shown in figure 7.8, and are further described in section 7.7.2.

6.3.2 Surface quality of TEIFU microlenses

The surface quality of a lens affects the imaging capabilities and the scattered light performance. The surface quality of macro-lenses is usually tested using a standard interferometric technique such as those described in Malacara (1978). These techniques become more difficult to apply with microlenses due to the smaller dimensions of the surface under test. For accurate testing of microlens surfaces specialised equipment has to be used. At the National Physical laboratory a purpose built Twyman-Green interferometer (Mersereau *et al.*, 1993) was developed to test their microlens arrays.

The surface quality and radius of curvature of the TEIFU input test microlens array was tested using a ZYGO New View 100 3D surface structure analysing microscope[6]. This instrument was available in the University of Durham, Department of Engineering[7]. The New View 100 is a scanning white light interferometer with a microscopic capability. A $\times 40$ magnification Mirau objective was used for the measurement to provide a field of view slightly larger than the lens size. The output of the instrument is a 3D map of the lens surface obtained by scanning the white light fringes along the z axis to build up a picture of the lens surface. A view of the lens surface can be seen in figure 6.4. A software mask has been applied to the scanning region so that only one lens is seen in the field of view. This makes the lens under study easier to view as it removes the surface measurement errors that occur at the sharp interface between adjacent lenses.

The surface profile obtained from a cut across the centre of the lens (figure 6.4) in the x direction is shown in figure 6.5. From this profile the sag height can be determined, if

[6]More details can be found at http://www.zygo.com/

[7]The department of engineering is acknowledged for the use of the Zygo interferometer.

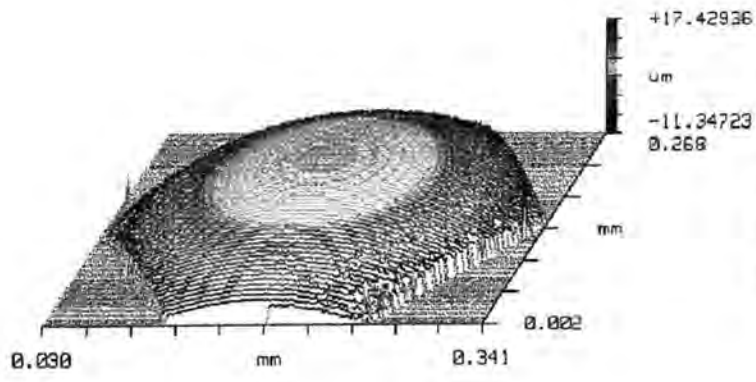

Figure 6.4: Oblique view of the microlens surface profile obtained with the ZYGO 3D surface structure analyser.

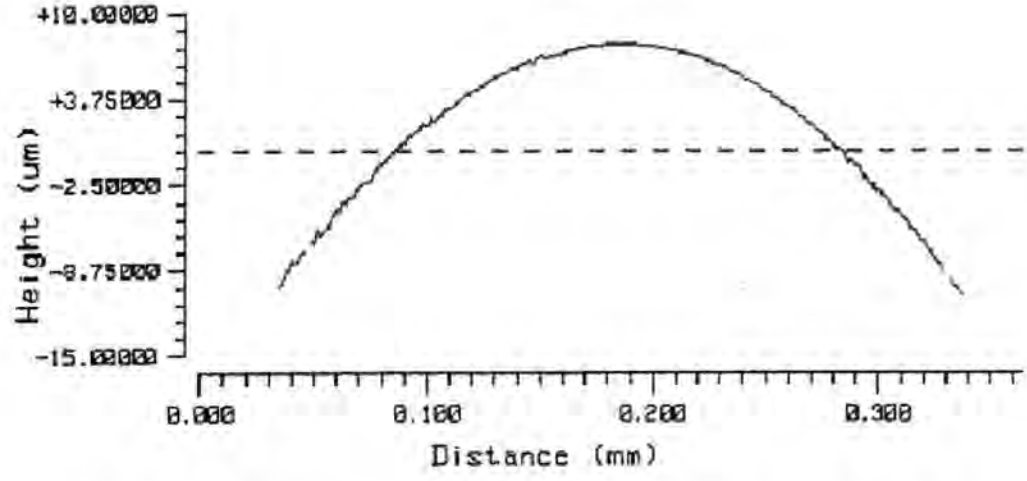

Figure 6.5: Surface profile cut across the centre of the lens surface shown in figure 6.4. The cut is not smooth but shows small defects in the lens surface profile.

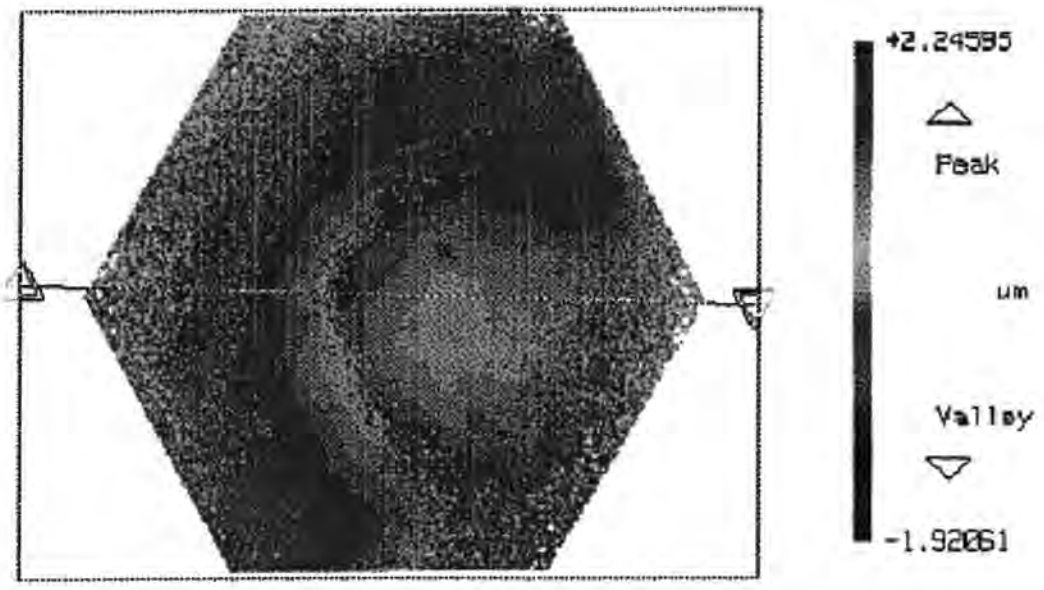

Figure 6.6: View of the microlens surface residuals after the sphere has been removed. A quasi-circular feature can be seen slightly offset from the centre of the lens. The peak-valley surface error is 4.2μm with an RMS of 0.25μm.

required. If the best fit sphere is removed from the surface profile the surface defects and deviations from the sphere can be seen, as shown in figure 6.6. The regions towards the edge of the lens show more noise due to the lower intensity of fringes obtained at the lens edges. This reduction in intensity is due to the large inclination of the lens edges to the optical axis of the microscope reducing the amount of reflected light. It is also thought that some of the 'noise' near the lens edges could be partly due to real surface defects such as the 'orange peel' structure seen in photographs of the microlens surface. An example of orange peel can be seen in the photograph in figure B.8. It is unfortunate that the surface defects occur in a region which is difficult to measure. A circular surface defect can be seen in the centre of the lens. The profile of this defect can be seen more clearly in figure 6.7. This defect looks similar to a circular mark seen in photographs of the SMIRFS-IFU input lenses, as shown in figure 6.21. If these defects occur in different lenses arrays then this may indicate a common manufacturing defect.

There are two types of surface defect that can be classified according to their scale length. Large scale defects, such as the large discontinuity in the centre of figure 6.7, will broaden the core of the microlens PSF. Surface defects with a small scale length, such as the scatter in

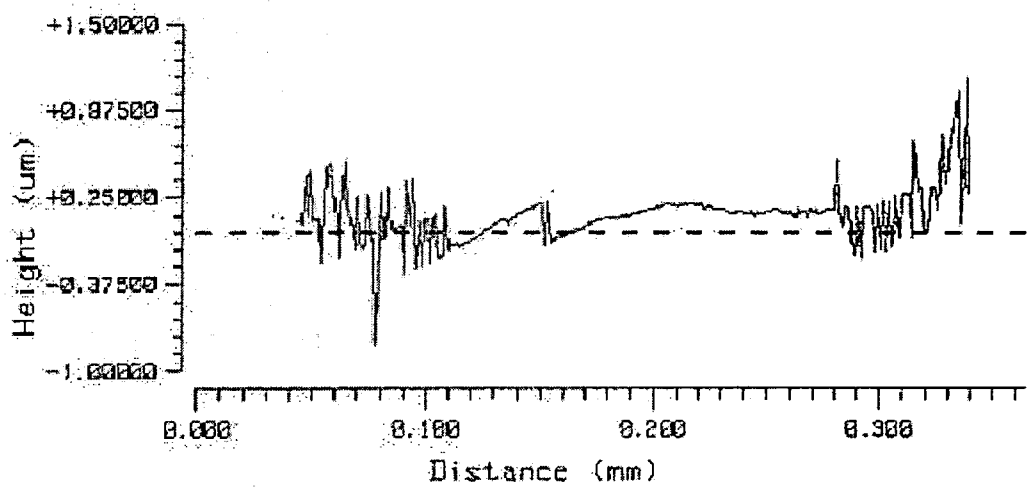

Figure 6.7: Surface profile cut across the lens surface shown in figure 6.6. The RMS error in the residual is 0.2μm which is approximately $\lambda/6$ in optical path depth (transmission).

the residual fit, will put power into the wings of the PSF. The surface roughness is thought to be the cause of the scattered light observed in measurements of the microlens PSF described in section 6.3.5. The RMS residuals in the fit to the lens surface is $\sim$ 0.2μm. The *Total Integrated Scattering* (TIS) of an optical surface (Nussbaum *et al.*, 1997) can be estimated from the following formula:

$$TIS \approx \left(\frac{4\pi\delta}{\lambda}\right)^2 \tag{6.5}$$

where δ is the RMS surface roughness. At a wavelength of 543nm the measured surface roughness for the TEIFU microlenses will cause a TIS of approximately 21% which is in reasonable agreement with the scattered light measurement described in section 6.3.5. Of the other lens profiles measured some showed large defects due to scratches, or surface contamination possibly caused by dust particles. It should be noted that even with the surface roughness the lens profile is still a good fit to a sphere.

The radius of curvature was measured for a selection of the test lenses and found to be 629 $\pm$ 2μm. This value was found to decrease slightly when measured nearer the centre of the lens implying that the lens is not spherical, or the measurement is biased by the noise present towards the lens edges. This value is in disagreement with the manufacturers specification of 0.73mm. The reason for this discrepancy is thought to be a calibration error with the instrument which was still being commissioned when the microlens was measured. The P-V change in the radius of curvature from lens to lens was less than 1%. The focal

length of the lenses will show a similar variation but ±1% is within the specification on focal length.

6.3.3 AOA epoxy refractive index

During manufacture AOA measure the focal length of the microlens at 633nm. It is therefore necessary to know how the focal length will vary with wavelength, particularly if the microlens has been designed for use in the infrared and large chromatic aberration is expected. The epoxy dispersion data available from AOA was rather limited (4 data points). It was decided to measure the refractive index of the epoxy directly from the TEIFU microlens sample. The method used was to measure the change in the focal length of the microlens with wavelength. If both the radius of curvature and the focal length of the lens are known then the refractive index of the lens material can be calculated from equation 6.2.

The experiment consisted of four parts summarized as follows:

1. Absolute measurement of microlens focal length at two He-Ne laser wavelengths 543nm (green) and 632.8nm (red).
2. Relative measurement of chromatic focal shift between 400nm and 1000nm.
3. Calibration of chromatic focal shift of the microscope objective.
4. Calibration of microscope z-axis distance scale.

The TEIFU lens was illuminated with type-II illumination such that the focus occurred in air. This is how the lenses are tested by the manufacturers and allows direct comparison of results. The absolute focal length of the microlens was found by first measuring the position at which the microlens focus occurs and then moving the microscope z-axis stage to bring the lens surface into focus. The focal length of the lens is then simply the distance moved by the microscope z-axis stage which can be read off the micrometer. This is a standard technique for measuring the focal length of microlenses as described in Hutley *et al.* (1991). Using type-II illumination also avoids calibration problems due to refraction at the substrate surface causing shifts in the position at which the microscope measures the focus.

The absolute focal length of the microlens was measured at both $\lambda = 543nm$ and 632.8nm using a collimated laser beam as the light source. Images of the PSF were taken using the COHU CCD as described in section 6.2.3. The CCD camera output was also connected to a TV monitor to allow simultaneous visual observations to be made. The focus was initially set by eye using the TV monitor to observe the position of the MCI focus. Exposures were taken at the focus and at positions 10, 20, 30, 40 and 50μm either side of the focus. Dark frames were taken accompanying each exposure to allow accurate background subtraction. The microscope was then refocussed from the PSF to the lens surface and the distance measured. The accuracy with which the focus on the lens surface can be determined by eye is $\sim \pm 2\mu$m.

Each set of exposures was analysed using a computer programme, custom written by Robert Content, for the reduction of frame grabbed 8-bit images. Each image was background subtracted and the centroid of the PSF found. The measured encircled energy was then normalised to equal 100% at a radius of 9μm. Normalising the total energy contained within a fixed aperture in this way removes the effect of any intensity variation in the light source.

The position of the best focus can then be found from a graph of energy contained within a fixed aperture versus focus position as shown in figure 6.8. The best focus is defined to occur at the position of maximum enclosed energy (i.e. gradient=0). The aperture chosen had a radius of 2.7μm which is similar to the predicted Airy radius of 2.8μm. This radius produces the largest change in enclosed energy for a given change in focus and allows the focus to be found more accurately. The aperture is also big enough that the signal to noise is still high even when defocusing reduces the number of photons within the aperture. The data were fit[8], by linear regression, with either a parabola or a hyperbola to find the maximum. In some cases it was found that a hyperbola represented a better fit to the data.

Data measured at 543nm is plotted in figure 6.8 along with the fit to the data. Also shown is the theoretical prediction of the encircled energy within the same aperture produced using Zemax optical ray tracing software. The focal point can be determined in this way to an accuracy of $\pm 2\mu$m. The measured focal length of the microlens was found to be 1.421 ± 0.002mm at $\lambda = 543$nm and 1.436 ± 0.002mm at $\lambda = 632.8$nm. This is slightly

[8]Note this work was carried out in collaboration with Dr. Robert Content and he is gratefully acknowledged.

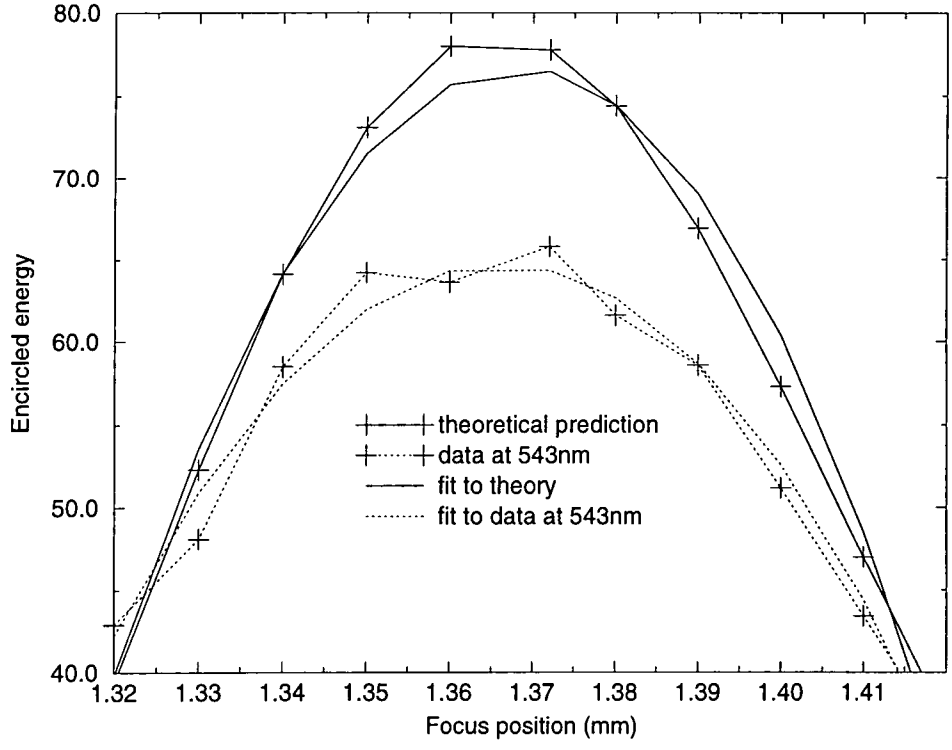

Figure 6.8: Plot of encircled energy within a fixed aperture, radius = 2.8μm, versus focus position for the TEIFU microlens. The focus of the microlens occurs at 1.37mm. The solid line shows the theoretical prediction from Zemax and the dotted line shows actual data taken at 543nm. Also shown is the quadratic fit to the data from which the correct focus position can be calculated. Note the measured data has been shifted slightly in focus position to coincide with the theoretical prediction. The difference in peak EE between the measurements and the predictions is due to the normalisation process.

smaller than the manufacturers specified value of 1.460mm at $\lambda = 632.8$nm. This difference is probably due to measurement errors and a slightly different definition of best focus. Other measurement criteria will produce a different definition of best focus.

The refractive index of the microlens epoxy was not calculated using these measurements as it was uncertain whether the quoted microlens radius of curvature was accurate. The known refractive index values (from AOA) and the quoted radius of curvature, $R = 0.73$mm, predict a focal length of $f_{air} = 1.37$mm as shown in figure 6.8. This is less than the measured focal length implying that the quoted radius of curvature is too small. It should also be noted that the calculation of refractive index has to include a correction for the spherical aberration of the lens. The best focus with S.A. will be different to the paraxial focus predicted by equation 6.2. For the TEIFU microlens the paraxial focal length is 3.6% longer than the best focus.

The focal length of the microlens is now known absolutely at two wavelengths. For other wavelengths the shift in focus with wavelength was measured. The microlens was illuminated with monochromatic light produced by an Oriel grating monochromator. A voltage stabalized Tungsten lamp was used as the light source. Light from the monochromator was made to pass through a pinhole to define a point source with which to illuminate the microlens. The diverging beam was collimated by either a 50mm or 85mm Pentax camera lens. The PSF produced by the microlens was observed with a $\times 10$ magnification microscope objective. Two monochromator gratings were used during the experiment blazed for the blue and the red. The experiment was limited to the wavelength range 440-1000nm by the efficiency of the detector and the brightness of the light source in the blue.

At each wavelength the approximate focus position was set by eye using the MCI method described in section 6.1.4. The micrometer position at this focus was then recorded and a series of exposures, and background frames, were taken at the focus and at positions 60μm, 40μm, 20μm either side of the focus. After the exposures had been completed the wavelength was changed and the process repeated.

The accuracy of finding the MCI focus by eye was found to be $\pm 6\mu$m compared with $\pm 2\mu$m obtained by using the fit to the data. There is a reproducible offset of -4μm between the focus chosen by eye and the optimum focus determined from the data. This result indicates that measuring the microlens focus by eye is accurate enough for most purposes.

The measurement of chromatic focal shift for the microlens also includes a chromatic shift due to the microscope optics. This was measured independently by focusing on a microscope slide illuminated with the same monochromator setup. The microscope slide was lightly covered with 1 micron powder to aid accurate focusing. The chromatic focal shift due to the microscope was then removed from the microlens data.

The last part of the experiment was to calibrate the non-linear behaviour of the z-axis stage. The cause of this behaviour is thought to be a worn thread in the axis drive. This was done by moving the stage in 25 micron intervals, as measured on the z-axis micrometer scale, and measuring the actual displacement with a vernier micrometer.

After the effects of the microscope chromatic aberration and z-axis non-linearity have been removed from the microlens chromatic focal shift data the dispersion curve of the microlens material can be calculated. The change in refractive index, δn_l, is related to the chromatic focal shift, δf, by the equation 6.6.

$$\delta f \approx \frac{\delta n_l R}{(n_l - 1)^2} \tag{6.6}$$

The calculated dispersion curve is shown in figure 6.9. Due to the relatively small number of data points the curve is best fit using the Conrady dispersion formula, equation 6.7:

$$n_l = n_o + \frac{A}{\lambda} + \frac{B}{\lambda^{3.5}} \tag{6.7}$$

with $n_o = 1.48937, A = 1.52886 \times 10^{-2}$, and $B = 3.546 \times 10^{-4}$. The refractive index data was made to match the existing AOA data. The refractive index could have been calculated independently had the radius of curvature of the lens surface been accurately known. The important thing to measure is the change in refractive index and not the actual refractive index itself as it is this that is used to calculate the change in focal length. The Conrady formula can be used to calculate the following values for refractive index and dispersion[9]: $n_d = 1.518 \pm 0.001, v_d = 49.9$. These values are slightly different to those quoted by AOA of $n_d = 1.516, v_d = 56.1$.

Figure 6.9 shows the measured data points, with error bars, and the best fit curve using the Conrady dispersion formula. The letter 'c' indicates the refractive index at 1.65μm predicted using the Conrady formula. Also shown are the dispersion curves for BK7 glass calculated

[9] n_d is the index of refraction at 587.6nm and v_d is the Abbe number given by $(n_d - 1)/(n_F - n_C)$

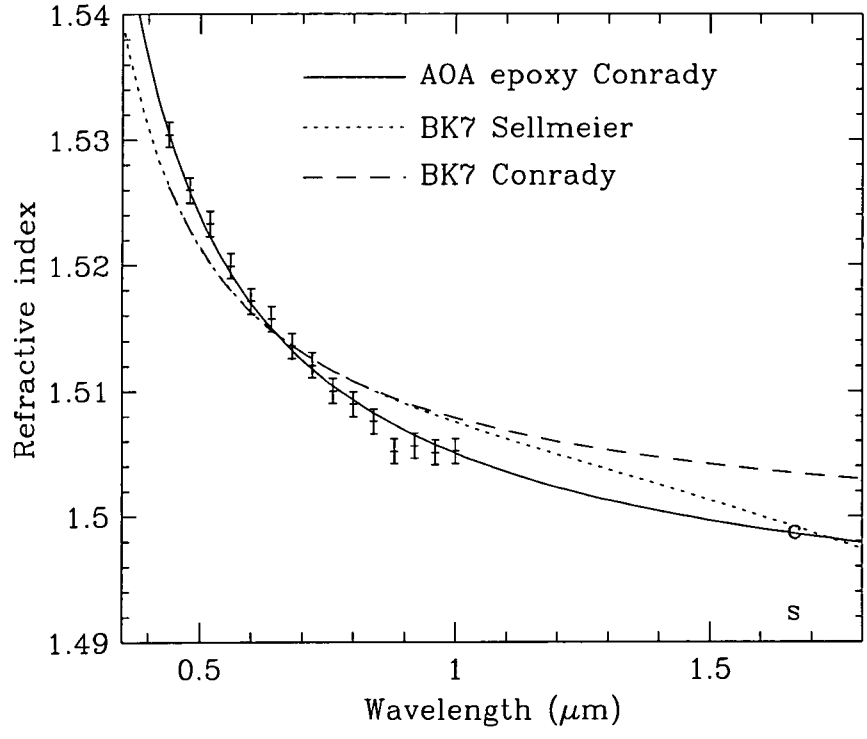

Figure 6.9: AOA UV curing epoxy refractive index curve. The measured data points are shown with error bars and the best fit to the data with the Conrady formula (equation 6.7). 'c' and 's' indicate the refractive index at 1.65μm calculated with the Conrady and Sellmeier formulae respectively. Also shown are the Conrady and Sellmeier dispersion curves for BK7 glass which has a similar value of n_d to the AOA epoxy but a lower Abbe index. The Conrady fit to BK7 overestimates the refractive index at wavelengths greater than 1μm. At these wavelengths it is better to use the more accurate Sellmeier formula.

using the Conrady formula and Sellmeier's (Born & Wolf, 1980, p97) formula. Sellmeier's formula contains more coefficients and is a better model of the dispersion in the infrared than the Conrady formula. The figure shows that the Conrady and Sellmeier data for BK7 agree up to $\sim$ 1μm and then begin to diverge. Above $\sim$ 1μm the Conrady formula over estimates the refractive index and should be used with caution. If the Sellmeier formula is fit to the measured epoxy data then the predicted refractive index at 1.65μm (indicated by 's') is lower than the Conrady prediction by 0.5%. To obtain higher accuracy it was planned to measure the refractive index directly in the infrared using a critical angle method (Longhurst, 1973, p89). However this experiment was never performed. It is unknown whether the characteristics of the epoxy will vary from batch to batch.

The change in focal length between 632.8nm, manufacturer's measurement, and 1.65μm is 4.7% if the Sellmeier formula is used. If the microlens array is to be used in the H-band (i.e. the SMIRFS-IFU) then the thickness of the substrate has to be corrected for the chromatic aberration so that the fibres remain at the focus. Otherwise the pupil image will be blurred leading to loss of light. A 4.7% change in focal length will lead to approximately a 10% loss of light at the fibre core. The chromatic aberration caused by the microlens can be reduced by using a high dispersion (flint) glass substrate, as described in Parry *et al.* (1997). The combination of microlens and substrate then acts as an achromatic doublet.

6.3.4 AOA epoxy Transmission

It is a well known characteristic of epoxies that they absorb light at certain wavelengths, particularly in the infrared region. As the AOA epoxy is UV curing it also absorbs strongly in the blue region (UV curing is achieved by the absorption of light). The transmission of the UV epoxy needs to be accurately known in order to assess its suitability for use in infrared or blue wavelength optimised instruments.

Two samples of microlens epoxy were obtained from AOA in order to measure the transmission. Each sample consisted of a flat slab of epoxy measuring about 10mm square. The first sample was 60μm thick which is typical of the thickness used in manufacturing microlenses. The second sample was 1mm thick to achieve high absorption.

The transmission of the samples was measured using a Perkin-Elmer UV/VIS/NIR Lambda

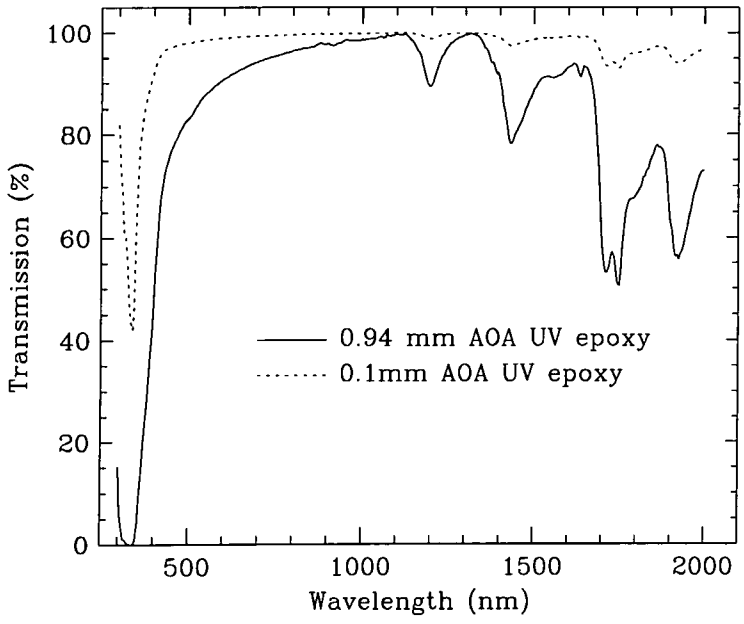

Figure 6.10: Plot of the internal transmission of 0.94mm thickness, solid line, and 0.1mm, dotted line, of AOA UV curing microlens epoxy. 0.1mm is typical of the total thickness of epoxy present in an IFU.

19 atomic absorption spectrophotometer. This is a dual beam spectrometer[10] which measures the atomic absorption spectra of a sample. The 1mm sample was placed in the sample beam and the 60μm sample was placed in the reference beam. Using the dual beam system in this way removes the effect of reflection losses (the reflection losses are the same in both the sample beam and the reference beam and so are calibrated out) at the surface of the sample and measures the *internal transmission.* The internal transmission is therefore measured for a 0.94 mm thickness of epoxy. The resulting absorption spectrum of AOA UV curing epoxy is shown in figure 6.10.

The spectrum shows the expected strong absorption feature in the ultraviolet at $\sim$ 350nm but also shows significant absorption at 500nm. Absorption within the microlens could become a problem for IFUs intended for use in the blue region of the spectrum, particularly if thick lenses are required. Similarly the large infrared absorption features may prevent use in infrared instruments. Absorption is less serious of course if the epoxy thickness can be kept to an absolute minimum. It was thought that the thickness of the epoxy layer could be increased at will to compensate for manufacturing errors in the substrate thickness and/or the microlens focal length. However the absorption losses in the epoxy are too high to compensate for manufacturing errors without degrading the throughput of the microlens array.

[10]full details of this instrument can be found at the Perkin-Elmer www site:
http://www.perkin-elmer.com:80/uv/1900.html

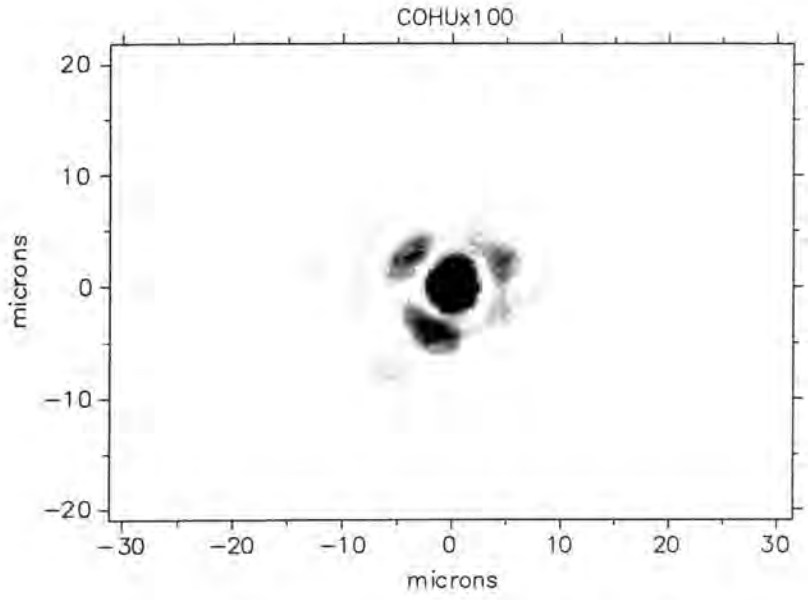

Figure 6.11: Magnified image (×100) of the PSF obtained with the TEIFU input microlens array. The first Airy ring can be clearly seen and the six spikes of the hexagonal diffraction pattern.

With future manufacturing developments it may be possible to obtain microlenses which are manufactured directly in glass substrates. The appropriate glass type for the wavelength region of interest could then be chosen. It may be possible to transfer epoxy microlens shapes into glass substrates using the etching techniques already described in section 6.1.2. This process is still under investigation and not currently available.

6.3.5 TEIFU input microlens PSF

After the completion of the refractive index measurement the TEIFU input lens PSF was measured in more detail. Initial observations of the PSF were taken with the COHU CCD camera and a microscope magnification of ×100. Type-I illumination was used to simulate the illumination characteristics produced when in use on a telescope. Multiple images and background exposures were combined using the method already described in section 6.2.3.

An image of the TEIFU input lens PSF can be seen in figure 6.11. The first Airy ring can be clearly seen which initially suggests that the performance of the lens is good and comparable to diffraction limited performance. The azimuthally averaged PSF obtained from this image is plotted in figure 6.12. The plot shows the observed Airy radius is $\sim 3\mu$m, a value similar to the predicted theoretical value of 2.8μm. The theoretical PSF is also plotted for comparison. The figure also shows a comparison of the performance of the AOA lens with the NPL microlens. The NPL lens is described in more detail in appendix B.1.

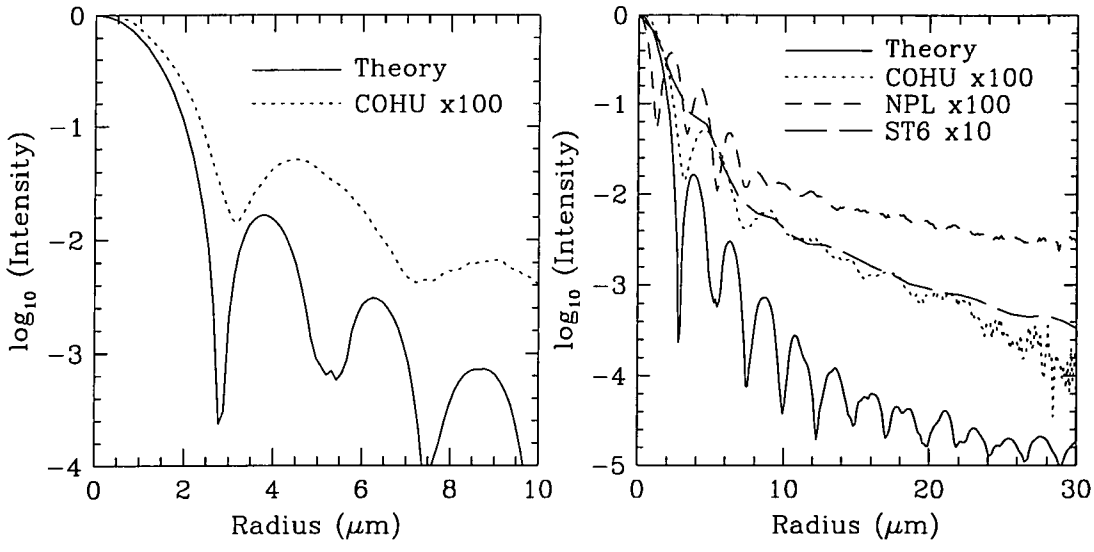

Figure 6.12: Azimuthally averaged PSF of the TEIFU input microlens. The left-hand plot shows an enlarged view near the centre of the PSF taken with ×100 magnification and the COHU CCD camera. The observed Airy radius is seen to be slightly larger than the theoretical prediction of $\sim 2.8\mu$m. The right-hand plot shows a comparison of the TEIFU PSF, labelled COHU ×100, with the NPL microlens PSF, labelled NPL ×100. Also shown is the TEIFU PSF taken with the ST6 camera at ×10 magnification.

The AOA lens PSF has less light in the wings than the NPL lens and the performance is closer to the diffraction limit. It is partly because of this improved performance that the AOA microlenses were chosen in preference to the NPL lenses for use in the IFUs being built. The AOA lenses also have a higher fill factor and there are less limitations on the lens focal ratios and sizes that can be produced.

However, the ×100 COHU CCD images only show the performance of the lens over a very small field of view. The COHU CCD does not have adequate performance to be extended to observe larger fields of view due to the limited dynamic range, fixed integration time and high read out noise. To measure the PSF to larger radii the COHU CCD detector was replaced with an SBIG ST6 CCD as previously described in section 6.2.3. The combination of ST6 CCD and a ×20 magnification objective provides a field of view of which covers the entire area of the lens. The PSF obtained with the ST6 camera is plotted in figure 6.12 for comparison with the COHU CCD data.

The PSF measured over the full area the lens is shown in figure 6.13. It can be seen that the PSF doesn't continue to fall in intensity with increasing radius, as might have been

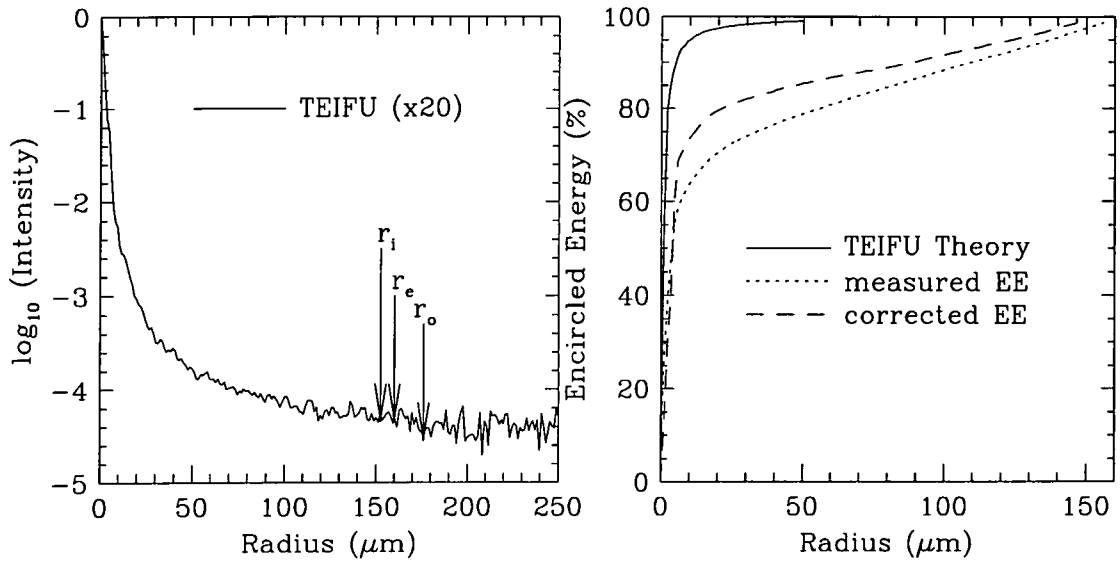

Figure 6.13: Plot of the TEIFU input microlens PSF and encircled energy data taken with $\times 20$ magnification and the ST6 CCD. The inside radius, r_i, the equivalent radius, r_e, and the outside radius r_o have been marked. The PSF levels off due to the presence of scattered light. The encircled energy plot shows the theoretical performance, the measured EE, and the corrected EE. At small radii approximately 20% of the incident light is lost due to scattering.

predicted from the $\times 100$ COHU data, but levels off at large radii. The PSF then increases in intensity past the outside radius, r_o, due to the light from the surrounding lenses. It should be noted that the PSF of one lens contains a contribution due to scattered light from the surrounding lenses. This background level of diffuse light dramatically affects the encircled energy performance of the lens. Plots of azimuthal encircled energy versus radius are shown in figure 6.14. The encircled energy plots have been normalised to equal 100% encircled energy at the equivalent radius, r_e, for each lens.

The equivalent radius, r_e, is defined as the radius of an equivalent circular lens that has the same total area as the lens being tested. As an example, the area of a hexagonal lens is given by:

$$A_{hex} = \frac{1}{2} r_i r_o 6 = 2\sqrt{3} r_i^2 = \pi r_e^2 \tag{6.8}$$

so r_e is the radius of a circle with the same area as the hexagon. Therefore the equivalent radius is 1.05 times larger than the inside radius for a hexagonal lens. The equivalent radius for the TEIFU microlenses is therefore 160μm.

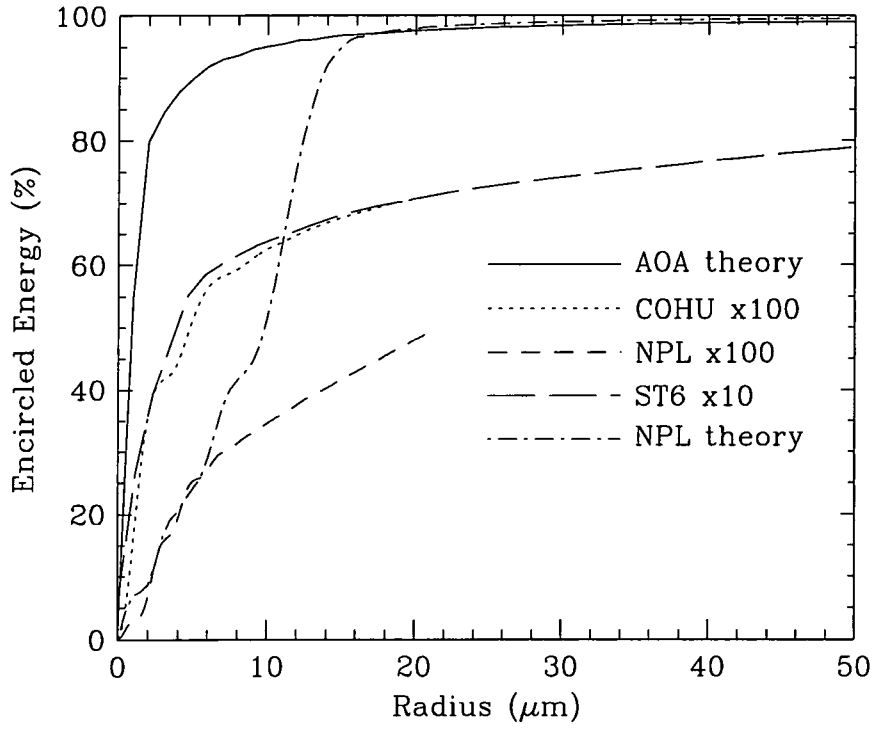

Figure 6.14: Plot of encircled energy for the TEIFU input lens test sample. The encircled energy is normalised to 100% at the equivalent radius, r_e, as defined in the text. The $\times 100$ magnification data only reaches an encircled energy of 64.5% within the field of view of the COHU CCD camera. The NPL data is also normalised to the correct encircled energy using the data described in appendix B.1.

The area occupied by the ×100 COHU CCD image only contains 74% of the total encircled energy contained within r_e. If the high magnification image was wrongly assumed to contain most of the light then misleading EE performance figures would be obtained. Although the central PSF looks near to the diffraction limit the EE performance of the TEIFU input lenses is actually degraded by the presence of a large amount of scattered and diffuse light. The measured EE is typically 20-30% less than that predicted from diffraction theory (Zemax). *Light that, ideally, should be contained within the core of the PSF, i.e. within the Airy radius, is being scattered into the wings of the PSF up to the radius of the lens.* Figure 6.14 shows the EE curve obtained with the COHU CCD closely matches the curve obtained with the ST6 CCD indicating consistency in the data. The difference at small radii is due to better sampling of the PSF with the higher magnification image. The encircled energy performance of the NPL lens is also shown in figure 6.14 with the maximum value normalised in the same way as already described. The NPL lens has lower encircled energy performance than the AOA lens. This is partly to be expected due to the presence of large aberrations introduced by the NPL microlens manufacturing technique. The NPL lens performance is described in more detail in appendix B.1.

The purpose of the microlenses is to reimage the telescope pupil onto the core of an optical fibre. Only a small portion of the scattered and diffuse light will enter the optical fibre. The scattered light that does not enter the fibre is lost and this represents a throughput loss in the system. The scattered light level at large radii is a severe limitation to the performance of these microlenses and is a result not previously described in the literature.

6.3.6 Scattered light

Clearly the scattered light performance of the TEIFU lenses (and in fact all AOA lenses tested) is cause for concern and requires further investigation. A simple explanation may be that the scattered light is actually due to instrumental effects and not due to the microlenses. Dust and imperfections on the lenses of the microscope and the CCD as well as internal reflections will all contribute to the scattered light produced by the measurement apparatus.

To measure the instrumental scattered light a pinhole was observed using ×20 magnification and the ST6 CCD. Care was taken to ensure the microscope setup was the same as when imaging microlens PSFs. Both 10μm and 25μm pinholes were used as they are similar in

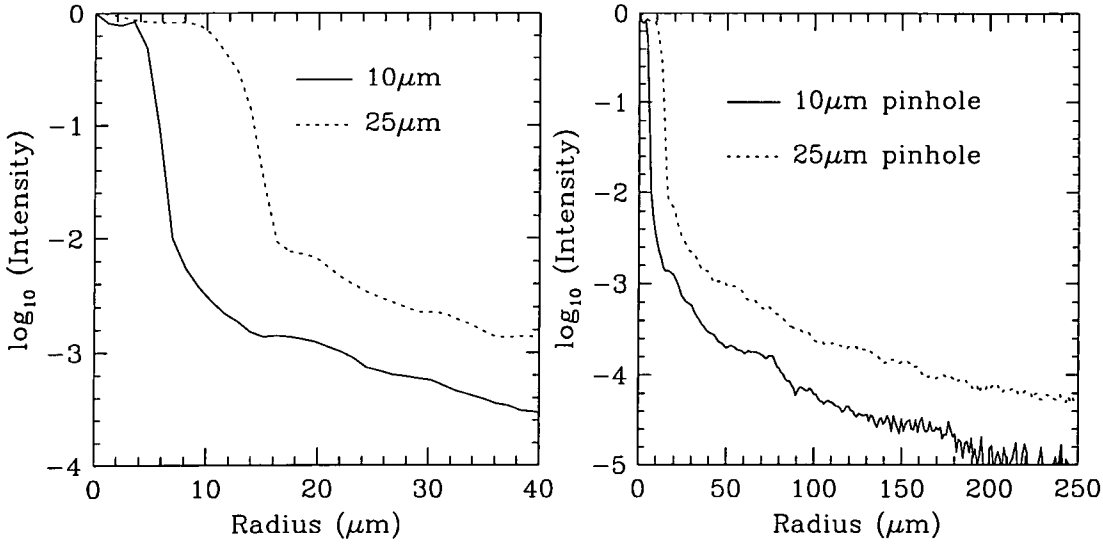

Figure 6.15: Plot of the PSF obtained by observing 10μm and 25μm pinholes. The scattered light outside the area of the pinhole is due to the microscope.

size to a microlens PSF (the Airy radius). Diffraction by the pinhole produces a diverging beam with a similar numerical aperture to the microlenses being tested. The diverging beam produced by the 10μm and 25μm pinholes has a numerical aperture of 0.066 (F/7.6) and 0.026 (F/19.2) respectively at 543nm. It is important that the numerical aperture produced by the pinhole is similar to the microlenses, as then the microscope is illuminated in the same way, and the scattered light performance can be expected to be similar to when observing microlenses.

The PSFs obtained from the pinhole images can be seen in figure 6.15. The pinholes were uniformly illuminated using a laser beam therefore, with perfect imaging, the PSF should be a tophat function. The measured PSF shows the presence of a large amount of diffuse and scattered light similar to that observed with the microlens PSFs. Some light will be present in the wings of the PSF due to diffraction by the microscope optics. It should be noted that diffraction broadening by the microscope[11] will also affect the measurement of microlens PSFs in the same manner. If the scattered light is due to diffraction the intensity would fall with radius according to the power law: Intensity $\propto r^{-3}$ (Content, 1997a). The observed PSF however falls as Intensity $\propto r^{-1.5}$ indicating the diffuse light is due to instrumental effects.

[11]The limiting resolution of the microscope with the ×20 objective is 0.5μm.

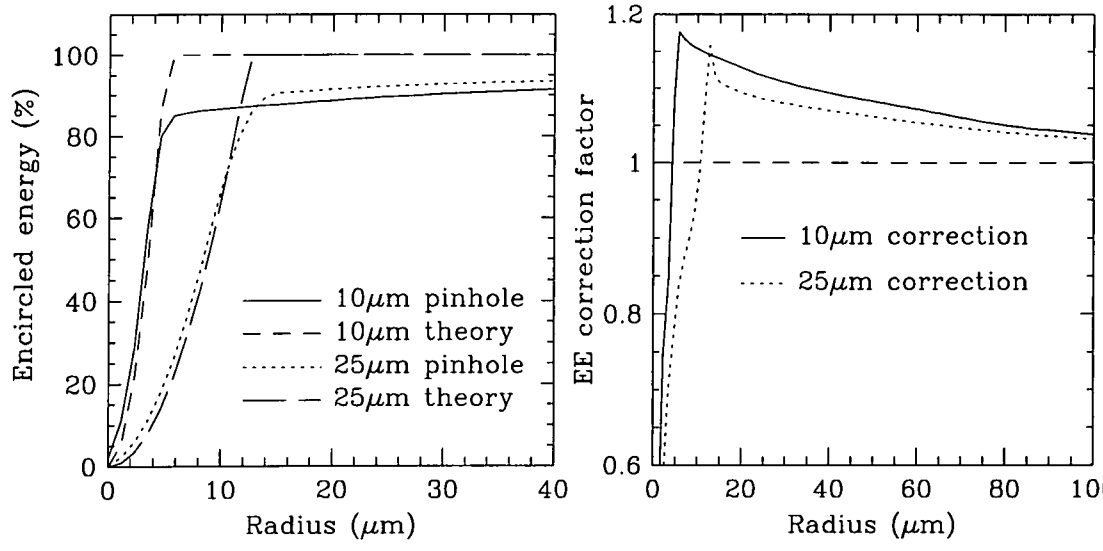

Figure 6.16: The left plot shows a comparison of the theoretical EE curve for a pinhole and the observed EE curve. The right plot shows the ratio obtained by dividing the theoretical EE curve by the measured EE curve.

How the instrumental scattered light affects the encircled energy performance can be seen in figure 6.16. The EE curve rises steeply (EE $\propto r^2$) up to the radius of the pinhole at which point there is a sharp turn over. The EE curve then continues to rise more slowly as the scattered light is integrated. Approximately 10-15% of the total light contained within the radius of the pinhole is scattered outside the radius of the pinhole. This result can be expected to be the same for the microlens EE i.e. 10-15% of the light that is contained within the Airy radius will be scattered by the microscope. The pinhole size was deliberately chosen to be similar to the Airy radii therefore the production of scattered light by the microscope should be similar. An *encircled energy correction factor* can be calculated by taking the ratio of the theoretical pinhole EE to the measured pinhole EE. By then applying this correction factor to a measured EE curve the scattered light will be effectively pushed back into the centre of the PSF. This correction factor is also plotted in figure 6.16. Application of this correction factor to a microlens EE curve will correct for the scattered light contribution by the microscope but the scattered light due to the microlens will remain.

Figure 6.13 shows the result of applying the EE correction factor to the EE curve for the TEIFU input microlens. The EE performance is improved but is still $\sim$ 20% less than the theoretical prediction. This confirms that the TEIFU microlens produces a significant

amount of scattered light.

6.4 SMIRFS-IFU microlenses

Prior to installation on the SMIRFS-IFU instrument both the SMIRFS-IFU input microlens array and the output array were tested to characterize their performance. In particular the lens pitch was measured to check the microlenses had the same spacing as that defined by the optical fibre bundles.

6.4.1 SMIRFS-IFU microlens pitch

The pitch of the SMIRFS-IFU input and output microlens arrays was specified to be 412μm and 793μm respectively. This pitch is determined by the spacing between the fibre cores in the input fibre bundle, as described in section 7.3.2. For the output bundle the pitch is determined by the requirement to reimage the fibre cores onto a common pupil and is slightly smaller than the actual fibre spacing. The lens pitch was measured by various techniques summarized as follows:

Lens measurement In this technique the lens spacing is determined by observation the microlens surface with the microscope and measuring the distance between adjacent lenses with the microscope travelling stage. Errors are introduced by the accuracy with which the microlens boundary can be positioned and calibration errors with the travelling stage.

Lens imaging CCD images of the lens surface are taken from which the lens to lens distance can be measured. Again the precision with which the position of the lens boundary can be found affects the accuracy. The accuracy is also limited by the calibration of the microscope plate scale as described in section 6.2.3

PSF imaging The lens pitch can also be determined by measuring the distance between the microlens PSFs centroids from CCD images. This assumes there is no difference between the lens spacing and the PSF spacing. The accuracy is limited by the determination of PSF centroids and the calibration of microscope plate scale. However the pitch can be determined from an image containing many PSFs.

Array	Technique	Pitch	Error
Input	Lens measurement	$409.8 \pm 3.0\mu$m	travelling stage (0.3%)
Input	Lens imaging	$411.5 \pm 3.7\mu$m	plate scale (0.2%)
Input	PSF imaging	$411.2 \pm 3.0\mu$m	plate scale (0.2%)
Output	Lens measurement	$793.0 \pm 5.0\mu$m	plate scale (0.2%)
Output	PSF imaging	$795.9 \pm 3.3\mu$m	plate scale (0.2%)

Table 6.4: Summary of measured microlens pitch, measured using various techniques, for the SMIRFS-IFU microlens arrays. The specified values are 412μm for the input array and 793μm for the output array.

The lens to lens spacing was therefore measured independently of the PSF-PSF spacing to avoid any systematic errors introduced by the measurement technique. The results are summarized in table 6.4. In all cases the measured lens pitch matches the specified lens pitch within the measurement uncertainties. More information about the SMIRFS-IFU output microlenses, including an image of a lens block, can be found in section 7.7.2.

The spacing between PSF image centroids for the input microlens array was measured from a $\times 3$ magnification CCD exposure which contained images of 39 PSFs. By observing many PSFs simultaneously any changes in the microlens pitch with position in the lens array can be detected. The centroid position of each PSF was determined using the IRAF routine *qphot*. A computer programme (Lewis, 1996) was then used to calculate the regular hexagonal grid which best fits the PSF positions. The output of the software is the fit to the lens pitch and the RMS errors. The software also produces a residual plot of the the difference in position between the PSF and the ideal grid as shown in figure 6.17.

The result of the fit to the PSFs is a measured PSF-PSF spacing of $411.2 \pm 3.0\mu$m which is less than 0.3% smaller than the specification. This small difference is partly due the calibration of the microscope plate scale which has a limiting accuracy of 0.2%. The slight increase in the size of the residual with radial distance from the centre of the image is thought be due to optical distortions in the microscope and not a real distortion in the lens array.

6.4.2 SMIRFS-IFU input microlens PSF

The SMIRFS-IFU input microlens PSF was measured using type-I illumination to simulate the illumination characteristics of the telescope (UKIRT). An image of the SMIRFS-IFU

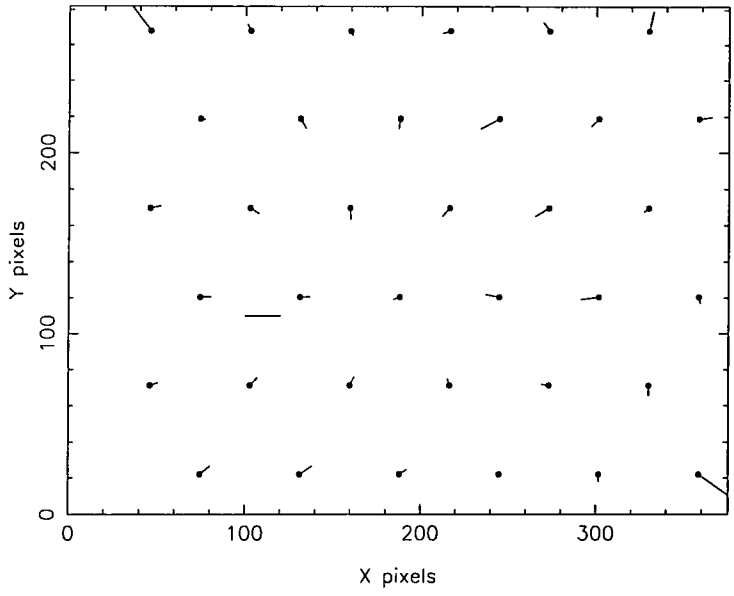

Figure 6.17: Plot of residuals from the hexagonal array fit to the microlens PSF centroid positions. The scale error bar shown is 20μm. The RMS errors show what looks like the presence of a radial distortion.

input microlens PSF is shown in figure 6.18. The measured SMIRFS-IFU input microlens PSF is shown in figure 6.19. The measured Airy radius from the $\times 40$ PSF of 8.4μm is in very good agreement with the theoretical prediction of 8.6μm. The PSF shows the presence of scattered light at large radii in a similar fashion to that already observed with the TEIFU input lenses. The $\times 10$ PSF[12] shows how the intensity levels off at $\sim 10^{-4}$ of the peak intensity at the lens edge before rising again. The input lens shows very good imaging characteristics but with an overall background of diffuse light. A 600 micron pinhole was placed in front of the lens array to act as a mask so that just one microlens is illuminated. The resulting PSF, labelled mask, shows the PSF continues to decrease in intensity but that some light is scattered into the area occupied by the adjacent lenses.

The corresponding EE plots are shown in figure 6.20. The first plot shows a comparison of the $\times 20$ data with the $\times 40$ data. The $\times 40$ EE was measured using both type-I and type-II illumination and the performance was found to be identical in both cases. Therefore the scattered light losses will be the same for light both entering or leaving the lens. The $\times 20$ EE data has been corrected for the instrumental scattered light using the procedure described in section 6.3.6. This correction is only applicable to the instrument set-up with the $\times 20$ magnification objective as other objectives are expected to have different scattered light characteristics. The EE performance shows $\sim 10-30\%$ scattered light losses depending on the radius.

[12]The PSFs are all normalised by the peak intensity

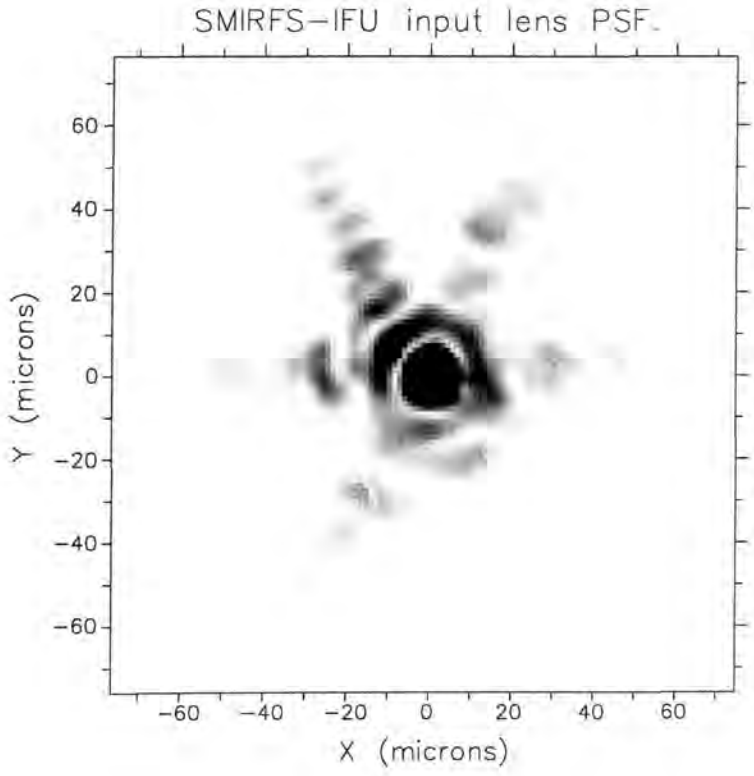

Figure 6.18: Image of the SMIRFS-IFU input microlens PSF taken with ×20 magnification. The Airy disk is clearly visible as are the six diffraction spikes.

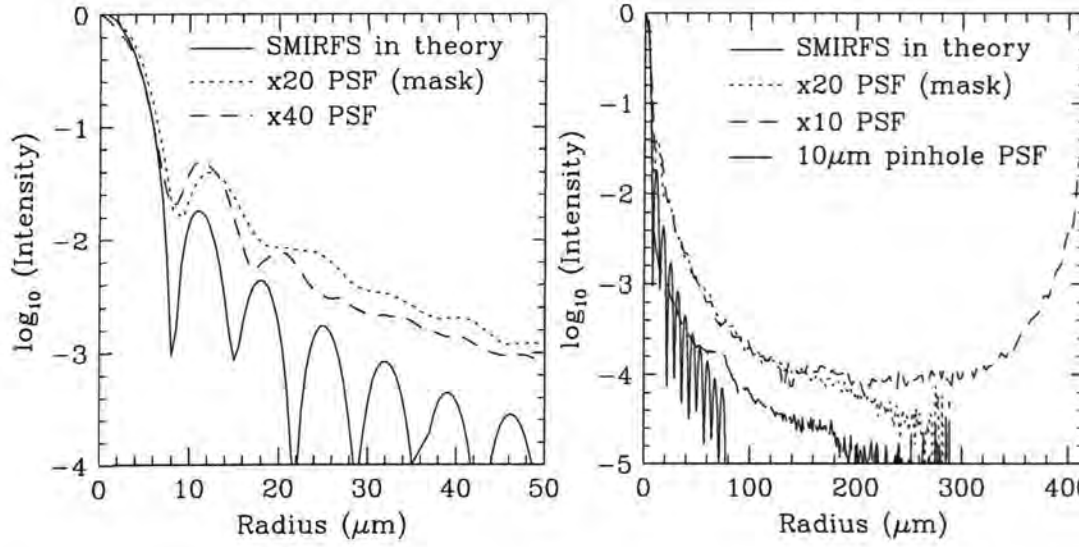

Figure 6.19: Azimuthally averaged PSF plots for the SMIRFS-IFU input microlens. The ×20 PSF was obtained with the pinhole mask in place.

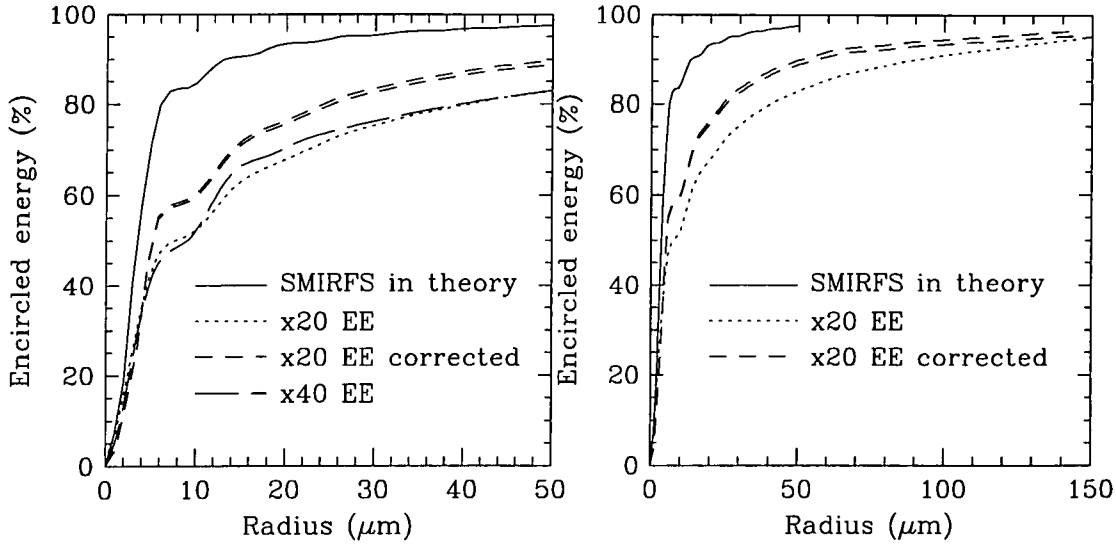

Figure 6.20: Azimuthal encircled energy curves for the SMIRFS-IFU input microlenses. The curves have been normalized to 100% at r_e by integration of the PSF. The error in the extrapolation of EE is shown by the two lines of the corrected EE curve.

Again the cause of the scattered light is thought to be roughness on the microlens surface. An image of the SMIRFS-IFU input microlens surface can be seen in figure 6.21. The image was taken using a special technique to highlight features on the lens surface. The microscope is first focussed onto the lens surface and an image is taken. Another image is then taken with the microscope defocused from the original position by a few microns. The first image is then divided by the second image. This removes any flat field variations and the effect of any dust etc on the microscope optics whilst the lens surface detail is enhanced in contrast. All the detail seen in figure 6.21 is therefore real structure on the surface of the microlens. Most of the surface defects are confined to the edges and corners of the microlenses with some surface features being common to all lenses. There is a small loss in fill factor due to the interface between lenses where the lens is not well defined. This was estimated to be $\sim 2.5 \pm 1\%$.

6.4.3 SMIRFS-IFU output array

The SMIRFS-IFU output microlens PSF was measured, using type-I illumination, at $\times 20$ magnification. An image of the PSF can be seen in figure 6.22. The resulting azimuthally averaged PSF is shown in figure 6.23 next to the corresponding EE curve. The measured

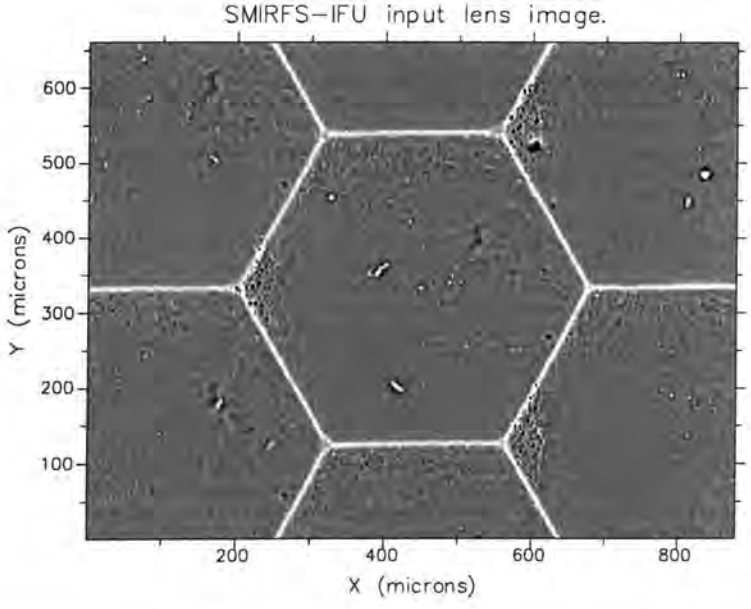

Figure 6.21: Image of the SMIRFS-IFU input microlens surface. Lens surface defects can be seen clearly in the lens corners. There is a slight loss in fill factor at the lens edges. Note the faint circular defect near the centre of the lens which was also seen with the TEIFU input lenses (figure 6.6).

Airy radius of 6μm is larger than the predicted radius of 4.3μm indicating some blurring of the PSF is present. This is not surprising considering the square geometry of the lenses which produces an asymmetric diffraction pattern. The field of view of the $\times$20 magnification image[13] is too small to cover the entire area of the output microlens. In order to normalize the EE energy at the equivalent radius ($r_e = 447\mu$m) in the usual manner it was necessary to extrapolate the measured PSF to larger radii. The contribution to the integrated EE from the modelled light curve can then be calculated. This extrapolation increases the uncertainty in the EE curve. Upper and lower limits are given to the EE curves depending on whether the extrapolated PSF was assumed to remain constant in intensity (lower curve) or continue to fall in intensity (upper curve) with radius. The resulting error bounds for the EE curves are shown as a cross hatched regions in the EE plot.

The SMIRFS-IFU output lens EE plots show that $\sim 20-40\%$ of the incident light is scattered by the lens. The EE performance is worse for the output lens than for the input lens. The cause of the increase in scattered light is unknown but is likely to be due to lower surface quality, particularly at the lens edges and corners. An image of the SMIRFS-IFU output microlens surface can be seen in figure 7.8.

[13]Only $\times$20 PSF images were taken for the output lens in order to allow the scattered light correction to be applied.

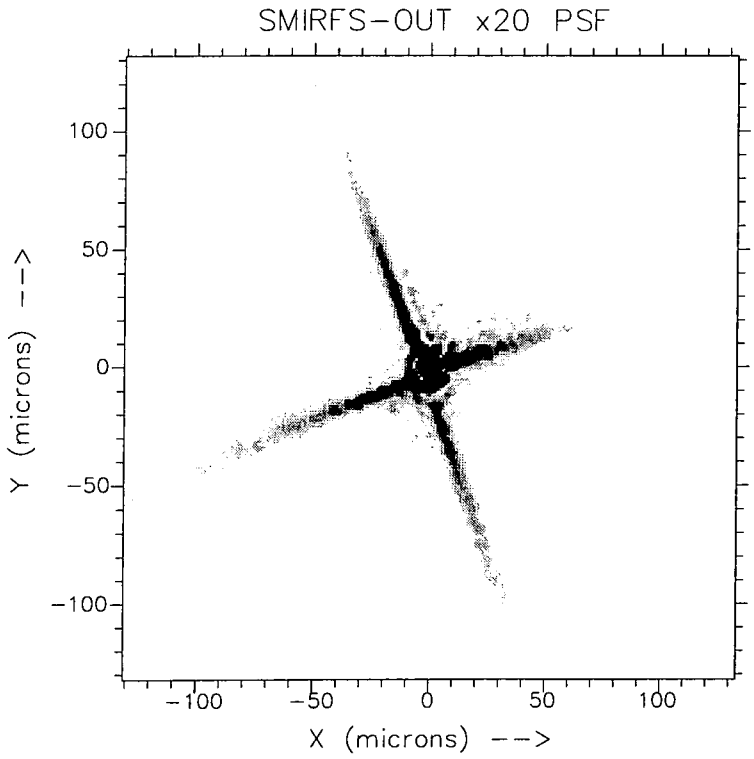

Figure 6.22: Image of the SMIRFS-IFU output microlens PSF taken with ×20 magnification. The four diffraction spikes are caused by the square shape of the lens. The diffraction spikes are much more intense than those measured with hexagonal lenses.

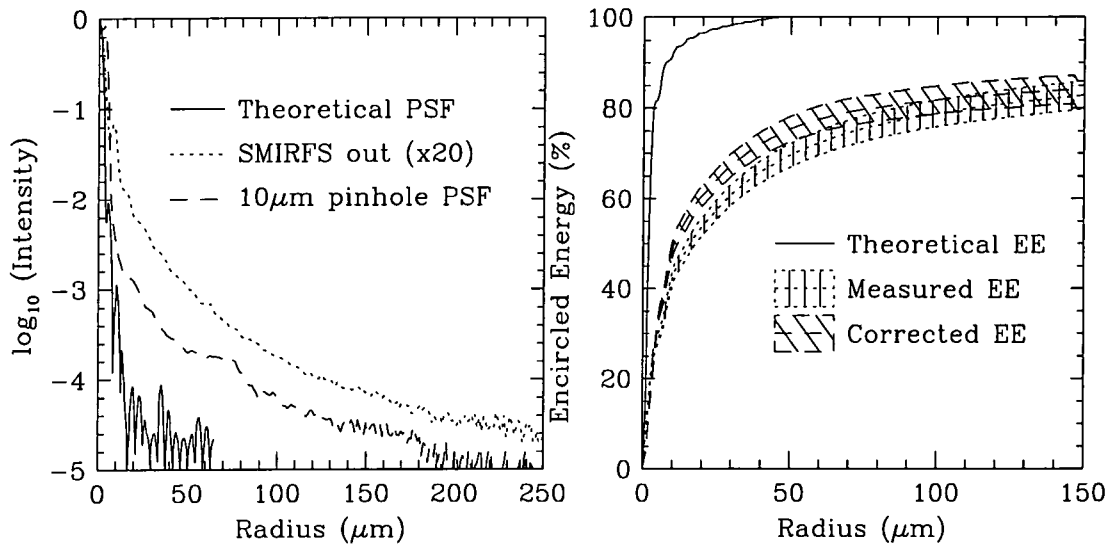

Figure 6.23: The left plot shows the behaviour of the SMIRFS-IFU output microlens PSF with radius. The theoretical PSF is also plotted for comparison. The predicted Airy is 4.3μm and the measured Airy radius is $\sim$ 6μm. The right hand plot shows the theoretical EE, the measured EE and the corrected EE. The error bounds produced by the extrapolation of the PSF to larger radii are also shown.

Technique	Pitch	Error
Lens measurement	1.674 ± 0.006mm	travelling stage (0.5%)
Lens imaging	1.674 ± 0.006mm	plate scale (0.2%)
PSF imaging	1.710 ± 0.009m	plate scale (0.2%)

Table 6.5: Summary of measured microlens pitch, measured using various techniques, for the SAURON microlens array. The specified pitch is 1.7mm. Note the PSF pitch is larger than the lens pitch.

6.5 SAURON microlenses

As part of a collaboration with the Observatoire de Lyon, France, the microlens array to be used in the SAURON instrument was tested in Durham. SAURON is a TIGER type (i.e. lenslet only) instrument for use on the William Herschel Telescope. A brief description of this type of instrument is given in section 4.2.4. The microlenses required for SAURON are larger and faster than those required for fibre-lens integral field applications. The lens specification is listed in table 6.1. The test lenses were supplied as 0.2mm epoxy lenses on a 1mm thick silica substrate. The large aperture and the spherical surface profile produces a significant amount of spherical aberration even with type-I illumination. The SA produces a longitudinal aberration of 0.2mm and a circle of least confusion which is $\sim 12\mu$m in diameter, i.e. they are no longer diffraction limited. Images of the surface of the SAURON microlens can be seen in figures B.7 and B.8.

The size of the SAURON microlenses was measured using a travelling microscope, and directly from an image of the lens, the results are listed in table 6.5. The microlens diameter was found to be $\sim 2\%$ smaller than the specified diameter. The spacing between the microlens PSF centroids was also measured and the result is listed in table 6.5. The lens spacing determined in this way is different from the spacing measured from direct observation of the lens surface. The reason for the difference is unknown, however the PSF spacing is in better agreement with the lens size specification, and it is the PSF spacing that is important for the operation of the SAURON instrument. This does indicate, however, that there me be some problem with the PSF pitch being slightly different to the pitch of the microlens surface.

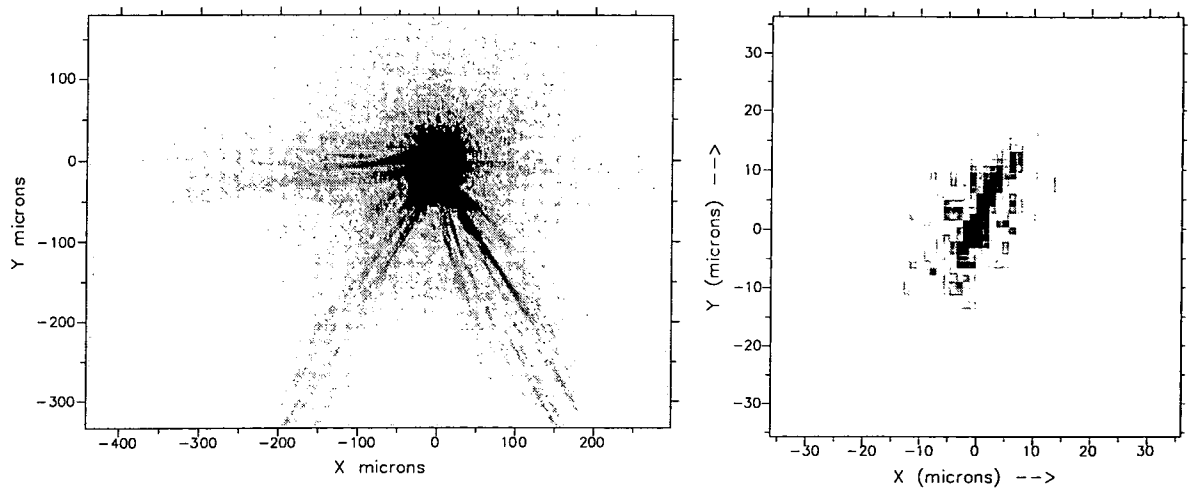

Figure 6.24: Image of the SAURON microlens PSF taken with the ST6 CCD and ×10 magnification, left image, ×20 magnification, right image. Note the elongation of the PSF in the ×20 image. The PSF is much larger than the expected circle of least confusion. No Airy disk is seen due to the aberrations of the lens. Asymmetric diffraction spikes can be seen.

6.5.1 Sauron PSF

PSF measurements were carried out with type-I illumination as this is the configuration used in the SAURON instrument and also reduces the amount of spherical aberration. An image of the SAURON microlens PSF taken with ×10 magnification can be seen in figure 6.24. The image shows an elongated core without an Airy disk. The lens is far from diffraction limited, with a 2.5 waves of S.A, but this should not prevent the observation of an Airy pattern. The lack of an Airy pattern indicates the lens surface has aberrations in addition to the expected S.A. The spherical aberration of this lens produces a circle of least confusion which is 6μm in radius whereas the observed PSF is elongated over $\sim$ 20μm. The diffraction spikes also appear more intense on one side of the PSF than the other.

The azimuthally averaged PSF is plotted in figure 6.25. The ×10 and ×20 PSF data is normalised by the central intensity giving the appearance that the ×20 PSF has higher intensity in the wings. However the ×20 data is a good fit with the ×10 data if a correction is applied to the intensity normalisation. The ×3 data is also shown but it should be noted that the ×3 microscope objective has an NA less than that of the SAURON lens so the PSF is expected to be altered due to vignetting by the objective. The ×3 PSF does show the same characteristics as exhibited by the other AOA lenses tested. It levels off at $\sim 10^{-5}$ of

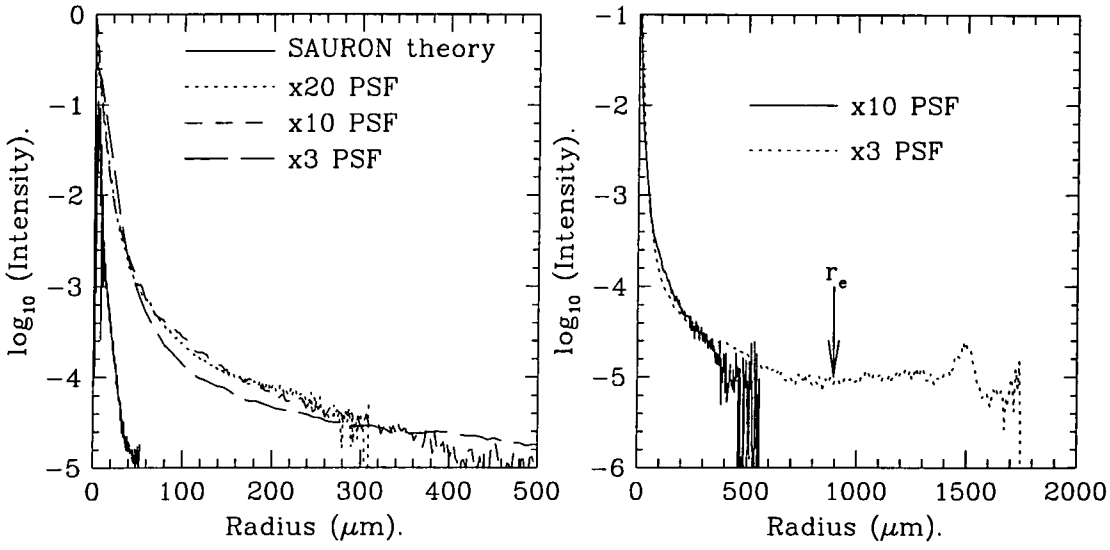

Figure 6.25: Azimuthally averaged PSF plot for the SAURON microlens.

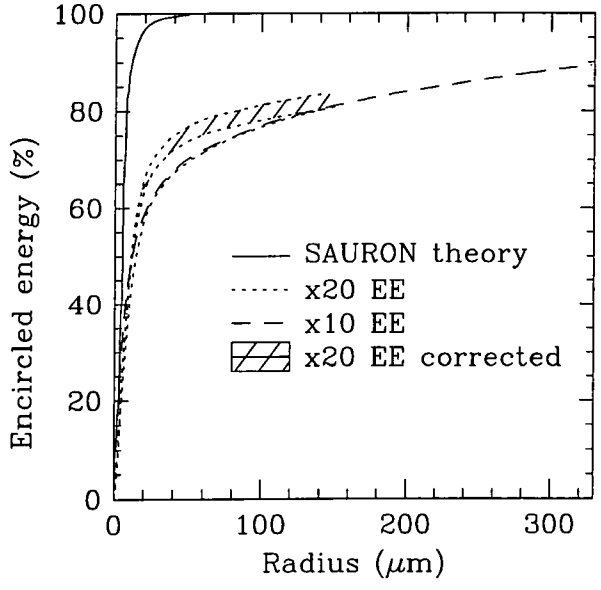

Figure 6.26: Azimuthal encircled energy plot for the SAURON microlens. Both the ×10 and ×20 EE curves are shown for comparison. The data has been normalised to 100% at r_e by extrapolation of the PSF. The errors in the EE normalisation are shown by the shaded region in the plot for the corrected EE.

the peak intensity before increasing again due to the adjacent lenses.

The encircled energy performance is plotted in figure 6.26. The encircled energy has been normalised to 100% at the equivalent radius (r_e = 893μm) by extrapolation of the PSF data in the same way as described in section 6.4.3. The upper and lower estimates for the corrected encircled energy are shown by the shaded region in the figure. Approximately 20-40% of the incident light is scattered from the core of the PSF to larger radii. The surface quality of the SAURON microlenses looks poor in comparison with the other AOA lenses tested and this is thought to explain the poor scattered light performance. The SAURON lens surface showed considerable 'orange peel' type structure concentrated in the corners of the lenses. An image of the SAURON lens surface can be seen in appendix B. The entire lens surface was also covered in arc shaped scratch marks. Some defects were also seen in the epoxy such as bubbles and trapped particles. The conclusion is that AOAs manufacturing technique is not as well suited to producing larger, greater than 1mm, microlenses as it is too smaller lenses.

This degradation in performance was considered serious enough for the SAURON instrument to be redesigned to incorporate microlenses of superior quality. Scattered light is a problem in TIGER type IFUs because the image formed by the microlens array is reimaged directly onto the detector. The scattered light will cause cross talk between adjacent lenses, and spatial elements, leading to an effective broadening of the spatial resolution. Scattered light in a lens-fibre based IFU is less problematic as it is masked by the fibre and the spectrograph slit.

6.6 Summary of results

In total four AOA microlens arrays and one NPL microlens array were tested. As the AOA lenses are all manufactured with a similar technique it is possible to compare their performance to look for trends with lens parameters. The NPL lens will not be expected to show the same trends as it was manufactured differently producing very different performance. A full description of the performance of the NPL microlens array is given in appendix B.1.

The NPL microlenses were rejected for use in IFS due to their poor performance in comparison with the AOA microlenses. The reasons leading to this decision can be summarized as

follows:

- AOA lenses have a higher fill factor.
- AOA lenses produce better image quality.
- Encircled energy performance of AOA lenses is better.
- AOA lenses have less limitations on numerical aperture.

NPL microlenses were not suitable for fibre-microlens based IFUs of the type being built. They may however find applications in other areas of Astronomical instrumentation, such as single object fibre spectroscopy, where single high NA microlenses are needed (i.e. not lens arrays).

Figure 6.27 shows a comparison of the four AOA microlens PSFs and EE curves. The PSFs have been plotted as the logarithm of radius divided by focal length versus the logarithm of intensity. The abscissa is therefore in units of off-axis angle (or numerical aperture) and allows comparison of lens PSFs independently of the lens aperture and focal length. The shift between the curves in intensity is due to the normalisation of the PSFs at the peak intensity. It is notable that all the PSFs fall in intensity with the same power law which is $I \propto r^{-2}$. Only the TEIFU measurement has sufficient field of view to show that the PSF approximately levels off at numerical apertures greater than that of the lens due to the light contribution from the adjacent lenses.

The encircled energy curves in figure 6.27 show the general trend that the larger aperture lenses have poorer performance than the small lenses. This may be because the larger lenses have a greater surface area with which to scatter light producing poorer EE performance. The manufacturing method may also favour production of small, less than 0.5mm, high NA lenses. However there do not seem to be any hard and fast rules with which to predict the performance of AOA lenses for future instrument designs.

A suitable *figure of merit* that accurately describes the performance of a lens is difficult to define due to the large number of characteristics possessed by any one lens. The Airy radius, $R_A = 0.61\lambda/\mathrm{NA}$, is invariant for lenses with the same numerical aperture so a figure of merit can be related to the Airy radius. A suitable figure of merit is the encircled energy at five

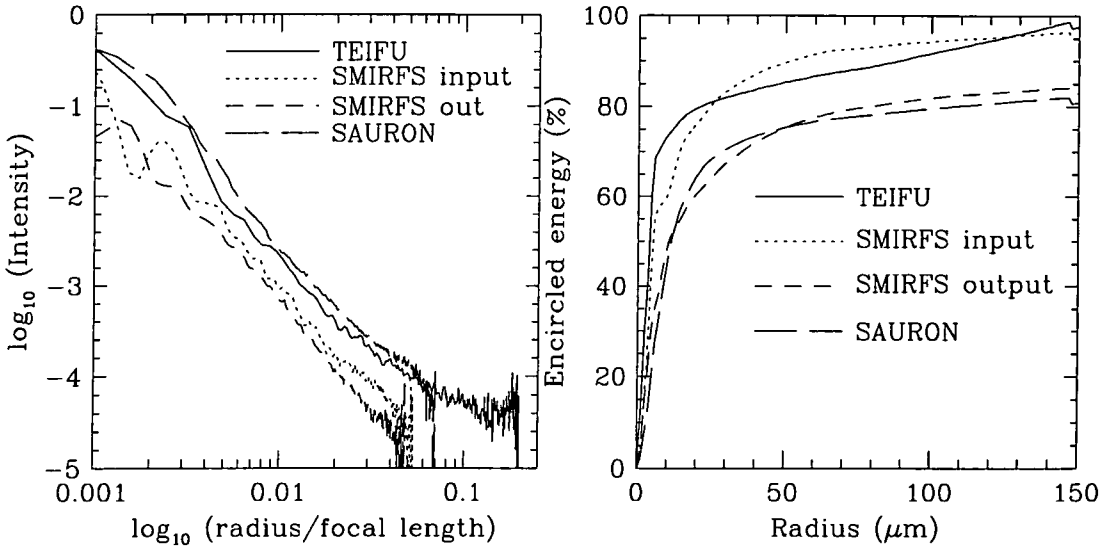

Figure 6.27: Comparison of PSF and EE curves for the four AOA microlens arrays tested. The PSF is plotted as the logarithm of radius/focal length versus log intensity as this effectively normalises the PSFs to the same scale.

Lens	D_l(mm)	NA	$R_A^T(\mu m)$	$R_A^M(\mu m)$	$EE5R_A^T$	$EE5R_A^M$	FOM
SMIRFS in	0.412	0.038	8.6	8.2	96.9%	88.0%	0.91
SMIRFS out	0.793	0.066	4.3	5.8	96.9%	62.5%	0.64
TEIFU	0.305	0.104	2.8	3.2	96.5%	77.0%	0.80
SAURON	1.700	0.190	1.3	—	69.3%	30.0%	0.43
NPL	0.495	0.300	1.0	1.2	28.9%	25.0%	0.86

Table 6.6: Summary of microlens PSF test results. $EE5R_A^T$ denotes the theoretical prediction of EE at five times the Airy radius and $EE5R_A^M$ denotes the experimentally measured value. An $EE5R_A^T$ of 96.9% is consistent with a diffraction limited lens. The figure of merit is denoted by FOM.

times the Airy radius. The theoretically predicted value of encircled energy at five times the Airy radius is denoted $EE5R_A^T$. The value of $EE5R_A^T$ is listed in table 6.6 for each microlens tested. A *diffraction limited* lens has $EE5R_A^T$=96.9% independent of wavelength and NA. Also listed is the experimentally measured value of encircled energy at five times the Airy radius, denoted by $EE5R_A^M$. The figure of merit, FOM, is given by equation 6.9:

$$FOM = \frac{EE5R_A^M}{EE5R_A^T} \tag{6.9}$$

therefore a lens which performs perfectly will have FOM=1. This figure of merit is also independent of the aberrations of the lens such that a lens which produces aberrations consistent with those predicted will still have FOM=1. The measured FOM for each lens is listed in table 6.6. The table shows that lenses which have a measured Airy radius, R_A^M, which is approximately equal to the theoretical Airy radius, R_A^M have a high FOM. The SAURON microlens which has no visible Airy disk, due to large aberrations, has the worst FOM.

Another trend is that smaller AOA lenses have higher merits than the larger AOA lenses. Not enough data is available to predict how FOM varies with NA independently of lens aperture. A surprising result is that the NPL lens has a high FOM. This result was obtained with a 0.1mm defocus. This means that although the imaging properties of the lens are poor, as expected at a large defocus, the encircled energy performance is good. The NPL lenses may prove useful if they are used to couple light into a fibre that is adequately oversized to accept the blurred image. However, oversizing of the fibres in this way cannot always be tolerated due to increases in thermal background and loss in resolution etc. that are caused with oversized fibres.

6.7 Antireflection coatings

None of the microlens array samples tested had antireflection (AR) coatings. Ideally broad-band AR coatings are required to cover the entire operating range of the instrument. For the SMIRFS-IFU the absence of AR coatings on the input and output microlens arrays causes an 8% loss of light due to Fresnel reflection. Conventional AR coatings, such as single layer MgF_2, are difficult to apply to delicate epoxy lenses due to the extreme conditions

experienced inside the coating plant. Heating of the epoxy during application of the AR coating causes the epoxy to expand. When the epoxy cools this causes the AR coating to crack. It is also unknown whether the correct thickness of coating can be accurately applied to the highly structured lens array surface. A possibility for future investigation is the application of Sol-Gel coatings, as described in appendix A.1, to microlens arrays. The Sol-Gel coating can be applied at room temperature by dip coating thereby causing minimum stress to the microlens epoxy. It is possible dip coating may produce more uniform coatings than vacuum beam deposition as the liquid will follow undulations in the lens array surface more closely.

6.8 Summary, conclusions & future developments

An investigation was made into available microlens technology to find microlens arrays suitable for use in the integral field units being constructed. Test samples were obtained from Adaptive Optics Associates and the National Physical Laboratory. The NPL lenses were rejected due to the unacceptable image quality. The NPL lenses also had a lower fill factor than the AOA lenses and limitations on the numerical aperture that could be manufactured. The AOA lenses were found to be of good quality. The AOA microlenses had excellent positional accuracy and consistency of focal length. The image quality was also found to be good. However the background level of scattered light caused by the surface quality of the AOA lenses is a problem. The scattered light losses are typically 20% in the visible per lens surface. For an IFU constructed with microlens both at the input and output of the fibre bundle this represents a severe loss in throughput.

The University of Durham Astronomical Instrumentation Group is now working in collaboration with AOA to develop microlenses with improved surface quality. It is hoped that the experimental techniques described in this chapter can be used to advantage for the future characterisation and development of microlens arrays. Some of the microlens test results presented in this chapter have been published in Lee *et al.* (1998) .

Two sets of AOA microlenses were successfully used with the SMIRFS-IFU instrument. If the scattered light losses cannot be improved in the future, or an alternative microlens supplier found, the question has to be asked would bare fibre bundles be better. The argument

against bare fibre bundles is the loss in fill factor produced by the close packing of fibres. However, this loss is similar to loss in throughput caused by the microlens. The clear advantage with microlenses comes from their ability to convert the focal ratio of the beam which propagates in the fibre. This allows efficient coupling from the telescope to existing longslit spectrographs without the need for dedicated fibre spectrographs.

There is still much to be done to improve the performance of microlenses still further. Large aperture fast lenses produce significant spherical aberration due to the spherical surface shape. It is therefore desirable to have lenses with conic surfaces. These were unavailable at reasonable cost at the time of writing. A significant advantage would be the production of microlenses directly in glass substrates. This would allow the lenses to be antireflection coated without risk of damaging the surface. The glass can also be chosen to have good transmission in the wavelength region of interest. The current epoxy lenses have poor transmission in the blue. The rapid growth in the number of astronomical institutions that are currently constructing IFUs which incorporate microlens technology will no doubt lead to improvements being made.

Chapter 7

SMIRFS-IFU construction

Abstract

This chapter describoes the mechanical design and construction of the SMIRFS-IFU. At each stage in the assembly process the components were tested and the results of these tests are described. In general the assembly process was successful with a few minor problems occuring such as adhesive problems and components becoming loose during polishing. From the experience gained in this valuable prototyping exercise it is expected that the problems can be overcome in the design and construction of future integral field units.

7.1 Introduction

The SMIRFS-IFU is the first microlens-fibre IFU to be built in Durham. It is a modest project re-using many of the parts of the existing SMIRFS multi-fibre system. It is effectively a prototype, and technology demonstrator, for the more ambitious future TEIFU and finally GMOS-IFU projects. The techniques developed and difficulties encountered in the construction of the SMIRFS-IFU will provide valuable information for the construction of larger IFUs. However the SMIRFS-IFU is also an instrument capable of doing useful science and certainly provides a unique observing capability for UKIRT. The SMIRFS-IFU was constructed over a period of one year, being completed in June 1997 and subsequently commissioned on the United Kingdom Infrared Telescope. This chapter describes the construction phase of the SMIRFS-IFU project. In particular the quality control aspect of the construction phase is emphasised. Only through careful attention to achieving accurate tolerances in the manufacture can the highest instrument performance be realised. Areas in

which the performance was non-optimal are discussed and recommendations for improvements for future designs of IFU are given. It should be noted some of the work described in this chapter was carried out by Dr. Roger Haynes, such as fibre polishing and assembly of the tube array. This work is included due to its relevance to the other work described.

7.2 Alterations to SMIRFS

The design and capabilities of the original SMIRFS instrument have already been described in section 5.2. As the SMIRFS-IFU is an upgrade to the existing SMIRFS instrument many of the original components are essentially the same. The major difference is the change from the multi-object fibre bundle to the integral field fibre bundle.

To accommodate the new fibre bundle both the FPU and the SPU had to have minor alterations. The FPU was changed to accommodate a new thicker (3mm instead of 1.2mm) field plate. The thicker field plate was needed to support the heavier IFU fibre bundle. The capability to rotate the input microlens array, to match the orientation of any astronomical object, was not provided in the SMIRFS-IFU. Some adjustment could be made by rotation of the field plate. In some cases, however, it may be best to have the IFU orientation aligned with the telescope axes (right ascension and declination) to facilitate mosaicing of multiple IFU exposures. Provision was made for the later addition of a rotating IFU mount should such an upgrade be required in the future. The SPU was modified to allow the new IFU output slit to be mounted onto the SPU. Modifications were also made to the kinematic mount access ports to facilitate easier adjustment. This is because the optical alignment of the IFU output slit is more critical than the alignment of the multi-object output slit. The optical alignment is made difficult by the need to accurately register each IFU fibre with a single pixel.

To reduce the production of scattered of light within the SPU the interior walls of the SPU were repainted with NEXTEL paint. This paint may also help to reduce thermal emission from the walls of the SPU. It is unknown, however, whether thermal emission from the SPU itself was a problem in the original version of the SMIRFS instrument. This paint has low thermal emissivity and reflectivity. The metal surfaces of the new IFU output slit unit were treated with 'metal black' to prevent corrosion and reduce reflectivity. The metal black

treatment was not completely successful as the treated surface became difficult to bond to the fibre ferrules.

7.3 The Integral Field Fibre Bundle

The main component of the SMIRFS-IFU is the integral field fibre bundle. The function of the fibre bundle has been described in section 4.3. In summary the fibre bundle provides a method of reformatting the two-dimensional input field into a one-dimensional slit. Microlenses are used to convert the focal ratio from the telescope to one which is suitable for use in fibres. The technological difficulty is in accurately registering the array of fibres with the array of lenses. The mechanical requirements of the fibre bundle can be summarised as follows:

- Accurate positioning of the optical fibres with respect to the input microlens array.
- Optical fibres should positioned with the minimum of mechanical stress to reduce the possibility of losses caused by stress induced focal ratio degradation.
- Accurate positioning of the fibres on a curved focal plane at the output slit.

The main difficulty to be overcome is accurate positioning of the optical fibres. The tolerance on fibre positioning is typically $\pm 10\mu$m. Accurate fibre positioning is required at the input so the fibres coincide with the pupil images produced by the microlens array. If the fibres are not positioned in a regular hexagonal grid then light will be lost due to vignetting. At the output slit the fibres have to be accurately positioned to project a pupil image in the correct direction and to match the pixel spacing on the detector.

7.3.1 Fibre positioning

The SMIRFS-IFU input bundle requires the fibres to be spaced $\sim$ 0.4mm apart in a regular hexagonal grid. The SMIRFS-IFU output slit requires the fibres to be placed on a curved surface $\sim$ 0.8mm apart. The small spacing and desired accuracy (typically $\sim \pm 5\mu$m) means fibre positioning presents a difficult mechanical problem. A fibre holder cannot be made using conventional machining techniques due to the small size.

The following ideas were investigated as possible ways of achieving the fibre positioning specification at the input:

- Micromachining of brass plates.
- Etched glass substrates.
- Micro-tube arrays.

The first possibility is to drill a regular array of small diameter holes in thin Brass plates. The holes would be large enough in diameter to allow the optical fibre to be glued in place. A limitation of this technique is the maximum thickness of brass plate that can be drilled is around seven times the drill diameter. As the outside diameter of the fibres is only 195μm this means a single Brass plate is too thin to adequately support the fibres without inducing mechanical stress. The use of more than one Brass plate to support the fibre leads to alignment problems between the plates. The fibres are also required to be packed closely together. The proximity of the drilled holes to each other implies a narrow wall thickness and the manufacturers felt that the wall might collapse during machining.

The FUEGOS group at the Observatoire de Meudon, Paris (Baudrand, 1997), investigated the use of etched glass substrates. It is a straightforward lithographic procedure to etch a regular array of holes into a glass substrate and the thickness of the substrate can be a few millimetres. This technique requires the removal of the fibre buffer up to a certain depth for correct positioning in the glass substrate. This procedure was thought to increase the risk of fibre breakages and deemed unacceptable. The problem of small wall thicknesses also applies to this technique.

The standard method for mounting fibres in multi-object spectroscopy (Rasilla *et al.*, 1993) is to locate them inside stainless steel micro-tubes (ferrules). The steel tube protects the fragile fibre during the polishing process and is readily fixed to mechanical apparatus. The length of the ferrule also helps to support the fibre along its length thereby reducing mechanical stress. It is clear that the ferrules can be packed into a grid which will automatically produce hexagonal close packing. This produces what is known as a *tube array.* The spacing between the tubes will be determined by the tube diameter. Tube arrays provide a simple and cost effective technique and were chosen for use with the SMIRFS-IFU input bundle.

Variation in tube diameter	$\pm 2\mu$m
Error in position of tube within regular hexagonal array	$\pm 7\mu$m
Position of fibre within ferrule	$\pm 7\mu$m
Error in positioning of matching microlens	$\pm 3\mu$m
Total error budget	$\pm 10\mu$m

Table 7.1: Summary of the sources of RMS positioning error in microlens-fibre alignment and the error budget for each source of error. An RMS positioning error of $\pm 10\mu$m can be expected to produce a throughput loss of $\sim 6\%$.

7.3.2 Tube arrays

A thorough investigation was carried out into the production of accurate tube arrays. A report on this investigation can be found in Lewis (1996) . The main problem to be addressed was assembling the ferrules into a regular close packed hexagonal grid. A slight bend in the ferrule or burring on the edge can easily cause the hexagonal grid to become distorted i.e. a dislocation in the regular grid is produced. There is also a positioning error produced by movement of the fibre inside the ferrule. The sources of error and the contribution of each to the total fibre positioning error budget are summarised in table 7.1.

These errors give a total positioning error budget which determines the throughput degradation that can be expected due to fibre positioning errors. The throughput losses, at the input array, due to fibre-microlens misalignment errors, estimated using the error budget, are $\sim$6%. This loss is simply estimated from the area of the input pupil image that is vignetted by the offset fibre core.

The tube arrays were manufactured using hypodermic Steel tubing produced by Coopers Needles Limited, Birmingham. For production of the SMIRFS-IFU standard gauge 27 tubes were chosen providing a nominal outside diameter of $406 \pm 20\mu$m. This closely matches the desired spatial sampling of 0.6 arcseconds. The ferrules were provided in 20mm lengths. The inside diameter is 203μm which is a adequately oversized to allow the fibre to fit (buffer diameter 195μm) inside the ferrule without risk of fouling or increased mechanical stress. Samples of fibre were sent to Cooper's Needles Ltd so that they could supply tubing from stock ferrules which would accommodate the fibres.

The outside diameter of the ferrules needs to be known very precisely as the pitch produced

by the ferrules defines the pitch of the input microlens array. The manufacturers specification on pitch is only known to an accuracy of $\pm 20\mu$m. Only ferrules from the same draw[1] can be guaranteed to have the same diameters, with ferrules from different draws showing variations. The ferrules for the SMIRFS-IFU all came from the same draw. The ferrules were sent to Teesside Metrology to be measured precisely. The outside diameter was determined to be $412.1 \pm 1.5\mu$m.

The inside diameter was measured using a travelling microscope and found to be $\sim 205\mu$m. The tolerance on the inside diameter, in extreme cases, may prevent the fibre from being inserted into the ferrule. The minimum clearance between the inside diameter of the ferrule and the buffer diameter of the fibre is an issue which is unresolved. In Schectman (1993) a clearance of $10 - 20\mu$m is recommended. For example, tests showed that 140μm buffer fibre would not fit inside an 152μm ID ferrule. The fit will depend on the manufacturing tolerance of the ferrules and fibres and also on the cleanliness of the inside of the tube. Defects inside the ferrule will clearly causing fouling. Forcing a fibre into a ferrule which is too small, or dirty, will cause stress induced FRD and may also prevent enough glue from entering the tube to provide adequate adhesion. To avoid contamination of the inside of the ferrules cleanliness is therefore a high priority during the assembly process.

There is then a limit to the size of fibre that will fit inside a ferrule of given inside diameter. The requirement that the fibre is always slightly smaller than the inside diameter of the ferrule therefore produces a fundamental limit to the error budget as there will always be some movement of the fibre within the ferrule. Therefore there will always be some small loss associated with fibre positioning, unless oversized fibres are used, i.e. fibres which are larger than the pupil image.

7.3.3 Input tube array

The input tube array for SMIRFS-IFU was constructed by clamping a large number of ferrules within an aperture. The ferrules automatically form a hexagonally close packed structure within the aperture when they are densely packed. The ferrules are inserted into a U-shaped piece of metal known as the tube holder. A clamping section is then inserted

[1]The ferrules are made using a drawing (extrusion) process.

into the U shape to secure the ferrules in position. The clamping action provides enough force to secure the ferrules without the need for adhesive. The rectangle formed by the U shape and the clamp has to be made accurately to ensure correct packing of the ferrules. The tube holder was manufactured by wire erosion as this a simple, cost effective, technique capable of providing adequate manufacturing tolerances. A photograph of the assembled input tube array containing fibres, taken after polishing, can be seen in figure 7.6. The manufacturing tolerance on the rectangular aperture is $+10\mu$m, i.e. undersizing cannot be tolerated. The tube holder was designed to accommodate 15×11 ferrules. The tube array is deliberately oversized to improve the positioning accuracy of the central 11×7 active tube array as positioning errors mostly occur at the periphery of the tube array (Lewis, 1996). The recommendation is to include at least two redundant rows either side of the active array. The straight edge was the 11 ferrule edge. The actual size of the fibre holder was found to be smaller than specification so one row of tubes had to be left out and smaller packing tubes inserted instead to account for the difference in size.

After assembly a CCD image of the tube array was taken and analysed to measure the pitch of the ferrules. The pitch of the ferrules was found to be $412 \pm 3\mu$m. This is an important result as this defines the centre to centre spacing between the fibre cores and hence the pitch of the input microlens array.

Input fibre assembly

The original plan was to assemble the fibre bundle at the output end first. This meant if there were fibre breakages then the output slit block could simply be disassembled and started again. If breakages occur at the input bundle then they are much more difficult to repair. However, due to manufacturing difficulties with the output slit blocks the assembly process was begun at the input bundle.

After assembly of the input tube array the fibres were inserted into the ferrules. Each ferrule was cleaned by insertion of a spare length of fibre to remove any contamination from within the ferrule. The fibres were then glued into the ferrules using two part cyanoacrylate adhesive (Araldite). This adhesive was chosen for its low shrinkage properties on curing. The fibres were inserted in groups of six, each group of six corresponding to one output slit block (section 7.3.4). Care was taken to ensure the fibres were assembled in the correct order

as it is crucial for the operation of the IFU that neighbouring fibres at the input are also neighbouring fibres at the output. The six fibres of each group were also inserted into red plastic protective tubing.

When all the fibres were secure the whole fibre bundle was immersed in a bath of Epotek 301/2 adhesive to glue the ferrules into place. This adhesive was specifically chosen for its excellent wicking properties, long pot life and low viscosity. The glue completely wicked through the empty ferrules, and the small regions between ferrules, to the other side of the fibre bundle. After the glue had cured excess glue was removed from the polishing surface and the area where the conduit fixes to the fibre bundle and the conduit was fixed in place over the 12 groups of six fibres.

7.3.4 Output tube array

The output slit focal surface has to be curved to match the focal plane of the slit projection unit. It was decided it would be too difficult, and expensive, to produce microlens arrays on a curved substrate with the same radius of curvature as the output slit focal plane. Even if the microlens array could be produced on a curved surface there still remains the problem of how to polish optical fibres that are also positioned on a curved surface. The normal solution to this problem is to approximate the curved focal surface with a number of flat blocks. The output slit assembly is described in more detail in section 7.3.5. Each block is positioned and angled to best approximate a curved focal plane. The 72 fibres of the SMIRFS-IFU were split up into 12 blocks of 6 fibres. Approximating the curved focal plane with 12 sections produces the best compromise between matching the curved focal plane and complexity of assembly.

Tube arrays were not needed at the output slit as the inter-fibre spacing is quite large. Instead a 'comb' was used to accurately position the fibres on the output slit blocks as illustrated in figure 7.1. The comb consists of an precisely machined U-shaped piece of metal which fits over the slit block. The fibre positioning comb was manufactured using wire erosion techniques to provide the necessary accuracy. The comb has six grooves which define the positions of the fibres.

It should be noted that the initial plan was to fix the fibres directly to the output slit

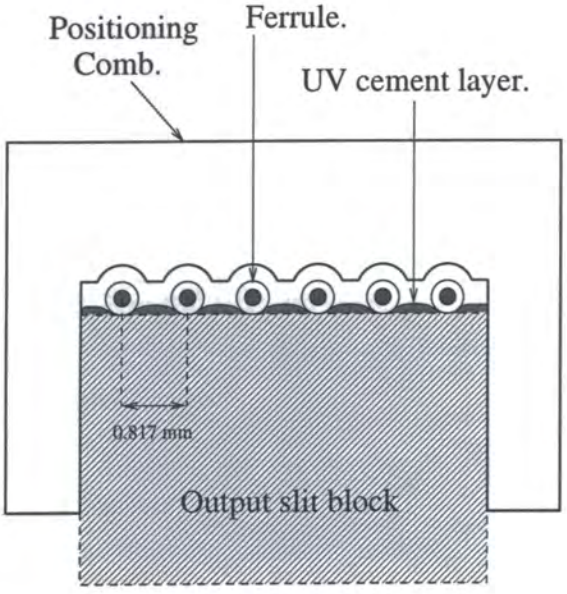

Figure 7.1: Diagram of the output slit fibre/ferrule positioning comb. The ferrules are initially held in place by a thin layer of adhesive. The comb is then put in place over the slit block. The ferrules spacing is determined accurately by the grooves cut into the comb. The glue is still wet when the comb is applied so the ferrules move into position.

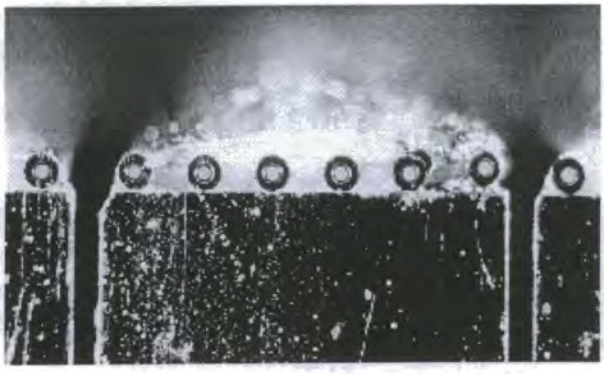

Figure 7.2: Microphotograph of a polished output slit block. The ferrule at the right edge of the central slit block lifted away from the slit block during the polishing process. It can be seen to be out of place. This problem is caused by lack of glue at the slit block edges.

blocks without using ferrules. To do this a thin layer of UV curing adhesive (Vitralit 4280, see section 7.5.4) was applied to the end of the slit block, near to where polishing will take place, as shown in figure 7.1. Then the fibres are laid along the top of the block and the comb is placed over the fibres. The fibres are then adjusted until they sit correctly in the grooves within the comb. The glue can then be cured and the comb removed. However, this method did not work satisfactorily due to problems with accurately controlling the fibre positioning. The build up of static charge on the fibres during preparation caused them to stick together. The plastic deformation the fibres retain after being wrapped around the transport reel also causes them to bend and twist during assembly making accurate positioning impossible.

To solve this problem it was decided to first glue ferrules to the slit blocks, using the same comb arrangement, and then glue the fibres inside the ferrules in the normal way. This alleviates the problem of positioning twisty fibres as they are held firmly inside the ferrules. This method does however increase the positioning error due to the extra components involved.

As before a thin layer of UV curing adhesive was applied to the top of the slit block near the end to be polished. The ferrules were then placed inside the comb, with the comb lying on its back. The slit block was then inserted into the comb until a firm seat was made and the ferrules adjusted individually so that they were level with the polishing face of the slit block. The comb was positioned 4mm from the polishing surface so that glue did not contaminate the polishing surface or enter and foul the ends of the ferrules. Once the UV curing cement had been cured the comb was removed and more UV cement applied to fix the tubes firmly in place. The positioning accuracy of the ferrules was then measured on a travelling microscope to ensure correct assembly.

The design specification was for a ferrule spacing of 817μm but the actual positions of the ferrules showed considerable differences. The largest positioning error was 23μm from the nominal position. It was also noted that the ferrules did not bed down correctly on the slit block but in some cases were raised above the block by $\sim$ 10μm. The distance of the outer edge of the first and last ferrule to the edges of the slit block was 158 and 204μm so the entire tube array is shifted sideways by $\sim$ 20μm.

It was decided the ferrule positioning errors were unacceptable and improvements could be made. The ferrules were reglued to the slit block but this time the comb was positioned right at the polishing end of the block rather than 4mm back from the end. This meant there

was a higher risk of the glue entering the ferrules. A second comb was also positioned at the other end of the slit block to secure the ferrule during gluing. This technique achieved more accurate positioning of the ferrules and they were bedded down to the block more uniformly. The global RMS positioning error was found to be 7.5μm from the nominal position. Two sources of error contributed to the global error: 4.5μm RMS due to manufacturing technique and 6μm RMS due to incorrect manufacturing of the comb. The RMS error of the grooves in the comb was measured separately. One of the grooves in the comb was found to be $\sim$ 12μm from nominal the position.

After the position of the ferrules had been checked further glue was applied to the output slit blocks to pot the ferrules in place ready for polishing. The potting glue used was RS araldite two part epoxy.

7.3.5 IFU output slit.

The most major modification to SMIRFS is the complete redesign of the output slit unit to accommodate the 72 fibres and 12 microlens array substrates. The optical design, discussed in section 5.3, requires that the output slit be curved, with a radius of 214mm, to match the focal plane of the spherical SPU mirror. The optical axis of the fibres also has to be tilted by 3° because of the off axis operation of the SPU. Finally the axis of each of the 12 slit blocks needs to point at the pupil image position. The slit unit consists of a base plate which has been machined with a 3° tilt. The 12 slit blocks are then fixed to the base plate. The position of each slit block is required to be as accurate as possible to decrease the effect of optical aberrations and vignetting of the pupil image. To achieve high accuracy the slit blocks were located with dowel pins. A mechanical drawing of the complete output slit assembly can be seen in figure 7.3. The upper surface of the slit blocks (where the ferrules sit) is ground to define a level surface such that all the fibres are located in the same plane and pointing at the same angle. The spacing between each block is required to be accurate as this ultimately defines the spacing between the output microlenses. Errors in the positioning of the slit blocks could mean there is not enough room for microlens substrates to be attached and affects the number of elements that can be positioned along the slit. The clearance between the output slit blocks is only 0.3mm. A picture of the output slit block can be seen in figure 7.2 illustrating the small clearance.

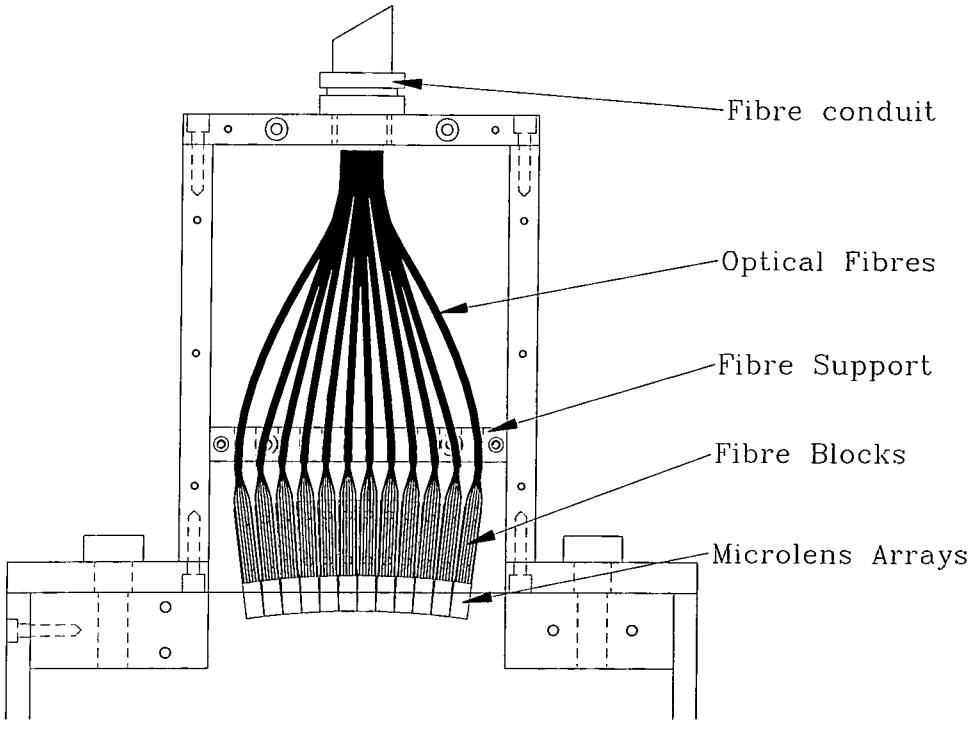

Figure 7.3: Mechanical assembly drawing of the SMIRFS-IFU output slit assembly. There are 12 output slit blocks each supporting 6 fibres arranged on a curved focal plane (radius=200mm). Note that the microlens arrays are individually orientated to point at the SPU pupil.

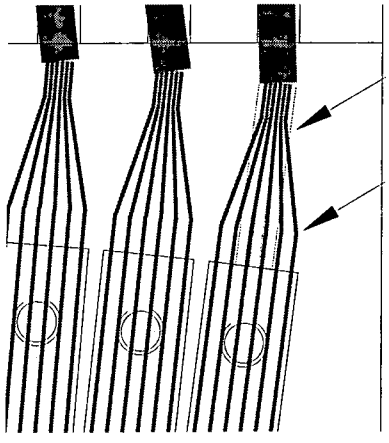

Figure 7.4: Enlarged view of the SMIRFS-IFU output slit from figure 7.3 showing the fibre routing from the fibre support to the output slit block. The outer fibres clearly have to be bent to reach the outer edge of the slit block, indicated with arrows, causing FRD.

A number of manufacturing difficulties were met with the IFU output slit blocks. The positioning of the slit blocks was not to the desired accuracy so the gap between blocks varied according to position on the slit. The blocks had to be moved to different locations until they gave the best approximation to the correct performance. Also the edges of the blocks were deburred during manufacturing producing a chamfered edge causing difficulties when gluing the ferrules to the blocks. A photograph of an assembled slit block can be seen in figure 7.2.

7.4 Choice of fibre.

The optical fibre used in the SMIRFS-IFU was low OH^- step index Silica fibre from Polymicro technologies[2]. The fibres are short, only 1.2m in length, so absorption in the fibre is negligible regardless of the fibre doping being used i.e. Ultra low OH^- could have been used equally well. Alternatively Ceramoptec fibre could have been used but Polymicro fibre was chosen in preference because of its superior FRD performance and scrambling properties. Scrambling is the ability of the optical fibre to produce a uniform output beam, without radial or azimuthal structure (Watson & Terry, 1995; Barden *et al.*, 1993). A full report of the scrambling and FRD properties of different types of fibre can be found in Haynes (1996). The scrambling performance is important for the SMIRFS-IFU due to the short lengths of fibre being used as scrambling is better with long fibres. Fibre with a Polyimide buffer was chosen because of Polyimide's superior structural properties and the ability to get Polyimide with a small buffer diameter. Acrylate and Silicone buffers are too thick to be accommodated within the ferrule. Polyimide is hard and does not deform during polishing causing the production of rounded fibre ends. Polyimide also has superior bonding performance than other buffer materials. The specification of the SMIRFS-IFU optical fibre is summarised in table 7.2

7.5 Adhesives

An important factor in the construction of the SMIRFS-IFU was the choice of appropriate adhesive to assemble the various components. A number of areas were identified that required

[2]More information about Polymicro optical fibres can be found at http://www.polymicro.com/

Core cladding ratio	1.1
Core diameter	$151 \pm 2\mu$m.
Cladding diameter	$166 \pm 2\mu$m.
Buffer diameter	$195 \pm 3\mu$m.
Numerical aperture	0.22 ± 0.02
Transmission range	380-2500nm
Core material	low OH^-
Polyimide concentricity	$\pm 1\mu$m.

Table 7.2: Specification of Polymicro FIP-150165195 optical fibre used in the SMIRFS-IFU

the use of specialised adhesives. These areas are listed below.

- Optically transparent adhesive to attach microlens array substrates to tube arrays.
- Adhesive to glue ferrules into tube array.
- Adhesive to fasten fibres into ferrules.
- Adhesive to fix fibres or ferrules to output slit blocks.

Adhesive types that were identified for each purpose are described below.

7.5.1 UV curing cement

The first requirement listed is to attach the fused Silica microlens substrates to the tube arrays. This adhesive has to be optically transparent at the operating wavelength of the SMIRFS-IFU. The refractive index of the adhesive has to be similar to that of fused Silica to minimise reflection losses. It is also an advantage that the glue is fast-curing so that once the microlens array is correctly aligned with the tube array it can be fixed in place immediately without having maintain alignment for long period during curing. It should also be possible to remove the adhesive, if necessary, with suitable solvents. This is so that excess adhesive can be removed from the edges of the slit blocks to prevent fouling with the adjacent blocks. It may also be necessary to remove the adhesive from the microlens substrate should bubbles appear.

It was decided to use UV-curing cement to bond the microlens substrates to the tube arrays as it satisfies all of the requirements listed. After a thorough search of the available adhesives

Viscosity at 25°C	300 cps
Refractive index of cured polymer	1.56
Linear shrinkage on curing	1.5%
Pre-cure time	10 s
Curing time	600s

Table 7.3: Properties of Norland UV curing adhesive NOA-61. The units of viscosity are listed in centipoise. The SI equivalent of 1000cps is 1Pas. For comparison water has a viscosity of 1 cps, Glycerin 1490 cps and light machine oil 100cps at 20°C.

Norland optical adhesive number NOA 61 was chosen. The properties[3] of this adhesive are listed in table 7.3

Yoder (1995) recommends NOA-61 for use with optical joints between glass and metal. The refractive index mismatch between NOA-61 and fused Silica is ~ 0.1 resulting in Fresnel losses of $\sim 0.13\%$ at each glue-glass boundary. These are considered acceptable losses considering the difficulty of obtaining glue with an exact index match to fused Silica. Other adhesives short listed were Ablestick LCR 000/1.46, Vitralit 7104 and 7105 or Summers UV-74. These were rejected either due to long delivery times or excessive cost.

UV cement tests

As the correct performance of this adhesive is crucial to the optical performance of the IFU a number of tests were carried out. The transmission properties of NOA-61 were measured in the same fashion as the microlens epoxy sample already described in section 6.3.4. Two samples of different thicknesses were prepared so that the absolute internal transmission of the difference in thickness between the two layers could be found. A sample was made by gluing four ferrules of known thickness to a microscope slide to make a container for the adhesive. Another microscope slide was then placed over the adhesive and the excess allowed to squeeze out. This produces a slab of adhesive of known thickness, defined by the ferrules, for testing. After all the excess glue had been removed the glue was cured by exposure to a UV light source. Excess glue is readily removed by washing with Ethanol and wiping with a tissue. A thin sample was made with gauge 30 ferrules, 0.3mm outside diameter, and a

[3]A full technical specification for this adhesive can be found at:
http://www.norlandprod.com/adhesives/noa61.html.

thick sample with gauge 21 ferrules, outside diameter 0.811mm. Each sample is identical except for a different thickness of adhesive such that reflection losses and absorption losses in the microscope slides are identical. These losses are calibrated out by measuring the transmission of the thick sample with respect to the thin sample producing a measurement of the internal transmission of the difference in thickness between the two samples.

Care was taken during the preparation of the samples to avoid formation of bubbles within the layer of adhesive, however, after the glue had been cured bubbles began to form in the thick sample. It was noted that the cured glue is not actually hard but remains soft and pliable, rather like stiff jelly. Glue could also be peeled off the glass substrate quite readily. The formation of bubbles was thought to be due to the soft glue peeling away from the glass substrate. The area of the bubbles then spread until it entirely covered the sample area. A difference in transmission was clearly visible, by eye, due to the extra reflection losses. The transmission of the adhesive was measured directly after preparation and was not affected by bubbles. After a period of days all of the samples were noted to have formed bubbles.

Figure 7.5 shows the transmission of the adhesive. The transmission curve shows absorption features that are similar to those seen in the microlens epoxy transmission curve i.e. the absorption band at $\sim 1.75\mu$m. The absorption feature at $\sim 1.4\mu$m is similar to the OH absorption feature in fused Silica so that the total losses near this feature might be quite severe. The noise level on the transmission curve is approximately 0.01%. For comparison the transmission of a microscope slide is also shown. It has a featureless spectrum so does not produce residual features in the adhesive spectrum. Absorption peaks occur in both the J and H-band windows but as the thickness of glue is small, less than the thickness of epoxy for the lenses, the absorption losses due to the adhesive are expected to be small. Figure 7.5 also shows the transmission of 0.1mm of adhesive as an estimate of what the glue losses might be. The actual thickness of glue in the SMIRFS-IFU is unknown but is unlikely to be more than 0.1mm. The absorption losses due to a 0.1mm thickness of adhesive are 0.7% in J and 2.3% in H, integrated over the entire band. The peak absorption in the bands will be greater than this average value leading to the possibility of the spectral signature of the adhesive imprinting itself on the astronomical spectra. However, no clear evidence of this effect, which is expected to be small, was seen in the measured spectra described in chapter 9. Absorption losses may become significant in the U, B, and K-bands. It is

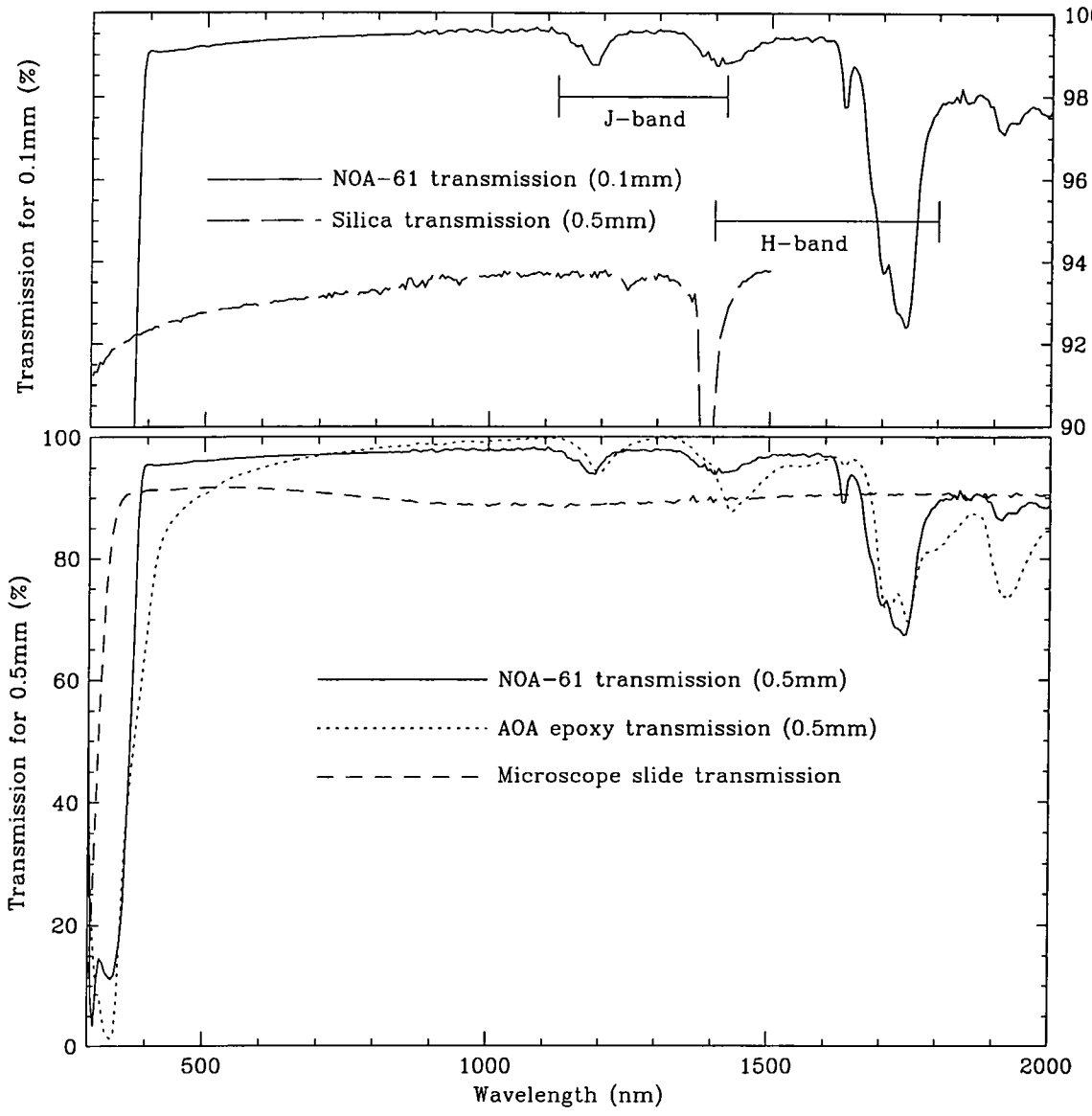

Figure 7.5: The bottom figure shows the internal transmission of 0.5 mm of NOA-61 UV curing adhesive. Also shown for comparison are the internal transmission of 0.5mm of microlens epoxy and the transmission of a microscope slide. The upper plot shows the internal transmission of 0.1mm of NOA-61, an estimate of the glue thickness in the SMIRFS-IFU, and the transmission of 6mm of fused Silica including reflection losses. The Silica transmission curve is adapted from figure A.4. The positions of the J and H-bands are marked.

very intriguing to note that the measured absorption features do not appear in transmission spectrum shown on the manufacturers data sheet, see appendix C figure C.1. This indicates that manufacturers data is not always to be relied upon!

7.5.2 Slow curing epoxy

At first it was thought that the IFU input tube array would need to be assembled by individually gluing each ferrule into place inside the tube holder, see section 7.3.3. As the assembly time of the entire input array is likely to be many hours this required an epoxy with a long cure time so that tubes could be adjusted before the epoxy begins to cure. Epoxies with cure times up to 1 week are available (Epotek 354). It was later discovered that the ferrules were adequately held in place by the force exerted by neighbouring tubes. An adhesive is still required however to pot the fibres and ferrules into place when assembly is complete and the requirement for the potting glue is also a long cure time. This allows the glue sufficient time to penetrate all the gaps in the tube array. Therefore an adhesive with good wicking properties is also required. Intertronics Epotek 301 was chosen for this application. It has a pot life of 1 day, a low viscosity of 260 cps[4] and therefore good wicking properties. The amount of linear shrinkage on curing is only 1.4% which is low and will keep the amount of stress induced in the fibres by the curing process to a minimum.

7.5.3 Gluing fibres into ferrules

Gluing optical fibres inside ferrules is now a standard technique (Rasilla *et al.*, 1993). The main requirement is that the adhesive should be low shrinkage upon curing. If the glue shrinks during curing this will exert mechanical stress on the optical fibre leading to increased FRD. The glue must also have adequate bond strength between the metal ferrule and the Polyimide fibre buffer to support the fibre during polishing. Araldite two part cyanoacrylate epoxy, Tra-Bond BA-F1135C, or EpoTek 353ND was used by Lewis (1993) due to the low shrinkage properties and low viscosity. The quoted linear shrinkage of Araldite is 2%. The clearance between the inside diameter of the tubes and the outside diameter of the fibre was measured to be $\sim 5\mu$m sufficient to allow adequate glue penetration.

[4]The units of viscosity are centipoise. For comparison water has a viscosity of 1 cps, Glycerin 1490 cps and light machine oil 100 cps at 20°C.

7.5.4 Gluing ferrules to slit blocks

This adhesive is required for the initial attachment of the ferrules to the output slit blocks. It was originally planned to attach the fibres directly to the slit blocks but this idea was abandoned due to the problems described in section 7.3.4. The adhesive has to have a reasonably long pot life to allow time for the ferrules and comb to be positioned correctly. UV curing epoxy was used for this purpose, it has a long pot life and can then be cured quickly when the ferrules are in position. Vitralit 4280 anaerobic threadlock was chosen for this application. It is also readily removable if mistakes are made.

7.6 Fibre polishing.

Polishing of the fibre bundles was carried out by Dr. Roger Haynes. A full description of polishing techniques can be found in Haynes (1995) and Lewis (1993). A short description of the polishing techniques used is given here for completeness.

The polishing procedure was as follows:

1. Initial preparation (roughing off) of slit block surfaces using fine grade wet and dry (1000 grit) emery paper to remove large blocks of material such as protruding fibre ends, residual patches of glue and uneven metal surfaces such that all surfaces are flush.

2. Further roughing off with 5 micron paper to improve surface quality in preparation for wet polishing.

3. Initial lapping with 3 micron Aluminium oxide powder as a water suspension on a cast Iron lapping plate.

4. Final wet polish with 0.03 micron Aluminium oxide colloidal suspension polishing solution and Polyurethane polishing plate.

Lapping and polishing were carried out on a standard Logitech polishing machine. Two special polishing mounts were constructed to polish the fibre bundles of the SMIRFS-IFU. The first mount locates the input fibre bundle in place inside the polishing jig. A second

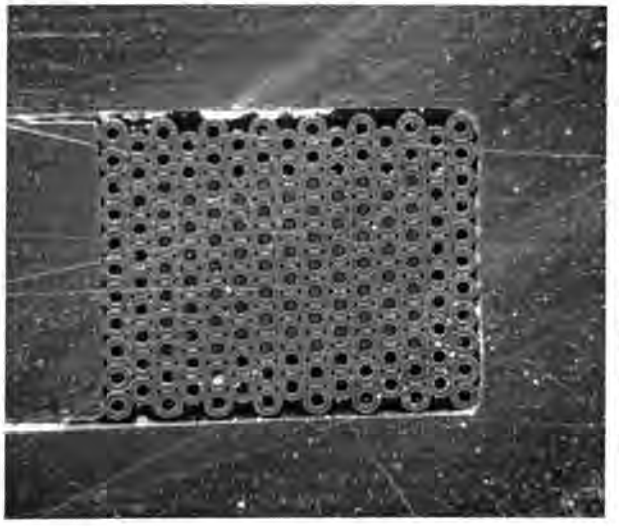

Figure 7.6: Photograph of the polished input fibre bundle. Although there are some scratches visible on the steel tube holder very few of the scratches cross the fibre array. After polishing the fibre bundle has a mirror like appearance.

mount was constructed to allow all twelve output slit blocks to be mounted simultaneously inside the polishing jig so that they could be polished at the same time.

The final surface finish of the input fibre bundle was of very high quality. Figure 7.7 shows an interferogram of the input array. The interferogram shows circular fringes due to the formation of a slight radius of curvature on the input bundle surface during polishing. 'Rounding off', as it is known, is often caused during polishing due to tilting of the polishing jig as the polishing plate rotates. The fringes show a sag height across the input array of $\sim 1\mu$m. The radius of curvature is too small to affect the performance of the IFU. The changing sag height across the array will become filled by the adhesive leading to slight variation in glue thickness across the array. In an extreme case a radius of curvature on the input array would lead to the fibre faces being non-telecentric (they are polished at an angle) thus introducing a small increase in the input focal ratio. Figure 7.6 shows a photograph of the finished input fibre bundle surface. A number of scratches can be seen. It is thought most of the scratches were caused after polishing by handling of the input bundle and not the polishing procedure. Note that the number of scratches present on the fibres is minimal. A picture of a polished output slit block can be seen in figure 7.2. Again some scratches can be seen on the surface of the metal slit block.

Polishing of the output slit blocks was less successful than the input fibre bundle. A number of ferrules broke loose during the polishing process and consequently these fibres had a poor surface finish. There are a number of contributing factors to the ferrules breaking loose. Ferrules at the edge of slit blocks were more likely to be loosened as they are held in place

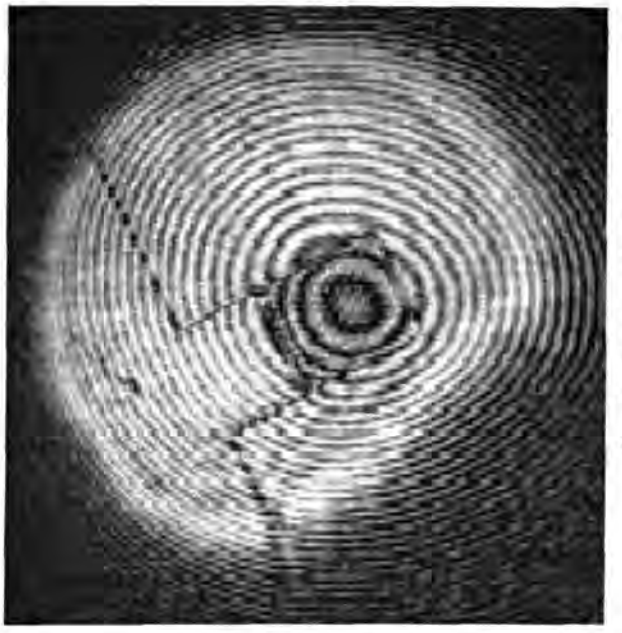

Figure 7.7: Interferogram of SMIRFS-IFU input fibre bundle after polishing. The fringes are centred on the tube array which can be seen as a rectangle in the centre of the interferogram.

with much less glue due to the proximity of the ferrules to the edge of the slit blocks. Ferrules were also thought to be knocked out of place by the radial grooves in the polishing plate. In extreme cases the polishing process could also loosen the fibre from inside the ferrule. It was noted from the fibre flat-field, section 8.3, that the low throughput fibres were the ones that had become unglued during the polishing process.

Another problem was that the potting glue, RS araldite, was removed by polishing at a faster rate than the harder UV cement. This meant that in some cases the ferrules were not held by araldite and were free to move under the cyclic stresses of the polishing process. Where ferrules had lifted from the slit block grit could build up underneath the ferrule and force it further away from the slit block. In some cases it was possible to reglue the displaced ferrule to the slit block for better positioning accuracy but nothing could be done about the surface finish of the fibre. There is still some debate on the issue of whether the fibre finish is important if the fibre is to be bonded to a glass substrate. If index matching glue is used to bond the fibre to the glass substrate then it is thought that the glue will fill the scratches in the fibre surface and no reflection losses or scattering will occur due to scratches. However it is unknown whether the glue will penetrate the smallest scratches. Initial fibre preparation is still necessary to remove large scale defects. Clearly this is an important area where more research is needed. If the amount of polishing can be minimised this may result in a substantial time saving and reduce the risk of fibre damage occuring during polishing.

7.7 SMIRFS microlenses

7.7.1 Microlens array substrates

The glass substrates for the SMIRFS microlens arrays were specified after AOA had produced the test lenses. The SMIRFS-IFU input test lens had a focal length, in air, of 5.35mm and the output lens 5.95mm. The test lenses specify the focal length that AOA have managed to achieve in the manufacturing process (there is a certain amount of uncertainty in the manufacturing process). These measurements were made by AOA at a wavelength of 632.8nm. The correct thickness of substrate can then be calculated using the chromatic focal shift data described in section 6.3.3. The substrate thickness has to match the microlens focal length in the H-band at 1.65μm. The substrates were manufactured by Achro-Optics, St Leonards-on-Sea, from fused Silica grade 'Spectrosil-B'.

The substrates were checked before being sent to AOA for manufacturing errors. The dimensions, surface quality, and wedge angle[5] of the substrates were checked. Both the input and output microlens substrates were found to have been made to specification. The largest wedge angle measured was 0.25° on an output lens substrate leading to a slight defocus across array of 22μm. The substrates were then forwarded to AOA for the microlenses to be applied to the surface of the substrates.

7.7.2 SMIRFS-IFU output block quality check

A total of fourteen output microlens arrays were returned by AOA whereas only twelve are needed in the instrument. A microphotograph of a SMIRFS-IFU output microlens array can be seen in figure 7.8 and a diagram in figure 7.9. It can be seen from figures 7.8 and 7.9 that there are a total of 18 microlenses present in the output microlens array. Each microlens is given a number in figure 7.9 for future reference. The 'active' microlenses are numbers 7-12 inclusive, i.e. the central six lenses. The active lenses are square, as required by the optical design. To properly define the shape of the microlens it has be surrounded by neighbouring lenses. This is a requirement of the manufacturing technique used by Adaptive Optics Associates. Therefore each active microlens has two 'spare' microlenses on either

[5]The angle between the front and back surfaces of the substrate.

side, i.e. the shape of lens 8 is defined by being surrouded by lenses: 2, 7, 9 and 14. The spare lenses have a different shape to the active lenses.

The difficulty in manufacturing the output microlens arrays comes from the proximity (40μm) of the lenses to the substrate edge. This requires very accurate positioning of the microlens array with respect to the substrate and it is easy to damage the edge lenses. The output arrays were tested in order to find two for rejection. A number of faults were found with all the output arrays. The width of the lenses in the spectral direction, indicated in figure 7.9 as S_1, was found to be undersized by 3%. Lens 12 was also consistently undersized by 4%. Undersized lenses will lead to a throughput loss at the output slit due to increased vignetting. The gap between the edge lenses and the edge of the substrate, shown as L and R in figure 7.9, was found to vary between arrays. The average measured value is L=77μm and R=54μm and the specified value was 45μm This implies an increase in the total dead space from 90μm to 130μm. In extreme cases the edge lens (Lens 7 or 12) was actually positioned at the edge of the substrate leading to the loss of part of the lens surface. It was also noticed that lenses 11 and 12 were offset in their spectral position from lenses 7-10. The offset was approximately 10μm in the direction of lenses 17 and 18. Again this positioning error will lead to a small reduction in the overall throughput as the projected pupil will appear in the wrong position. A summary table of the output array test results can found in appendix C.

As well as positioning errors the lenses also had various surface defects. A few lenses were found to have bubbles present in the epoxy. Some lenses displayed a 'fuzzy' appearance due to the presence of large areas of small scale surface defects. A few cracks were also seen in the lens surfaces. Of the two arrays rejected one had severe damage to 25% of the lens surface and the other had part of lens 12 missing due to it being positioned over the edge of the substrate. The problems at the substrate edges were partly due to the lack of a bevelled edge. This meant edge breakages could occur more easily.

It is clear from figure 7.8 that their is a large amount of dust and debris on the lens surface. The epoxy microlenses were found to be particularly prone to attract dust. This is thought to be due to the slight 'stickiness' of epoxy that remains[6], even after curing. The epoxy may

[6]This property was tested. A layer of UV epoxy was applied to a microscope slide and cured. Even after full curing the epoxy was found to still feel tacky and soft, indeed a finger print could be formed with pressure.

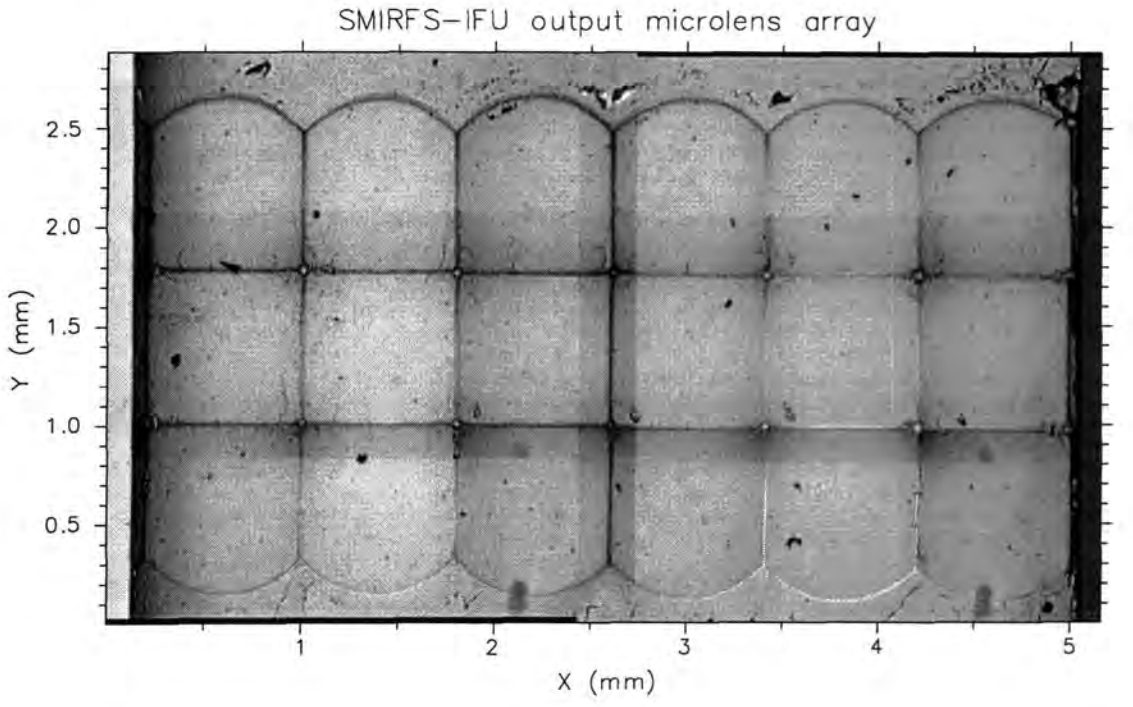

Figure 7.8: Mosaic of four CCD images of the SMIRFS-IFU output microlens array. This image should be compared with the diagram in figure 7.9. The microlens surface has 'orange peel' at the lens edges and corners. There is also a small loss in fill factor due to the defect at the corner of each lens. The marks seen on the surface are dust, scratches etc. Note the proximity of the lens array to the edge of the substrate.

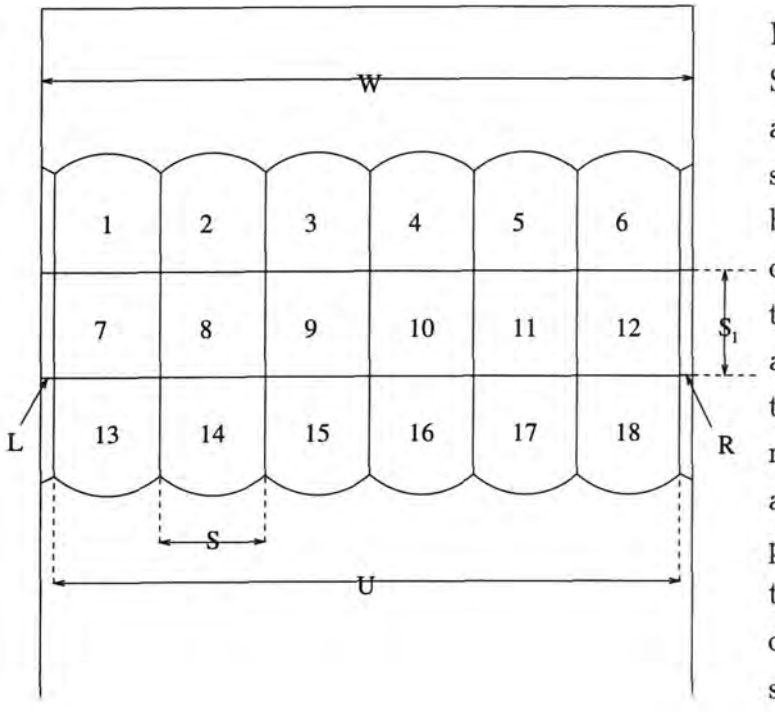

Figure 7.9: Schematic of SMIRFS-IFU output microlens array. W is the width of the substrate, U is the width occupied by the microlenses, S is the width of the individual microlens, S_1 is the height of the microlens. L and R are the distances between the substrate edge and the left or right microlens edge. The lenses are numbered for identification purposes with lenses 7-12 forming the active array. A picture of the output microlens array can be seen in figure 7.8.

also be prone to build up of static charge which would attract dust particles. It is dangerous to attempt to remove the dust due to the fragility of the lens surface. It was found that some dust could be removed by blowing with a compressed air source. This 'attractiveness' to dust, and the difficulty in cleaning, may be a problem with epoxy lenses. Marks at the edges of the lens array are due to defects in the epoxy. Note also the small gaps between lenses and the dead space in the corners of the lenses. The defects at the lens edges and the dead space highlights the difficulty in producing lens arrays with high fill factor. The stripes across the image are due to the overlap region of the four separate image used in producing the mosaic. Contamination on the lens surfaces may lead to small variations in the throughput of the lenses.

7.7.3 Fibre bundle FRD test

Before the microlenses were attached to the fibre bundle some simple focal ratio degradation tests were carried out to test the performance of the fibre bundle. The fibre bundle input end was illuminated with a collimated, on axis, laser beam as shown in figure 7.10. The resulting FRD cone emerging from the output fibre end was viewed on a target screen situated two metres from the fibres.

Initial measurements of the fibre output focal ratio showed that an FRD cone of approximately F/8 is produced with a collimated input beam. This FRD performance was worse than that expected for a collimated input beam. The fibre conduit was slightly adjusted by hand during the FRD test and found to alter the FRD characteristics when moved. The fibre conduit is a section of corrugated steel hosing used to protect the fibres. The corrugations had been stretched during manufacture and the conduit had since shrunk causing the conduit to become shorter than the fibres. This was causing mechanical stress to be induced in the fibres. Simply unscrewing the conduit, to relieve the mechanical stress, improved the FRD performance. The FRD was reduced, to an FRD cone of approximately F/10, simply by inserting a spacer between the end of the conduit and the input bundle. The spacer corrected for shrinkage of the conduit and relieves the mechanical stress.

During illumination of the input fibre bundle it became clear that the FRD produced by fibres in the centre of the input array was visually worse than for fibres at the edges. This was found by illuminating individual fibres near the centre and then comparing with fibres

at the edge. A possible cause for this may be the confinement of the fibres in the centre of the bundle by the surrounding fibres. A large number of fibres are packed into a small area at the entrance to the tube array and it may not be possible for fibres to take up a stress free position, particularly in the centre. However, a quantitative assessment of the magnitude of this effect was not performed. It is clear though that there are various mechanisms that contribute to FRD that require further investigation if the causes of FRD are to be fully understood and reduced.

Finally the effects of the output fibre bundle on FRD were investigated. The input bundle was illuminated with a stripe as before to simultaneously illuminate an entire output slit block. The output fibres were then masked so that only one was observed. The mask was then moved to allow the other five fibres to be observed. The two fibres positioned at the edges of the output blocks displayed more FRD than the central four fibres. The cause of this is thought to be due to the smaller bend radius the edge fibres have to travel through from their attachment point in the output slit unit to the position where they enter the ferrules. This is illustrated in figure 7.4. Simply moving the edge fibre to a larger bend radius relaxed the FRD observed. The point at which the fibre enters the ferrule is a well known (Rasilla *et al.*, 1993) high stress area and the fibre entering a ferrule at a slight angle will increase the stress induced FRD. This problem could not be fixed before telescope commissioning but was listed as one of the assembly areas that could be improved at a later date by a slight modification to the output slit unit.

The final FRD cone measured, after modifications, was approximately F/10. The FRD tests were only done qualitatively, by visual inspection of the FRD cone projected onto a test target. It is clear for future IFU construction, in order to minimise FRD caused by the construction process, more quantitative results will be needed. A full investigation could not be done with the SMIRFS-IFU due to time constraints.

The major sources of FRD were thought to be the routing of the fibre at the output slit block, stress induced by the conduit, and stress the centre of the fibre bundle. These problems can be improved in future designs of IFU. A strain relief loop along the fibre length will prevent problems with the conduit. More investigation of the effect of the input tube array on FRD is also needed. The properties of the adhesives used in the assembly process may also need checking, to ensure low shrinkage properties, prior to assembly. Fibre routing improvements

will decrease the stress of fibres entering ferrules. Stress can be reduced inside the ferrule by use of strain relief tubing. The fibre is inserted into a Polyimide tube before insertion into the ferrule. The Polyimide tubing acts as a buffer between the fibre and the ferrule. This technique is commonly used in multi-object fibre assembly. FRD is reduced but at the expense of additional fibre positioning errors within the tube. There is then a trade off between losses due to fibre positioning errors and FRD losses. Stress may also be reduced by the use of fibres with a thicker buffer, although the thickness of the buffer is somewhat limited by the manufacturing process. Large diameter fibre buffers may also be non-concentric with the fibre core.

The large number of possible causes of FRD described in this section clearly indicates that more research is needed to fully understand the causes of FRD and how to avoid them. However, some important lessons have been learned by this preliminary study of FRD that will benefit future IFU projects. As FRD is a major contributing factor to throughput losses in fibre instruments it is crucial that it is fully understood.

7.7.4 Alignment of output microlens array

The output microlens arrays were fitted to the output slit blocks using a special alignment jig constructed in the optics laboratory. The input fibre bundle was illuminated using a collimated laser beam which had been expanded using cylindrical lenses to produce a stripe, as shown schematically in figure 7.10. All six fibres corresponding to each output slit block can then be uniformly illuminated at the same time. The input fibre bundle was mounted on an X-Y stage so that the bundle could be moved to illuminate the required fibres. The final cylindrical lens in the beam expander was fixed to a tip-tilt stage for alignment purposes.

Each output microlens array must be correctly positioned in spatial position (along the slit), spectral position (across the slit) and rotation. Spatial or spectral misalignment will cause the pupil image to appear in the wrong position and will lead to vignetting inside CGS4. Rotation of the microlens array with respect to the six fibres will also lead to pupil misalignment and variable vignetting. The whole alignment jig is capable of be rotated about the centre of curvature of the output slit. During alignment the optical axis of the output microlens is vertical. This is necessary so that the block which is being positioned is

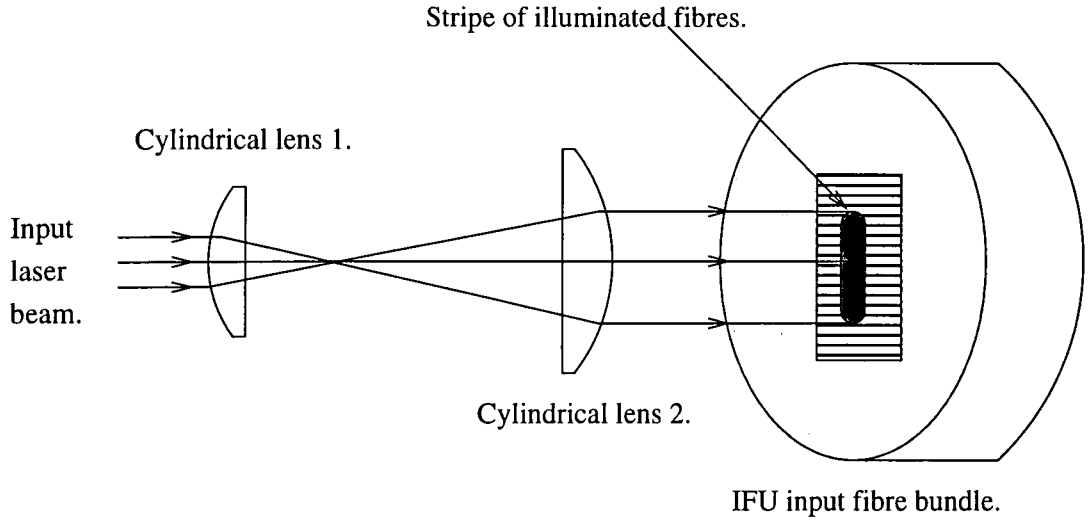

Figure 7.10: Diagram showing the method of illuminating the input fibre bundle for testing purposes and alignment of the output microlens arrays. The two cylindrical lenses act as a beam expander, in one dimension only, to produce a collimated stripe with which to illuminate a row of fibres.

facing directly upwards otherwise the block would keep moving to one side due to gravity. The output slit block is tilted on the alignment jig to remove the 3° tilt required by the SPU.

The pupil image occurs at $\sim$ 200mm from the output at 632.8nm. A circular aperture mask, the same diameter as the pupil image, was then placed at the position of the pupil image. The location of the pupil image with respect to the output microlens array can be seen in the optical diagram shown previously in figure 5.1. This allows the edges of the pupil image to be viewed whilst the centre of the pupil image passes through the mask and onto a target screen located on the laboratory ceiling. The distance from the microlens to the target was $\sim$ 2m. The target is also carefully positioned directly above the microlens being aligned to define a common optical axis for all microlenses. Correct alignment is achieved when the six pupil images coincide at the pupil mask with the minimum of blurring around the edges. The correct spectral and spatial alignment can also be checked as the projected light has to be centred on the target on the roof. The ceiling target shows a line of six pupil images. The rotation of the lens array is correct when the six pupil images are parallel to the spatial direction.

The microlens array substrate is first put in place without any glue present to check for fouling with the adjacent microlens substrates. The substrate and output slit block surfaces

are then cleaned using ethanol and an air blower to remove dust and grease. Then a small amount of UV curing adhesive, NOA-61, is applied to the surface of the slit block with a hypodermic syringe. Care must be taken to ensure there are no bubbles formed when the glue is applied is these will causes reflection losses and weaken the glue bond. Even tiny bubbles will spread out dramatically, under the action of surface tension, when the substrate is applied. The substrate is then placed on the slit block, again checking for bubbles. The surface tension between the substrate and the slit block is sufficient to secure the glass block in place whilst the alignment is done. The substrate is moved into position with feeler gauges and cotton buds. The viscosity of the glue provides sufficient lateral force that the substrate can be moved accurately by nudging it with the cotton bud. The alignment is done in a darkened environment so that UV light from the tungsten lights has minimal effect on the UV curing cement. Once the substrate is in the correct position the glue is pre-cured by exposure to the UV light source for about 1 minute. A final check is then made on the alignment and the glue is finally cured for a further 5 minutes.

An estimate of the alignment accuracy can be made from the size of the blurring at the edges of the pupil image seen on the target placed at the centre of curvature of the output slit, as discussed in the following section. Measurements of the final accuracy of output block position, made during telescope commissioning, are described in section 8.5.3.

7.7.5 Alignment of input microlens array

The input microlens array was attached to the input fibre bundle after the output microlens arrays had been fixed onto the output slit. The output slit was illuminated with a diverging $F_y/1$ beam (F_y denotes the focal ratio of a cylindrical lens). The centre of divergence of the illuminating beam was placed at the centre of curvature of the output slit as shown in figure 7.11. Cylindrical lenses were used to produce beam divergence in one dimension only. The $F_y/1$ beam overfills the output slit, which subtends $F_y/3.3$ at the centre of curvature, so that the gaussian intensity profile of the laser beam was approximately uniform over the length of the slit. The laser beam was aligned with the output slit by adjustment of the rod lens which is mounted on a tip-tilt stage. The output slit assembly was also tilted by 3° so that the fibre axes are perpendicular to the input laser beam. This is necessary as the slit blocks are angled at 3° in order to point correctly at the spherical mirror inside the SPU, as

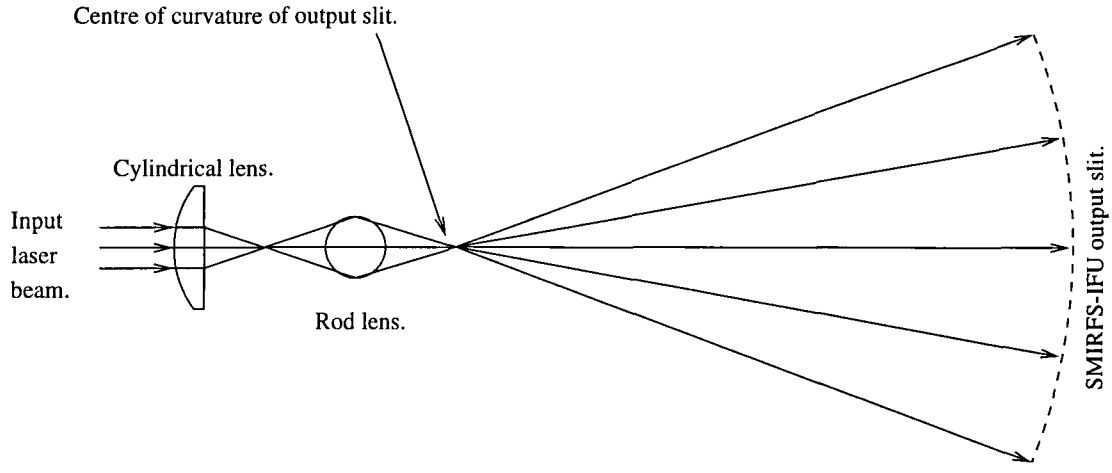

Figure 7.11: Illumination of the SMIRFS-IFU output slit for testing purposes and alignment of the input microlens array. The input beam is made to diverge in one dimension by use of a cylindrical and a rod lens. The diverging beam is centred at the centre of curvature of the output slit such that the beam is normal to the fibres.

described in section 5.2. The $F_y/1$ beam illuminates all 72 output lenses simultaneously with approximately uniform illumination. This reduces any bias which might affect positioning of the input lens array. Such a bias might result if the output lenses illuminated were aligned incorrectly or bad fibres were illuminated. The input alignment is simultaneously averaged over all lenses on the array reducing bias effects. The pupil image produced by the input microlens array was viewed on a target screen located on the ceiling of the optics laboratory. The distance from the array to the target was two metres. Ideally the input array alignment target would be positioned at the correct telescope exit pupil position, as was done for the alignment of the original SMIRFS instrument (Haynes, 1995). The distance required is that from the UKIRT secondary mirror to the focal plane, $\sim$ 11m, which is too long to be accommodated in the optical laboratory, 2m being the maximum distance available.

The optical axis of the input array was defined using a plumb-bob as shown in figure 7.12. The plumb line hangs from the centre of the alignment target fixed to the ceiling of the optics laboratory. The fibre input bundle was then positioned directly underneath the plumb-bob. The input microlens array is then correctly aligned in X-Y when the centre of the pupil image coincides with the centre of the target. This assumes that the optical axis of the input fibre bundle is parallel with the plumb line.

Once the fibre bundle was correctly fixed in position under the plumb-bob it was cleaned

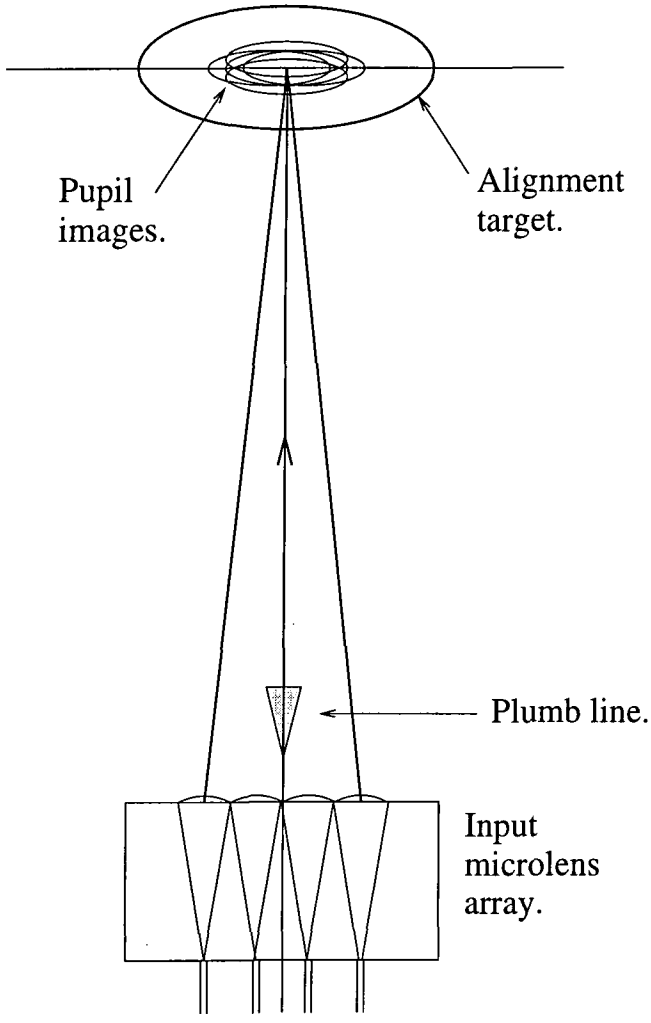

Figure 7.12: Schematic of SMIRFS-IFU input microlens alignment jig. The optical axis of the input fibre bundle is defined using the plumb-bob. The back projected pupil image is then observed on the alignment target. 72 overlapping pupil images are formed producing a blurred edge to the pupil image. A minimum blurring is observed when the microlens array rotation is aligned correctly.

with Ethanol and a layer of UV curing cement applied to the surface of the tube array. As quite a large area of glue is required extra care has to be taken to avoid the production bubbles. The cleaned microlens substrate is then placed on the glue and allowed to settle for a few minutes before alignment can begin. This allows excess glue time to flow from under the substrate. The alignment is again done using a cotton bud to shift and rotate the substrate to align the pupil image position with the target. The rotation is set correctly when the smallest blur circle is observed. When alignment is achieved the substrate is fixed in place by exposing the UV cement to the UV light source.

There are three degrees of freedom in positioning the input lens array: linear movement in X (along the long axis of the lens array), Y (the short axis of the array), and rotation of the microlens array with respect to the tube array. A small X-Y misalignment of the lens array with respect to the tube array does not cause a problem as it causes the projected pupil image to occur slightly off-axis. This can be easily corrected by pointing adjustment of the IFU at the telescope. This is done by adjustment of the telescope pickoff mirror until the telescope exit pupil is correctly imaged onto the optical fibre. The rotation is much more critical as the effects of rotation cannot be removed at the telescope. The pupil image produced by the input array was approximately 56mm in diameter at the distance of the alignment target. A photograph of the pupil image can be seen in figure 7.14. A rotation of the input lens array causes a blurring at the edge of the pupil image due to the large number of overlapping but slightly offset images, as shown in figure 7.12. A 0.3° misalignment produces a blurring of about 5mm. Given that a diffuse edge is seen anyway because of microlens aberrations and diffraction an additional 5mm blurring at the edges is difficult to observe. This limits the accuracy with which the rotation of the lens array can be aligned. This problem also occurs, but to a lesser extent, with the output arrays. A rotation of 0.3° centred on the corner lens of the input array produces a misalignment at the diagonally opposite corner of 23μm with a corresponding drop in throughput of 20%. The drop in throughput is calculated from the area of the pupil image that is vignetted by the fibre core.

The positioning error in X-Y was estimated to be 0.5cm at the target (or 18μm at the microlens substrate) corresponding to an angular error of $\sim$ 9 arcminutes. This error is readily corrected at the telescope by applying an equal, but opposite, tilt of the input array with respect to the telescope optical axis to bring the pupil image back to the correct position.

A few hours, after the substrate had been fixed in place streaks began to appear in the glue which eventually spread to form bubbles. This is similar behaviour to that seen in the glue test samples described in section 7.5.1. The bubbles appear after the glue has been cured and then spread slowly with time. By the time the SMIRFS-IFU was unpacked at the telescope the bubbles had spread even further but did not obscure the fibres. The cause of these bubbles is not known. They could be due to outgassing by the adhesive, vacuum bubbles caused by the adhesive becoming unstuck from the bonded surfaces, or contamination on the surfaces. It is also possible that the adhesive layer was not fully cured and the bond between the glass and the adhesive remained liquid. The prevention of bubbles is clearly an area in which further laboratory investigation is required.

7.7.6 Baffling and FRD

The numerical aperture of the fibres used in the SMIRFS-IFU is 0.22 i.e. the fastest focal ratio they can accept is F/2.3. Each fibre in the IFU is aligned with the optical axis of one microlens. However the acceptance cone of the fibres is such that the fibres will also transmit off-axis illumination from the microlenses surrounding the central microlens. This is illustrated schematically in figure 7.13. The central microlens reimages the telescope exit pupil (the secondary mirror) onto the fibre core. The surrounding lenses will image the background sky or the telescope dome onto the fibre. Optical fibres do preserve angular information to some extent but some of the background light will be transmitted to the spectrograph because of radial scrambling. To prevent background light from being imaged onto the input fibre bundle, and eventually contaminating the measured spectrum, a baffle was constructed. The baffle consists of a cylindrical tube which is placed in front of the input microlens array. The baffle then restricts the angular field of view of the microlens array to the region around the telescope secondary (the pupil) and prevents background light from entering the system. A baffle is not required at the output lens array as baffling is provided within the CGS4 spectrograph by the cold stop.

If the output slit is illuminated, as described in section 7.7.5, then the back projected image of the fibre produced by the input microlens can be viewed on a screen. A photograph of this image is shown in figure 7.14. The photograph shows the central pupil produced by the central microlens, which corresponds to the telescope secondary, and six surrounding pupils

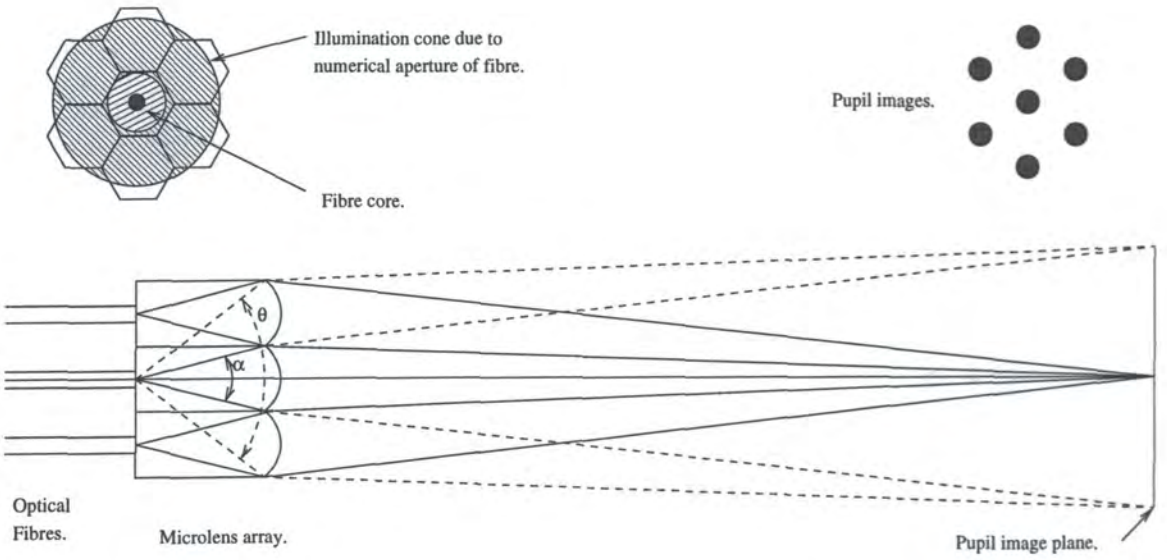

Figure 7.13: Diagram of pupil projection by the SMIRFS-IFU input array. The acceptance cone of the fibre, θ, views light from the lenses, and pupils, surrounding the central lens. Unless a baffle is installed this will increase the background light by a large factor. A photograph of the pupil image is shown in figure 7.14. The acceptance cone needs to be limited to α by the baffle.

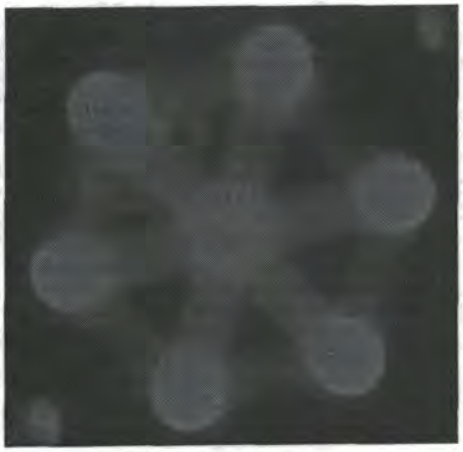

Figure 7.14: Photograph of the back projected pupil image formed by the input microlens array. The central pupil is that which corresponds to the telescope secondary. The other pupils project onto the sky. If the IFU were unbaffled then the fibres would receive background sky contamination from these areas on the sky. Note the diffraction spikes and the blurring of the pupil image edge.

due to the surrounding lenses. By back illuminating the output microlenses the focal ratio entering the optical fibres is approximately F/7.5. This is much faster than the focal ratio of the input microlenses which are F/13. Therefore a significant amount of light is seen in the pupil images surrounding the central image. This is simply due to the fast focal ratio. The outside six pupil images should each contain approximately one third of the energy contained within the central pupil image. A quantitative analysis of the projected pupil images was not performed. It should be possible to quantify the effects of FRD losses in the fibre from the ratio of the flux within the various pupil images produced at both the input and the output. The diffraction pattern, produced by the hexagonal lenses, can also be seen in figure 7.14 as the low intensity stripe between the pupil images.

From the back projected pupil image much can be learned about FRD losses within the fibre bundle. The throughput of the fibre bundle can be estimated from the ratio of the amount of light within the central pupil image to the integrated light over all pupil images. A full quantitative analysis was not done, however, due to time constraints. Providing a baffle for the SMIRFS-IFU was straightforward as the instrument only works in the J and H-bands. Providing a baffle for a K-band IFU would be much more difficult due to thermal background issues i.e. a cold stop might be required in the fore optics.

7.8 Summary & Conclusions

The construction of the SMIRFS-IFU provided valuable lessons in the techniques of producing a lenslet-fibre IFU system. This will help improve the performance of future IFUs through improved manufacturing techniques.

The construction of the input tube array was a success although some more work needs to be done to investigate the minimum clearance between the fibre buffer and the ferrule. This will decrease further the error budget for fibre positioning. Errors in fibre positioning contribute to throughput losses so it is important to continue to further improve positioning techniques in order to reduce throughput losses. Some problems were encountered with the output slit blocks, such as ferrules becoming loose during polishing, mainly due to unsuitable choice of adhesives and the close proximity of the ferrule to the edge of the slit block. These problems can be overcome in future with a different design of slit block. The optical cement used to fix

the microlens array to the tube array was also found to have problems due to the formation of bubbles. Clearly more investigation of adhesive technologies and techniques is needed if these problems are to be overcome in future IFU projects.

Polishing of the tube arrays was successful but time consuming. Savings may be possible if it can be shown that the fibre finish is less important because the fibres are optically contacted to substrates. An assortment of testing and alignment equipment was developed in the optical laboratory to attach the microlens arrays to the tube arrays. The microlenses were attached successfully except for the formation of bubbles in the optical adhesive. The accuracy with which the microlenses can be aligned was also found to be limited somewhat by the aberrations of the microlenses blurring the projected pupil image used for alignment.

The performance of the completed bundle was qualitatively assessed in the laboratory and found to be good. However, the FRD performance of the fibres was found to be poorer than expected. Due to lack of time throughput losses caused by FRD were not measured. The following areas were identified as contributing to the fibre FRD: fibre routing at the output slit, mechanical stress caused by the conduit and stress within the input tube array. With care in the mechanical design of future IFUs these problems can be reduced. Fibre FRD is a major loss mechanism in IFU fibre bundles and will need quantitative analysis if it is to be properly understood and kept to a minimum. FRD is noted as an important area which requires further investigation if its effect is to be minimised in future designs of IFU.

Chapter 8

SMIRFS-IFU commissioning

Abstract

This chapter describes the detailed tests that were performed on the SMIRFS-IFU during commissioning on the United Kingdom InfraRed Telescope. The instrument was commissioned during three nights in June 1997. Commissioning was a success and the instrument performed correctly. This chapter describes the installation of the instrument on the telescope, the alignment process, and the diagnostic tests which were carried out. The performance of the instrument is described in detail and suggestions made for improvements for further use and future IFU design. Observations were made of a spectrophotometric standard star to characterize the throughput of the instrument. The total system efficiency of the SMIRFS-IFU was found to be 2.8% in the J-band and 2.6% in the H-band. The measured efficiency of the SMIRFS-IFU is then compared with the theoretical prediction to identify any areas of unexpected throughput loss. Focal ratio degradation is identified as the major loss mechanism.

8.1 Introduction

This chapter describes the installation of the SMIRFS-IFU at the United Kingdom InfraRed Telescope (UKIRT) and the subsequent diagnostic tests which were carried out including throughput measurement. The SMIRFS-IFU was commissioned in June 1997 during one day and three nights of telescope time. Access to the telescope was needed during the day to allow engineers to assist with fitting the SMIRFS-IFU to the telescope. An extensive series of on telescope tests were then carried out to completely characterize the performance of the instrument. As the SMIRFS-IFU is a prototype, manufactured using developing technology, it is very important to accurately know the areas of performance which are non-optimal and can be improved in future designs of IFU.

Various calibration tests were performed both on the SMIRFS-IFU and CGS4 to distinguish between effects due to the SMIRFS-IFU and effects due to CGS4 alone. In this way it was found that various effects which needed calibration, such as instrument flexure, could be attributed to either the IFU or CGS4 alone. The fibre to fibre throughput variation was measured in detail to look for manufacturing defects which influence the fibre flat-field. It was also very important to accurately measure the optical aberrations of the IFU, and CGS4, as it is the final detected point spread function that limits the accuracy with which the integral field data cube can be constructed.

Perhaps the most important parameter that characterizes the performance of an instrument is the throughput. Unfortunately, due to time constraints, the throughput of the SMIRFS-IFU was not measured in the laboratory during the construction phase (chapter 7). However, the important question is: what is the throughput of the instrument in use on the telescope? The instrument throughput on the telescope may be different than that measured under different test conditions in the laboratory. After the instrument had been successfully installed on the telescope it was therefore decided to carry out a series of observations of spectrophotometric stars in order to characterize the throughput of the instrument. Measurement of the SMIRFS-IFU efficiency is described in section 8.6. It is important to know the throughput of the instrument for comparison with the predicted performance. This comparison serves to highlight any problems, either on the telescope, or during the construction process, that contribute to cause throughput loss. Only by clearly understanding the throughput loss mechanisms which occur both on the telescope, and due to non-optimal construction methods, can the appropriate corrective measures be applied to the future designs of IFU.

It should be noted at this early stage, however, that the atmospheric conditions during the observing/commissioning run with the SMIRFS-IFU were extremely variable. Therefore the measurements of SMIRFS-IFU throughput presented in this chapter may include some errors due to atmospheric changes which may have occurred during the observations.

8.2 Set up and alignment.

Initial set up and alignment of the slit projection unit (SPU) was done in the optics laboratory at the Joint Astronomy Centre at sea level before the instrument was transported to the

telescope. A collimated laser beam was used to illuminate the IFU input array, as described in section 7.7.4 and figure 7.10, thus projecting an image from the output slit. An alignment target was then fixed in place behind the SPU in a position corresponding to the CGS4 input slit. The SPU mirrors were then adjusted to reimage the IFU output slit to the correct place on the target. The bench alignment procedure is the same as for the SMIRFS multi-fibre system as described in detail in (Haynes, 1995). This setup procedure places the mirrors in approximately the correct start positions ready for final adjustments to be done at the telescope.

The instrument was installed on the telescope during daylight on 19 June. Telescope engineers were available to remove the CGS4 calibration unit and assist with interfacing the SMIRFS-IFU to UKIRT. First the field plate unit (FPU) is mounted to the west port of the telescope instrument support unit. The slit projection unit slots into the area previously occupied by the CGS4 calibration unit. The FPU and the SPU are common to both the SMIRFS-IFU system and the SMIRFS multi-fibre system. A full description of how these components fit to the telescope can be found in Haynes (1996). The IFU input bundle and baffle were then fixed in place on the FPU, using the new IFU field plate (described in section 7.2), and a check was made to confirm that the protruding baffle did not interfere with the rotation of the telescope pickoff mirror. The SMIRFS-IFU was mounted on the field plate such that the position angle of the long axis of the field of view was approximately 30 degrees.

8.2.1 Alignment of pickoff mirror.

UKIRT has four ports on the instrument support unit available for mounting instruments. The west port is normally used for visiting instruments. The light from the telescope secondary mirror is directed to any one these ports by means of a movable folding flat mirror called the pickoff mirror. The pickoff mirror has a dichroic coating which reflects incident infrared radiation whilst allowing most of the visible radiation to pass straight through to the telescope acquisition and guidance system. To align the optical axis of the IFU input with the optical axis defined by the secondary mirror it is necessary to slightly adjust the tip-tilt of the pickoff mirror. This was achieved using a Helium-Neon laser to back illuminate the IFU output slit, as previously shown in figure 7.11, thus projecting a spot of light from

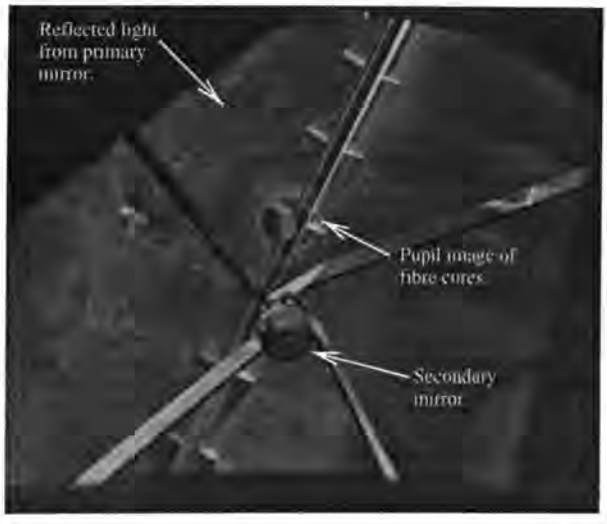

Figure 8.1: Photograph of the back projected IFU pupil image illuminating the telescope secondary mirror. When the the system is correctly aligned the halo of light surrounding the shadow of the secondary mirror should be positioned symmetrically.

the input array up towards the secondary mirror. The pickoff mirror is then adjusted until the projected beam is aligned with the secondary. The laser light from the IFU input forms a pupil image on the secondary mirror as shown in figure 8.1

The projected pupil image slightly overfills the secondary mirror so the shadow of the secondary mirror can be clearly seen on the dome surrounded by a halo of laser light. To align the optical axis of the input bundle correctly with that of the secondary mirror it is necessary to adjust the pickoff mirror until the halo is symmetrically situated around the shadow of the secondary mirror. This method of alignment automatically removes the effect of any misalignment of the input microlens array made during manufacture (section 7.7.5) i.e. the pupil images produced by the microlenses are made coincident with the fibre cores. With an F/36 beam it is crucial that the alignment is done carefully as a 0.2° pointing error corresponds to reduction in throughput of $\sim$ 18% (Haynes, 1995). The accuracy with which this alignment was achieved was estimated to be $\sim$ 0.1° leading to a throughput loss of approximately 8% (section 8.7.1).

To properly back illuminate the output slit the laser beam is made to diverge using a short focal length cylindrical lens which produces an approximately uniform one-dimensional diverging beam which illuminates the output slit. The diverging lens is situated at the pupil position of the output slit which corresponds to the centre of curvature of the slit. This is similar to the method of illumination used in the alignment of the input microlens array with the fibre array as described in section 7.7.5. The lens is mounted on a tip-tilt stage to obtain accurate alignment of the diverging laser beam with the IFU output microlens

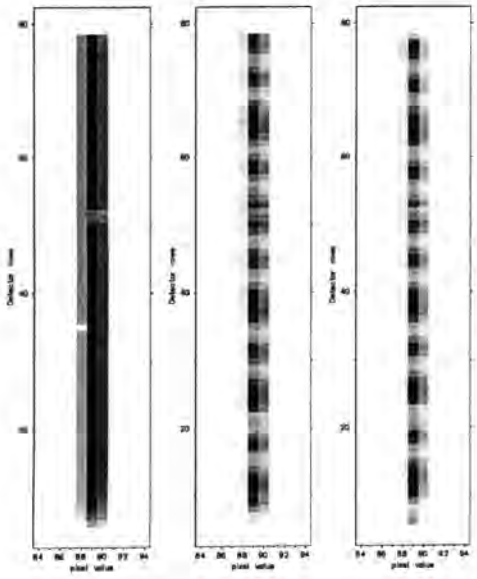

(a) (b) (c)

Figure 8.2: Series of three undispersed, m=0, slit alignment images. (b) and (c) were taken with the setup mask, shown in figure 8.4, in position on front of the IFU.
(a) shows an image of the CGS4 slit without the integral field unit, FWHM=1.929 pixels.
(b) shows an image of the IFU slit, FWHM=1.47 pixels. There are only 11 spots visible and vignetting can be seen at the ends of the slit indicating the magnification is too large, $M = 6.727$, $y_{\text{offset}} = 4.436$.
(c) shows a final image taken after the magnification had been correctly adjusted. Twelve spots are now seen and vignetting is less, $M = 6.494$, $y_{\text{offset}} = 5.767$.

arrays. Illuminating every microlens on the the output slit simultaneously uses all fibres in the alignment of the IFU input bundle with the secondary mirror. This avoids any systematic effects which may arise by using just a few fibres which may be badly positioned and produce a misalignment.

The pickoff mirror offset was found to be (-70, -90) in encoder units. Changes in this offset will occur if the IFU is not replaced accurately on the field plate following removal. The pickoff mirror offset needs to be checked to ensure correct alignment of the IFU with the telescope each time the telescope is run up (i.e. after the encoders are reset) and after the input bundle has been removed for calibration purposes.

Whilst aligning the pickoff mirror a check was made that the baffle was functioning correctly and not vignetting any part of the input beam. The baffle consists of a long cylindrical tube and if it installed incorrectly it may vignette the science beam and allow background light to enter the IFU. The baffle is described in more detail in sections 8.4 and 7.7.6. The baffle was found to be performing correctly.

8.2.2 Alignment of slit projection unit.

After alignment of the pickoff mirror the next step is to align the SPU so that the image of the IFU output slit, formed by the SPU, coincides with the CGS4 entrance slit. First the CGS4 grating angle is set to allow zero order exposures. Then zero order 'white light'

images of the CGS4 slit and the IFU slit are taken and the offset between the two slit images is measured. The 45° mirror inside the SPU is then adjusted laterally by the appropriate amount to remove the offset. The necessary offset of the 45° mirror to produce a given pixel shift on the detector is known from ray tracing calculations.

The initial shift between the two slits is quite large so the 4 pixel wide CGS4 slit is used initially to view an area as large as possible. The CGS4 image rotator is also used to produce a rotated image of the IFU output slit. By measuring where the rotated IFU slit image crosses the CGS4 slit image the lateral adjustment of the 45° mirror can be calculated providing the CGS4 slit position angle is known.

The final adjustment of the SPU is made with the two pixel wide slit. This is the slit that will normally be used for observations with the IFU. There is a small change in position between the 4 pixel wide slit and the 2 pixel wide slit within CGS4 which necessitates further fine adjustment. A zero order image of the two pixel wide slit is taken, as shown in figure 8.2(a), and the centroid is measured using the *imexam* package within IRAF. Then a zero order IFU slit image is taken and the centroid measured, figure 8.2(b). Note that figure 8.2(b) shows a zero order IFU image taken with the magnification setup mask in place. This does not affect the measurement of the centroid position. The 45° mirror is then adjusted by the appropriate amount so the two slits exactly coincide. At this point the CGS4 image de-rotator is also adjusted so the IFU slit image is exactly parallel to the CGS4 slit image. The final slit misalignment was less than 0.1 pixels on the detector corresponding to 80μm at the CGS4 slit and the rotator angle was set such that the measured rotation of the IFU slit was less than 0.2 pixels from vertical over the array ($< 0.2°$).

During the alignment of the IFU slit a number of problems were found with the repeatability of the CGS4 slit position. These are listed below:

- The 4 pixel wide slit and the 2 pixel wide slit do not reposition at the same place inside the instrument. An offset to the position of the 45° mirror has to be applied when changing from the 4 pixel slit to the 2 pixel slit of typically 1.7 pixels on the detector.
- When restarting the CGS4 instrument on a different night the 2 pixel wide slit may datum at a slightly different position. This offset has to be measured and a correction made to the position of the 45° mirror at the start of each observing run.

- The image position of the CGS4 and IFU slits on the detector changes when the slit wheel and grating are datumed. However the two slit images remain aligned which implies that the shift is due to a change in the grating angle. The CGS4 manual states that the repositioning accuracy of the grating is 1 pixel when the grating is moved from a higher to a lower grating angle.

- The dome-flat count rate decreased by 3% after the IFU slit alignment had been corrected. This implies that the IFU slit should be aligned to peak up the count rate rather than centering on the CGS4 slit. This possibly suggests that the IFU slit is centred on the CGS4 slit but the optical axes of the SPU and CGS4 do not coincide. The angular misalignment of the optical axes will lead to vignetting losses at the pupil whilst the slits seem to be in good alignment.

Because of these problems it is necessary to check the alignment of the IFU slit each time the CGS4 instrument is restarted and after any change to the CGS4 slit to ensure optimum performance. If the slits aren't aligned correctly when the instrument is prepared for observing there will be a loss in efficiency. The loss in efficiency due to a slit misalignment of 0.1 pixels is approximately 4%, however the actual slit misalignment was normally better than this. The prediction of vignetting losses at the CGS4 slit are described in section 8.7.10.

8.2.3 Set up of IFU magnification and offset

The SMIRFS-IFU was initially designed for use with the CGS4 short camera, although it can be also used in the future with the long camera. The short camera has a focal length of 150mm which produces a plate scale at the detector of 1.25 arcseconds per pixel. The plate scale at the CGS4 slit is such that 0.8mm maps to one pixel. The SMIRFS-IFU is designed to be used with each element of the IFU mapping to one pixel on the CGS4 detector. Crosstalk between adjacent fibres on the detector can be tolerated as long as the fibres are from adjacent areas on the sky. The effects of crosstalk are discussed more thoroughly in section 5.4.

As the spectra are so tightly crammed onto the detector it is crucial that the magnification of the slit projection unit is set correctly, otherwise vignetting will occur at the ends of the

slit. Ideally the elements of the IFU also need to be aligned so that each element is imaged onto only one pixel rather than being shared between two pixels. The shift in the spatial direction (the y-axis) on the detector between the IFU element and the pixel is known as the offset. The magnification of the SPU is adjusted by moving the spherical mirror in the z direction (the z direction is that defined by the optical axis of the spherical mirror) to change the object and image distances thus altering the magnification. The offset is changed by adjusting either the tilt of spherical mirror or the fold mirror. Only when the magnification and offset are set correctly will the first and last elements of the IFU output slit not be vignetted by the CGS4 slit.

To correctly measure the magnification and offset a mask was designed to fit in front of the IFU input microlens array. This mask covers the centre of the lens array, as seen in figure 8.4, so that only the edge lenses are illuminated. This arrangement produces 12 equally spaced 'spots' of light on the detector, each spot corresponding to a small group of illuminated lenses. A setup mask image can be seen in figure 8.2(b). When the magnification and offset are correctly adjusted the spatial position of the centroid of each of the spots on the detector is given by the following equation:

$$y_{\text{position}} = y_{\text{offset}} + Mn \tag{8.1}$$

where n is the number of the spot and M is the magnification. The spots are numbered from 0 to 11 with the lowest number spot being at the bottom of the detector. When the system is set up correctly the optimum values of magnification[1] and offset are $M = 6.5$ and $y_{\text{offset}} = 6.0$. To change the magnification of the SPU by 1% requires the spherical mirror to be moved in the z direction by 1.94 mm. This value was predicted with optical ray tracing, using the Zemax optical design software, by Robert Content. By measuring the position of each of the spots the magnification and offset can be calculated by a least squares fit to equation 8.1 and the SPU can then be adjusted accordingly. A cross section of a magnification image can be seen in figure 8.3.

The initial magnification was found to be $M = 6.68$ meaning one of the spots was completely off the end of the slit, as seen in figure 8.2(b). To reduce the magnification from 6.68 to 6.5

[1]Note that the actual magnification produced by the spherical mirror within the SPU is unity. The magnification at the detector is actually the spacing between adjacent spots, which is directly proportional to the magnification produced by the SPU.

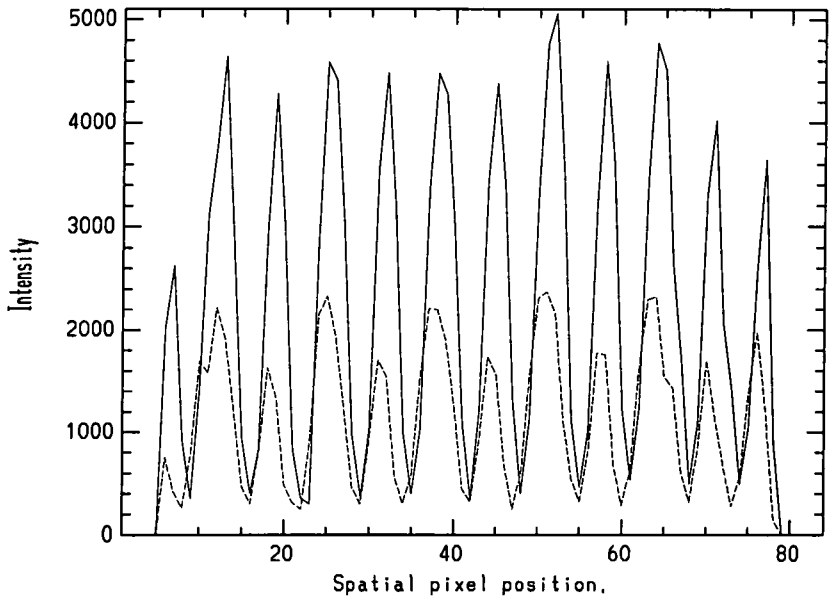

Figure 8.3: Spatial cross section from a dispersed H-band magnification set-up image. The solid line is the cross section for 23rd June and the dashed line is for 21st June. Twelve spots of light are seen. A change in the magnification and offset between the two images is visible by comparing the centroid positions of the spots. Note the non-uniformity of the spots which makes measurement of magnification more difficult.

the spherical mirror had to be moved outwards by a total of 9mm. It should be noted that this value does not agree with the shift predicted by ray tracing which should have been $\sim$ 6mm. It is unknown why the ray tracing predictions and the actual SPU behaviour do not agree. The large movement of the spherical mirror made it necessary to further adjust the position of the 45° mirror to remove the offset in the slit position caused by moving the spherical mirror. The error in the final value of y_{offset} was too small to be accurately corrected with the kinematic mounts fitted to the SPU mirrors. Note also that y_{offset} varies according to position on the detector due to image distortions within CGS4, as explained in section 8.5.5. The zero order image obtained with the final settings of M and y_{offset} can be seen in figure 8.2(c). Twelve spots can be seen without vignetting. The final value of y_{offset} must be known as it is used as a parameter in the IFU image reconstruction software to specify the position of the first spectrum on the chip.

Errors in the measurement of magnification, mainly due to centroiding errors on the spots, are typically $\sim$ 0.3%. The current design of magnification set up mask, known as the thin mask, makes it quite difficult to obtain accurate centroids on the spots as they are too closely spaced and often vary in intensity as seen in figure 8.3. Fibre throughput variations will also bias the centroid position. In the future for more accurate measurement of the magnification a new mask design will be needed such as the 'big mask' design proposed in figure 8.4.

The FWHM of the zero order IFU slit image in the spectral direction gives some measure of the focus of the SPU. At a magnification of $M = 6.68$ the FWHM was measured to be 1.48 pixels (figure 8.2(b)) but this reduced to 1.32 pixels at $M = 6.5$. The spherical mirror was moved beyond the the optimal magnification position to find the position at which the FWHM reached a minimum i.e. the position of best focus with the SPU. The FWHM was found to decrease further but this position of the spherical mirror produces the wrong magnification. By moving both the 45° mirror and the spherical mirror the appropriate amounts it may be possible to achieve a better focus with the correct magnification but this was not done due to lack of time.

8.2.4 Summary of alignment procedure

This section briefly summarises the steps in the SMIRFS-IFU alignment procedure described in the preceding sections.

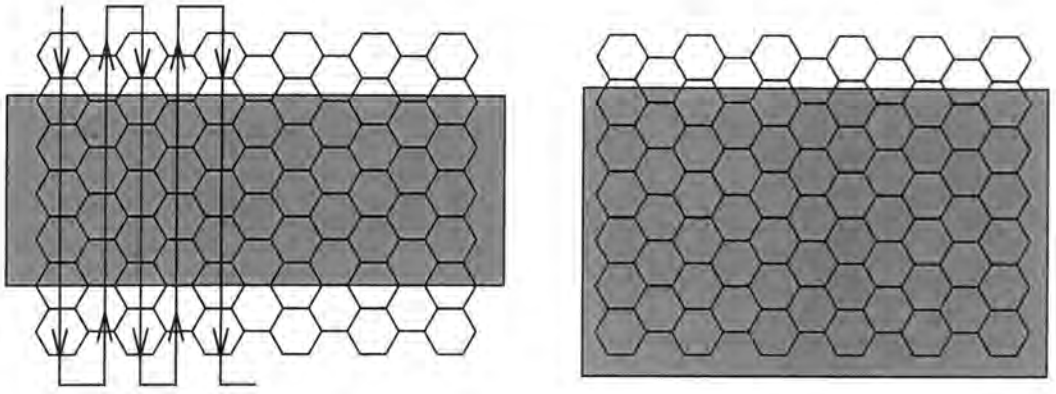

Figure 8.4: Schematic to show the operation of the magnification setup mask. The mask on the left is the 'thin mask' design, the mask on the right is the 'big mask' design. The thin mask allows 12 groups of ~ 2.5 lenses to be illuminated thus producing 12 spots of light on the image. The mapping of the input field to the slit is indicated by the arrows. Note the reversal at the end of each row, it is this that produces 12 spots. The big mask is a redesign to only allow 6 groups of lenses to be illuminated.

1. Determine the pickoff mirror offset by back illumination of IFU output slit to project an image of the fibre pupil onto the secondary mirror. Also check performance of the baffle to confirm it is not vignetting the input beam.

2. Align the principal axis of the IFU at the correct position angle for the observations

3. Mount IFU output slit in SPU and use zero order images to align IFU slit with CGS4 slit by moving the 45° mirror and the position angle of CGS4 de-rotator.

4. Use the thin mask images to measure the image magnification and adjust by moving the spherical mirror. If necessary the spatial position of the slit on the detector can be adjusted by tilting the 45° mirror.

8.2.5 Instrument flexure tests

The initial set up of the SMIRFS-IFU was done with the telescope pointing at the Zenith. This is the usual parking position for the telescope and allows easy access to the Cassegrain focus to work on the instruments. However, because of the problems experienced with the non-repeatability of the CGS4 slit position, described in section 8.2.2, it was decided to investigate how the position of the telescope affected the position of the CGS4 slit and the

Telescope position	y_{offset}	M	HA	Dec	Spatial shift
Zenith	5.277	6.497	$0h$	10°	0.0
North	5.169	6.520	$0h$	59°	−0.11
South	5.795	6.475	$0h$	−39°	0.52
East	6.243	6.452	$-4h$	0°	0.97
West	5.421	6.458	$+4h$	0°	0.14

Table 8.1: Variation in magnification and offset for dispersed H-band images with telescope position (flexure in spatial direction). The observed spatial shift (in pixels) is measured with respect to the position observed at zenith. The spatial shift is simply the change in the offset.

set up of the IFU. Flexure needs to be accurately mapped, if possible, to allow the instrument to be correctly adjusted for observations at any position on the sky. This ensures that the magnification, offset, and slit alignment is correct for every observation.

The telescope was slewed to various positions and a series of exposures were taken in various instrument configurations to measure any flexure that might be present. Dispersed H-band SMIRFS-IFU dome flat-field spectra were taken with the magnification set-up mask in place. From these images the change in magnification and offset with telescope position can be measured. Changes in magnification and offset are equivalent to flexure in the spatial direction (along the slit). Dispersed images were used as they give a more accurate measurement of magnification and offset than zero order images. To measure flexure in the spectral direction zero order slit images were taken. The SMIRFS-IFU slit was also removed to allow flexure measurements in the spectral direction to be taken with CGS4 alone. Flexure in the spectral direction causes the centroid position of the zero order slit image to shift on the chip with changing telescope position.

The results of the flexure tests are summarised in tables 8.1 and 8.2. Table 8.1 lists the change in magnification, M, and offset, y_{offset}, with telescope position. Table 8.2 lists the shift of the zero order slit image centroid in the spectral direction with telescope position. The dispersed H-band set-up mask images show there is a change in both the magnification and offset with telescope position. The largest change occurs when the telescope is moved from North to East with the magnification changing by 1% and the offset by 1.1 pixels. If a telescope slew of this type was needed during observing then the SMIRFS-IFU would need

Telescope slew	Slit	Centroid	Offset	Shift
Start with telescope West.	IFU	89.98	+0.33	0.00
West → Zenith	IFU	89.65	0.00	−0.33
Zenith → East	IFU	88.84	−0.81	−0.81
East → Zenith	IFU	89.36	−0.29	+0.52
Zenith → West	IFU	89.61	−0.04	+0.25
West → Zenith	IFU	89.31	−0.34	−0.30
Zenith (IFU) → Zenith (CGS4)	CGS4	89.26	−0.39	−0.05
Zenith → West	CGS4	89.51	−0.14	+0.25
West → East	CGS4	88.67	−0.98	−0.84
East → Zenith	CGS4	89.18	−0.47	+0.51
Zenith (CGS4)→ Zenith (IFU)	IFU	89.23	−0.42	+0.05

Table 8.2: Variation in IFU/CGS4 slit image centroid with telescope position (flexure in the spectral direction). Values for Centroid, Offset and Shift are in pixels. Hour angle and Declination are as listed in table 8.1. The offset is the measured spectral shift between the centroid measurement at Zenith and the current position. Shift is the spectral shift between the previous position and the current position. Note the CGS4 and SMIRFS-IFU slits remain aligned to within 0.1 pixels accuracy after removal and replacement of the IFU slit.

adjustment between the two observations. The cause of the magnification change may be a movement of the SPU spherical mirror along the z-axis. The change in offset may be due to a change in tilt of the mirrors inside the SPU and/or movement of a component inside CGS4 and/or a bulk shift of CGS4 with respect to SMIRFS.

In the spectral direction (table 8.2) both the movement of the IFU slit and the CGS4 slit show similar behaviour. The maximum change in the slit image centroid position, of ~ 1 pixel, occurs in moving from East to West. The SMIRFS-IFU slit and the CGS4 slit do however remain aligned, to an accuracy of < 0.1 pixels, after each telescope movement. This suggests that either the IFU slit and the CGS4 slit are moving together by the same amount, which is unlikely, or the flexure originates inside CGS4 i.e. due to a component between the slit and the detector. Given the slight change in the zero order image position each time CGS4 is restarted, which may be due to the grating not resetting to the same datum position correctly, it is likely that some part the spectral flexure is due to a change in the grating angle. The slit image does not always return to the same place on the detector after the telescope has been moved implying there is some mechanical hysteresis within CGS4. This is illustrated by the -0.34 pixel shift between the two Zenith observations taken with the SMIRFS-IFU. The SMIRFS-IFU slit had to be removed to allow the CGS4 slit flexure test to be performed. When the SMIRFS-IFU slit was replaced it relocated to within 0.05 pixels (40μm) of its original position. This indicates the SMIRFS-IFU slit can be removed and replaced at will during commissioning without disturbing the alignment of the optics.

Results of CGS4 laboratory flexure tests performed on a telescope simulator, taken from Ramsay-Howat (1994), described a spatial shift of 1.14 pixels and a spectral shift of 0.304 pixels when CGS4 was moved from $+60°$ to $-60°$ altitude on the telescope simulator. This offset in the spatial direction is very similar to the result for the SMIRFS-IFU offset so it seems likely that the spatial offset can be attributed to the CGS4 spectrograph. The spectral flexure with SMIRFS and CGS4 is three times worse than the published values. However, more recent tests of the CGS4 flexure (CGS4, 1997) describe a 0.4 pixel spectral shift from transit going West and 0.6 pixel going East. These results are in reasonable agreement with the measured SMIRFS-IFU and CGS4 results. It is therefore likely that most of the observed flexure is due to CGS4 alone.

It should be noted that there is no change in the spectral point spread function with telescope

position. The variation of spatial point spread function with telescope position was not measured but is not expected to be any different in behaviour to the spectral PSF.

8.3 Relative fibre throughput.

Due to manufacturing difficulties it is unlikely that the throughput of every fibre in the SMIRFS-IFU will be the same. Many factors such as: focal ratio degradation, mechanical stress, and surface finish, will contribute to make each fibre perform slightly differently from its neighbour. In order to allow accurate comparison of the scientific data obtained from different fibres (different spatial elements) it is therefore necessary to accurately know the throughput of each fibre. For example, removal of fibre to fibre throughput variations is necessary to allow correct comparison of line fluxes, equivalent widths and emission line ratios. The fibre to fibre transmission variation also needs to be removed to allow the integral field image to be reconstructed. Although variations in the fibre transmission are a nuisance to astronomers, structure in the fibre flat-field can be useful as a diagnostic of the manufacturing process. By careful examination of the flat-field structure the areas in the manufacturing process which lead to low throughput fibres can be identified and remedied. As an example, it has already been described in section 7.6 that fibres situated at the edge of slit blocks were more likely to become loose during the polishing process. This manufacturing problem then preferentially produces low throughput fibres at the edges of slit blocks, something that can be readily seen in the fibre to fibre flat-field variation.

At this point the distinction between the fibre to fibre flat-field and the detector flat-field should be highlighted. The fibre to fibre flat-field measures the change in transmission between different fibres and allows the throughput of each fibre to be corrected to some average value. The detector flat-field is obtained by taking a spectrum of a uniform blackbody source without the SMIRFS-IFU in place. The detector flat-field allows the removal of pixel to pixel response variations, i.e. cosmetic defects on the chip, and is therefore completely separate from the fibre flat-field.

To measure the throughput of each element it is necessary to both uniformly illuminate the entire SMIRFS-IFU input field of view and correctly simulate the correct input focal ratio i.e. simulate the telescope exit pupil. The standard way of achieving this is by observing

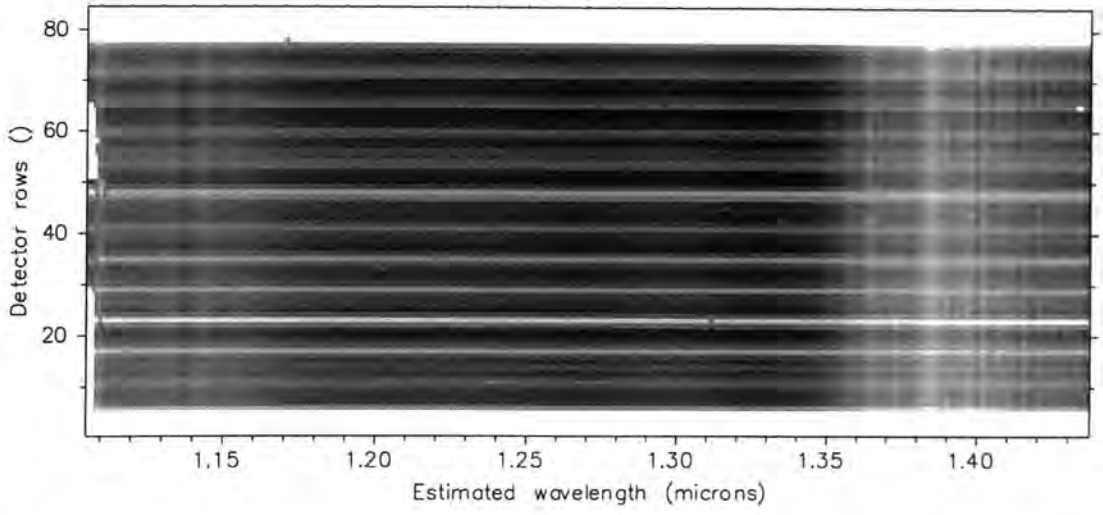

Figure 8.5: Image of a J-band fibre to fibre dome flat-field spectrum. Low intensity pixels are shown as light, high intensity pixels as dark. The broken fibre occurs at detector row 23. Bad pixels have been removed using the procedure described in section 9.3.

uniform sky or by illuminating the telescope from the inside of the dome. Illumination in this way ensures that the same amount of flux enters each fibre. Therefore variations in measured flux at the detector are due to fibre throughput variations and not changes in illumination conditions across the IFU field of view.

Dome flat-fields were obtained by pointing the telescope at the wind-blind located inside the telescope dome. A Tungsten-Halogen flood lamp was used to illuminate the wind-blind producing a reasonably uniform diffuse source. Sky flats were also taken during the evening twilight whilst the sky brightness was still sufficient to provide high signal to noise. An example of a J-band fibre to fibre dome flat-field exposure can be seen in figure 8.5. A number of features are immediately apparent. The broken fibre can be seen at detector row 23. Other low-throughput fibres can also be seen as light stripes. Pixels which have been masked by the bad pixel mask are seen as white i.e. at the extreme left of the image.

The reconstructed J-band fibre to fibre dome flat-field image (shown in figure 8.6) shows how the regions of low signal on the detector map to specific IFU elements. Purpose written software was used to perform the image reconstruction. To reconstruct the dome flat-field image a value of $y_{\mathrm{offset}} = 6.0$ was used. The first and last few IFU elements on the reconstructed image have low throughput due to vignetting by the CGS4 slit. This vignetting is an optical property of CGS4 and cannot be compensated for by changing the magnification

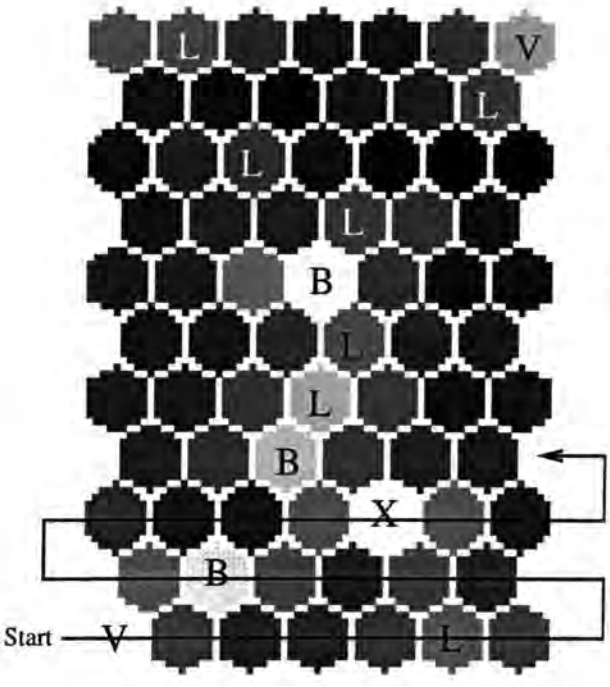

Figure 8.6: Reconstructed integral field image of the J-band fibre to fibre dome flat-field. The first lens, corresponding to detector row 6, is indicated by 'start'. The letters indicate the following: V = vignetted pixels, B = bad fibres, X = broken fibre, L = low throughput fibres. The period of defective fibres is approximately every sixth element.

or offset. The position of bad and broken fibres corresponds exactly with their expected positions from tests carried out in the laboratory during assembly, as described in chapter 7. It is noticeable that there is a regular dip in the fibre throughput with a period of roughly six elements. These elements are labelled 'L' on the reconstructed image except where they are already labelled with a V, B or X. This period corresponds to the number of fibres on each output slit block. The loss in throughput is probably a result of the fibres at the edge of the output blocks being under more stress than those at the centre of the blocks which leads to increased focal ratio degradation. The increased FRD leads to vignetting by the output microlenses thus reducing throughput. This regular dip approximately every sixth element can be seen more clearly in figure 8.7 where the low throughput elements have been marked for clarity. The increased stress at each edge fibre is thought to be due to the fibre routing with the edge fibres having to be tightly curved in order to reach the correct position on the output slit blocks.

Another possible contribution to the periodic dip in throughput is the overlarge interfibre gap between adjacent output slit blocks. This will appear as a decrease in throughput at the edges of the blocks. This effect was seen in the laboratory during optical tests as described in section 7.3.5. Due to the coarse sampling with the CGS4 detector along the slit it was not possible to determine whether the periodic variation is solely due to the over large gap

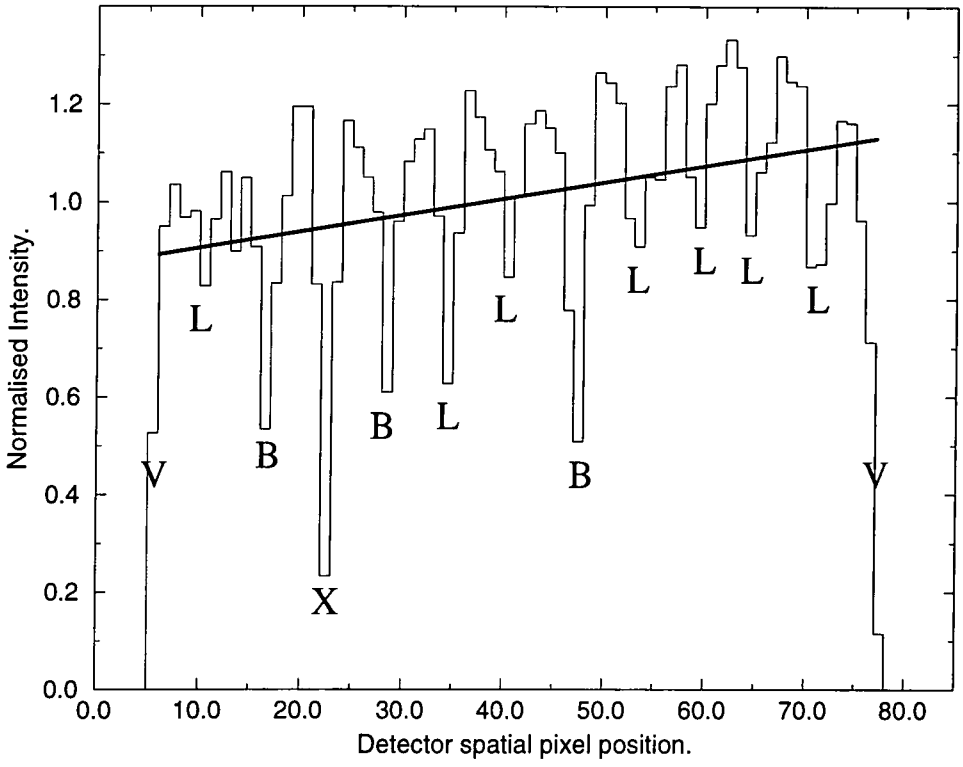

Figure 8.7: Cut along the spatial direction of the fibre to fibre dome flat-field image shown in figure 8.5. The letters indicate the following: V = vignetted pixels, B = bad fibres, X = broken fibre, L = low throughput fibres. The solid line shows the best fit to the intensity in (Intensity = 0.00334x + 0.873) the area occupied by the fibres. The fit shows there is a considerable gradient across the flat-field. The intensity increases by 24% from left to right although this may be slightly biased by the bad fibres being predominantly on one half of the detector.

between slit blocks or real fibre to fibre throughput differences. It is clear that a thorough investigation of fibre to fibre throughput variations is required if the loss mechanisms which contribute to throughput variations are to be fully understood and eventually remedied.

The spatial cut across the fibre to fibre flat-field shown in figure 8.7 also shows a significant gradient in intensity along the slit. There are various mechanisms which could attribute towards the observed gradient summarised as follows:

1. Angular misalignment of the SMIRFS-IFU slit with the CGS4 slit.
2. Some sort of variable vignetting across the input array, possibly caused by incorrect positioning of the baffle or by bubbles present at the interface between the fibre bundle and the microlens array substrate.
3. Real variation in intensity across the dome and sky flat-field field of view.
4. Rotational misalignment of the input microlens array major axis with respect to the fibre bundle major axis.

The SMIRFS-IFU slit was carefully aligned with the CGS4 slit using the procedure described in section 8.2.2. The maximum slit rotation was measured to be less than 0.1° and the offset between the centroid of the CGS4 slit and the SMIRFS-IFU slit was $\sim$ 0.1 pixels. The image of the SMIRFS-IFU slit at the CGS4 slit is assumed to have a Gaussian profile with a FWHM of $\sim$ 1.1 pixels. The amount of vignetting produced by transmission of this profile through the two pixel wide CGS4 slit can then be calculated (this process is described in section 8.7.10). The observed change in intensity across the fibre flat-field of 24% requires the slit misalignment to amount to a linear shift of 0.6 pixels or a rotation of 0.6° both of which are much greater than the measured values for misalignment. Therefore misalignment of the slits can only account for a few percent of the observed flat-field gradient at most.

Variable vignetting by bubbles can only account for a maximum change in intensity across the flat-field of 8% (this loss is produced by two additional air-glass surfaces). The gradient across the flat-field would also require the bubbles to have variable surface densities across the SMIRFS-IFU field of view. However the SMIRFS-IFU input bundle was examined for the formation of bubbles and none were seen covering the field of view so this source of loss

can also be discounted. A misalignment of the baffle could cause variable vignetting across the field of view but this didn't seem to be the case. Vignetting of the telescope beam by the baffle would have been observed when the back projected IFU pupil image was used to align the SMIRFS-IFU with the secondary mirror as described in section 8.2.1. Vignetting would have been clearly seen as a shadow on the pupil image which occurs at the secondary mirror and it can be seen in figure 8.1 that no such shadow occurs.

Variations in the illumination across the dome flat-field screen could cause the observed change in intensity across the dome flat-field image. However the sky flat-field images also exhibited the same gradient. It is thought to be unlikely that the sky shows such significant variations in brightness over such a small field of view. Dome-flats are more likely to show illumination variations due to the difficulty of illuminating the flat-field screen. The similarity between the dome and sky flat-field exposures, described in more detail in section 8.3.1, indicates that both are uniform as it is very unlikely that both sky and dome flats will show the same variation in intensity.

The most likely mechanism that can account for a 24% change in intensity across the fibre to fibre flat-field is a rotation of the input microlens array with respect to the tube array. For there to be a gradient across the entire input field of view requires the centre of rotation of the input microlens array to be off the tube array. If, for instance, the centre of rotation was at the centre of the tube array the throughput would be maximum in the centre and would fall off either side. Assuming that the centre of rotation occurs at element 72, where maximum transmission occurs[2], a rotation of the microlens array with respect to the fibre array of approximately 0.3° is required to produce the observed change in intensity across the flat-field. Given the uncertainty in the alignment of the input microlens array with the tube array during manufacturing, described in section 7.7.5, it is possible a misalignment of 0.3° did occur.

8.3.1 Removal of fibre throughput variation

The root mean square (RMS) variation in the fibre to fibre response is $\sim$ 20%, normalised to the mean, for the J-band dome flat-field and $\sim$ 21% in the H-band. The twilight sky flat-field

[2]This is maximum transmission of the fit to the flat-field, the actual element with highest transmission is element 63

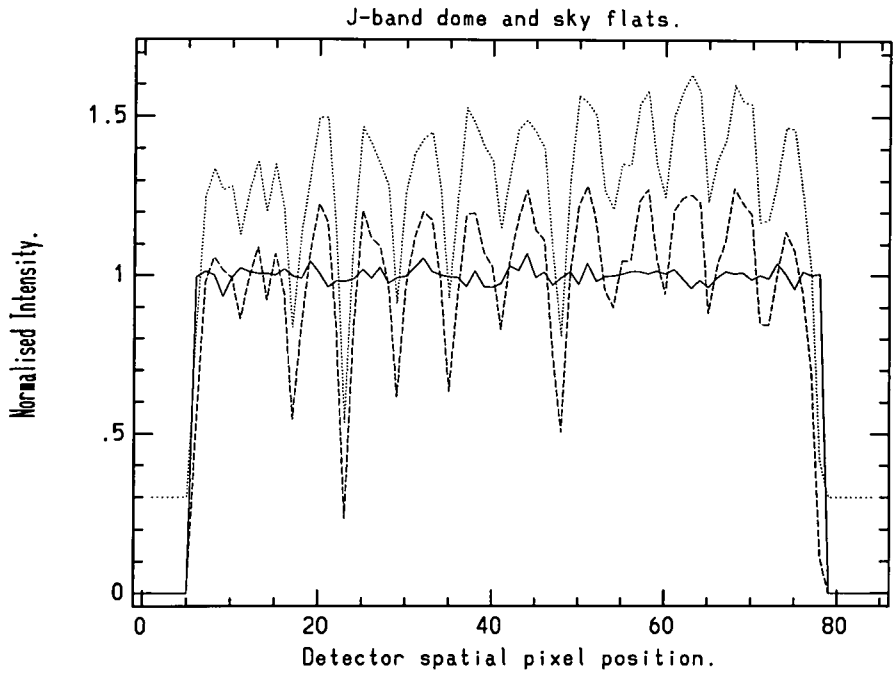

Figure 8.8: Cut along the slit of J-band dome flat-field (dotted line) and sky flat-field (dashed line) images. The dome flat-field exposure has been offset by 0.3 in intensity for display purposes. The solid line shows the result of flat-fielding the sky exposure with the information from the dome flat-field.

exposures show similar behaviour. If the broken element and the three bad fibres are ignored then the residual fibre to fibre variation reduces to an RMS of $\sim$ 14%. A comparison of a J-band dome flat-field with a twilight sky flat-field is shown in figure 8.8.

Figure 8.8 also shows the result of using a J-band dome flat-field exposure to correct the relative fibre to fibre throughput variations in the J-band twilight sky exposure. After flat-fielding the residual RMS throughput variation decreases to 2.4% in both the J and H-bands. This value is consistent with photon statistics which would produce an RMS of 2.7%. The flat-field correction is done using the IRAF tasks[3] *response* and *illumination*. First *response* is used to remove the overall shape of the flat-field spectrum and correct for pixel to pixel response variations due to bad pixels. The quality of the flat-field correction is better if regions of bad pixels are also removed. Then *illumination* is used to correct the

[3]Note the section on data reduction (section 9.3) describes an alternative method for removing the flat-field variation. It is not needed here as there is no change in y_{offset} between the dome-flat and the skyflat observations

remaining slit illumination function (the change in intensity of the flat-field along the slit). The flat-field correction is applied simply by dividing the exposure to be flat-fielded by the output image produced by the *illumination* software. It was found that the dome flat-field produced higher accuracy in the flat-field correction as the spectrum is less complex than the sky spectrum. The structure in the sky spectrum produces residuals in the flat-field correction. The flat-field correction is also best carried out in the wavelength region which is free from atmospheric absorption features, again to avoid structure in the spectrum.

The accuracy with which dome flat-field exposures can be used to correct flat-field variations in the twilight sky flat-field exposures means that the dome flat-field is a good approximation to the illumination produced by the twilight sky. The distribution of illumination on the IFU from the dome-flat must be very similar to that obtained when pointing at sky. This is justification for the earlier assertion that the illumination pattern from the dome and sky are uniform. This means dome flat-field exposures can be used on the science images without worrying about differences in optical path between the two sets of exposures. This is particularly useful if for some reason sky flat-fields are not available.

An attempt was made to flat-field one night's data with the dome flat-field from another night but this did not work well due to the change in y_{offset} between the different nights. This change in offset can be seen in figure 8.3 where there is a shift between the centroids of the spots of $\sim$ 1 pixel. It is possible to shift the dome flat by the appropriate amount in software but this also shifts the position of bad pixels which creates problems when the flat-field is applied. This is why it is important to remove detector flat-field variations and fibre throughput variations separately. This is explained in more detail in section 9.3.

8.3.2 Changes in magnification

By comparing the spatial cross sections of the J and H-band dome flat-field exposures, as shown in figure 8.9, it is possible to see that there is a small change in magnification between the J and H-band exposures even though they were taken only minutes apart. At one end of the slit (low pixel values) the low throughput fibres in the J and H-bands are aligned but become progressively out of step as pixel value increase. The value of y_{offset} remains the same for both J and H exposures but the H-band exposure has a magnification which is higher by 0.6%. This corresponds to a 0.4 pixel misalignment between the spectra and the detector

pixels over the 72 elements. This change in magnification is also apparent if a J-band dome flat is used to flat-field an H-band exposure with the quality of flat-field correction getting gradually worse with spatial position across the chip due to the magnification change.

The cause of the change in magnification may be some anamorphic effect due to the change in grating angle between first order (H-band) and second order (J-band) or a chromatic effect due to the lenses inside CGS4. If the IFU is initially set up to do J-band science observations it will be necessary to reset the position of the spherical mirror inside the SPU before H-band observations can be performed to correct for the change in magnification otherwise the spectra will no longer be aligned with the pixels. Other than the change in magnification there is very little difference between J and H-band flat-fields indicating that the IFU has similar fibre to fibre throughput variations at both wavelengths.

The magnification was also found to vary slightly from night to night. The H-band magnification was found to be 0.3% smaller on 23rd June than it had been on 21st June. Part of the nightly change in magnification is thought to be due to temperature variations. The drop in temperature of about 25°C when the SPU was moved from the warm sea level laboratory environment to the telescope dome will cause the SPU to shrink contributing $\sim 0.1\%$ to the measured change in magnification.

8.3.3 Relevance of flat-field results to IFU manufacturing

The fibre to fibre throughput variation indicates several areas in the IFU manufacturing process which need to be improved in order to obtain better performance. The regular drop in throughput, with a period of approximately six fibres, indicates that there is a problem with the fibres located at the edge of the output slit blocks. There are two loss mechanisms operating here: Stress-induced FRD because of the fibre routing to the edge fibres (section 7.7.3), and polishing defects with edge fibres (section 7.6). The fibre to fibre throughput variation can be improved in future IFU designs by better polishing procedures and more careful fibre routing. The oversized gap between the output slit blocks is also thought to contribute to the regular dip in fibre throughput. This highlights the need to obtain high accuracy in the mechanical construction and assembly of components.

The slope on the fibre to fibre flat-field is thought to be due to an angular misalignment of the

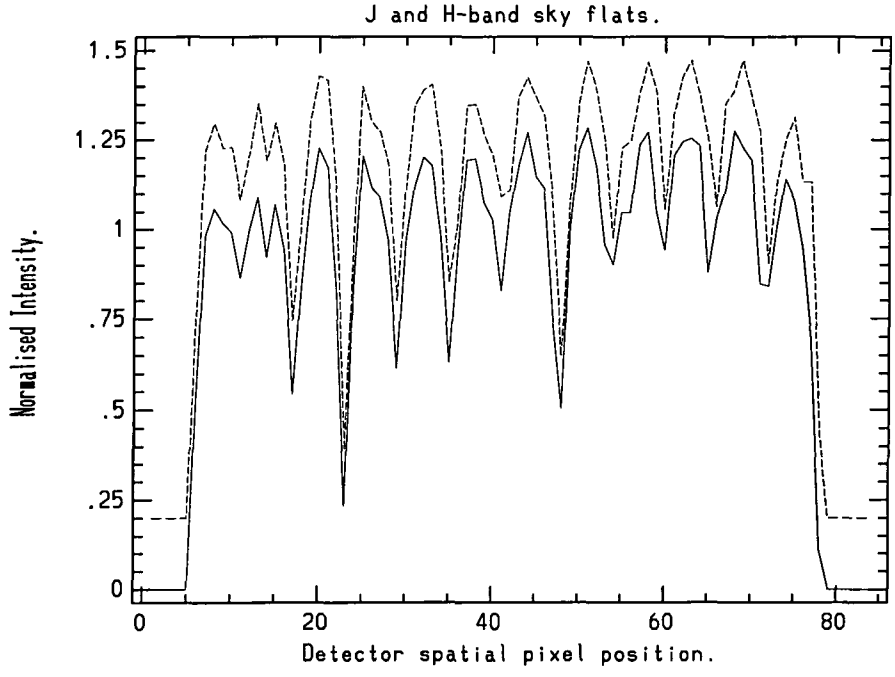

Figure 8.9: Comparison of J (solid line) and H-band (dashed line) sky flat-fields. The H-band sky flat-field has been offset slightly in intensity for display purposes. The two flat-fields show very similar behaviour. There is, however, a change in magnification between the two flat-fields resulting in a misalignment of the spatial elements with the pixels.

input microlens array with respect to the tube array. The limiting accuracy of the angular alignment process was estimated to be 0.3° which is enough to account for the observed variation in throughput across the array. Clearly more accurate methods of aligning the microlenses with the tube arrays need to be found. This process is also made more difficult by the aberrations introduced by the microlenses.

It should be noted that the similarity in structure between the J-band and H-band flat-field exposures indicates the fibre to fibre throughput variations are independent of wavelength. If the throughput variations were a strong function of wavelength then a change in the flat-field structure (i.e. higher RMS fibre to fibre variation) might be expected between the J and H-bands. This means diffraction is not a major loss mechanism in the SMIRFS-IFU. The dominant causes of the fibre to fibre throughput variation is then thought to be FRD losses and optical misalignments, such as rotation of the input microlens array with respect to the tube array, as these are independent of wavelength.

8.4 Performance of baffle.

The function of the baffle is to prevent light from entering the input microlenses and fibres at large angles. The full range of angles, also known as the acceptance cone, that the fibre transmits to the output is determined by the numerical aperture of the fibre. The fibres used in the SMIRFS-IFU, described in section 7.4, have a numerical aperture of 0.22 producing an acceptance cone of approximately F/2.3. The large acceptance angle would allow background light from the microlenses surrounding the on-axis lens to enter the fibre. This means that the sky is imaged onto the fibre increasing the amount of background light that enters the system. A full description of the function of the baffle can be found in section 7.7.6. Baffling is not required at the SMIRFS-IFU output slit as CGS4 has an internal Lyot stop.

It is interesting to measure just how much additional light is admitted to the SMIRFS-IFU if the baffle is removed. A series of dome flat exposures were taken with and without the baffle in place to measure the increase in background light when the baffle is removed. The dome flat-field light source was measured to be stable over the time period of the exposures. Figure 8.10 shows a comparison of the spatial cross section of the H-band dome flat-field exposure with and without the baffle in place. Without the baffle in place the amount of

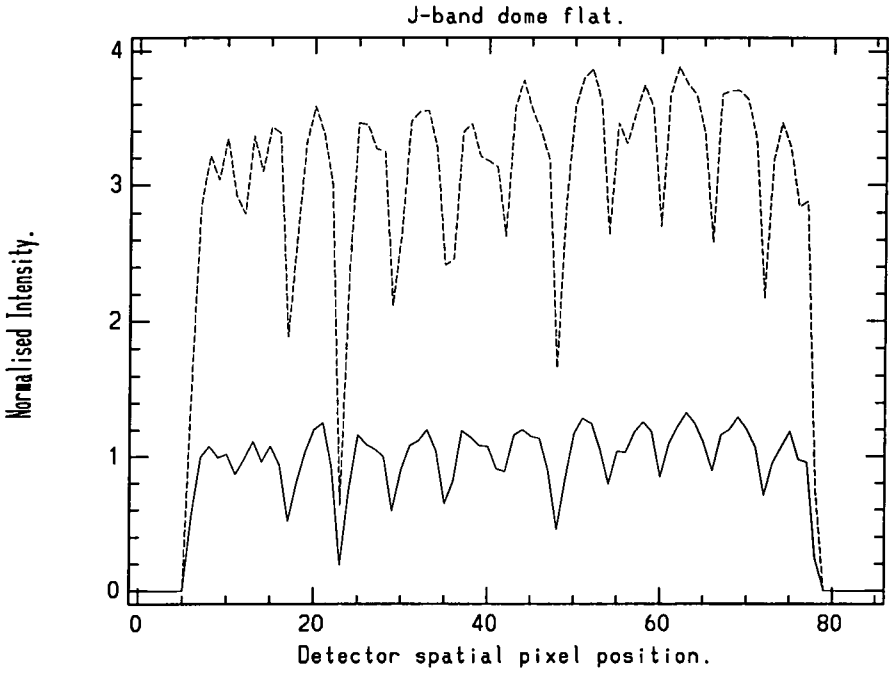

Figure 8.10: Comparison of H-band dome flat-fields with and without the baffle in position. The dome flat-field with the baffle in place is shown with a solid line. Note the large increase in intensity, due to increased background light, which occurs without the baffle (dashed line).

light entering the IFU increased by a factor of 3.02 in the J-band and 3.15 in the H-band. No results were obtained on the sky but they are expected to be similar. The large increase in background light when the baffle is removed indicates that provision of adequate baffling is crucial in the design of an integral field unit. The difference removing the baffle has on flat-field illumination conditions can also be seen in figure 8.10. Removing the baffle effectively blurs the flat-field by increasing the amount of scattered light. Un-baffled flat-field exposures show an RMS fibre to fibre throughput variation which is 10% higher than baffled flat-field exposures.

8.5 SMIRFS-IFU point spread function

The final detected point spread function of the integral field unit is defined by the convolution of the IFU output slit image with the aberrations present in the SPU and CGS4 optics but truncated by the CGS4 slit in the spectral direction. It is the detected PSF which limits the final spectral resolution of the instrument. The PSF also limits the spatial resolution that can be achieved in the reconstructed integral field image. The spectral resolution of the system can be measured directly from the FWHM of unresolved emission features in a wavelength calibration spectrum. Measurement of the spatial PSF of the complete system is complicated by the fact that the image is under-sampled in the spatial direction by the CGS4 detector.

Optical ray tracing shows that the aberrations introduced by the slit projection unit are negligible. Therefore the detected PSF is determined by the aberrations of the output microlens and the CGS4 optics. The aberrations introduced by the CGS4 optics are described in Ramsay-Howat (1994).

8.5.1 Spectral PSF

The profile of the point spread function in the spectral direction can be measured from features in the wavelength calibration spectrum. To observe a wavelength calibration spectrum the IFU input bundle was first removed from the FPU and then illuminated using a small arc lamp mounted about 2 feet away. A small diffusing screen was placed in front of the arc lamp to provide more uniform illumination of the IFU. The arc exposures were done with

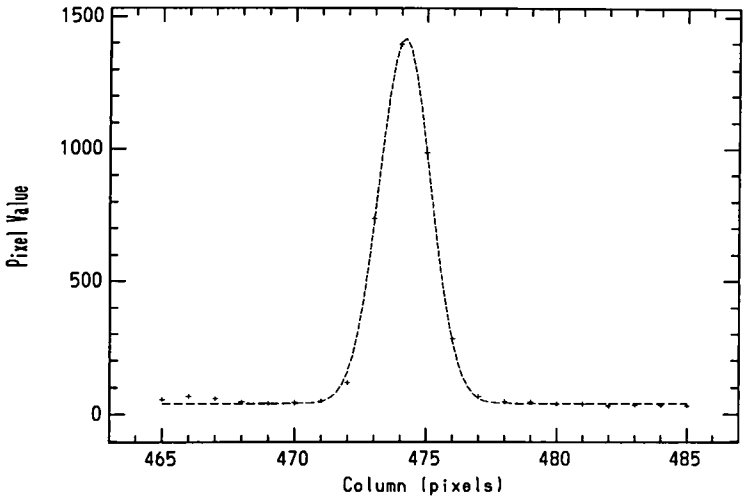

Figure 8.11: Spectral PSF of an Argon arc line at 1.4097μm. The PSF is an average of 5 detector rows. The best Gaussian fit to the data gives a FWHM of 2.286 pixels with (2 × 2) sampling. A Gaussian is a very good approximation to the observed spectral PSF.

the baffle in place as the baffle helps to define the correct focal ratio to illuminate the IFU. This helps to reduce differences in the spectral PSF that might be introduced because the arc lamp does not illuminate the IFU through the telescope.

To accurately measure the PSF of the IFU in either the spatial or spectral direction the detector has to be dithered to avoid problems with undersampling of the PSF. Arc line observations were done using a 2 × 2 sampling pattern in the spectral direction. This means that each observation consists of four interleaved exposures where the detector is dithered by half a pixel in the spectral direction between each exposure. Using a sampling pattern of 2 × 2 effectively halves the size of the pixels. The CGS4 slit width is however always referred to in terms of the width of undithered pixels. Dithering is not available in the spatial direction. An example of the spectral PSF obtained from observations of an Argon arc lamp can be seen in figure 8.11. The FWHM of the spectral PSF was measured by using software to fit a Gaussian to the data points. The effect of undersampling on the PSF can be measured by looking at the dithered exposures individually before they are interleaved. This gives a FWHM of 0.3 pixels or 1.2 pixels depending on whether the PSF is sampled by one or two pixels across the FWHM.

The average spectral FWHM of 15 Argon arc lines distributed over the entire J-band is 2.22 pixels (with 2 × 2 sampling) although this varies by ±10% according to position on the detector. The J-band dispersion is measured to be 0.662 nm/pixel (second order) so the width of the spectral PSF gives a limiting wavelength resolution element of $\Delta\lambda$ = 1.46nm. This gives a resolution R, where R= $\lambda/\Delta\lambda$, of 870 at λ = 1.27μm which is equivalent to using

a 1.1 pixel wide slit with CGS4. For comparison the predicted[4] CGS4 J-band resolution with a 1 pixel wide slit is R=998. The SMIRFS-IFU is normally used with the 2 pixel wide CGS4 slit to cut down scattered light whilst not vignetting the output beam from the IFU slit. It should be noted however that the limiting resolution of the SMIRFS-IFU is determined by the IFU output slit and not the CGS4 slit.

In the H-band the average spectral FWHM of Argon arc lines is 2.26 ± 0.1 pixels (with 2×2 sampling). The measured H band dispersion is 1.322 nm/pixel (first order) giving a limiting wavelength resolution element of $\Delta\lambda = 3.0$nm. This produces a resolution of R=583 at $\lambda = 1.745\mu$m. The theoretical prediction for the resolution of CGS4 in the H-band, with the one pixel wide slit, is R=681. The IFU resolution is therefore equivalent to using a 1.17 pixel wide slit with CGS4.

For comparison the spectral FWHM obtained from arc line observations of the one pixel wide slit with CGS4 alone is $\sim 1.15 \pm 0.05$ pixels. Therefore the measured width of the SMIRFS-IFU slit is very similar to the one pixel wide CGS4 slit. The SMIRFS-IFU slit width was designed to be the same as the one pixel wide slit. This suggests that the optical aberrations present with the SMIRFS-IFU are confined to CGS4 otherwise the IFU slit width would be expected to be broader than the CGS4 slit width. This also suggests that the limiting spectral resolution will be the same for the SMIRFS-IFU as it is with the CGS4 one pixel wide slit. The SMIRFS-IFU provides the capability to obtain high spectral resolution observations of an extended object (or a point source in bad seeing conditions) without the loss of light associated with using a narrow slit. This is one of the major advantages of integral field spectroscopy over traditional longslit spectroscopy.

8.5.2 Change in spatial PSF across detector

Initially it was planned to measure the spatial PSF produced by a single IFU element of the SMIRFS-IFU by illuminating the IFU through a pinhole. The pinhole size is chosen to allow only one input microlens to be illuminated at one time. The measured spatial (and spectral) PSF is then due to the contribution from one IFU element only. However this method failed as placing the pinhole in front of the IFU required the removal of the baffle. By removing

[4]Values from the CGS4 users manual, (CGS4, 1997).

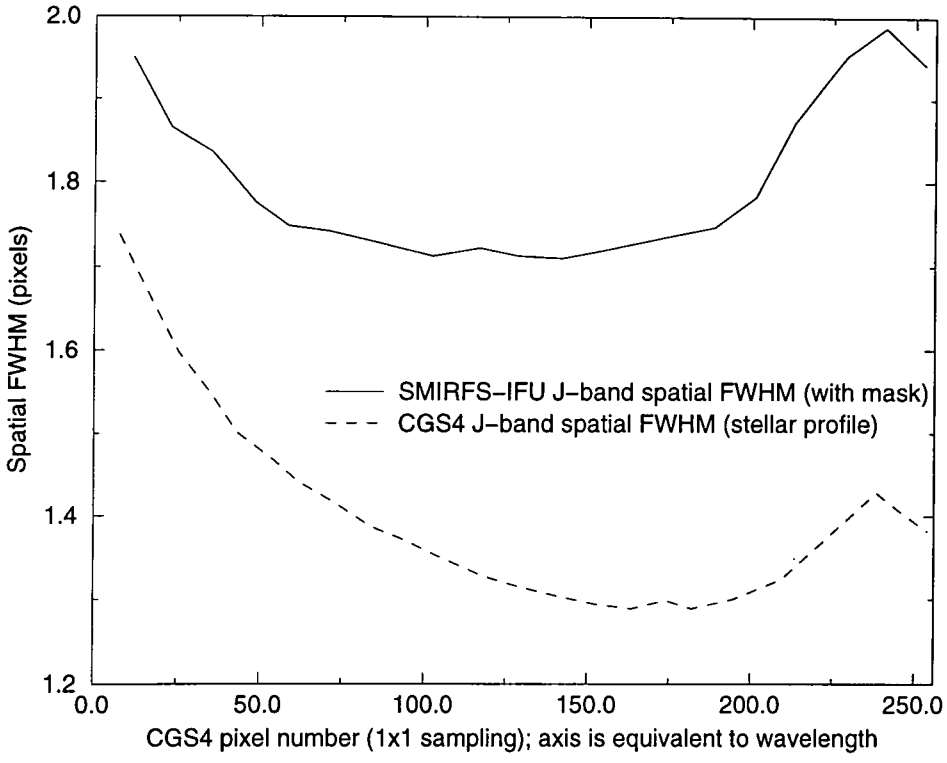

Figure 8.12: Plot to show variation in spatial PSF with detector position (the X-axis also corresponds to wavelength) The solid line shows the spatial FWHM of the IFU in the J-band measured from the mask image shown in figure 8.15. The dashed line shows the spatial FWHM of CGS4 alone measured from the stellar profile in a standard star exposure. Some of the PSF variation in the star exposure will be due to the seeing variations with wavelength as tip-tilt correction works better at longer wavelengths.

the baffle the illumination conditions are sufficiently different, due to increased angle of illumination, that the spatial PSF produced is blurred. Measurement of the spatial PSF was also made difficult by the undersampling of the CGS4 detector in the spatial direction. Therefore the spatial PSF produced by one element could not be measured.

However, it is possible to obtain an indication of the change in the FWHM of the spatial PSF with wavelength by using the magnification set-up mask. The 'big mask' was placed over the SMIRFS-IFU field of view, as indicated in figure 8.4, allowing only the edge lenses to be illuminated. Illuminating the IFU in this way produces six narrow spectra on the detector, as shown in figure 8.15, with each spectrum being due to the contribution from the small group of edge lenses which are illuminated. Illuminating two lenses in this way avoids problems with undersampling in the spatial direction as a minimum of two pixels is always

illuminated. Although this does not give the spatial PSF produced by one element it does allow the variation of spatial PSF across the detector, i.e. the variation of spatial PSF with wavelength, to be measured as shown in figure 8.12. It can be seen that the spatial PSF is narrower in the centre of the detector (on axis) than it is at the edge of the detector. This result shows the same behaviour as the spectral PSF which also shows a broadening towards the edge of the detector. Also shown in figure 8.12, for comparison, is the spatial FWHM of a stellar spectrum obtained with CGS4 alone. The stellar spatial FWHM shows similar behaviour with significant broadening towards the edges of the detector. The SMIRFS-IFU curve is broader, in comparison with the stellar spatial FWHM, because of the blurring caused by illuminating more than one input microlens.

The broadening of the spatial PSF at the edge of the field is consistent with the theoretical ray tracing predictions for CGS4 described in Ramsay-Howat (1994). The theoretical predictions show a 20% rise in the 80% encircled energy diameter at the extreme edge of the detector. This is similar to the percentage change observed in the spatial PSF shown in figure 8.12. This broadening of the spatial PSF at the edge of the detector means that the spatial resolution of the reconstructed integral field image will be degraded at wavelengths which map to extremes in detector position. This is an important systematic effect that should be accounted for when analysing integral field data.

8.5.3 Change in spectral PSF along IFU slit.

The width of the spectral point spread function, for each IFU element, is related to the FRD performance of that fibre. It is the FRD cone from the fibre which illuminates the output microlens defining the effective slit width. Fibres with low FRD can be expected to underfill the output lens producing a smaller effective slit width. This gain in resolution with low FRD (or if the input source underfills the input microlens) is a particular advantage of the pupil imaging operation of the SMIRFS-IFU, as described in Haynes (1995). Therefore the spectral PSF produced by each IFU element provides information about the FRD performance of that fibre. This helps to highlight areas of manufacturing difficulty which preferentially produce fibres with high FRD.

The spectral PSF is also sensitive to any defocus which is present in the image of the SMIRFS-IFU fibre slit. This defocus can be caused by incorrect installation of the IFU

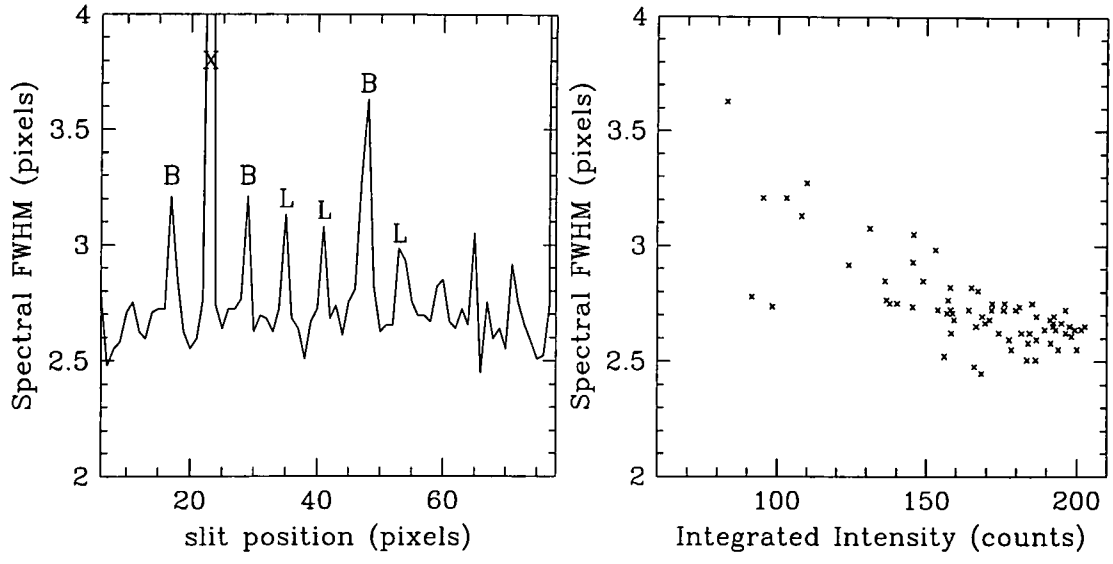

Figure 8.13: The left plot shows the variation of spectral FWHM versus fibre position on the detector. The spike at slit position=23 is due to the broken fibre, labelled 'X'. Damaged fibres, labelled 'B', and low throughput fibres, labelled 'L', have higher spectral FWHM. There is no significant change in spectral FWHM along the IFU slit. The right plot shows the correlation between low intensity (i.e. low throughput fibres) and broader spectral FWHM.

slit in the slit projection unit or manufacturing defects in the construction of the slit. The spectral shift between one PSF and the next also provides information about the shape of the IFU output slit i.e. is the slit straight? The slit is thought to be slightly irregular due to the manufacturing difficulties encountered with the slit blocks described in section 7.3.5.

An accurate measurement of the spectral PSF at each position along the slit can be obtained from the arc line wavelength calibration exposures. To achieve this the spectrum from each detector row, corresponding to each IFU fibre, was cross-correlated with a template spectrum obtained from detector row 42. Detector row 42 was chosen as the template spectrum as it is a region of the detector which is free from the effects of bad pixels. The result of the cross-correlation is a relative velocity shift, which is related to the position of the IFU output lens in the spectral direction, and a velocity dispersion which is related to the width of the spectral PSF. The cross-correlation was done in pixel units rather than wavelength units so that the results could be directly related to distances at the IFU slit. The resulting plot of spectral FWHM versus slit position can be seen in figure 8.13.

Figure 8.13 shows no evidence of a change in spectral PSF with position along the output

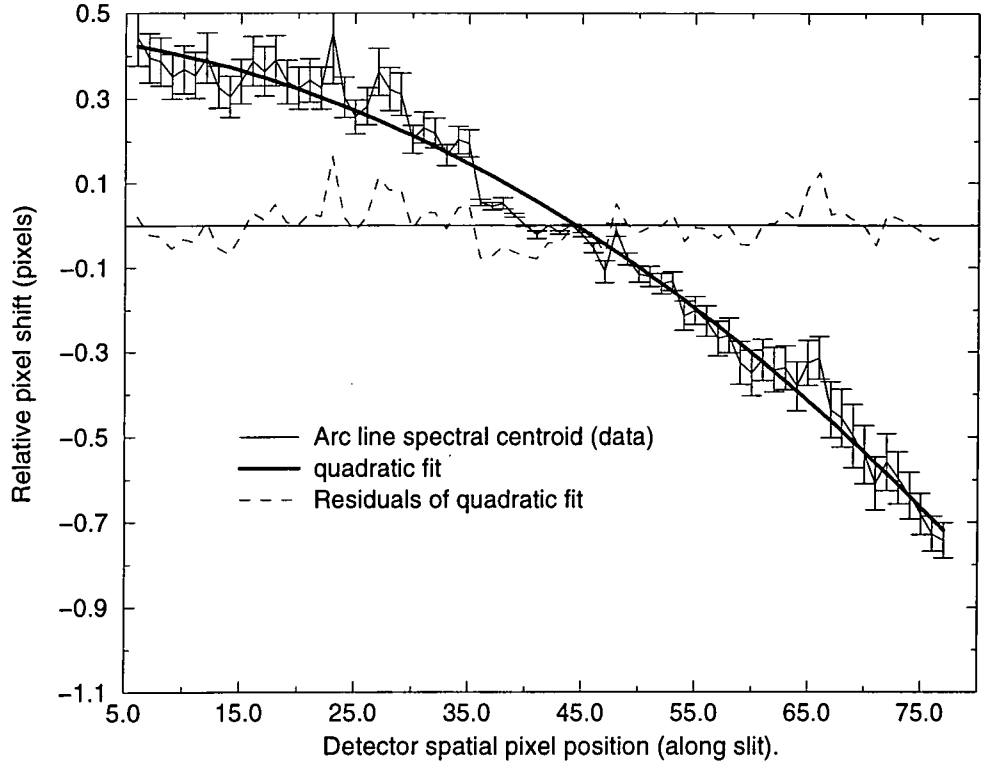

Figure 8.14: Graph of the IFU slit image centroid spectral shift, with respect to the template spectrum, versus fibre position along the IFU slit. Detector row 42 was used as the template spectrum. Error bars are shown to indicate the uncertainty in the measurement of centroid position. The IFU slit image is curved as a consequence of the off-axis operation of the spectrograph optics. The curved slit image can approximated by a quadratic as shown by the solid line on the graph. The residuals from the best fit indicate the accuracy with which the IFU slit was constructed i.e. no slit block is out of position by more than $\sim 80\mu$m.

slit. This indicates that the SMIRFS-IFU output slit is not placed at an angle with respect to the SPU focal plane. There are however peaks corresponding to the positions of low throughput fibres and fibres which were damaged during manufacturing. Low throughput fibres are indicated in figure 8.13 by 'L' and damaged fibres by 'B'. Figure 8.13 also shows the correlation between integrated intensity, which is related to the throughput of the fibre, and the spectral FWHM. Fibres with low intensity, and hence low throughput, produce a broader spectral FWHM. If low throughput fibres correlate to fibres with high FRD then this suggests that high FRD fibres produce a slightly broader spectral PSF at the IFU output slit. The broader PSF is expected as the high FRD fibres will overfill their respective microlenses producing a broader effective slit width. Low throughput and damaged fibres usually occur at the edges of the slit blocks and were indeed measured to have high FRD as described in section 7.7.3. The variation in spectral FWHM from fibre to fibre means that the spectral resolution of the IFU will also vary. Care has to be taken when interpreting the IFU data to remove the effect of spectral resolution variation between the IFU elements.

The cross-correlation also produces an accurate measurement of the relative shift of the test spectrum with respect to the template spectrum. Figure 8.14 shows a plot of the relative shift in spectral position of the IFU slit image with respect to the template spectrum. The graph shows that the image of the IFU slit on the detector is curved. The IFU slit image is also at an angle, of approximately 0.7°, with respect to the detector. A slightly curved slit image is expected due to the off-axis operation of the spherical mirror within the SPU, and as a consequence of the CGS4 grating operating out of the plane of dispersion. The curved slit image can be approximated by a quadratic function. The residuals from the quadratic fit indicate the positioning errors which occurred in manufacturing the IFU output slit. If a slit block was badly positioned (in the spectral direction) it would show up in the residual plot as a group of six fibres offset from all the others. The scatter of the residual plot about zero indicates that none of the IFU slit blocks were badly positioned. The slit block at detector rows 36-41 shows a small offset of approximately 0.1 pixels corresponding to 0.08mm at the slit.

The measurement of spectral FWHM and slit image shape are useful diagnostics in characterization the performance of the IFU. These diagnostics can be used in the construction of future IFUs to improve performance. In particular the measurement of spectral FWHM

provides an accurate way of mapping the positions of fibres with increased FRD.

When reducing the SMIRFS-IFU data it is necessary to remove the effect of the curved slit image to obtain accurate wavelength calibration for each integral field spectrum. This can be achieved using the *transform* package within IRAF. This package maps the shape of the slit image and applies a transformation to remove the shape leaving a straight slit image. Therefore the shape of the slit image and the manufacturing defects do not interfere with the quality of the IFU data.

8.5.4 PSF of reconstructed IFU image

The integral field image was reconstructed using a specially written piece of software. The value of y_{offset} has to be known for the software to extrapolate correctly between pixels which contain information from more than one IFU spatial element. The reconstructed integral field images of standard star exposures, described in section 8.6.1 allow the PSF produced by the star to be measured. The reconstructed stellar PSF had a FWHM of approximately 1.9 arcseconds (the weather conditions were far from optimal during the standard star observations). The measured FWHM in the X direction on the IFU was found to be about 20% broader than the FWHM in the Y direction. The FWHM was found by fitting a gaussian to the reconstructed IFU stellar image. The X axis of the IFU is the direction in which the spatially contiguous elements on the sky are also spatially contiguous on the detector (the shorter axis of the IFU). The reconstructed stellar profile is slightly broadened in the X direction because of the undersampling of the IFU slit in the spatial direction and the crosstalk between adjacent elements on the detector. This broadening effect in one dimension is a consequence of the one fibre per pixel construction of the IFU. This is discussed in more detail in section 5.4.

8.5.5 Spatial position of spectrum.

It is a characteristic of the CGS4 spectrograph design that the spectra are not exactly aligned with the detector rows. The spatial position of the spectrum varies with wavelength due to the distortion caused by the off-axis aberrations of the CGS4 optics. To properly extract the spectrum of each IFU element it is necessary to know the relationship between detector

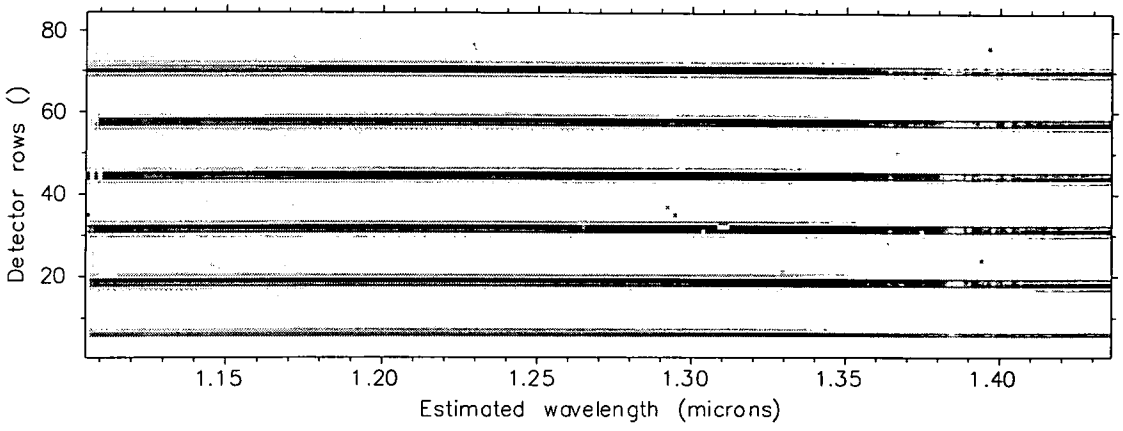

Figure 8.15: J-band magnification set-up mask exposure taken with the 'big-mask' design described in section 8.2.3 and shown in figure 8.4. Each spectrum is due to approximately two adjacent IFU elements being illuminated. As well as measurement of magnification the spectra can be used to calibrate the image distortions of CGS4 and the variation in spatial PSF with detector position.

position and the spatial position of the spectrum. This relationship can be measured from the magnification setup exposures described in section 8.2.3 and shown in figure 8.15. The magnification set-up image produces a series of well spaced narrow blackbody spectra with which to map the distortion of the CGS4 optics.

A graph of the variation in spatial centroid position of the spectrum with detector position can be seen in figure 8.16. The centroid positions, which are fit every 5 pixels, are shown as crosses and the fit to the data is the shown by the dashed line. The fit to the data is a second order Legendre polynomial. It can be seen that the spatial centroid position of the spectrum varies by over half a pixel across the width of the detector. This means that if the IFU spectra have been carefully aligned with the detector pixels at the centre of the chip the spectra will be misaligned by half a pixel at the edge of the chip. Therefore the value of y_{offset}, as defined in section 8.2.3, is variable with position on the detector. The variation in spatial centroid of the spectrum is due to distortion introduced by the CGS4 optics. Each of the five spectra in the image were measured to see if there is any change in the shape of the distortion with detector spatial position. The coefficients of the Legendre polynomial fit to the data were found to vary by only a few percent indicating the distortion is constant across the detector.

If only a narrow wavelength region of the spectrum is of scientific interest it is possible to

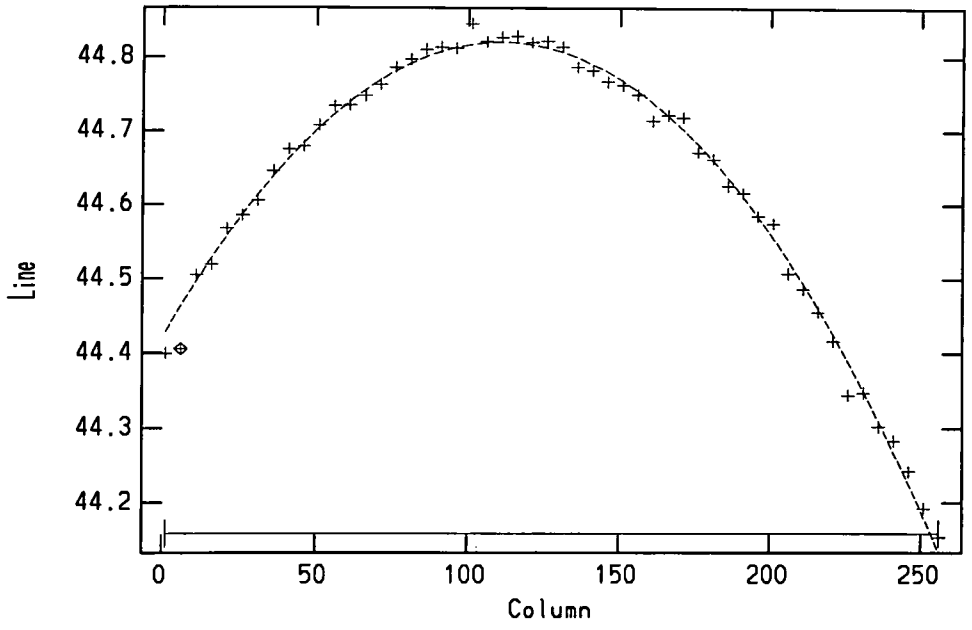

Figure 8.16: Plot of the variation of spectrum spatial position across the detector. The crosses show the measured spatial position of the spectrum (labelled as line) versus detector position in the wavelength direction (labelled as column). The dashed line is the fit to the data with an rms of 0.01 pixels. This trace is for the central spectrum shown in figure 8.15.

set the correct value of y_{offset} for that region and ignore the rest of the spectrum i.e. assume y_{offset} is constant over small regions. If, however, a larger portion of the spectrum is needed it is necessary to calibrate out the distortion of the CGS4 optics. Standard astronomical data reduction software, such as the *transform* package in IRAF, can be used to remove the affects of distortion and rebin the data so that each spectrum is positioned to lie along one detector row. The value of y_{offset} will then be constant with wavelength.

8.6 SMIRFS-IFU Efficiency

The efficiency of the SMIRFS-IFU can be characterized in two ways: the *total system efficiency*, η_{IFU}, and the efficiency of the SMIRFS-IFU alone, T_{IFU}. The total system efficiency is the ratio of the number of photons detected to the number of photons incident above the Earth's atmosphere. Therefore the total system efficiency includes the affects of atmospheric absorption, telescope losses, losses within SMIRFS-IFU and CGS4. It is important to know the total system efficiency accurately in order to calculate instrumental sensitivity

i.e. whether the object of interest can actually be observed with adequate signal to noise. The efficiency of the SMIRFS-IFU alone is found from the ratio of the SMIRFS-IFU system efficiency to the CGS4 system efficiency, η_{CGS4}. The measured throughput of the SMIRFS-IFU can then be compared with the theoretically predicted value. This helps to highlight uncertainties in the design of IFUs where the efficiency of components cannot be accurately predicted, or is lower than expected.

8.6.1 SMIRFS-IFU system efficiency

To measure the efficiency of the SMIRFS-IFU, T_{IFU}, two sets of observations are required. First the total system efficiency of the SMIRFS-IFU is determined from observations of a spectrophotometric standard star. Then the IFU is removed from the telescope and the same standard star is observed with CGS4 alone, from which the system efficiency of CGS4 can be determined. It is important that the atmospheric conditions do not change during the observations otherwise a misleading value of efficiency may be measured. A direct comparison can then be made of the number of photons detected with the SMIRFS-IFU to the number of photons detected with CGS4. This ratio gives the actual throughput of the IFU in isolation, independent of atmospheric losses, telescope losses etc, which are assumed to be the same with and without the SMIRFS-IFU. The system efficiency does include losses resulting from overfilling of the spectrograph pupil (the diffraction grating) due to broadening of the input beam by the IFU optical aberrations.

However, due to the unstable weather conditions experienced during the observing run, it was not possible to measure the efficiency of the IFU in comparison with CGS4. The time needed to remove the IFU from the telescope, reconfigure CGS4, and observe the standard star is approximately one hour. During this time the atmospheric conditions may have changed preventing meaningful results from being obtained. The best that could be done was to observe a standard star with the IFU alone and calculate the overall system efficiency.

The standard star HD203856 was observed with the SMIRFS-IFU in a beam-switched sequence to subtract the night sky. Each observation consisted of a 'quad exposure' which consists of the following exposure sequence: object, sky, sky, object. A telescope nod of 60 arcseconds East was used for background sky observations. The airmass at the beginning and end of the observations was $\sim$ 1.1. After the first J-band exposure was taken

the instrument pickoff mirror was then moved to a different offset such that the standard star illuminates a different part of the IFU input array. The position of the pickoff mirror, described in section 8.2.1, determines where the object falls in the field of view of the IFU. This helps to ensure that the efficiency is measured with a large sample of the IFU spatial elements. Otherwise the efficiency may be measured with spatial elements with high, or low, efficiencies introducing systematic effects into the throughput measurement. Further H-band and J-band exposures were taken after adjustment.

The number of photons per second, Φ, from a star of magnitude m arriving at the Earth's atmosphere can be calculated from the following formula:

$$\Phi = \frac{\pi D^2 f_\nu(0) \Delta\lambda}{4\mathrm{h}\lambda} 10^{-0.4m} \tag{8.2}$$

where D is the diameter of the telescope (3.8m) , $\Delta\lambda$ is the bandwidth, λ is the central wavelength of the observation, h is Planck's constant and $f_\nu(0)$ is the absolute spectral irradiance for magnitude $m = 0$. Tabulated values for $f_\nu(0)$, taken from Zombeck (1989), are 1.65×10^{-23} $\mathrm{Wm^{-2}Hz^{-1}}$ in the J-band and 1.07×10^{-23} $\mathrm{Wm^{-2}Hz^{-1}}$ in the H-band. The J-band is defined as $\lambda = 1.12 - 1.42\mu$m and the H-band as $\lambda = 1.40 - 1.80\mu$m.

The magnitude[5] of the standard star HD203856 is $m = 6.926$ in the J-band and $m = 6.887$ in the H-band. The predicted value of Φ for these magnitudes are listed in table 8.3. Also listed is the observed integrated intensity, I, for the standard star exposure. The integrated intensity is the sum of counts over the entire IFU field in the appropriate wavelength region. The standard star exposure was not corrected for the fibre-fibre flat-field variations in order to measure differencies in transmission between different areas on the IFU.

The overall system efficiency of the SMIRFS-IFU, η_{IFU}, can be calculated using the following equation:

$$\eta_{IFU} = \frac{\mathrm{IG}}{\Phi t n s} \tag{8.3}$$

where G is the detector gain (6 electrons per data number) and t is the length of the exposure in seconds. Two other factors which need to be included are s, the sampling correction factor, and n, the number of summed spectra in the final spectrum. The observations were made with the detector used in (2×2) sampling mode which means that each image consists of

[5]Magnitudes obtained from UKIRT reference manual.
http://www.jach.hawaii.edu/UKIRT/astronomy/calib/ukirt_stds.html

Band	UT	Airmass	Exposure (s)	I	Φ	η_{IFU}
			$t \times m \times (s_1 \times s_2)$	(photons/s)	(photons/s)	
J	14:01	1.073	$5 \times 10 \times (2 \times 2)$	5.296×10^6	114×10^6	2.8%
H	14:34	1.092	$5 \times 10 \times (2 \times 2)$	2.546×10^6	59×10^6	2.6%
J	14:41	1.099	$5 \times 10 \times (2 \times 2)$	4.745×10^6	114×10^6	2.5%

Table 8.3: Summary of SMIRFS-IFU standard star exposures and IFU system efficiency. The exposure time is listed as $t \times m \times (s_1 \times s_2)$ where t is the exposure time, m is the number of averaged observations and s_1, s_2 denote the sampling pattern of the detector.

observations made at four detector positions, with the detector shifted by 0.5 pixels between each observation. When the four separate images are interleaved it effectively doubles the exposure time so the sampling correction factor s=2 is used to correct for this. The number of summed spectra, n, is only relevant to CGS4 observations , discussed in the next section, therefore with IFU observations $n = 1$. The calculated values for the IFU system efficiency are listed in the final column of table 8.3.

The results of the IFU system efficiency show that the H-band efficiency is slightly lower than in the J-band. There is also a 12% variation in the J-band system efficiency between the two sets of observations. This variation is partly because the throughput of the IFU varies with position on the input bundle due to the bad fibres (this is the systematic effect that was mentioned earlier). If the fibre-fibre throughput variation is removed from the two J-band standard star observations the difference in system efficiency between the two observations reduces to 4%. Care has to be taken when applying the fibre flat-field to standard star observations to avoid any changes in the measured flux level which would be equivalent to a change in efficiency. The remaining variation may be due to small changes in atmospheric transmission occurring during the observations.

8.6.2 SMIRFS-IFU sensitivity

The limiting sensitivity can be estimated from the measured total system throughput of the SMIRFS-IFU and the published values for CGS4 sensitivity. The limiting sensitivity with the short camera and the 75g/mm grating is:

- J-band 3-sigma 1 hour = 0.9×10^{-19} Wm^{-2}arcsec^{-2}

- H-band 3-sigma 1 hour = 2.3×10^{-19} Wm^{-2}arcsec^{-2}

These values increase by a factor of 1.4 if beam switching is used. Despite the non-optimal design, this system gives significant advantage over a series of stepped longslit exposures. The advantage is roughly similar to the difference between CGS4 on UKIRT and a slit spectrograph on Gemini (e.g. GNIRS).

These limits are dramatically improved with the long camera and the high dispersion grating which produces high enough resolution to allow digital masking of OH emission lines. The SMIRFS-IFU is intended for use with the long camera in the future. The long camera also provides 2 pixels per fibre sampling in the spatial direction.

8.6.3 CGS4 system efficiency.

CGS4 observations of the standard star HD203856 could not be done during SMIRFS-IFU commissioning due to the atmospheric conditions. However, an opportunity arose to obtain CGS4 observations of HD203856 during service observing[6] on 13 August 1997, allowing the CGS4 system efficiency to be measured. Two and four pixel wide slit observations were obtained in the J and H-bands at the same central wavelengths as the previous SMIRFS-IFU exposures, and at the same airmass. This gives a direct comparison of the CGS4 system efficiency with the previously measured SMIRFS-IFU system efficiency. Of course this assumes that the atmospheric conditions are similar on the two different occasions. Two and four pixel wide slit observations were done so that an adjustment to the counts with the 4 pixel wide slit could be made, if necessary, to account for slit losses.

Each observation consisted of two sets of quad exposures (object, sky, sky, object). With the IFU a sky exposure is taken by nodding the telescope by $\sim$ 1 arcminute away from the object but with CGS4, sky exposures are taken by nodding the object along the slit of the spectrograph. This is a more efficient way of observing with a longslit spectrograph. In the 'object' position the lower half of the slit receives light from the star and the top half of the slit receives background. The telescope is then nodded to move the star along the slit to the 'sky' position so that the top half of the slit now receives light from the

[6]The staff observers at the Joint Astronomy Centre, Hilo, are acknowledged for kindly providing the service observations of HD203856.

Band	Slit	UT	Airmass	Exposure (s) $t \times m \times (s_1 \times s_2)$	I (photons/s)	Φ (photons/s)	η_{CGS4}
J	2pix	08:58	1.10	$0.4 \times 35 \times (2 \times 2)$	1.832×10^6	114×10^6	6.0%
J	4pix	09:19	1.08	$0.2 \times 70 \times (2 \times 2)$	0.487×10^6	114×10^6	3.2%
H	2pix	09:53	1.07	$0.4 \times 35 \times (2 \times 2)$	1.257×10^6	59×10^6	8.0%
H	4pix	10:15	1.07	$0.2 \times 70 \times (2 \times 2)$	0.452×10^6	59×10^6	5.7%

Table 8.4: Summary of CGS4 standard star exposures and system efficiencies. The exposure time is as defined in table 8.3.

star and the bottom half of the slit receives background. This results in two spectra in the reduced image, a positive spectrum corresponding to the object observations and a negative spectrum corresponding to the sky observations. The positive and negative spectra were extracted using the optimal extraction procedure *apall* in IRAF and combined to give the standard star spectrum. Because two sets of observations go to make up the final standard star spectrum this means the correction factor, n, used in equation 8.3 is $n = 2$ for CGS4 observations. A summary of the observations, integrated intensities, and calculated CGS4 system efficiencies can be found in table 8.4.

Table 8.4 shows some unexpected results for the CGS4 system efficiency. Most noticeable is that the summed intensity, I, is less for the 4 pixel wide slit observations than for the 2 pixel wide slit observations including the correction for exposure time. This is unusual as the wider slit might be expected to admit more flux leading to higher counts. The intensity with the 4 pixel wide slit drops by $\sim 47\%$ in the J-band and $\sim 32\%$ in the H-band compared with the 2 pixel wide slit intensity. This leads to lower values for the overall system efficiency with the 4 pixel wide slit. This unusual behaviour may be explained by a number of possibilities:

Slit angle: There is a change in the rotation of the slit between the 2 and 4 pixel wide slit observations (this is readily seen in the data). With the 2 pixel wide slit the angle of the slit image on the detector is 1° anticlockwise from vertical but this changes to $-1.4°$ when the 4 pixel wide slit is used. The two nodded spectra with the 2 pixel wide slit have equal intensity indicating that the star in nodded correctly along the slit. With the 4 pixel wide slit however the positive spectrum has 40% less counts (in both J and H) than the negative spectrum indicating that the star is being nodded off the slit.

Slit position: not only does the angle of the slit image on the detector change but the position changes too. There is a 3.5 pixel offset between the position of the 2 pixel wide slit image and the 4 pixel wide slit image. If the star is aligned with the 2 pixel slit and then observed with the 4 pixel wide slit without checking the slit alignment the star may be vignetted. This movement of the slit was also observed with the IFU as described in section 8.2.2.

Atmospheric transmission: this is unlikely to cause a large change in count rate over such a short period of time. Individual observations showed only a few percent variation in count rate.

Therefore the 4 pixel wide slit result is discounted as it is clear that the standard star was not correctly centred on the slit during these observations. It is possible the astronomer performing the service observations did not 'peak-up' the spectrograph correctly during the four pixel wide slit observations. This would then lead to a lower count rate. It is also possible that the 2 pixel wide slit observations are in error. This problem does however illustrate one of the advantages of observing with an IFU. The large field of view of the IFU makes acquisition easier and avoids slit losses.

The 4 pixel wide slit observations were required to calculate a correction factor to the system efficiency to account for slit losses. This can also be estimated by analysis of the spatial profile of the stellar spectrum. The spatial profile of the stellar spectrum can be accurately fit by a Gaussian of 1.3 pixels FWHM. The variation in the spatial profile across the detector is plotted in figure 8.12. Assuming that the spatial profile of the standard star PSF at the entrance slit to CGS4 is also a gaussian of 1.3 pixels FWHM, i.e. ignoring the effect of image aberrations inside CGS4, then the vignetting caused by a 2 pixel wide slit on the gaussian stellar image amounts to 7%. The actual amount of vignetting is likely to be less than this had the effect of the CGS4 optical aberrations been removed first. In the H-band the spatial profile is narrower than this, due to more optimal tip/tilt correction at longer wavelengths, so slit vignetting will be less than 7%. So only a very small correction, if any, is needed to correct for slit losses with the two pixel wide slit.

Note from table 8.4 that the CGS4 H-band efficiency is 33% higher than the J-band efficiency. The reason for this increase is thought to be the higher efficiency of the 75 g/mm diffraction

Band	Wavelength	η_{IFU}	η_{CGS4}	T_{IFU}
J	$1.12 - 1.42\mu$m	2.8%	6.0%	46.7%
H	$1.40 - 1.80\mu$m	2.6%	8.0%	32.5%
J	$1.12 - 1.42\mu$m	2.5%	6.0%	41.7%

Table 8.5: Summary of SMIRFS-IFU system efficiency, CGS4 system efficiency and SMIRFS-IFU throughput. The difference between the two J-band measurements is thought to be due to flat-field variations in the IFU and atmospheric variations. Note that the H-band efficiency is lower than the J-band efficiency.

grating in the H-band compared with the J-band. Grating efficiency curves could not be obtained for the 75 g/mm grating but the efficiency curve for the 40 g/mm grating (CGS4, 1997) does show that the H-band efficiency is 35% higher than the J-band efficiency.

8.6.4 SMIRFS-IFU throughput

The throughput of the SMIRFS-IFU alone, T_{IFU}, can now be found from the ratio of the SMIRFS-IFU total system throughput, η_{IFU}, to the total system efficiency obtained with CGS4, η_{CGS4}, i.e. $T_{FIU} = \eta_{IFU}/\eta_{CGS4}$. This ratio cancels the effect of common path losses experienced by both CGS4 and the SMIRFS-IFU such as atmospheric transmission, telescope reflection losses and losses within CGS4. The throughput of the SMIRFS-IFU is calculated using the CGS4 system efficiency obtained from the two pixel wide slit observations, the four pixel wide slit observation being discounted for the reasons already mentioned in section 8.6.3. The calculated throughput of the SMIRFS-IFU for both the J and H-bands is listed in table 8.5.

The throughput of the SMIRFS-IFU was measured over the entire J and H pass-bands. The throughput was also measured for monochromatic light to look for throughput variations with wavelength but the SMIRFS-IFU throughput was found to be constant with wavelength within a pass-band. It is clear however, from the table 8.5, that there is large change in the throughput of the SMIRFS-IFU between the J-band and the H-band.

8.7 SMIRFS-IFU efficiency prediction

In this section a theoretical prediction of the SMIRFS-IFU throughput is presented for comparison with the measured value, discussed in the previous section. Each of the loss mechanisms present in the optics of the SMIRFS-IFU is considered in some detail. In most cases the magnitude of the throughput loss was measured for each component during construction of the SMIRFS-IFU in the laboratory. However, measurements could not be done on all the individual components due to time constraints. In some cases the transmission loss due to a particular mechanism is estimated from qualitative assessment done in the laboratory. Careful theoretical analysis of the mechanisms which lead to loss of throughput, coupled with actual measurements of throughput made on the telescope, serves to highlight areas in the manufacture and design of the SMIRFS-IFU that may be improved in the future. Alterations can also be applied to the design and manufacture of future IFU projects (TEIFU and GMOS-IFU) with the aim of building IFUs with improved performance.

In the following analysis of the SMIRFS-IFU throughput the transmission of each component in the optical train is denoted by the symbol T_x, with the subscript x identifying the loss mechanism. A summary of the throughput loss mechanisms is given in table 8.6 together with the magnitude of each loss and the predicted throughput.

8.7.1 Input pupil misalignment

A loss in throughput will occur if the optical axis of the SMIRFS-IFU input microlens array is not aligned correctly with the optical axis of the telescope. This will cause the pupil image of the secondary mirror, formed by the microlenses, to be offset from the fibre core and vignetting will occur. The throughput loss is calculated from the area of the circular pupil image that is intercepted by the fibre core. The transmission averaged over the entire fibre array is given by T_{mis} although losses for individual lenses may be greater than this due to individual fibre positioning errors. Due to the slow focal ratio of the system a misalignment as small as 0.2° produces a throughput loss of 17%. The input microlens array was carefully aligned with the telescope optical axis using the procedure described in section 8.2.1. The maximum error in the alignment was estimated during alignment at the telescope to be $\sim$ 0.1° producing a throughput loss of $\sim$ 8%. The accuracy of the alignment process was

limited somewhat by the aberrations of the input microlens array blurring the projected pupil image. As this is a geometrical loss it is independent of wavelength.

8.7.2 Reflection losses

There are two air-glass surfaces, the surfaces of the microlens arrays, in the SMIRFS-IFU both of which are uncoated. The transmission of an air-glass interface is denoted by T_{ag}. Anti-reflection coatings could not be applied to the microlens surfaces due to the fragility of the microlens material (UV-curing epoxy) previously explained in section 6.7 . Fresnel's reflection losses will occur at each microlens surface producing a total loss in throughput of $\sim 8\%$. This loss is also approximately independent of wavelength as the refractive index does not change appreciably over the J and H-bands.

8.7.3 Absorption in microlens epoxy

The microlens arrays are manufactured using a UV-curing epoxy material which absorbs a small amount of the incident light. The combined transmission of the microlens material for both the input and output microlens arrays is denoted by T_{epoxy}. A graph of the internal transmission of the epoxy versus wavelength is shown in section 6.3.4. The total thickness of epoxy used in manufacturing the lenses is unknown but is estimated to be not more than approximately 50μm for each lens. The average absorption for a 100μm thickness of epoxy is 2.7% in the H-band and is considerably less in the J-band. Therefore a throughput loss of 2.7% in the H-band is an upper limit.

8.7.4 Transmission of Adhesive

The UV-curing adhesive used to fix the microlens arrays to the fibre bundles absorbs some of the incident light as shown in the graph in figure 7.5. The total thickness of the adhesive layer between the microlens array substrate and the fibres , at both the input and the output, is unknown. The glue thickness is expected to be quite small, however, as the effect of surface tension whilst the glue is still liquid causes most of the excess glue to leave the bond area leaving only a thin layer of adhesive remaining. The transmission of the adhesive layer , T_{glue}, is calculated from the absorption spectrum (figure 7.5) assuming a total thickness of

100μm. This gives a transmission of 99.3% in the J-band and 97.7% in the H-band. Again these figures represent upper limits. The drop in transmission in the H-band is due to the absorption feature centred at $\sim 1.75\mu$m.

There may be additional losses in the adhesive layer due to the formation of bubbles. It was noted in section 7.7.5 that bubbles began to form in the adhesive layer on the input microlens array only hours after the array had been fixed in place. Fortunately the bubbles did not spread far enough to reach the active area of the input fibre array. Micro-bubbles may also be present in the glue layer which are too small to see by eye but lead to scattering losses. The presence of bubbles over the active fibres would introduce two additional air-glass[7] surfaces leading to increased Fresnel's reflection losses. Note that a bubble within the glue layer may also act as a small lens although it is unknown how this would affect transmission. The formation of bubbles was only observed on the input microlens array not the output. Losses due to bubbles are denoted by T_{bubb} but are thought to be negligible unless the bubbles spread with time. The reflection losses due to the bubbles are independent of wavelength.

8.7.5 Microlens-fibre misalignment

Due to manufacturing tolerances there may be a small misalignment of the pupil image with respect to the fibre core (this is in addition to misalignment errors with the telescope optical axis). This misalignment will vary from fibre to fibre and occurs both at the input and output microlens arrays. The fibre-lens alignment error budget, which determines the positioning accuracy and hence throughput losses, is discussed in more detail in section 7.3.2. The measured fibre-lens alignment error is $\sim 10\mu$m RMS at the output and $\sim 10\mu$m RMS at the input. The throughput loss due to microlens-fibre misalignment at both the input and output to the fibre bundle is denoted by T_{ifl}. The fibre core and the pupil image can simply be regarded as uniform circles if geometrical optics is assumed. The reduction in throughput, due to a misalignment of the pupil image with the fibre core, is then found from the area of overlap of the two circles represented by the fibre core and the pupil image. This simple treatment does not take into account the additional losses due to blurring of the pupil image by the microlenses due to optical aberrations and diffraction broadening. Diffraction losses are discussed separately in section 8.7.8. A misalignment of the fibre with the microlens at

[7]In fact the bubbles are thought to be in a vacuum so it will be a vacuum-glass interface

the output causes the projected pupil image to appear at the wrong position inside CGS4. This will cause vignetting inside CGS4 at the Lyot stop and at the diffraction grating both of which are at pupil positions. An RMS misalignment of 10μm produces a reduction in throughput of 6% at the input array and output arrays.

8.7.6 Scattered light losses

Scattered light caused by imperfections on the surface of the SMIRFS-IFU microlenses is thought to contribute significantly to throughput losses and is a major cause for concern. The measurement of scattered light for the SMIRFS-IFU microlenses is discussed in more detail in sections 6.4.2 and 6.4.3. Each microlens produces a background level of diffuse and scattered light which extends over the entire area of the microlens. There is also a variation in surface quality between the SMIRFS-IFU input microlenses and the output microlenses such that the output microlenses produce more scattered light. Only a small fraction of the scattered light produced by the input microlenses is captured by the optical fibre. Most of the scattered light at the input is lost leading to a reduction in throughput. Scattered light produced by the output microlenses will be blocked by the baffles present inside CGS4.

The scattered light losses are predicted by equation 6.5 to be inversely proportional to the wavelength squared. The total scattered light loss can be estimated from the plots of azimuthal encircled energy, measured from the microlens point spread functions, shown in figure 6.27. At the radius of the fibre core (75μm) $\sim$ 7% of the light is lost outside the fibre for the SMIRFS-IFU input microlens. This value increase to $\sim$ 22% for the output microlens. These values need to be corrected for the wavelength dependence of scattered light given by equation 6.5. The combined transmission of the input and output microlenses, T_{scatt}, is listed in table 8.6.

Note, however, that there is some uncertainty in the accuracy of equation 6.5 to predict scattered light loss, especially as the amount of scattered light becomes large. Therefore the value of T_{scatt} given in table 8.6 is rather uncertain. Ideally it is necessary to measure the scattered light losses directly at infrared wavelengths. It is known, from the EE curves in figure 6.27, that a considerable amount of light is lost due to scattering at visible wavelengths. Clearly the subject of scattered light loss due to the surface quality of the microlenses is an area that requires more investigation.

8.7.7 Fibre transmission

The transmission of the optical fibre is denoted by T_{fibre}. The length of the fused Silica fibres used in SMIRFS-IFU is 1.2m. Typical attenuation figures for Ultra-low OH^- optical fibre in the near infrared are less 10dB/km with a small absorption peak at $\sim 1.4\mu$m where the attenuation increases to 60dB/km. Therefore absorption in the optical fibres is negligible for such a short length of fibre used in the J and H-bands.

There will also be losses at the ends of optical fibre due to the way the fibre ends were prepared. In most cases the fibre ends are finely polished, as described in section 7.6, with very few surface defects and hence good transmission. However in some cases the fibres became lose (or broke free altogether) during the polishing process leading to damaged fibre ends being produced. Typically the fibre end can become rounded and surface roughness is produced. The surface roughness will produce scattered light losses. As the fibres are glued to the microlens array substrate using index matching adhesive it is thought that many of the surface defects will filled in by the adhesive. It is unknown exactly what sort of an effect index matching glue has on reducing polishing defects. Microbubbles may also form in the glue layer at the end of the fibre leading to throughput losses. The end losses described will vary from fibre to fibre and are difficult to predict for the purpose of calculating efficiency. A total fibre ends loss of $\sim 2\%$ is therefore assumed averaged over all fibres at both the input and output ends.

8.7.8 Diffraction losses

Diffraction occurs at both the input and output microlens apertures and at the fibre core aperture. In this section diffraction losses, T_{diff}, due to the microlens apertures are considered with diffraction losses caused by the fibre core size being dealt with in the section on FRD losses (section 8.7.9). Note that diffraction by the fibre core can be thought of as an additional source of FRD and is therefore treated that section. The difference between the two sources of diffraction loss should be made clear. Diffraction by the microlens apertures causes a broadening of the pupil image leading to losses at the fibre core and the diffraction grating due to vignetting. Diffraction by the fibre aperture also causes additional broadening , and hence losses, but is a separate mechanism and is treated in the next section.

The effect of diffraction by the input microlens aperture is to blur the pupil image which occurs at the fibre core. This causes losses at the fibre edges as the fibre core is not large enough to accept the increased image size. This problem can be overcome in visible light IFU designs by using oversized fibre cores but in the infrared the fibre cores have to be kept smaller than the pupil image to prevent background light from entering the fibre. The throughput loss which is caused by diffraction broadening of the pupil image was found by convolving the diffraction PSF produced by the lens with a circular top hat function which represents the fibre core. From the convolved image the ratio of the integrated intensity within the fibre radius to the total integrated intensity was measured. This ratio gives the throughput of the fibre, the additional intensity being lost to the cladding of the fibre. This convolution process can also be used to calculate the throughput losses due to the optical aberrations of the SMIRFS-IFU microlenses. However tests of the microlens PSF, described in sections 6.4.2 and 6.4.3, showed the microlens PSF to be of high quality and consistent with the predicted diffraction-limited PSF. Therefore the throughput losses are adequately described by diffraction losses alone.

Diffraction by the output microlens causes the pupil image which occurs at the CGS4 pupil (the diffraction grating and Lyot stop) to become broadened. As the CGS4 pupil is of a finite size, throughput losses due to overfilling of the pupil can also be expected within CGS4. Diffraction losses at the output are more difficult to predict due to the lack of knowledge about the CGS4 optics, they are therefore estimated to be the same as at the input. Of course, diffraction losses are greater in the H-band due to the wavelength dependence of diffraction broadening.

8.7.9 Focal ratio degradation

Possibly with the exception of scattered light losses due to the microlens surfaces, focal ratio degradation is the dominant loss mechanism in the SMIRFS-IFU (and fibre IFUs in general). The effect of FRD is to cause the output focal ratio of a fibre to be smaller (faster) than the input focal ratio. FRD is therefore equivalent to a non-preservation of etendue. Normal FRD is caused by scattering at the core/cladding boundary within the optical fibre (Vanderriest *et al.*, 1994) producing a wider range of angles when the beam is totally internally reflected. The output focal ratio of the fibre is also broadened by diffraction which occurs at the fibre

core. This broadening is not due to the internal structure of the fibre so is not strictly FRD but the overall consequence is the same so it is included here as an additional source of FRD loss. The transmission loss due to the effects of FRD is denoted by T_{FRD}. The amount of FRD produced by the fibre is also dependent on the way in which the fibre is mechanically fixed. Mechanical stress induced by the components which hold the fibre will increase the amount of FRD. FRD is variable from fibre to fibre due to imperfections in the mechanical assembly process, and as such, the throughput can be expected to show variations from fibre to fibre.

The optical design of the SMIRFS-IFU allowed for the ~F/13 input beam to be degraded to approximately F/7.5 with minimal loss of throughput. The effect of FRD on the optical design was discussed in section 5.3.3. However, the magnitude of FRD that can be expected for a given input focal ratio and type of fibre is notoriously difficult to predict. Indeed the FRD tests which were performed during the construction phase of the SMIRFS-IFU (section 7.7.3) showed that the FRD performance of the fibre bundle was worse than expected. The output microlenses subtends an angle corresponding to F/7.5 at the optical fibre. Therefore light which exits the fibre outside this angle, i.e. faster then F/7.5, is vignetted by the output microlens and is lost from the optical system. During the construction phase the best FRD performance measured for the SMIRFS-IFU was an output beam of approximately F/10 (at 633nm) produced by a collimated input beam. It should be noted that the broadening of a collimated input beam to an output of F/10 is partly due to diffraction. Removing the effect of diffraction broadening reduces the amount of FRD to $\sim F/10.5$.

If the same amount of FRD broadening is applied to an F/13 input beam (the focal ratio produced by the input microlenses) the output focal ratio will be broadened to approximately F/5.8. This focal ratio overfills the output lenses such that approximately 24% of the light is lost, assuming uniform illumination with angle. This loss is even more severe when diffraction broadening is also included. Diffraction by the small aperture fibre core broadens the output focal ratio by an additional small amount producing a final output focal ratio of approximately F/5.5. This leads to a total transmission, T_{FRD}, of $\sim$ 67% in the J-band and $\sim$ 66% in the H-band. The H-band transmission is slightly lower due to the increased diffraction broadening with wavelength.

Note, however, that these calculations are based on the worst FRD that was observed during

construction and represent the extreme case. The actual FRD loss for a particular fibre may be expected to be less than this. As the other loss mechanisms present with the SMIRFS-IFU can be estimated with better accuracy, the losses due to FRD are left as a variable in table 8.6. The measured SMIRFS-IFU throughput, and the other loss mechanisms, can then be used to estimate the FRD loss for comparison with the above estimate.

The estimate of FRD losses presented here, in comparison with the other loss mechanisms summarised in table 8.6, clearly highlights the earlier statement that FRD is the dominant loss mechanism in a fibre based IFUs. It is very important to fully understand FRD losses to allow modifications to future IFU designs. Only if the design of IFUs is suitable to minimise FRD losses will maximum performance be obtained. FRD measurement, prediction, and modelling is therefore an area which requires further research to aid the design of future IFU projects.

FRD is also thought to be largely responsible for the fibre-fibre throughput variations that were measured in the fibre flat-field described in section 8.3. Fibres which experience increased stress will produce worse FRD and hence have lower transmission. The measured RMS variation in fibre transmission is 14%. This implies that the preceding calculation of throughput loss due to FRD is somewhat variable from fibre to fibre.

8.7.10 Slit projection unit losses

The two main sources of loss due to the slit projection unit are reflection losses and vignetting of the reimaged IFU output slit by the CGS4 slit. The loss mechanisms present in the SPU are summarised below:

- There are two reflecting surfaces present in the SPU. The spherical mirror is gold coated and the folding flat mirror is Aluminium coated. Both mirrors are a number of years old so it is likely that the coatings have degraded slightly somewhat due to aging. The reflectivity of the mirrors is estimated to be 97% for the Gold coating and 95% for the Aluminium coating producing a total transmission for the SPU mirrors, R_{SPU}, of 92%. This loss is approximately independent of wavelength in the region $1.2 - 1.8\mu$m.

- The image of the SMIRFS-IFU output slit at the CGS4 slit will be vignetted if the slit image and the CGS4 slit are not correctly aligned. The transmission of the slit is

denoted by T_{slit}. The alignment process was carried out very carefully, as described in section 8.2.2, to ensure high accuracy. The offset between the CGS4 slit and the SMIRFS-IFU slit image was measured to be 0.1 pixels on the CGS4 detector. The angular misalignment of the two slits was less than 0.2°. For the purpose of calculating the amount of vignetting caused by these alignment errors, the SMIRFS-IFU slit image is assumed to be a Gaussian with 1.1 pixels FWHM. The CGS4 slit is 2 pixels wide and vignettes the light in the wings of the Gaussian producing a variable vignetting of 3.2-5%. The amount of vignetting along the slit is variable because of the small rotation of the SMIRFS-IFU slit with respect to the CGS4 slit.

In the calculation of vignetting losses at the CGS4 slit it was assumed that the SMIRFS-IFU slit image is the same at the CGS4 slit as it is at the detector. The SMIRFS-IFU slit image was measured to be a Gaussian of 1.1 pixels FWHM from an arc spectrum as described in section 8.5.1. This simple treatment does not include the effect of optical aberrations produced by CGS4 which will broaden the measured profile. Therefore the actual amount of vignetting by the CGS4 slit is likely to be lower than that predicted.

8.7.11 Results of SMIRFS-IFU throughput analysis

The various SMIRFS-IFU throughput loss mechanisms, described in sections 8.7.1–8.7.10 are summarised in table 8.6. The values listed are estimates based on the data obtained during manufacture and the results of commissioning, and therefore may include some error. The calculated throughput of the SMIRFS-IFU is listed in the penultimate row for comparison with the measured throughput described in section 8.6.4. The theoretically predicted throughput in the J-band is lower than the measured value. This is likely to be due to an overestimate of the loss due to FRD. It was explained earlier that the FRD loss was for the worst case FRD. The measured J-band throughput implies that losses due to FRD are less at $T_{FRD} \sim 73\%$. Even with this correction FRD is still the major loss mechanism

The situation is less clear in the H-band where the theoretically predicted throughput is significantly higher than the measured value. The H-band throughput is expected to be slightly lower than the J-band throughput due to the combined effects of diffraction and transmission losses which are both worse in the H-band. However the low measured value

		J-band	H-band
Fibre bundle:			
Misalignment with secondary	T_{mis}	95.0%	95.0%
Fresnel reflection losses	T_{ag}^2	92%	92%
Transmission of microlens epoxy	T_{epoxy}	99.9%	97.3%
Transmission of adhesive	T_{glue}	99.3%	97.7%
Losses due to bubbles	T_{bubb}	100%	100%
Input fibre-lens misalignment	T_{ifl}	94%	94%
Scattered light losses	T_{scatt}	93%	97%
Fibre transmission	T_{fibre}	98%	98%
Diffraction losses	T_{diff}	94.5%	92.4%
FRD losses†	T_{FRD}	66%	65%
Slit projection unit:			
Reflectivity losses of mirrors	R_{SPU}	92%	92%
Misalignment of IFU/CGS4 slit	T_{slit}	95%	95%
SMIRFS-IFU throughput theory	T_{IFU}	**40.5%**	**39.0%**
SMIRFS-IFU throughput measured	T_{IFU}	**45%**	**32%**
SMIRFS-IFU throughput measured‡	T_{IFU}	*50%*	*46%*

Table 8.6: Summary of SMIRFS-IFU throughput loss mechanisms. † indicates the value is for the worst case FRD. ‡ indicates results obtained in the February 1998 SMIRFS observations (courtesy of James Turner).

for the H-band transmission implies the throughput estimate is too ambitious or there is some error in the throughput measurement. Given the non-optimal observing conditions experienced during the standard star observations, and the subsequent problems with the CGS4 service observations, the latter is more likely.

The reasonable agreement between the measured and predicted throughput in the J-band indicates that the throughput of the IFU can be estimated with some certainty. It is likely that most of the loss mechanisms will be improved in future design of IFUs. Losses due to misalignment with the secondary mirror will be less critical with IFUs used on faster telescopes. Fresnel's reflection losses can be eliminated by use of appropriate antireflection coatings. Absorption within the microlens epoxy and the adhesive layer can be minimised by choice of suitable materials. Microlens scattered light losses will be minimised by collaboration with microlens manufacturers (AOA) to develop improved manufacturing methods. Diffraction losses may be reduced by use of oversize fibres, as can fibre-lens misalignment errors. Losses due to the slit projection unit are, of course, intrinsic to SMIRFS and do not apply to other designs of IFU. If these improvements are made, for example reducing the effect of each loss mechanism by 50% and ignoring losses intrinsic to SMIRFS, then the theoretical throughput of an IFU increases to $\sim 80 - 90\%$ depending on FRD.

The loss mechanism which is most important to be addressed in future research is FRD. FRD is the major loss mechanism and also the most difficult to predict. Future IFU design has to be done carefully to minimise losses due to FRD. It is likely that to achieve the best performance that FRD tests should be done on the fibre bundle prior to the addition of the microlenses. In this way the microlens design can be adjusted to produce optimum FRD performance. The change in throughput with FRD is evident in the fibre to fibre flat-field shown in figure 8.7. The best fibres have a transmission that is $\sim 20\%$ higher than the mean indicating the throughput gain that can be achieved by reducing FRD.

N.B. Additional measurements of the throughput of the SMIRFS-IFU were obtained during February 1998 and these are listed in italics at the bottom of table 8.6. James Turner is acknowledged for providing these measurements. Note that the H-band throughput is only slightly lower than the J-band throughput consistent with the additional losses in the H-band compared with the J-band. These measurements were made after alterations to the SMIRFS-IFU fibre bundle to improve the FRD performance and are therefore expected to

show higher transmission.

8.8 Summary & Conclusions

This chapter described the set-up, alignment and test observations performed with the SMIRFS-IFU during commissioning in June 1997. Installation and alignment of the SMIRFS-IFU with the telescope was straightforward. There was a limitation to the accuracy with which the IFU optical axis could be aligned with the telescope due to the aberrations of the input microlenses. The need to align each spatial element of the IFU with a detector pixel produced some minor problems. The alignment changed between observing in the J and the H-bands requiring adjustments to be made between J and H-band exposures. Gravitational flexure, thought to originate within CGS4, also caused the IFU slit to become misaligned with the detector pixels. These problems simply mean that the observer has to be careful to carry out adequate calibration exposures during SMIRFS-IFU observing.

The relative fibre to fibre throughput variation for the SMIRFS-IFU was found to exhibit significant structure. A regular drop in the fibre throughput, with a period of approximately six pixels, was traced to a manufacturing problem. The cause was that fibres situated at the edge of the output slit blocks exhibited higher FRD and hence lower throughput. This fault can be remedied before further use of the IFU. The observed change in intensity across the fibre to fibre flat-field was thought to be due to an angular misalignment of the input microlens array with the tube array. Again the limitation to the alignment accuracy was attributed to the aberrations of the microlenses. The fibre to fibre flat-field can be readily removed from the data by use of dome flat-field or sky flat-field exposures to an accuracy consistent with photon noise.

The importance of adequate baffling was confirmed by the observation of a factor of two increase in the background light intensity when the IFU baffle was removed. This stresses the need for careful baffling in future IFU designs, particularly on infrared telescopes where the telescope itself is unbaffled.

Measurement of the spectral PSF of the SMIRFS-IFU indicated that the spectral resolution is as high as that obtained with CGS4 alone. This means the IFU can be used without degradation in spectral resolution but with the advantage of the larger field of view of the

IFU compared with the narrow CGS4 slit. This demonstrates the concept that an IFU can be fitted to an existing astronomical spectrograph without significantly degrading the spectral resolution of the instrument. The spectral PSF showed a small variation from element to element which, in some cases, was attributed to variations in the FRD performance of the fibres. Fibres with high FRD produce broader PSFs as they overfill their output microlens.

The poor atmospheric seeing conditions experienced during commissioning observations served to illustrate one of the advantages of integral field spectroscopy i.e. the action as an image slicer, providing high resolution observations of a point source, in bad seeing conditions, without the loss of light associated with using a narrow slit. The cross talk between adjacent IFU elements on the detector was found to introduce a blurring, along the corresponding axis, of the reconstructed IFU image of approximately 20%.

The second part of this chapter described observations of the standard star HD203856 to determine the total system throughput of the SMIRFS-IFU, telescope and CGS4. The total system efficiency was found to be 2.8% in the J-band and 2.6% in the H-band. The total system efficiency of the telescope and CGS4 was measured separately at a later date. The ratio of the system efficiency with SMIRFS-IFU to that with CGS4 provides a measure of the throughput of the SMIRFS-IFU alone. The throughput of SMIRFS-IFU was therefore found to be 47% in the J-band and 33% in the H-band.

The measured value of the SMIRFS-IFU throughput was then compared with the theoretically predicted value. The theoretical prediction of efficiency listed the various mechanisms which contribute to reduce the throughput of the SMIRFS-IFU. The major loss mechanism, and the one which is the most cause for concern, is focal ratio degradation causing vignetting at the output slit. Comparison of the measured IFU throughput and the predicted value show FRD losses of approximately 27%. The SMIRFS-IFU does perform as predicted, however, indicating that the construction was a success and there are no major loss mechanisms other than FRD. Further investigation of FRD and ways of reducing it is therefore identified as an important area which requires more research if future designs of IFU are to be improved.

Chapter 9

Observing with the SMIRFS-IFU

Abstract

This chapter describes astronomical observations performed with the SMIRFS-IFU after commissioning at UKIRT. Observations of the Seyfert Galaxy, NGC7469, are presented including analysis of the integral field data cube and a description of the data reduction process.

9.1 Introduction

The purpose of any astronomical instrument, of course, is to do astronomy and the SMIRFS-IFU prototype is no exception to this. The SMIRFS-IFU provides a unique capability to do integral field spectroscopy in the J and H-bands. The high spatial resolution provided by the UKIRT tip/tilt secondary mirror coupled with the high throughput, high resolution, and extended field of view of the SMIRFS-IFU, provides a powerful instrument with significant advantages over traditional longslit spectroscopy. This chapter begins by describing the techniques that need to be employed to obtain the best performance with the SMIRFS-IFU. The emphasis is on accurate calibration of the instrument during observing in order to obtain the highest accuracy in the reconstruction of the integral field data cube. The data reduction procedure used to produce the data cube is then described in some detail. Finally scientific observations of the Seyfert 1 galaxy NGC7469 are described. Despite the bad weather and the limited exposure time these observations demonstrate the enormous potential and information gathering ability of infrared integral field spectroscopy.

9.2 Observing with the SMIRFS-IFU

The SMIRFS-IFU is a slightly unusual instrument due to the requirement to keep the fibres accurately registered with the appropriate pixel. It is very important to carry out the necessary calibration exposures to determine the position of each fibre on the detector. This needs to be accurately known for correct reconstruction of the data cube. The following sections briefly describe the observing procedure for use with the SMIRFS-IFU.

9.2.1 Target acquisition

Target acquisition with UKIRT is done by means of the acquisition and guidance camera, called the cross-head camera, which is located at the Cassegrain focus of the telescope. For UKIRT common user instruments the position on the cross-head camera which corresponds to the centre of field of view of the instruments is already known. However, as the SMIRFS-IFU is a new instrument this offset has to be calibrated in order to accurately acquire objects within the IFU field of view.

The offset between the centre of the field of view of the cross-head camera and the SMIRFS-IFU field of view was found by observing a relatively bright star. The telescope was then scanned in a pattern on the sky until the star was located within the field of view of the IFU. Once the star is located on the IFU the integral field image can be reconstructed to reveal the exact position of the star. If the orientation of the IFU on the sky is known then the final offset to bring the star into the centre of the IFU can be calculated and applied to the telescope. Once this offset is known it is straightforward to acquire the next object providing the offset does not change with sky position. During commissioning the crosshead offset needed recalibrating from night to night as the IFU input was constantly being removed and replaced from the telescope leading to small changes in the offset. It is therefore important to check the cross-head offset before each nights observing to ensure accurate pointing of the IFU.

Because of the large field of view of the IFU compared with a narrow slit it is not absolutely necessary to have sub arcsecond pointing with the IFU. Small pointing errors can be accommodated within the field of view. If the object completely fills the IFU field of view it is however necessary to know where on the object the IFU is pointing.

It may be necessary to make some correction for atmospheric refraction if the observation is to be made at large, $> 45°$, zenith distances. This is because the cross-head camera which is used for field acquisition , and guiding, is sensitive to blue light (it is an IPCS system) that passes through the pick-off mirror whereas the observations will be carried out in J and H. At a zenith distance of 60° and a wavelength of $\lambda = 1.2\mu$m there is a 1.2 arcsecond offset between the blue image ($\lambda = 0.5\mu m$) used for guiding and the infra-red IFU image. For point like objects this is not really a problem as the source will still lie within the field of view of the IFU but for extended sources it makes calculating the IFU position on the object slightly more difficult.

9.2.2 Background subtraction.

When used in longslit mode background subtraction with CGS4 is done using the sky region available on the longslit image either side of the object. However with the SMIRFS-IFU the whole length of the slit is devoted to the IFU field of view and unless the seeing confined to a few spatial elements and the object is a compact source then there will not be any sky information available within the IFU field of view. In this case sky observations have to done for each individual object observation by nodding the telescope to a nearby region of sky that is free from contamination by the object. The size of this sky offset is dependent on how extended the object is but is typically 60 arcseconds.

Background subtraction was achieved via beam switching. This removes the background provided that it does not vary on a time scale faster than the time taken to perform the beam switch. Note that some background exposures can contain ripple that is not present in the object exposures. The cause of this is thought to be electronic pickup between CGS4 and the telescope. This problem occurred with the SMIRFS-IFU because the slit projection unit was not insulated, unlike the CGS4 calibration unit which it replaced. The ripple has the appearance of a sine wave, with a period of about 8 pixels, super-imposed over the spectrum with an amplitude of a few percent. It is straightforward to remove ripple by use of suitable data reduction software.

Beam switched observations were done in pairs, usually in the following sequence (called a 'quad exposure' in CGS4 jargon): object, sky, sky, object. By observing object and sky in this manner changes in temporal changes in the background intensity are followed by

the observations. This leads to higher accuracy in the background subtraction. Changes in atmospheric transmission are also accurately tracked.

Tests on sky minus sky exposures indicate that the background level varied by up to 5% during the exposures. Background subtraction can be achieved more accurately than this as changes in the background level are also matched by equivalent changes in the object counts i.e. if the object counts fall by 5% then the background level also drops by 5% indicating the change in count rate is due to fluctuations in atmospheric transmission. Object and sky exposures are done in pairs so that changes in atmospheric transmission are similar in both object and sky exposures and have the least effect on the accuracy of the background subtraction.

9.2.3 Exposure sequence

The following is a summary of the different types of exposures necessary to achieve correct performance of the SMIRFS-IFU. Many of the exposures are required for correct calibration of the SMIRFS-IFU in order to extract the integral field data cube. Calibration exposures are also described in the relevant sections in chapter 8.

- Magnification mask exposures to measure M and y_{offset}. Exposure times are typically 1 second for zero order images and 10 seconds for dispersed images.
- Detector flat-field exposures taken with CGS4 alone (no IFU) to determine the detector flat-field independent of SMIRFS.
- Dome flat-field exposures with SMIRFS-IFU. Exposure times are 2 seconds for H and 5 seconds for J. This calibrates the relative fibre to fibre throughput variation.
- Calibration arc exposures for accurate wavelength calibration. Argon exposures are 0.3 seconds in J and 1 second in H. Krypton exposures are 0.3 seconds in both J and H.
- 'Thin mask' exposures to calibrate CGS4 image distortions. Exposure times are the same as for dome-flats.

- Science observations (object + sky). Exposure times will have to be calculated using the known sensitivity described in section 8.6.2.

9.3 Data reduction procedure.

The data reduction procedure for SMIRFS-IFU data is slightly different from many other fibre based instruments due to the mapping of one fibre to one pixel. Therefore data reduction techniques applicable to multifibre spectra, which are normally separated by a few pixels, cannot be used. This section describes the data reduction steps that were developed for the reduction of SMIRFS-IFU. The production of the data cube from the 2D spectral image is also described.

9.3.1 Types of bad pixel

The main purpose of data reduction is to remove or reduce the effect of the various sources of noise in the data and to get the data into a format suitable for scientific analysis. With integral field data this format is typically a data cube with both spatial and spectral information. A major contribution to the noise in the data is from bad pixels on the detector. The types of bad pixel fall into various categories depending on the source of the noise. Each type of bad pixel requires a slightly different technique to remove its effect.

Dead pixels Dead pixels simply do not detect light. The positions are known from the CGS4 bad pixel mask and are flagged as bad pixels by the CGS4DR software. The CGS4 bad pixel mask for the detector configuration used with the SMIRFS-IFU contains the positions of 5974 known bad pixels. Most of these occur in the two rows either side of the active region on the chip, as seen in figure 9.1. Areas which are flagged by the bad pixel mask are ignored in the subsequent data reduction process.

Hot pixels Hot pixels are easily seen in long exposures as pixels with a count rate which is much higher than the local average. Hot pixels do not always subtract satisfactorily due to the higher noise associated with hot pixels. With 2×2 detector sampling the process of interleaving the separate dither positions causes hot pixels to be seen as

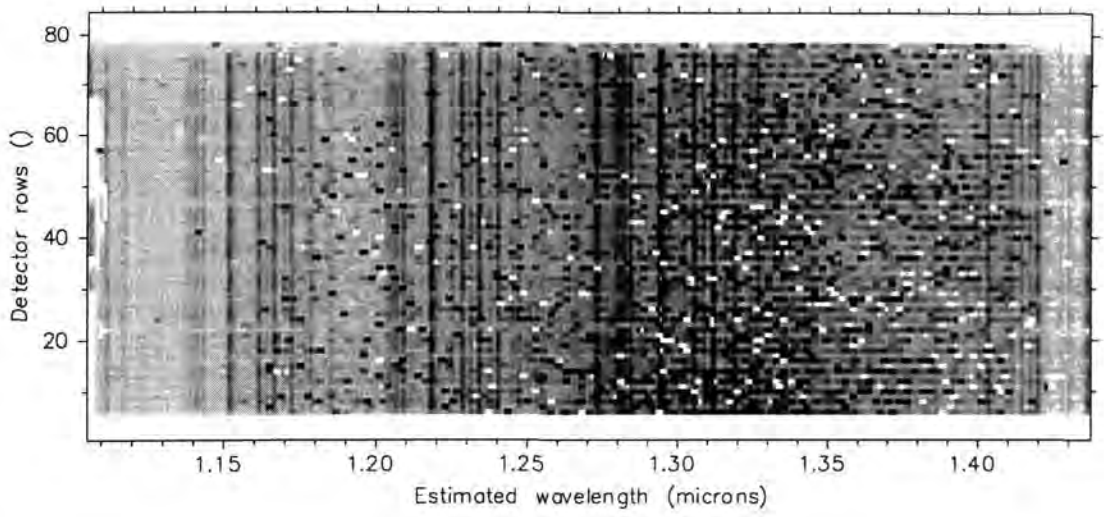

Figure 9.1: Sky exposure with threshold mask applied (photographic negative). Bad pixels which have been flagged by the threshold are shown in white. Remaining hot pixels are seen as dark spots. The night sky emission lines can be seen.

"hot stripes", as seen in figure 9.1. Hot pixels are normally removed by subtraction of a dark exposure.

Low response pixels These are regions of the detector where the quantum efficiency of the pixels is less the local average efficiency and are seen as regions with low count rates, as shown in figure 9.2 at detector position: $\lambda = 1.27\mu$m row=34. The effects of low response pixels can be corrected using a suitable detector flat-field exposure.

9.3.2 Removal of bad pixels

The first step in the data reduction procedure is normally to subtract the detector bias level and dark frames. However, due to the way the CGS4 detector operates, using non-destructive read mode[1] , there is no bias level present to be subtracted from the data. The detector does produce a dark current which can be removed by the subtraction of dark frames. Unfortunately it was found that subtraction of dark frames did completely remove the presence of hot pixels. It is thought that the intensity in hot pixels varies from exposure to exposure limiting the accuracy of the dark subtraction. Therefore an alternative method of removing hot pixels was developed.

[1]Non-destructive read mode is described in the CGS4 users manual.

It was found that hot pixels could be readily identified in sky frames as pixels with count rates significantly above the mean, as shown in figure 9.1. Similarly low response pixels can be also be identified as being significantly below the mean. Therefore a threshold level can be applied to the sky exposures to remove pixels with count rates outside certain limits. This effectively removes hot and low response pixels. The lower threshold cut off was set to zero and the upper threshold value was set to 500 counts. Pixels outside these limits are identified as 'bad pixels' by the software and are ignored in future data reduction steps, i.e. they are flagged as bad pixels producing a bad pixel mask. The upper threshold has to be set high enough to avoid thresholding the real data whilst low enough to exclude as many hot pixels as possible. The upper threshold value was set to 3σ above the mean after analysis of a histogram of count rate. The chances of removing real sky information are therefore $< 0.15\%$. In the final mask image there are 1173 pixels flagged as bad on the active area of the detector which accounts for 3% of the total active area. The bad pixel mask image is applied to all images to be used in the subsequent data reduction procedure. The threshold was applied to the sky exposures as the range of intensity is less than for object exposures. This makes determination of the threshold limits easier and there is less chance of the threshold removing real data. It should be noted in normal CGS4 observing this thresholding procedure is not used for object-sky pairs as subtracting the sky from the object automatically removes bad pixels which are common to both exposures. However in the case of the SMIRFS-IFU data this process was found to be unsatisfactory and the threshold technique was developed.

Once the bad pixel mask has been applied to the necessary images the next step is to subtract the sky exposures from the object exposures to produce background subtracted images. Exposures were taken in object-sky pairs and the sky exposure is subtracted from its paired object exposure. The resulting background subtracted images need to be checked for the presence of ripple, described in section 9.2.2, and the images de-rippled if necessary.

9.3.3 Flat-fielding

A drawback of observing with the SMIRFS-IFU is that fitting the instrument to CGS4 requires removal of the CGS4 calibration unit. It is the calibration unit that provides the ability to take arc and detector flat-field exposures. Removal of the calibration unit does

not adversely affect taking arc exposures but it does prevent the user from easily obtaining detector flat-fields. Detector flat-fields are normally produced with CGS4 by taking an exposure of a black body source located inside the CGS4 calibration unit. The observed spectrum is then modelled by a Planck black body curve at the temperature of the calibration unit source. Any deviations the spectrum shows from this model curve are mostly due to pixel response variations. Division of the spectrum by the curve produces the detector flat-field which is then automatically applied to all subsequent CGS4 exposures by the CGS4 data reduction software CGS4DR.

With the SMIRFS-IFU it is possible to use dome flat-fields instead of detector flat-fields to remove the effect of pixel to pixel throughput variations but this has to be done with caution. If there is a change in the magnification and offset values (section 8.2.3) between the dome flat-fields and the object exposures which are to be corrected then the flat-fielding process will not work as the fibre positions will no longer agree. Detector flat-fields are better because they are not affected by changes in magnification and offset of the slit projection unit. Application of detector flat-fields removes the effect of pixel to pixel response variations whereas dome flat-fields also remove the fibre to fibre throughout variations. Therefore, if the magnification and offset have changed, application of uncorrected dome flat-fields either does not correctly remove pixel to pixel variations, or does not remove the fibre to fibre variations properly.

When using the SMIRFS-IFU detector flat-fields have to be carefully 'manufactured' from the dome flat-field observations. Sky flat observations cannot be used as there is too much structure in the twilight sky spectrum. The dome flat-field image is first averaged in the spatial direction and then a small amount of smoothing is applied to the spectrum to produce a master dome flat spectrum. Each row of the dome flat image is then divided by this master spectrum to remove the overall shape of the spectrum. The residuals that are left are due to the pixel to pixel response variations. The dome flat image is then averaged in the spectral direction, in the appropriate wavelength region, to produce a map of the fibre-fibre throughput variations. If the entire wavelength range present on the detector needs to be detector flat-fielded then the image must first be transformed to remove the effect of the image distortions inside CGS4, section 8.5.5 The fibre to fibre variations are then removed from the dome-flat to produce the detector flat field. An example of a 'manufactured'

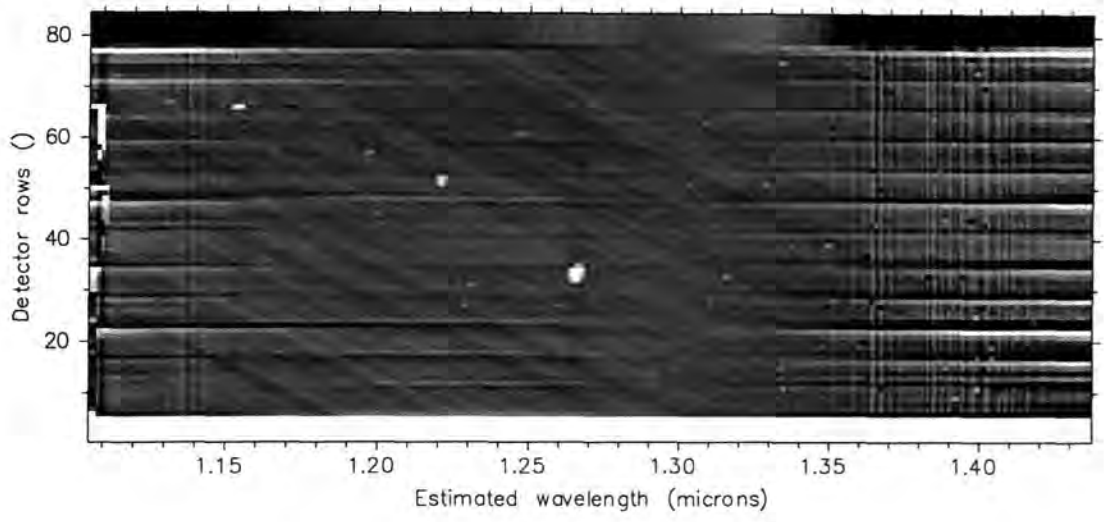

Figure 9.2: Manufactured detector flat field. Regions of low response pixels can be seen as light areas. This flat-field is centred on $\lambda = 1.27\mu$m, either side of this increasing residuals can be seen due to the change in y_{offset} across the chip. The flat-field does not work very well in the OH absorption region $\lambda > 1.35\mu$m.

detector flat-field can be seen in figure 9.2. The detector flat-field is then applied to all images to be used in the subsequent data reduction.

9.3.4 Final preparation

At this point the bad pixel mask information is still present in the images. The bad pixels can be removed by extrapolation from surrounding pixels with software. In regions where the bad pixels are densely populated the removal routine fails to extrapolate correctly and some bad areas will remain. This is only a problem at the extreme blue end of the detector and can be seen as the white area at the extreme left of figure 9.4.

Next the sky subtracted object exposures are added together using a combination algorithm that detects and replaces cosmic rays events present in the images. A cosmic ray event is usually characterized by a small number of saturated pixels.

At this point it may be necessary to apply a geometrical transformation to the image to remove the effect of CGS4 image distortions, described in section 8.5.5, so that the IFU spectra are perfectly aligned with the pixels across the chip. The transformation is only required if a large wavelength region is needed and can be ignored over small wavelength

regions.

The image now needs to be processed to remove the fibre to fibre throughput variations. Again fibre flat-fields need to be applied with caution in case the individual IFU spectra have shifted on the detector during the time between the dome-flat being taken and the object exposures being taken. The observations of NGC7469 (described in section 9.4) were taken on December 21st and the nearest dome flat-field that was available was taken two nights later. During this time the position of the IFU elements on the detector (the offset) had shifted by 0.75 pixels. The dome-flat is averaged in the spectral direction, again remembering to use the appropriate wavelength region, to produce another map of fibre to fibre throughput variation, this time with the effect of bad pixels removed. This map is then transformed by the appropriate amount to match the magnification and offset of the object exposure and the fibre flat-field is then applied.

The final step is to wavelength calibrate the data and apply a transformation to correct for any slope due to misalignment of the CGS4 slit with the spatial axis. The transformation also removes any residual misalignments of the IFU output lenses present in the data. The wavelength calibration was done using the Argon arc exposures. Krypton arcs were also available but were not used as the Argon arc exposures contained more lines evenly distributed over the detector producing a more accurate dispersion solution.

The result of the data reduction process is a science exposure which has the sky background removed, the effect of bad pixels removed, has been flat-fielded, wavelength calibrated and the IFU elements exactly align with the rows of the detector. Further data reduction steps will depend on the scientific information that is required. For instance it may be necessary to remove the effect of telluric absorption in the atmosphere by ratioing the observations by a standard star as described in (CGS4, 1997). The software used to achieve the data reduction steps described here is listed in appendix D.

9.3.5 Production of datacube

The final data analysis was done using an IRAF script written by Reynier Peletier (Peletier, 1997) called *linemap*. The author would like to acknowledge Reynier Peletier for providing the software. The software cross correlates each IFU spatial spectrum with a template

spectrum to obtain a radial velocity and velocity dispersion. The cross correlation can be carried out between specified wavelength limits to avoid problems with residual sky lines or low signal to noise regions. The software can also calculate equivalent widths, magnitudes or narrow band fluxes as specified by the user in a data file. The output of the software is a 3D datacube which contains spatial and spectral information in various forms, such as maps of equivalent width, velocity maps etc. The reconstructed images present in the output datacube are smoothed to allow suitable visualisation of the 72 IFU spatial elements. The software also applies a signal to noise ratio cutoff when the signal to noise ratio falls below a certain limit to avoid spurious results due to bad fibres and areas of low flux. Examples of the output from *linemap* can be seen in figure 9.7.

9.4 Science observations with SMIRFS-IFU

The SMIRFS-IFU was not only built as a prototype microlens-fibre based integral field unit to act as a technology demonstrator. The SMIRFS-IFU was also built with the intention of providing a novel observing capability with UKIRT and CGS4 to allow scientific projects to be studied. The initial scientific motivation was to measure the distribution of infrared emission lines in distant radio galaxies as a means of understanding the alignment between radio and optical structures. The SMIRFS-IFU is ideal for measuring emission line ratios over an extended object to reveal the ionisation source and the velocity field. Unfortunately due to the bad weather conditions experienced during commissioning of the SMIRFS-IFU this project could not be performed. However, there was an alternative project to obtain spectral line imaging of [FeII] emission in Seyfert-1 galaxies. During a brief break in the cloud the active galaxy NGC7469 was observed using the SMIRFS-IFU. This section briefly describes the results of the observations of NGC7469.

9.4.1 Description of NGC7469

NGC7469 is a Seyfert type 1.2 galaxy (RA=$23^h00^m44.4^s$, dec=08°36′16″) with an integrated J-band (RGO) magnitude of 11.02. A Seyfert galaxy is characterized by displaying nuclear emission line activity. A high spatial resolution HST image of NGC7469 is reproduced in figure 9.3. The figure also shows the location of the field of view of the SMIRFS-IFU with

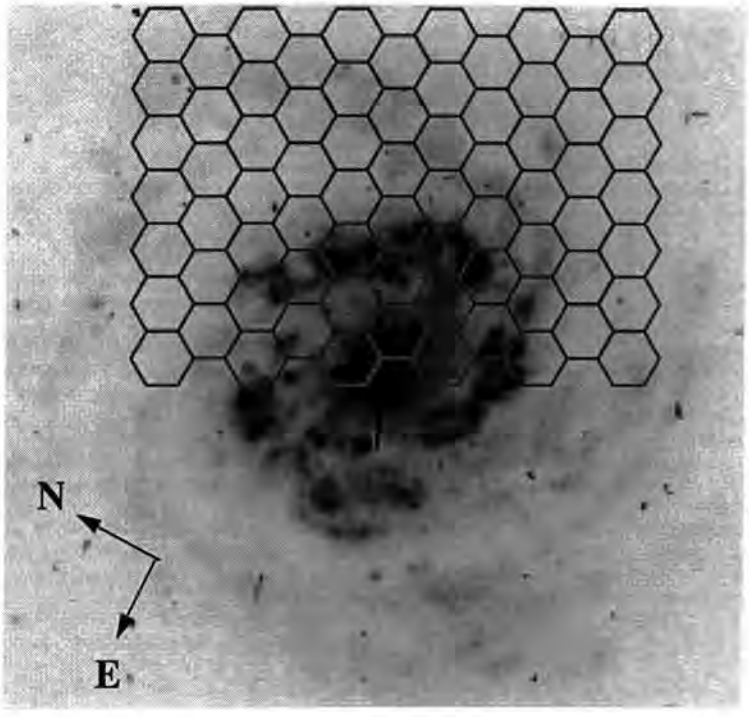

Figure 9.3: Location of the SMIRFS-IFU field of view compared with an HST WFPC2/PC image of NGC7469 (courtesy of M. Malkan. UCLA). The image is on a logarithmic scale to highlight structure (photographic negative).

respect to the galaxy. A well known property of NGC7469 (Mauder *et al.*, 1994) is it possesses a star forming region (approximately 3" diameter) surrounding the nucleus as seen in the HST image. The burst of star formation is believed to have been caused by interaction with the neighbouring galaxy IC 5283.

9.4.2 Results from NGC7469

Observations were made of NGC7469 of the region just adjacent to the nucleus (figure 9.3). The object was observed for a total of 1200 seconds in the J-band. Background subtraction was achieved via separate beam switched exposures. Observations were performed in the J-band to study the [FeII] emission feature at 1.2567μm and the Paβ emission feature at 1.2818μm. An image of the integral field spectrum after data reduction can be seen in figure 9.4. The two emission lines of [FeII] and Paβ can be clearly seen even in regions where there is little continuum emission. The corresponding spectrum is shown in figure 9.5 with [FeII] and Paβ emission indicated. The redshift of the spectrum is measured to be $4890 \pm 60 \mathrm{kms}^{-1}$ in good agreement with the published value of $4892 \pm 2 \mathrm{kms}^{-1}$ (Keel, 1996). Using the data shown in figure 9.4 it is possible to reconstruct the J-band image of NGC7469. The reconstructed image in continuum flux is shown in figures 9.6 and 9.7 (left plot). The J-band

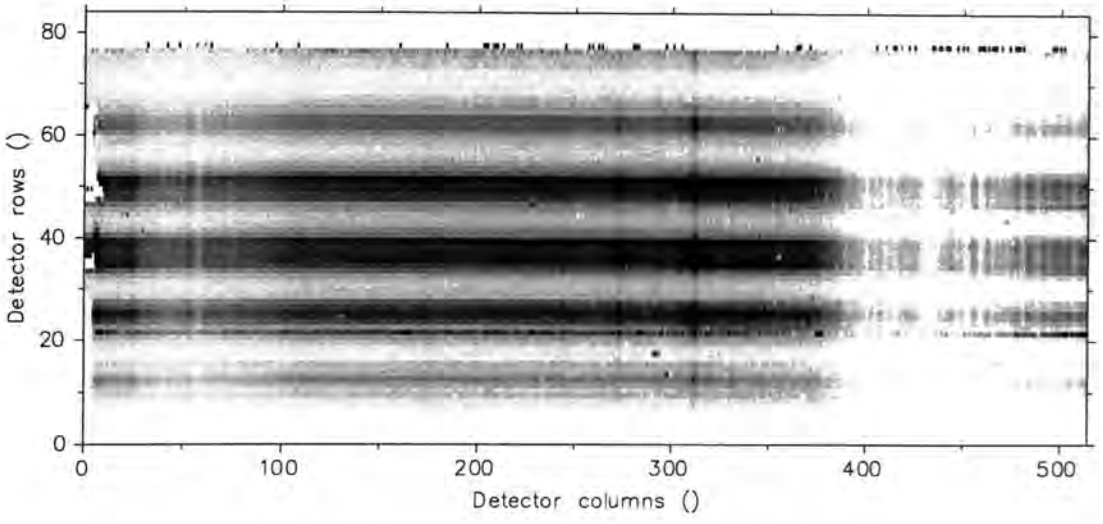

Figure 9.4: Coadded 1200 second exposure of NGC7469. The spectrum is in the region rows 6 to 78, other rows contain noise. The dead element can be seen at row 22 and contains noise created during the data reduction process. This is the image used to create the line ratio maps shown in figure 9.7. A spectrum from this image can be seen in figure 9.5

image shown in figure 9.6 was reconstructed during observing at the telescope using 'quick look' data reduction software written by Dr. Jeremy Allington-Smith. This allows the data to be examined in almost real-time, primarily to determine the pointing of the telescope and allow adjustments to be made. The images in figures 9.6 and 9.7 can be compared with the HST image (figure 9.3). The nucleus is clearly seen to the right centre of the reconstructed image. It should be remembered that integral field spectroscopy also allows the image to be reconstructed in any wave-band of choice, i.e. an image which maps the [FeII] emission rather than the continuum. The velocity dispersion or radial velocity at each spatial position can also be represented in terms of a reconstructed image.

Observations of Seyfert nuclei in the IR have the advantage that extinction from the dusty torus is less severe than in the optical allowing the physical environment in the galactic centre to be probed. [FeII] emission arises in regions of partially ionised Hydrogen (Fe^+ is excited by collisions with electrons) but these regions are uncommon due to the sharp transition between neutral and fully ionised Hydrogen. Iron is also expected to be mostly contained in dust grains rather than gas. Various mechanisms have been proposed in Seyfert galaxies which can contribute to [FeII] emission. The processes which contribute to this emission are:

1. X-ray illumination of NLR clouds where a large partially ionised region can be produced

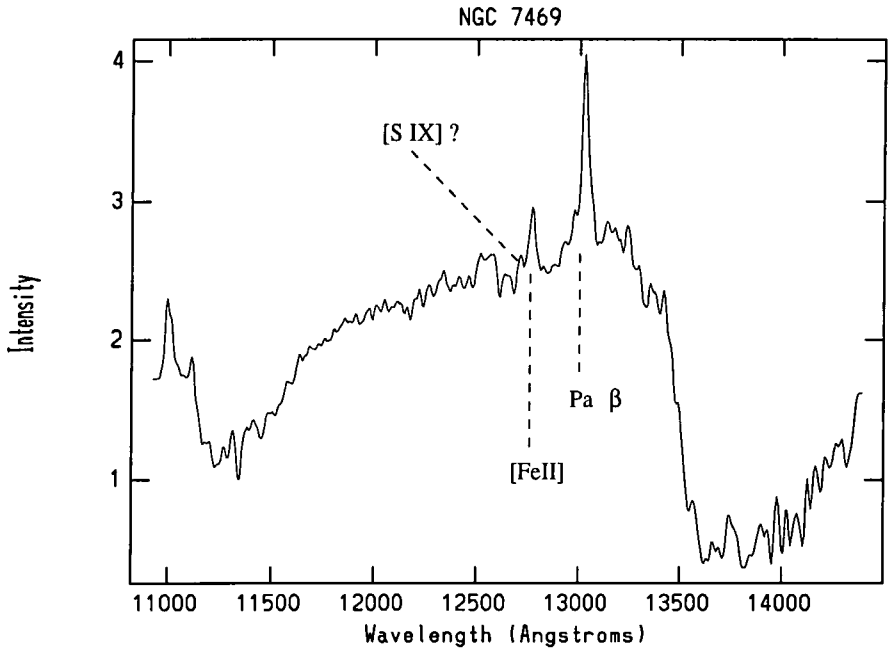

Figure 9.5: Spectrum of NGC7469 taken from near the nucleus on the IFU image. The emission lines of [FeII] and Paβ are clearly seen. Note the Paβ shows a narrow line component and a broad line component.

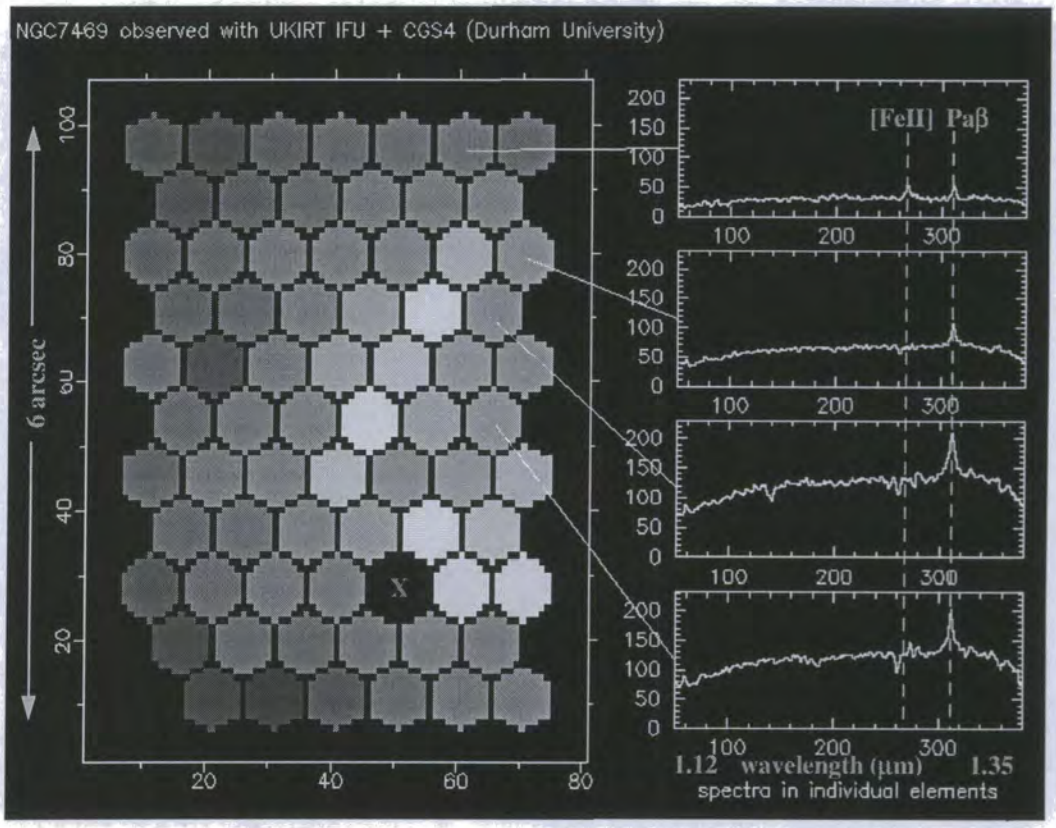

Figure 9.6: Reconstructed image of NGC7469 obtained with the quicklook data reduction software whilst observing at the telescope. The data can be examined at the telescope in almost real-time and the pointing of the telescope adjusted accordingly. Also shown are various spectra extracted from the positions indicated. The increase in [FeII] emission with radius is evident from the few spectra shown.

in clouds of large optical depth,

2. fast shocks from supernovae remnants in a circumnuclear starburst,

3. shocks from interaction of a radio jet and the ISM.

Shocks can destroy dust grains which contain iron enhancing the gaseous iron abundance (Knop *et al.*, 1996). An active galaxy such as NGC7469 possesses strong emission lines, however, in many cases the excitation mechanism for this emission is unclear. Two dimensional spectroscopy therefore provides a way of mapping emission features in order to determine the excitation mechanism. For example if the dominant excitation mechanism is shocks from the radio jet then the emission would be expected to be extended along the radio jet, as observed in NGC1068 (Blietz *et al.*, 1994). [FeII] emission in NGC7469 is associated with the circumnuclear starburst ring (Genzel *et al.*, 1995). Paβ recombination emission arises from photo-ionization from hot stars and is therefore an indicator of star formation.

The emission line ratio [FeII]/Paβ is a useful diagnostic (Simpson *et al.*, 1996) and as the lines are close together it is less affected by extinction than other line ratios. The right hand plot in figure 9.7 shows the image representation of the emission line ratio produced by dividing the [FeII] emission by the Paβ emission. The [FeII]/Paβ ratio shows a peak at the nucleus of the galaxy ([FeII]/Pa$\beta \approx 0.5$), falling off in the region of the starburst ring ([FeII]/Pa$\beta \approx 0.3$), before rising again at larger radii ([FeII]/Pa$\beta \approx 1.0$). The strength of the Paβ emission with respect to the [FeII] emission is evident from the spectrum in figure 9.5. Figure 9.6 also shows a number of spectra from NGC7469 and their position on the reconstructed J-band image is also indicated. These spectra also show evidence for the increase in [FeII] emission with increasing radius from the nucleus of the galaxy. The observed value of the [FeII]/Paβ ratio is in reasonable agreement with the values listed in Simpson *et al.* (1996). Low ratios (~ 0.01) occur in HII regions and high ratios (up to ~ 5) in supernovae remnants. Seyfert galaxies produce [FeII]/Paβ ratios in the range 1-10. The low ratio measured in NGC7469 is consistent with starburst activity near the centre with Seyfert activity becoming dominant outside the starburst ring where the [FeII]/Paβ ratio increases. The observed behaviour of the [FeII]/Paβ ratio broadly agrees with observations by Genzel *et al.* (1995) who found [FeII]1.644μm to be more centrally concentrated than Brγ. Brackett γ is also associated with starburst activity and is correlated to Paβ therefore

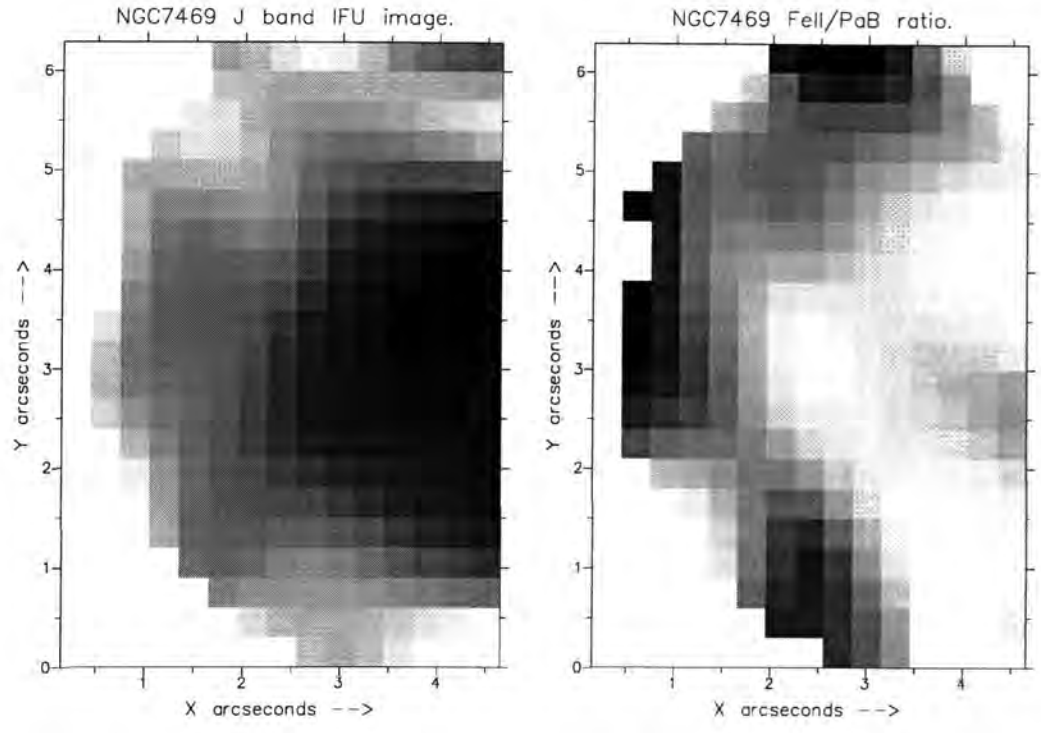

Figure 9.7: Reconstructed J band image of NGC7469 (left) and corresponding map of the line ratio FeII/Paβ (right). The data has been masked when the normalised intensity falls below 0.15 to remove regions with low signal/noise. The nucleus of the galaxy is just off the image (see figure 9.3). The line ratio shows enhancement nearer the nucleus and then falls off in the starburst ring before increasing again outside the starburst ring.

the two are expected to be similar in their spatial distribution. However, the ratio increases at a larger radius than that observed by Genzel *et al.* Genzel could not observe this increase because it was outside his field of view. An increase in the [FeII]/Paβ ratio is similar to the behaviour in the Seyfert 1.5 galaxy NGC4151 which shows an increase in the ratio with increasing radius from the nucleus (Knop *et al.*, 1996).

The spectrum of NGC7469 shown in figure 9.5 indicates that the Paβ emission feature consists of two components, a narrow line feature and a lower intensity broader feature. Paβ emission is usually broader than [FeII] emission indicating that the two features are produced in different environments or there is an additional source of velocity broadening in the Paβ emission.

It is clear from these preliminary observations of NGC7469 that integral field spectroscopy offers a powerful technique to probe the physical mechanisms operating within the galaxy.

The data presented here are in agreement with the findings of other authors but there is some evidence for an increase in the ratio of [FeII] emission to Paβ emission outside the region of the starburst ring. It is unknown whether this increase has been previously observed in NGC7469 although there is some evidence for an increase in the [FeII]/Paβ ratio with increasing radius in other Seyfert galaxies. The physical mechanism which causes this increase with increasing radius is uncertain.

9.5 Summary and conclusions

This chapter described how to observe with the SMIRFS-IFU in order to achieve optimum performance. Care has to be taken to accurately calibrate the SMIRFS-IFU so that the integral field data cube can be reconstructed without errors. The data reduction procedure is then described which mostly consists of removing bad pixels and applying the fibre to fibre flat-field. Care has to be taken to ensure that the fibre to fibre flat-field is accurately registered with the science image to ensure that noise is not introduced by flat-fielding. With careful data reduction and calibration integral field spectroscopy readily provides information in every pixel on the detector. This is a massive advantage over traditional techniques which only use a small fraction of the available detector area.

The results of observations of the Seyfert galaxy NGC7469 are also presented. Despite the bad weather conditions during observing the data clearly demonstrate the massive amount of information that can be obtained from the integral field data cube. The observations allow the [FeII]/Paβ ratio to be mapped over a large area of the galaxy. The measured [FeII]/Paβ ratio is consistent with a starburst ring surrounding the nucleus but also increases at larger radii. This is thought to be the first time this increase in [FeII]/Paβ with radius has been measured with NGC7469. Clearly great advances in the understanding of the physical processes operating within active galaxies are within reach via the use of infrared integral field spectroscopy as demonstrated by the preliminary results with NGC7469.

Chapter 10

Thesis summary

Abstract

This chapter briefly summarizes the work presented in this thesis. Conclusions arising from the work are discussed and future possibilities are also briefly discussed.

10.1 Thesis summary and conclusions

This thesis began with a brief discussion of the new generation of 8-m telescopes being built around the world. The excellent performance of these telescopes implies the need for a new generation of astronomical instrumentation with equivalent performance. Due to Durham's involvement in the Gemini multiobject spectrograph project (GMOS) this was given as an example of one of this new breed of state of the art instruments. The specification for GMOS was presented and two requirements found to be of particular note: the need for high spectral resolution, and the need for a high performance integral field spectroscopy capability. The investigation of methods with which to achieve these observing capabilities formed the basis of this thesis.

10.1.1 Immersed gratings

The first part of this thesis concentrated on the problem of obtaining high spectral resolution with an 8-m class telescope. The problem to be overcome is that, for a fixed collimated beam size, the maximum spectral resolution of a spectrograph is inversely proportional to telescope aperture. This implies that GMOS can only achieve a maximum resolution of 5,000 which

is half that for the same instrument on a 4-m telescope. The main constraint limiting resolution is shown to be the anamorphic factor of the dispersion system, which is limited by the camera aperture. After a review of the various methods of increasing resolution the use of immersed gratings is proposed as the best solution for use with GMOS. However, a review of the literature regarding previous work on immersed gratings indicated there was much confusion about their properties and a lack of experimental information regarding their performance. To verify the performance of immersed gratings it was therefore decided to build a prototype immersed grating and subsequently test it.

The theoretical predictions relating to immersed grating performance were derived and used to predict the performance of the prototype immersed grating. Immersed gratings allow higher resolution to be achieved via the prism's ability to reduce the anamorphic factor. The reduction of wavelength within the immersing medium also allows higher resolution via the use of higher diffraction orders and increased ruling densities that are not available without the use of immersion. A prototype immersed grating was then constructed by oiling a prism to a grating surface with Glycerol. This was found to be adequate for a small prototype but is not recommended for a large astronomical grating. Investigation of possible construction methods was recognised as an area where further research is required. The resolution and dispersion of the prototype was then accurately measured using a spectrograph constructed in the laboratory. The measured performance of the immersed grating was found to agree with the theoretical predictions verifying that immersed gratings do provide a method of increasing resolution. The additional dispersion produced by the prism glass was measured indicating that a slight gain in resolution can be obtained by the use of high dispersion glass prisms.

Next a thorough investigation of the efficiency of immersed gratings was conducted. It was found that the theoretical prediction of grating efficiency requires a full electromagnetic treatment and is beyond the scope of this work. However, it was found that the change in blaze wavelength, and the position of Rayleigh passoff anomalies could be predicted with reasonable accuracy with simple scalar theory. Experimental measurements of the efficiency of the immersed grating in comparison with the same grating un-immersed showed the peak blaze efficiency of the immersed grating to be approximately 15% lower. The position of the blaze peak is also shifted to longer wavelengths determined by the refractive index of

the prism. The reduction in efficiency was shown to be due to two loss mechanisms: air-glass reflection losses accounting for $\sim$ 8%, and metal-dielectric losses accounting for the remainder. Air-glass losses can of course be minimised by the use of suitable antireflection coatings and multi-layer Silica sol-gel coatings were proposed as a method of achieving this. Metal-dielectric losses occur due to the reduction in reflectivity of a metal surface with immersion and are difficult to avoid. However, with certain conditions (Littrow configuration with S-plane polarized light) it was found that the efficiency of the immersed grating is actually higher than that of the un-immersed grating. It is therefore concluded that it should be possible to use an immersed grating without any loss in efficiency.

Another objection to the use of immersed gratings is the production of ghosts within the prism. The intensity of various ghosts was measured for the prototype immersed grating with the brightest found to have an integrated intensity of $\sim$ 2% of the parent image. The intensity of ghosts can be reduced by the use of antireflection coatings on the surface of the prism and therefore ghosting is not a serious cause for concern.

It is thought that the work presented in this thesis shows that immersed gratings do provide a useful method for increasing resolution. Most of the uncertainties relating to their performance have been shown to not be a cause for concern and there are no major difficulties to be overcome. This work clearly demonstrates that immersed gratings can be used to more than double the resolution available with a spectrograph.

10.1.2 Integral field spectroscopy

The second part of this thesis was concerned with the development of a prototype microlens-fibre based integral field unit: the SIMRFS-IFU. This work began with an introduction to integral field spectroscopy which described the various methods by which it can be performed. The use of both microlenses and fibres to construct an IFU was proposed as it combines the advantages of both microlenses, i.e. continuous spatial coverage and high fill factor, and fibres, i.e. the ability to reformat the 2D focal plane to a 1D slit. A system of this type can also be constructed to match virtually any telescope and spectrograph. To demonstrate the technology it was therefore decided to build a prototype system, the SMIRFS-IFU, for use with UKIRT and CGS4. The construction of the prototype will also provide valuable lessons about the technology that will benefit future projects.

The optical design of the SMIRFS-IFU (performed by Dr. Robert Content) was then discussed. It was shown that microlens-fibre based IFUs provide a very efficient use of the available detector area as every pixel can contain useful information.

Perhaps the most important component, and the one about which the least is known, is the microlens array. A large amount of work was done on the testing of various microlens arrays to determine their suitability for use with IFUs. After tests of image quality on microlenses from the National Physical Laboratory and Adaptive Optics Associates (AOA) the latter were chosen for use with the SMIRFS-IFU due to their higher image quality. Further tests of AOA lenses showed them to have surface roughness which causes scattered light at a level of $\sim$ 20% at visible wavelengths. The scattered light performance was found to be worse for larger lenses. The conclusion was that AOA lenses are suitable for use in IFUs but their performance could be improved. There is now a collaboration between Durham and AOA with the aim of producing microlenses of higher quality.

The construction of the SMIRFS-IFU was then described. Overall the assembly of the SMIRFS-IFU was a success but a number of areas were identified for further investigation. The first was adhesive technology, as some problems were experienced with components becoming loose and bubbles forming in the adhesive layer between the microlenses and the fibres. The focal ratio degradation of the fibre bundle was also found to be worse than expected leading to significant throughput losses. Preparation of fibres with regard to reducing FRD is therefore identified as a key area to be improved.

Commissioning of the SMIRFS-IFU at UKIRT was a success apart from the problem of bad weather. The instrument was found to perform well with a high quality PSF produced at the detector and a measured throughput of $\sim$ 50% in the J-band. Measurements of the relative fibre to fibre throughput showed regular dips which were attributed to FRD caused at the edge of the fibre output slit blocks. As IFS using one fibre per pixel is a new technique in spectroscopy, the setup, calibration and subsequent data reduction with the SMIRFS-IFU was described in detail. The massive information gathering ability of IFS was demonstrated with observations of the Seyfert I active galaxy NGC7469.

The main conclusion is that microlens-fibre based IFU technology does provide a high performance technique for performing IFS. This is clearly demonstrated by the high performance (high spectral resolution, high spatial resolution, high throughput and multiplex) of the

SMIRFS-IFU. The lessons learned in the testing of microlens arrays, construction of the prototype IFU, and during commissioning, will allow future IFUs to be constructed to provide even higher performance.

10.1.3 Future prospects

The work on immersed gratings is thought to be at the stage where it can be applied to the construction of a full-scale immersed grating for use on a telescope. The main objections of efficiency loss and ghost images have been shown to not be a problem. The area to be addressed now is the techniques that can be used to manufacture a large immersed grating. It is thought that once the concept, and advantages, of immersed gratings has been demonstrated by providing a useful scientific benefit for a spectrograph then there may be more interest in their use. Immersed gratings do provide a way of increasing the resolution of GMOS to a level of around 10^4 with a 0.5 arcsecond slit and it is hoped that immersed gratings will be used with GMOS in the future.

The prospects for the work on microlens-fibre based IFUs are good. The Astronomical Instrumentation group in Durham is continuing development of IFUs for use with various projects. Following the success of the prototype SMIRFS-IFU the next project is the Thousand Element IFU for use with the WYFFOS fibre fed spectrograph and the ELECTRA adaptive optics system on the WHT. The construction and testing of the SMIRFS-IFU has provided valuable lessons which will allow TEIFU to be constructed with higher quality providing improved performance. After TEIFU the technology will be applied to the production of the various IFUs for use with GMOS. These will need the ultimate in performance if they are to match the high quality of the telescope. Looking further ahead, given the popularity of integral field spectroscopy already, it is very likely that the next step will be to provide a multiobject IFU capability. This will provide both the benefits of multiplex advantage, over a wide field of view, with the information gathering ability of IFS. The next step in technological advancement needed here is to miniaturise the construction of IFUs even further to allow as many as possible to occupy the telescope focal plane. Multiple IFUs are already proposed for use in the AUSTRALIS instrument (on which the author is now working) for the VLT and the FMOS instrument for Subaru.

It should be remembered that SMIRFS-IFU is an infrared instrument and there is much to

be done to provide a integral field capability in the thermal infrared. Use in the thermal infrared implies all the difficulties of minimising the thermal background. This requires another stage in technological advancement: the ability to cool integral field units. It may even be questionable whether IFUs for use in the thermal infrared need to be fully cooled if the thermal emission can be kept low by other means. The provision of IFUs in the infrared has already led to two main technologies being proposed: the use of image slicers (Content, 1998a), and the use of special purpose cooled microlens-fibre systems (Tecza, 1997).

It is interesting to note that the instrumentation group at MPIA, which is well known for constructing the first image slicer type instrument (3D) for use in the infrared, is now developing microlens-fibre based technology. In Durham, where most development has concentrated on microlens-fibre based IFUs, is now rapidly developing image slicer technology. This certainly is an interesting time to be building astronomical instruments. The development of state of the art instrumentation for 8-m telescopes is a fast moving game and there is much to be done to stay in the race!

Appendix A

Immersed grating appendix

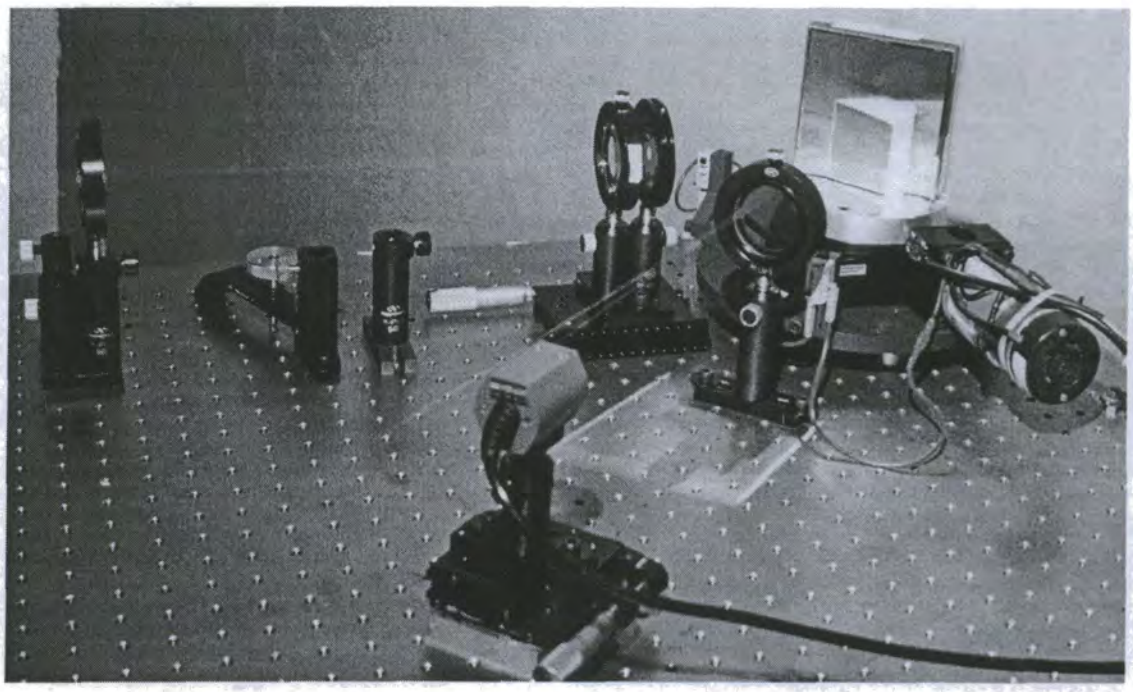

Figure A.1: Photograph of the test spectrograph on the optical bench in the laboratory. The variable slit mechanism has been removed for photographic purposes (note the two empty optical post holders). The immersed grating is mounted on the computer controlled rotating stage. The faint red line is a laser beam illuminating the spectrograph indicating the optical path.

A.1 Antireflection coatings

The large fraction, typically 50–80%, of the reduction in efficiency with using an immersed grating (described in chapter 3) is due to air-glass reflections at the surface of the prism.

Clearly if this loss is to be avoided a suitable broad-band antireflection coating needs to be applied to the prism entrance face. High performance antireflection coatings are also crucial in minimising the intensity of any ghost reflections associated with the prism surface. As the immersed grating may be used in configurations with a large angle of incidence at the prism the antireflection coating also needs to operate over a broad range of angles.

A.1.1 Silica sol-gel antireflection coatings

As a solution to this problem multi-layer Silica sol-gel antireflection coatings were investigated. Silica sol-gel coatings, also referred to as COLSI or Si-sol coatings, initially consist of a suspension of Silica spheres in a solution. When the solution is applied to an optic the solvent evaporates leaving behind a thin layer of Silica spheres. The diameter of the spheres varies depending on preparation conditions but is typically around 20nm. The index of refraction of the coating is related to the density of the Silica particles such that higher porosity produces a lower refractive index. Therefore by changing the size of the Silica particles the refractive index can be tuned within the range from 1.22-1.45 (Thomas, 1992). This means that by applying successive layers of coating, each with a slightly reduced refractive index than the previous layer, a graded index coating can be produced. Graded index coatings have the advantage of a reduced angular dependence with reflectivity, as described in Simmons *et al.* (1994) , a property which is an advantage for anamorphic immersion gratings. A graded index structure can also be achieved by chemical etching of the sol-gel film (Yoldas & Partlow, 1984). The ability to vary the refractive index of the sol-gel coating also makes it a very good match to a wide range of substrates. Note that sol-gel coatings aren't limited to coating Silica, other materials can also be coated using the sol-gel technique.

The sol-gel particles are produced in a chemical solution at approximately room temperature. The concentration of the reactants and the preparation time determines the size of Silica particles that are produced. Sol-gel coatings are usually applied to the optic by spin coating, or dip coating for larger optics. The application procedure for sol-gel coatings has a much lower risk factor than chemical vapour deposition methods which involve high temperatures and vacuums. Sol-Gel coatings are also relatively low cost. However, sol-gel coatings do have some disadvantages. The coating is porous so it can readily absorb contaminants such as water vapour. The coating is also very delicate, being removed easily by wiping. It can be

hardened considerably by chemical treatments (Salmon, 1996) but hardening does produces a small change in the antireflection properties of the film. After hardening the coating is able to be wiped for cleaning purposes.

Silica sol-gel coatings have been successfully used with the High resolution spectrograph (HIRES) on the Keck telescope (Epps & Vogt, 1993). Sol-gel coatings are also the proposed coating for DEIMOS (Cowley *et al.*, 1997). Multilayer coatings incorporating sol-gel coatings are also being used with GMOS (Davies *et al.*, 1997). The GMOS optics are coated with a multi-layer coating consisting of Methyl-Silicone, $n = 1.41$, and Silica sol-gel, $n = 1.22$, to produce a two-layer broad-band AR coating.

A.1.2 Evaluation of a Silica sol-gel coating

The requirements for the AR coating on an immersed grating are slightly different to that of a lens. The wavelength range is likely to be smaller and the coating must operate over a considerably larger range of angles. Clearly a full investigation of AR coating options is required to find a suitable coating for use with an immersed grating. As a starting point it was decided to obtain a single layer Silica sol-gel coating for evaluation purposes. The coating was supplied by I. N. Ross of Colsicoat, South Hinksey. A quarter wave of Sol-Gel, centred at 500nm, was applied by spin coating to both sides of a SPECTROSIL-B Fused Silica window. The transmission, before and after coating, was tested using the UV/VIS/NIR Lambda 19 spectrophotometer described in section 6.3.4. The results are plotted in figure A.4.

It is clear from figure A.4 that the performance of the Silica sol-gel coating is better than a MgF_2 coating, although MgF_2 does have the advantage of being more durable. The freshly coated window was found to have a maximum transmission of 99.6% peaking at 520nm. This implies the refractive index of the coating is approximately 1.24. After a period of a few months the antireflection properties of the coating were found to degrade slightly. After 10 months at standard laboratory conditions the coating was found to have degraded to 98.5% peak transmission at 550nm. As described in Salmon (1996), the degradation in performance is probably due to water absorption, and can be reversed by washing the coating with suitable solvents. It is interesting that the peak in transmission has shifted slightly redward. Absorption is also thought to be responsible for a change in the refractive index of the film leading to the redward shift. The durability of the coating was not tested.

More research is needed to procure suitable multi-layer films, with good performance over large angles, for use with immersed gratings.

Note: Silica sol-gel coatings may also prove useful for coating delicate microlens arrays. Silica sol-gel coatings are applied as a room temperature liquid so are unlikely to damage the delicate microlens surface. Application of the coating as a liquid may also provide a more even coat on the undulating surface of the microlens array than might be obtained with vacuum deposition methods. The application of Silica sol-gel coatings to microlens arrays is discussed in section 6.7.

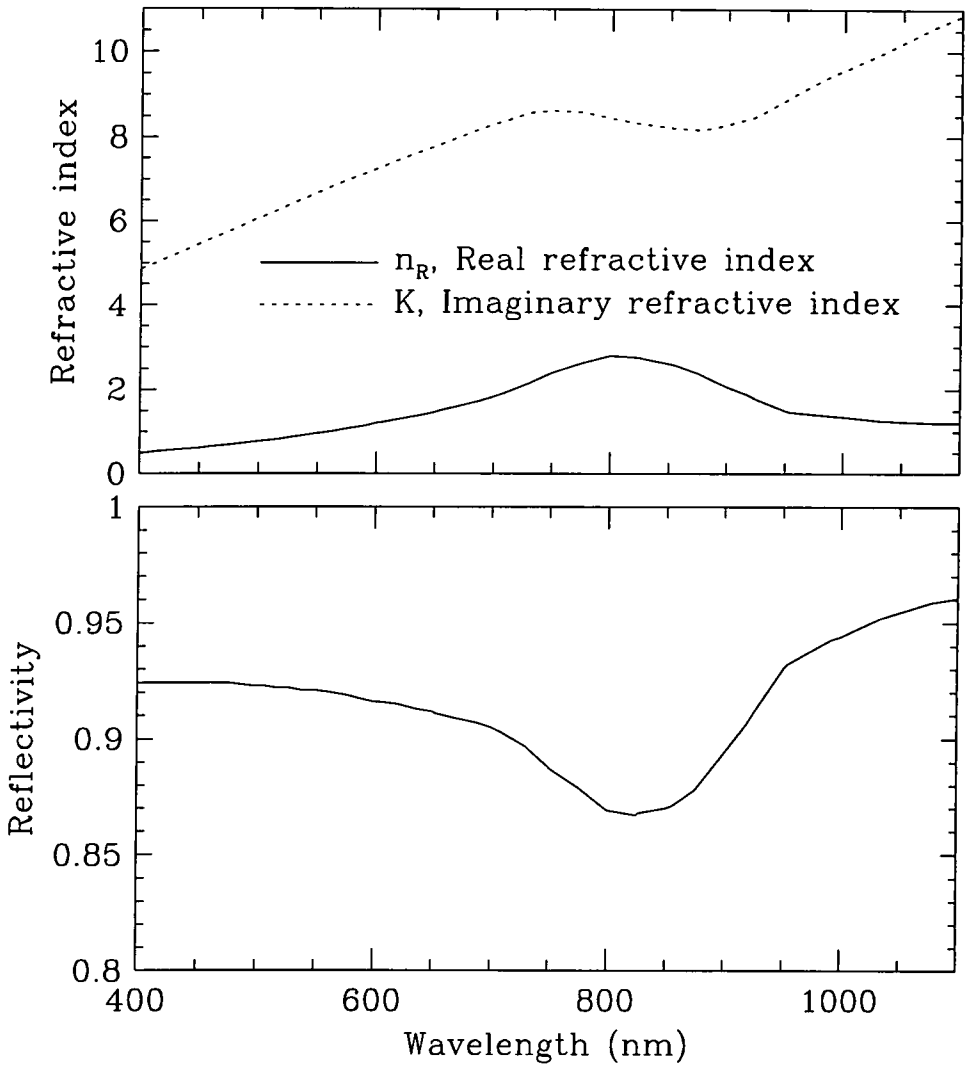

Figure A.2: Plot of the variation of the real and imaginary refractive indices of Aluminium with wavelength, data obtained from Hunter (1985). The lower plot shows the reflectivity calculated using the plotted values of refractive index, with $\psi = 45°$. The Aluminium absorption feature at $\sim$ 850nm corresponds to an increase in the real refractive index.

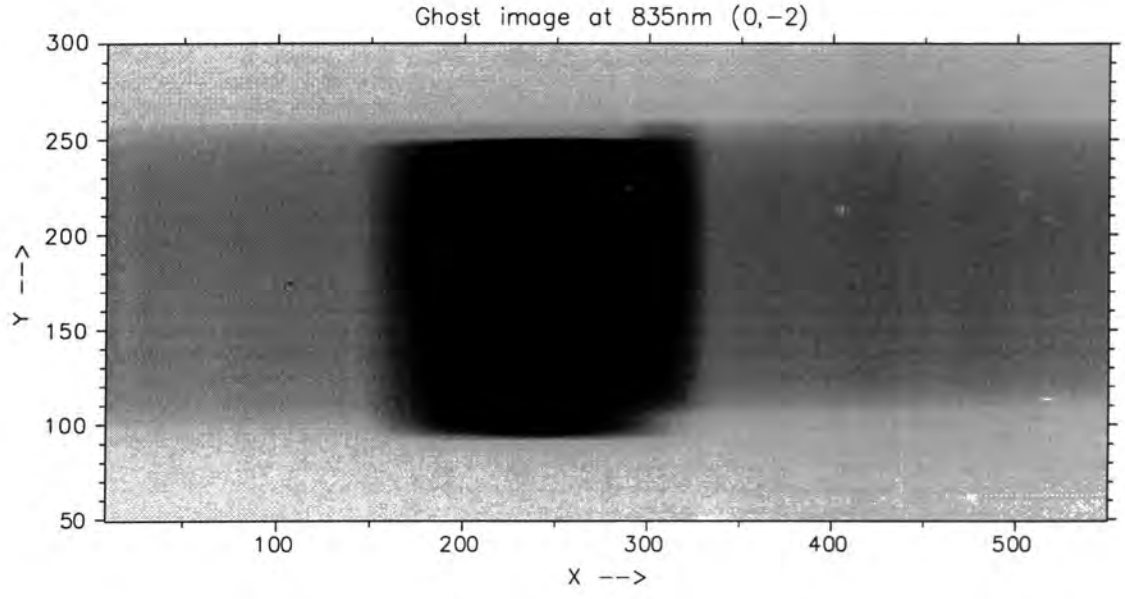

Figure A.3: Image of a ghost at 835nm taken in unpolarised light. The cause of the ghost is zero order diffraction, followed by Fresnel reflection from the prism, and finally second order diffraction. The ghost image is seen superimposed on a band of light caused by scattering at the grating surface. This 'scatter-band' can be seen at all wavelengths although it is very faint.

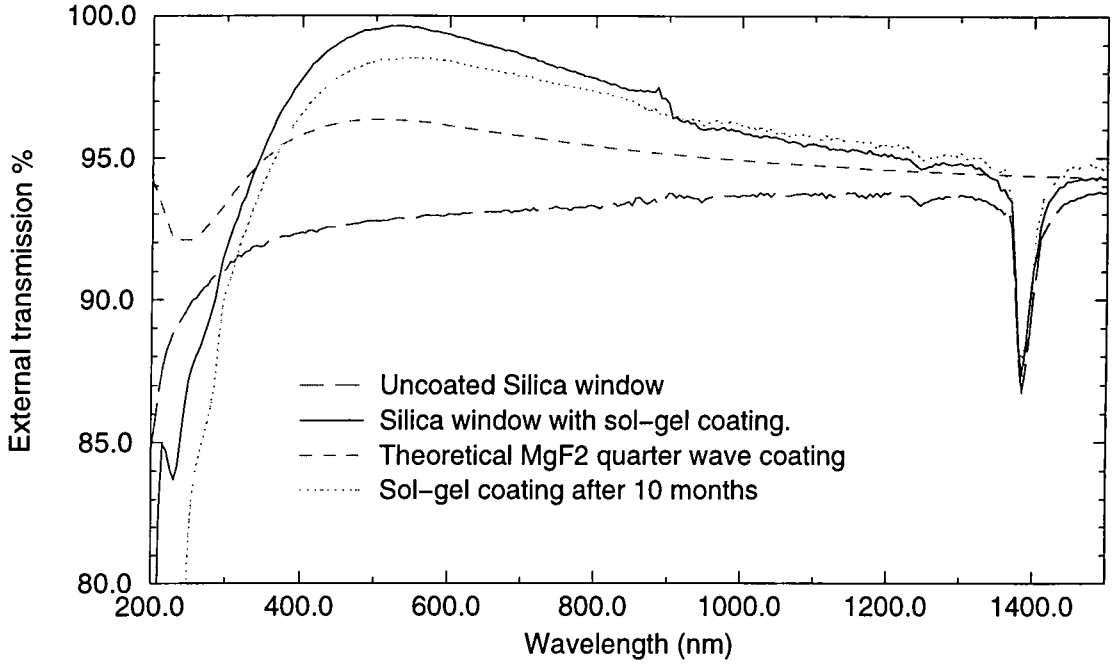

Figure A.4: Plot of the external transmission of a Fused Silica window coated with a quarter wave layer of Silica sol-gel antireflection coating. The upper plot is for the freshly coated sample, which degraded with time falling to a level shown in the lower plot. Also shown for comparison is the transmission of an uncoated Fused Silica window, and the transmission with a quarter wave layer of MgF_2. Clearly the sol-gel coating has better antireflection performance. The feature at 1400nm is due to absorption within the Silica.

Appendix B

Microlens appendix

B.1 National Physical Laboratory microlenses

Of the microlenses suppliers listed in section 6.1.3 two were chosen for further investigation; Adaptive Optics Associates, and the National Physical Laboratory. The aim is to find a suitable supplier of microlens arrays for the IFU projects under construction. Tests of the AOA lenses have been already been described in the chapter 6. A sample microlens array was also obtained[1] from the NPL for assessment purposes and the tests on that array are described here.

B.1.1 Manufacturing technique

The microlenses manufactured by the National Physical laboratory consist of 'islands' of photoresist on glass substrates. A full description of their manufacturing technique can be found in Daly *et al.* (1990). Their manufacturing technique is briefly described here as it is relevant to the later discussion of image quality.

The manufacturing technique adopted by the NPL is to produce lenses by melting small cylinders, or 'islands', of photoresist. A layer of photoresist is first spun onto a glass substrate to produce a flat layer of known thickness. The necessary thickness of photoresist to produce the desired lens shape is calculated in advance. The photoresist is then exposed to light through a photo-lithographic mask which defines the shape of the microlens. When the

[1]The author would like to thank Dan Daly, of the NPL, for providing the sample array.

photoresist is developed the exposed areas of photoresist are removed and cylindrical 'islands' of un-exposed resist are left behind. The photoresist is then heated until melting occurs and surface tension causes the liquid photoresist to flow into a lens shape. This method of producing microlenses is termed *moulded reflow technology.* A disadvantage of this technique is that the 'islands' of photoresist have to be separated on the substrate. If bridges are left joining the islands the resist tends to flow along them and severely distorts the lens shape. This reduces the maximum fill factor available by a small amount.

This manufacturing technique is best suited to producing fast lenses. This is because the action of surface tension works best on thick layers of resist. Thin layers merely produce islands with rounded edges rather than the correct lens shape. This limits the range of numerical aperture to between 0.25 and 0.6 (F/2 and F/0.8) if the photoresist has a refractive index of 1.6. The optimum focal ratio for the lenses is that at which the tangent to the lens edge is inclined at 26° (the contact angle) to the substrate . This is the angle naturally adopted by the photoresist due to surface tension producing an optimum lens shape of F/1.9.

Both the maximum lens aperture and sag height is limited by the thickness of photoresist that can be successfully applied to the substrate without surface defects, or the inclusion of dust or bubbles. Lenses with N.A. less than 0.25 can be made by producing the lens in photoresist of lower refractive index. Alternatively a low index cover glass can be cemented over the lens (Daly *et al.*, 1990) such that refraction at the lens surface is reduced producing a lens with increased focal length. Photoresists are available with refractive indices in the range 1.4-1.6. The addition of cover glass has the advantage that it protects the lens surface and can be easily antireflection coated.

The National Physical Laboratory can produce cylindrical lens arrays, crossed cylindrical lens arrays (which approximate lenses with rectangular aperture) and hexagonally close packed arrays with circular apertures.

B.1.2 Description of lens array

A sample microlens array was obtained from NPL for testing purposes. The parameters of this lens are listed in table 6.1. It should be noted that although the lens aperture is

0.495mm the lens spacing is 0.5mm due to the requirement to leave small gaps between the lenses. This reduces the fill factor from the maximum for hexagonally close packed circular apertures of 90.7% to 89%. The lenses were manufactured with Shipley S1400-37 photoresist which has a refractive index, after processing, of ~ 1.62.

A disadvantage of this photoresist is the transmission falls rapidly below 0.6μm. This is obvious from the red appearance of the lenses. The transmission is good in the range $0.6 - 2.0\mu$m. Whilst good transmission in the blue is not a requirement of the SMIRFS-IFU it does severely affect the performance of other proposed IFU projects such as TEIFU. Other photoresists are available with different transmission characteristics. The advantages of the NPL microlens arrays are: low cost, fast manufacturing time, and availability from a local company.

B.1.3 NPL microlens PSF measurement

The NPL microlens PSF was measured using Type-II illumination as this is how the lenses are tested during manufacture and allows direct comparison of results. Type-II illumination, however, produces large amounts of spherical aberration as illustrated in the ray trace diagram shown in figure 6.2. The longitudinal aberration is 0.24mm with the circle of least confusion, where the best focus occurs, 0.85mm from the lens surface. Type-II illumination produces approximately 5 waves of spherical aberration so the theoretical performance of the lens is far from diffraction limited.

The NPL microlens was tested using the same tests that were applied to the AOA microlenses. The aim of the tests is to compare the performance of the NPL lenses with the AOA lenses to determine the best lens for use. A comparison of the NPL microlens PSF with the AOA is shown in figure 6.13. It is clear from the PSF that the NPL lenses produce significantly more light in the wings of the PSF than the AOA lenses. The corresponding encircled energy plot is shown in figure 6.14. The EE performance of the NPL lenses is considerably worse than that of the AOA lenses.

The NPL microlens PSF measured with the COHU CCD and $\times 100$ magnification can be seen in figure B.1 and the images from which the PSF was measured in figure B.2. The measured Airy radius of $\sim 1.8\mu$m at the MCI focus is broader than the theoretical prediction of

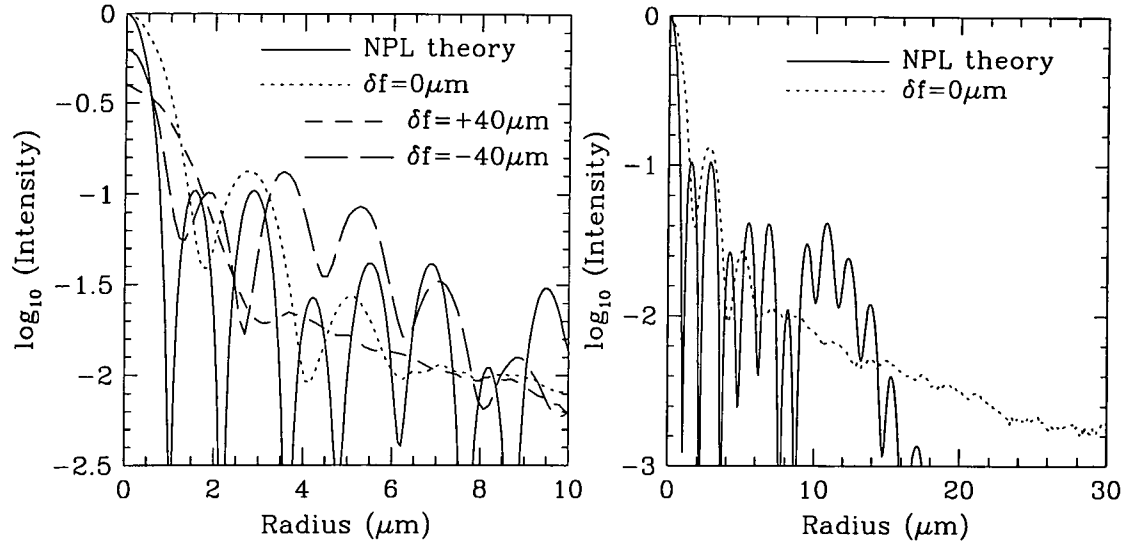

Figure B.1: Point spread function of NPL microlens test array taken with ×100 magnification. The labelled focus positions, δf, are measured relative to the MCI focus. The psf shows the radius of the Airy disk is $\sim 1.5\mu$m which is in agreement with the predicted value of 1.5μm. *May need to include diffraction limit in this plot.*

$\sim 1.0\mu$m. This suggests that aberrations in addition to S.A. are influencing the performance of the lens. The ring like structure observed in the PSF images, shown in figure B.2, inside focus ($\delta f = -40\mu$m) and the diffuse distribution of light seen outside focus ($\delta f = +40\mu$m) are consistent with the presence of S.A. An encircled energy plot from the ×100 PSF can be seen in figure 6.14. The EE plot shows that $\sim$ 50% of the energy is imaged outside the FOV of the ×100 image due to the aberrations of the lens.

Further PSF exposures were taken with the ×10 magnification objective to increase the FOV to cover the entire area of the lens. The image which was taken with a defocus of -200μm

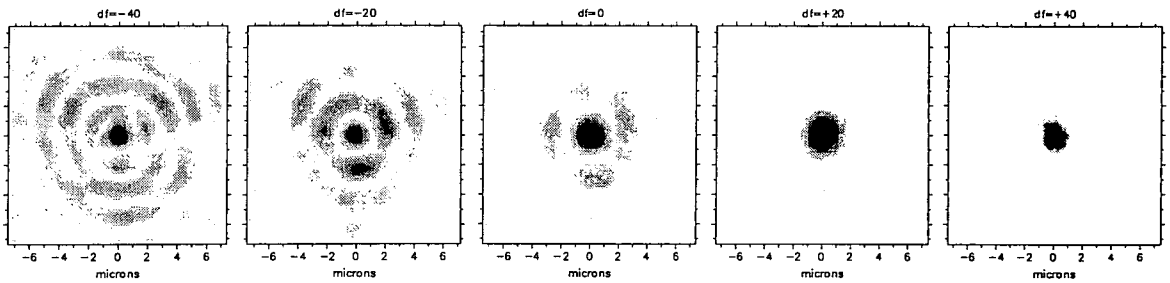

(a) δf=-40μm (b) δf=-20μm (c) δf=0μm (d) δf=+20μm (e) δf=+40μm

Figure B.2: NPL microlens through focus PSF images taken with ×100 magnification. Each image is 15 microns square. The central image was taken at the MCI focus.

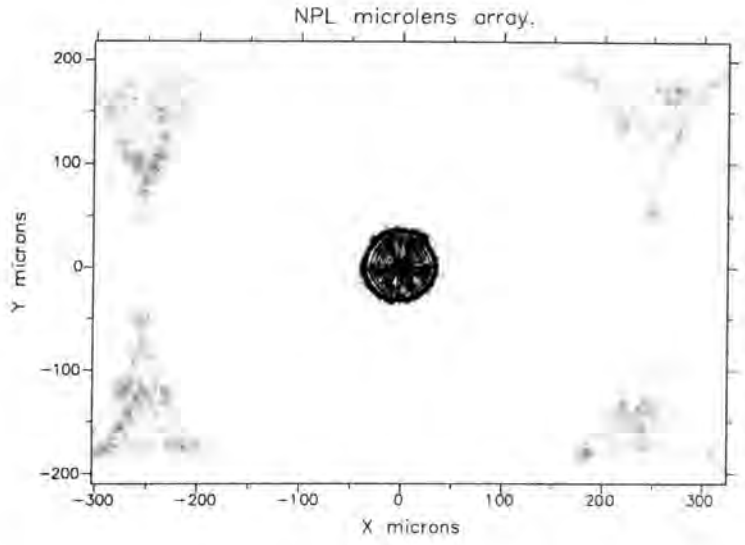

Figure B.3: Microphotograph of NPL microlens PSF taken at a defocus of -200μm. The diffuse light which fills the area between lenses can be seen. The loss in fill factor is 89%. The PSF shows a ring like structure.

from the MCI position can be seen in figure B.3. The triangular regions of diffuse light from the inter-lens gaps can be seen. The ring like structure seen in the PSF is thought to be due to regions of different focal length on the lens surface. Irregularities in the lens profile are caused because surface tension doesn't produce a perfect spherical shape, especially at the lens edge where the contact angle defines the radius of curvature. The PSF for the $\times 10$ images is plotted in figure B.4. Considerably more light is contained in the wings of the PSF than theoretically predicted. The scattered light is also a factor of ten higher than that measured with the AOA microlenses. The PSF rises in intensity at $r \sim 200\mu$m due to light in the inter-lens gaps.

The encircled energy performance is shown in figure B.5. The EE has been normalised to 100% at the lens edge by subtracting the contribution due to the inter-lens gaps. The EE performance at the MCI focus is only similar to the predicted performance up to an EE of $\sim 40\%$ at which point it becomes significantly worse. The EE performance can be improved by applying a defocus. The best EE performance, 80% EE within 26μm, being achieved at a defocus of -100μm. Images of the NPL microlens PSF with a defocus of -100μm can be seen in figure B.6.

The NPL microlenses have lower performance than the AOA microlenses tested. The NPL lenses produce more scattered light and have lower encircled energy performance. The NPL lenses are also restricted in the focal ratios that can be provided. Another disadvantage is that NPL lenses cannot be produced with 100% fill factor. It was therefore decided to adopt AOA microlenses for use with the IFU projects being built in Durham due to their better

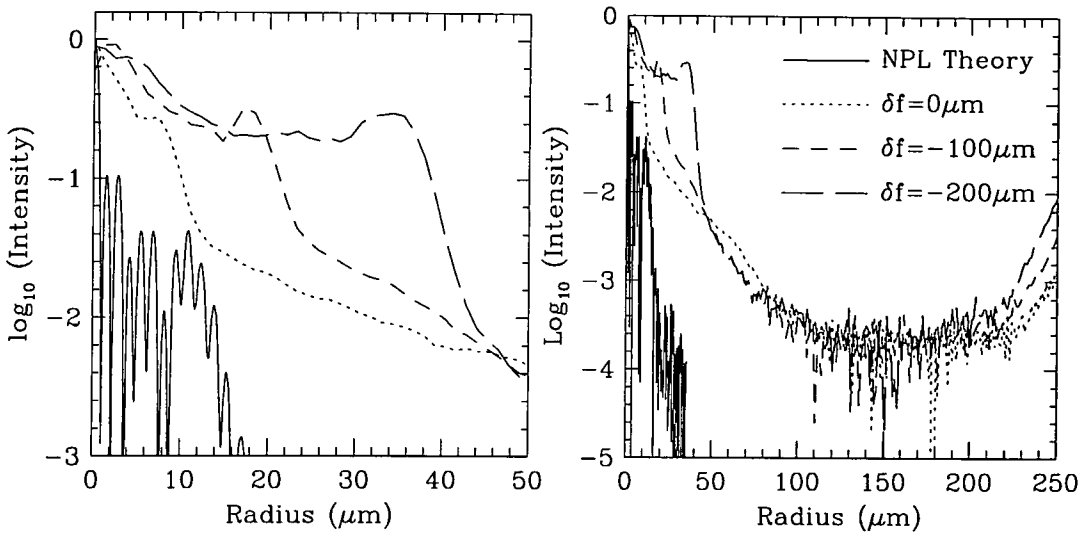

Figure B.4: Point spread function of the NPL microlens test array taken with ×10 magnification. The solid line shows the theoretical prediction at the MCI focus, the other lines show the measured psf for the labelled focus positions, δf, relative to the MCI focus.

performance and less manufacturing constraints. However, NPL lenses can be expected to be developed further to produce higher image quality. Therefore even though AOA lenses are currently the most suitable for use in IFS, NPL lenses, and lenses from other manufacturers should still be kept in mind for future developments.

B.2 SAURON microlens images

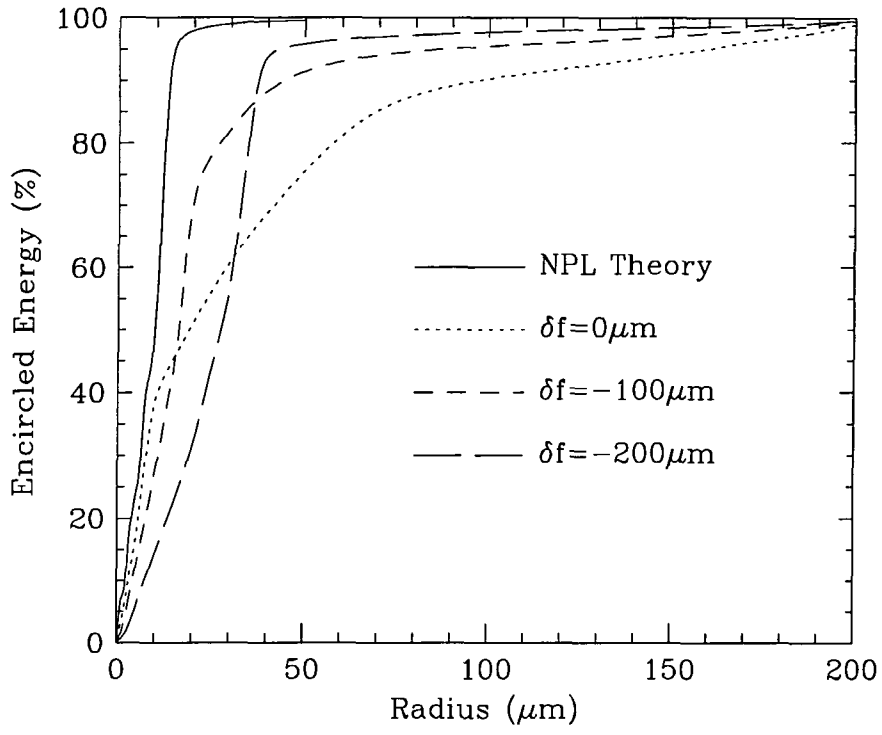

Figure B.5: Encircled energy plot for NPL microlens test array with ×10 magnification. The solid line shows the theoretical prediction at the MCI focus, the other lines show the measured encircled energy at the labelled focus positions, δf, relative to the MCI focus.

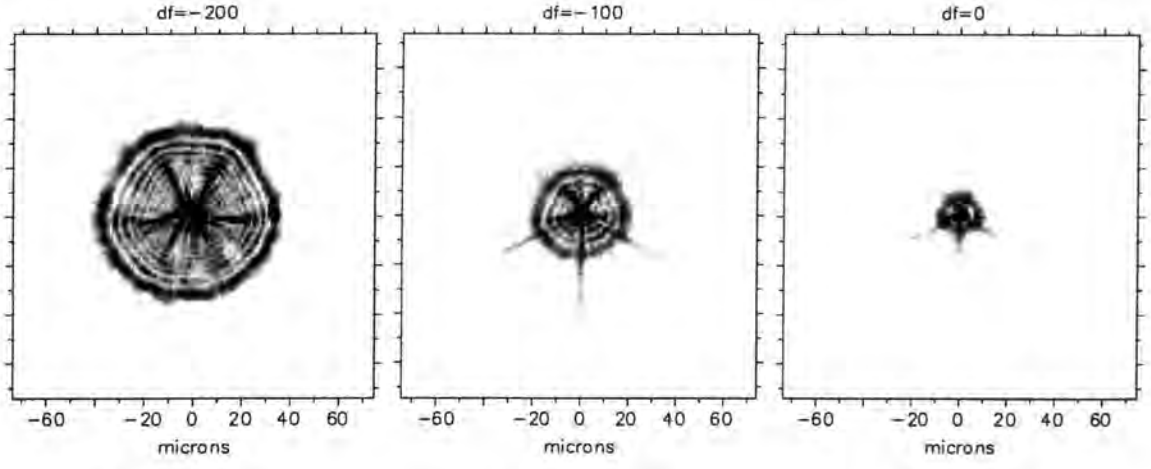

(a) δf=-200μm (b) δf=-100μm (c) δf=0μm

Figure B.6: NPL microlens PSF images taken with $\times$10 magnification. Each image is 150 microns square. The ring like structure in the images is thought to be caused by annular zones on the lens surface with slightly different focal lengths. The image with -100μm defocus has a high figure of merit for encircled enrgy performance but poor imaging capabilities.

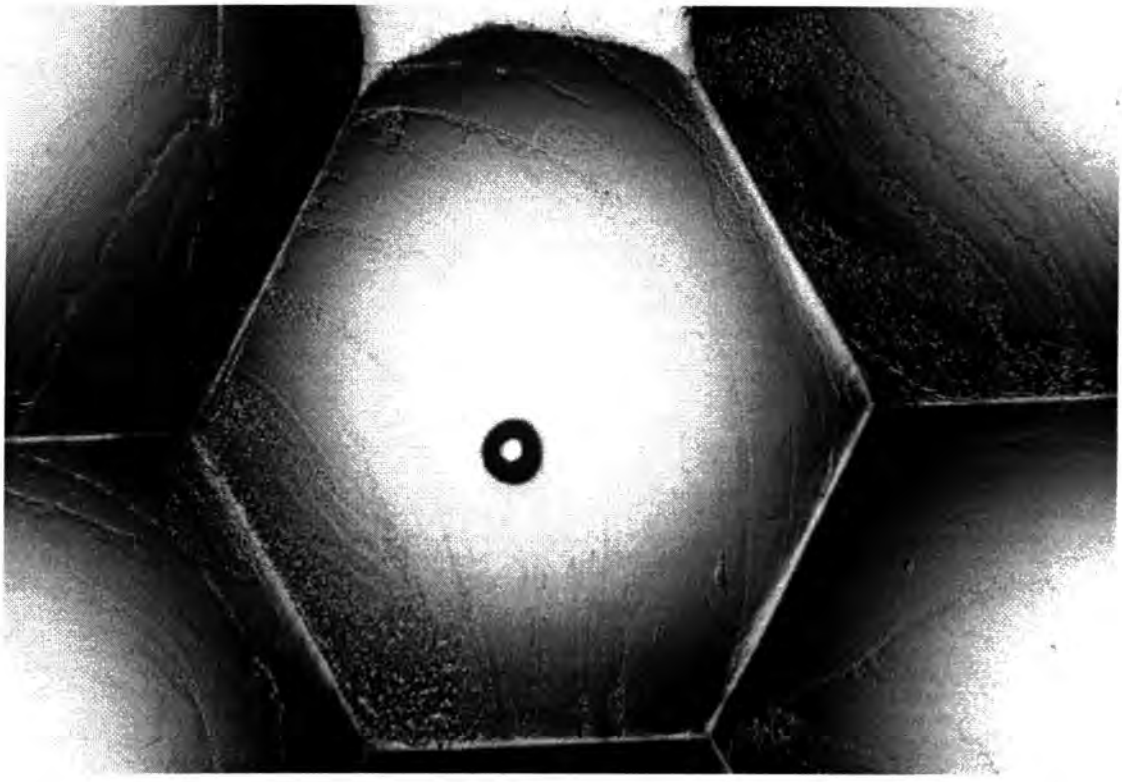

Figure B.7: Reproduction of a microphotograph of the SAURON microlens array surface taken with ×3 magnification and the 35mm camera attachment. The lens is 1.7mm across the faces. The circular feature seen in the centre is a bubble trapped in the microlens epoxy. A number of these were seen in the test sample. Bubbles seem to be a problem with thick layers of epoxy. This is an edge lens so the top edge is not well defined. Note the excellent fill factor achieved. There are considerable surface defects present on this lens.

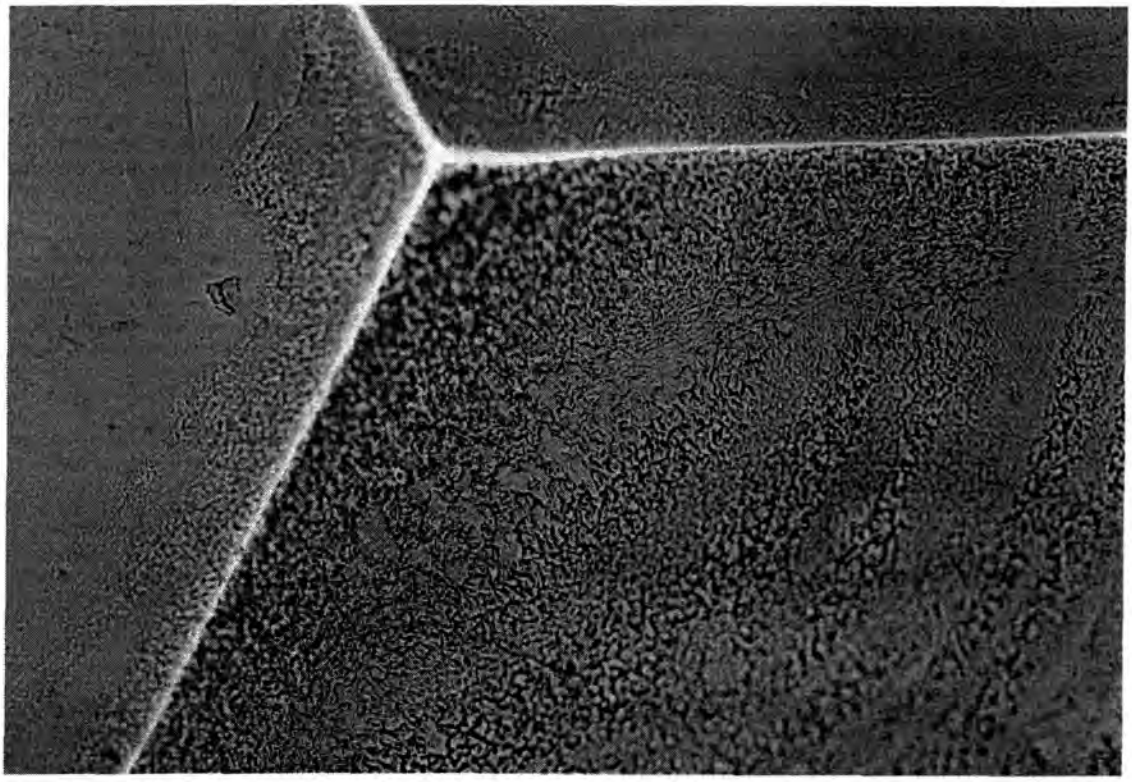

Figure B.8: Reproduction of a microphotograph of the SAURON microlens array surface taken with a microscope and a 35mm camera attachment. The severe marking (orange peel) on the surface of the lens is evident. This is thought to be the cause of the high scattered light and image quality obtained with this lens. The surface defects are worse in the corners than the centre of the lens.

Appendix C

SMIRFS-IFU construction appendix

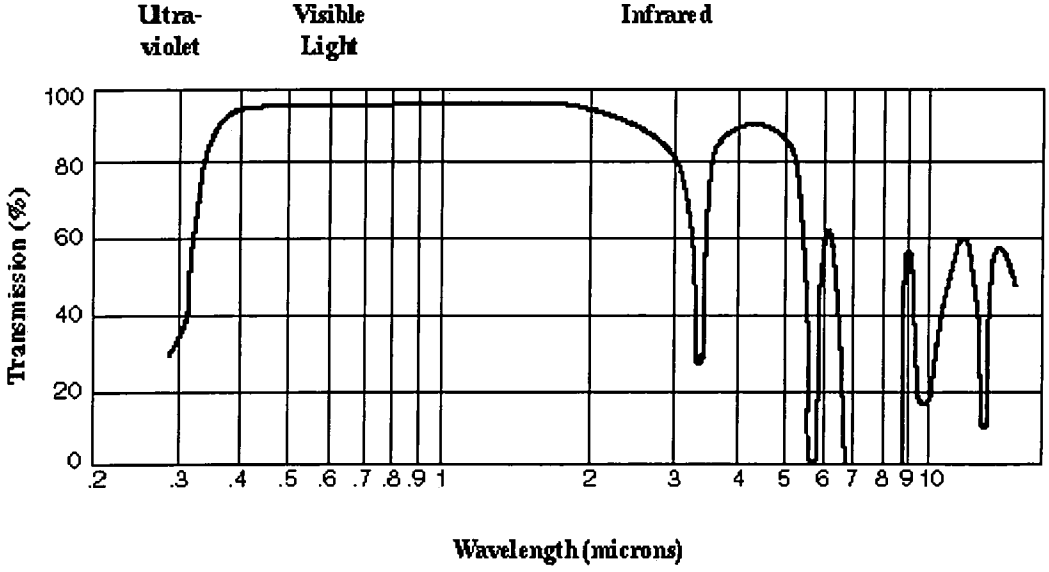

Figure C.1: The spectral transmission of Norland optical adhesive NOA 61 obtained from the manufacturers data sheet. This curve shows none of the spectral features seen in the spectrum of the test sample shown in figure 7.5. This implies that manufacturers data sheets cannot always be relied upon.

Block	L (μm)	R (μm)	W (mm)	U (mm)	Comments
19	79	58	-	-	
A*	187	704	-	-	Right lens over edge
B	77	37	-	-	
3	102	783	-	-	Right lens damaged
C	57	66	-	-	Epoxy over edge L and R
D	81	53	-	-	bubbles in lenses 9 and 11
11	50	71	-	-	
E	79	43	-	-	Slight damage R
F	83	813	-	-	L damaged, R edge obscured
G	88	37	4.723	4.848	lens 7 fuzzy
H	74	48	4.721	4.843	crack on lens 12
8*	70	51	4.724	4.845	severe damage to 25% of left lens
I	112	775	3.958#	4.845	lens at edge R
J	52	79	4.721	4.852	
Average	77.2 ± 18	54.3 ± 14.2			

Table C.1: L is the distance from the left edge of the substrate to the first lens, R is the distance from the last lens to the right edge of the substrate. Blocks A, 3, F and I the distance R is listed as from the fifth lens edge rather than the last lens either because the edge of the last lens id difficult to define or part of the last lens is missing over the edge of the substrate. W is the total length occupied by the 6 lenslets and U is the width of the substrate. The two blocks marked * were rejected. # indicates width of 5 lenses only. The microlenses are such that the first 5 lenses have the correct pitch of 793μm but the final lens, nearest the right hand edge, has a size of only $\sim$ 764μm. This accounts for the total dead space, given by L + R, being larger than the 80μm specified.

Appendix D

Summary of data reduction steps

The following is a list of the individual data reduction steps required to extract a clean, wavelength calibrated and distortion corrected spectrum from a SMIRFS-IFU integral field image. The software package used for each step is listed. This list is only intended as a guide to the data reduction process. The same results may also be achieved by using other data reduction packages not mentioned in this list. The order in which the steps are carried out may also be changed. Many of the steps are in the production of the detector flat-field from the dome-flat. Obviously this can be avoided if detector flat-fields can be produced with SMIRFS-IFU in the future. An example of a fully reduced science exposure can be seen in figure 9.4. It should also be noted that the data reduction sequence did not include the removal of the CGS4 spatial distortions as the wavelength region over which the data is useful is small enough that the effect of the distortions can be ignored.

Kappa: thresh Threshold sky exposures to remove a fraction of hot pixels and low pixels. Deviant pixels are set to the bad pixel value to produce a mask.

Kappa: isub Subtract thresholded sky exposures from object exposures to produce background subtracted images.

Masking Apply mask image to flat-field exposure.

Figaro: extract Extract average flat-field spectrum from masked flat-field exposure.

Kappa: gausmooth Smooth extracted flat-field spectrum with a gaussian convolution.

Figaro: isxdiv Divide flat-field exposure by smoothed flat-field spectrum.

Figaro: ystract Extract the spatial fibre to fibre throughput variation (a spatial cut) map within the appropriate wavelength range. The wavelength range has to be chosen carefully to avoid problems due to the curvature of the spectra on the chip.

Figaro: isydiv Divide the smoothed flat-field by the fibre to fibre throughput map to correct for the fibre to fibre throughput variations. This stage gives produces the detector flat-field exposure.

Figaro: idiv Detector flat-field correction, divide all images to be used in the subsequent data reduction by the detector flat.

Kappa: glitch. Deglitch all exposures to be used in subsequent data reduction steps to remove the pixels flagged as bad in the pixel mask produced earlier. The deglitch routine attempts to correct bad pixels by replacing the bad pixel with the local average calculated from its neighbours. This does cause some problems if there are a large number of bad pixels in one area, such as the extreme left edge of the chip, as seen in figure 9.1

Convert: ndf2iraf Conversion routine to convert STARLINK sdf format files to IRAF format files.

IRAF: imcombine. Combine sky subtracted images with cosmic ray rejection algorithm to produce final science image.

IRAF: ystract [1] The fibre to fibre variation map is extracted from the dome flat-field exposure within the appropriate wavelength limits.

IRAF: imshift The fibre to fibre throughput variation map has to be shifted by the appropriate amount so that the positions of the IFU elements in the science image to be flat-fielded and the flat-field map match exactly.

IRAF: isydiv The science image is divided by the shifted fibre flat-field map.

IRAF: identify This package is used to interactively identify features in the arc spectrum and calculate the dispersion solution. The arc line wavelengths are listed in the IRAF database linelists$argon.dat.

[1] Note this is the IRAF Figaro routine but is the same as the standard Figaro routine listed earlier.

IRAF: reidentify This package uses the output from identify to automatically reidentify the arc lines in the other detector rows and calculate the dispersion solution for each detector row.

IRAF: fitcoords This package uses the dispersion solution for each detector row calculated by reidentify to interactively fit a 2D surface to the dispersion solution at each detector row. This calibrates the effect of the image distortions of CGS4 in the wavelength direction, such as tilt of the slit image.

IRAF: transform This package uses the 2D surface generated by fitcoords to remove the distortions in the science image thus assuming there are no changes between the dispersion solution for the arc exposures and the science exposures, i.e. the spectrograph is stable. The package also wavelength calibrates the image in the appropriate format required by the user.

The last four data reduction steps (identify—transform) are used to apply the wavelength calibration. Note that this procedure can also be used to remove the image distortions introduced by the CGS4 optics, as described in section 8.5.5.

Bibliography

Allington-Smith, J. R. (1996). *Sampling in integral field spectroscopy.* Durham University, AIG, technical note.

Allington-Smith, J. R. (1997). A fibre multi-object spectrograph proposal for subaru. Private communication.

Allington-Smith, J. R. & Content, R. (1998). *PASP.* submitted.

Allington-Smith, J. R., Content, R. C., Haynes, R., & Lewis, I. J. (1997a). Integral field spectroscopy with the gemini multiobject spectrographs. In Ardeberg, A. L., editor, *Optical telescopes of today and tomorrow*, volume 2871.

Allington-Smith, J. R. *et al.* (1994). *PASP*, 106(703), 983–991.

Allington-Smith, J. R. *et al.* (1996). The GEMINI Multiple Object Spectrographs. In *Wide field spectroscopy.* Kluwer.

Allington-Smith, J. R., Haynes, R., Lee, D., & Sharples, R. M. (1997b). SMIRFS: report on second commissioning run. available at: http://star-www.dur.ac.uk/~jra/smirfs_rep_dec96.ps.gz.

Allington-Smith, J. R. & Lee, D. (1995). Dispersion elements. GMOS PDR documentation (section 6.3).

Arribas, S. *et al.* (1998). INTEGRAL: a matrix optical fibre system for WYFFOS. In D'Odorico, S., editor, *Optical Astronomical Instrumentation*, volume 3355.

Arribas, S., Mediavilla, E., & Rasilla, J. L. (1991). *Astrophysical Journal*, 369, 260–270.

Avila, G. & D'Odorico, S. (1993). Fibre optics in astronomical instruments at ESO. In Gray, P. M., editor, *Fibre optics in Astronomy II*, pages 90–105.

Bacon, R. (1994). The integral field spectrograph TIGER: results and prospects. In Comte, G. & Marcelin, M., editors, *Tridimensional optical spectroscopic methods in astrophysics*, volume 71 of *A. S. P. Conf. Ser.*, pages 239–249. A.S.P. IAU colloquium 149.

Bacon, R. (1996). Private communication.

Bacon, R. *et al.* (1995). *Astronomy & Astrophysics supplement series*, 113, 347–357.

Barden, S. C., Arns, J. A., & Colburn, W. S. (1998). Volume-phase holographic gratings and their potential for astronomical applications. In D'Odorico, S., editor, *Optical Astronomical Instrumentation*, volume 3355.

Barden, S. C., Elston, R., Amandroff, T., & Pryor, C. P. (1993). Observational performance of fibre optics - high precision sky subtraction and radial velocities. In Gray, P. M., editor, *Fibre optics in Astronomy II*, volume 37 of *ASP conference series*, pages 223–234.

Baudrand, J. (1997). Personal communication.

Bland, J. & Tully, R. B. (1989). *Astronomical Journal*, 98(2), 723–735.

Bland-Hawthorn, J. (1994). Tridimensional Spectroscopic Techniques: Conference Summary. In Comte, G. & Marcelin, M., editors, *Tridimensional optical spectroscopic methods in astrophysics*, volume 71 of *A. S. P. Conf. Ser.*, pages 369–381. A.S.P. IAU colloquium 149.

Blietz, M. *et al.* (1994). *ApJ*, 421, 92–100.

Bohlender, D. A. (1994). Users' Manual for the CFHT Fourier Transform Spectrometer.

Born, M. & Wolf, E. (1980). *Principles of Optics.* Pergamon Press, sixth edition.

Bottema, M. (1981). *Applied Optics*, 20(4), 528–530.

Buscher, D. F., Doel, A. P., Haniff, C. A., & Wilson, R. W. (1995). Visible-wavelength diffraction-limited imaging using low-order adaptive optics. In Tyson, R. K. & Fugate, R. Q., editors, *Adaptive Optical Systems and Applications*, volume 2534, pages 53–61. SPIE.

Casse, M. & Vieira, F. (1997). Comparison of the scrambling properties of bare optical fibres with microlens coupled fibres. In Ardeberg, A. L., editor, *Optical telescopes of today and tomorrow*, volume 2871.

CGS4 (1997). *CGS4 world wide web pages.* http://www.jach.hawaii.edu/UKIRT.new/instruments/cgs4/handbook.html.

Clapham, P. B. & Raine, K. W. (1969). *Enhancement of internal reflection from metal mirrors.* National Physical Laboratory. Report Op. Met. 6.

Comte, G. & Marcelin, M., editors (1994). *Tridimensional optical spectroscopic methods in astrophysics*, volume 71 of *A. S. P. Conf. Ser.* A.S.P. IAU colloquium 149.

Content, R. (1997a). Private communication.

Content, R. (1997b). New design for integral field spectroscopy with 8-m telescopes. In Ardeberg, A. L., editor, *Optical telescopes of today and tomorrow*, volume 2871, pages 1295–1305.

Content, R. (1998a). Advanced image slicers for integral field spectroscopy with ukirt and gemini. In Fowler, A. M., editor, *Infrared Astronomical Instrumentation*, volume 3354.

Content, R. (1998b). Image slicer for integral field spectroscopy with ngst. In *Infrared Astronomical Instrumentation*, volume 3356.

Cowley, D. J. *et al.* (1997). DEIMOS: a wide field faint object spectrograph. In Ardeberg, A. L., editor, *Optical telescopes of today and tomorrow*, volume 2871, pages 1107–1115.

Cuby, J. G., Dallier, R., Baudrand, J., & Czarny, J. (1993). Presentation of ISIS IR: A fibre-fed infrared spectrograph. Poster paper at IVth Canary islands winter school.

Daly, D., Stevens, R. F., Hutley, M. C., & Davies, N. (1990). *Journal of measurement science and technology*, 1, 759–766.

Davies, R. L. *et al.* (1997). GMOS: the GEMINI Multiple Object Spectrographs. In Ardeberg, A. L., editor, *Optical telescopes of today and tomorrow*, volume 2871, pages 1099–1106.

Dekker, H. (1987). An immersion grating for an astronomical spectrograph. In Robinson, L. B., editor, *Instrumentation for Ground Based Optical Astronomy*, pages 183–188. Springer-Verlag.

Dekker, H. (1992). Immersion gratings. In Tull, R., editor, *SST High Resolution Spectrograph E-mail Conference Communication 33.*

Dekker, H., Delabre, B., & D'Odorico, S. (1986). ESO's multimode instrument for the Nasmyth focus of the 3.5m new technology telescope. In Crawford, D. L., editor, *Instrumentation in astronomy VI*, volume 627, pages 339–348.

Dekker, H. & D'Odorico, S. (1992). *The Messenger*, 70, 13–17.

Dekker, H., D'Odorico, S., & Arsenault, R. (1988). *Astronomy & Astrophysics*, 189, 353–360.

Dekker, H., D'Odorico, S., & Fontana, A. (1994). *The Messenger*, 78, 16–20.

Diego, F. (1993). *Applied Optics*, 32(31), 6284–6287.

Diego, F. (1994). *Advice on immersion oils.* Private communication.

Dubath, P. & Meylan, G. (1994). *Astronomy and Astrophysics*, 290, 104–118.

Epps, H. W. & Vogt, S. S. (1993). *Applied Optics*, 32(31), 6270–6279.

Ferguson, J. P. (1996). *Theoretical grating efficiency prediction obtained with PC Grate software.* Private communication.

Fevre, O. L. *et al.* (1994). *Astronomy & Astrophysics*, 282, 325–340.

Fevre, O. L. *et al.* (1998). VIRMOS: Visible and Infrared Multi-Object Spectrographs for the VLT. In D'Odorico, S., editor, *Optical Astronomical Instrumentation*, volume 3355.

Fowles, G. R. (1989). *Introduction to modern optics.* Dover, second edition.

Garcia, A., Rasilla, J. L., Arribas, S., & Mediavilla, E. (1994). Bidimensional spectroscopy with optical fibres at the WHT and NOT. In Crawford, D. L. & Craine, E. R., editors, *Instrumentation in Astronomy VIII*, volume 2198, pages 75–86. SPIE.

Genzel, R. *et al.* (1995). *ApJ*, 444, 129–145.

Georgelin, Y. P. & Comte, G. (1994). The PYTHEAS concept and applications. In Comte, G. & Marcelin, M., editors, *Tridimensional optical spectroscopic methods in astrophysics*, volume 71 of *A. S. P. Conf. Ser.*, pages 300–307. A.S.P. IAU colloquium 149.

Gillet, F. *et al.* (1997). RPT-PS-G0075: Future Gemini Instrumentation.

GMOS (1995). GMOS PDR documentation.

GMOS OCD (1995). GMOS operational concepts document.

Graf, U. U., Jaffe, D. T., Kim, E. J., Lacy, J. H., Ling, H., Moore, J. T., & Rebeiz, G. (1994). *Applied Optics*, 33(1), p96–102.

Hargreaves, J. C., Gilmore, G., Irwin, M. J., & Carter, D. (1994). *Mon. Not. R. Astron. Soc.*, 269, 957–974.

Haynes, R. (1995). *Infrared Fibres in Astronomical Instrumentation.* PhD thesis, University of Durham.

Haynes, R. (1996). *Scrambling and Focal Ratio Degradation in* $50\mu m$ *core fibres.* Durham University, AIG, technical note.

Haynes, R., Allington-Smith, J., Content, R., & Lee, D. (1998a). Smirfs-ii multi-object and integral field unit spectroscopy at the ukirt. In *Fibre optics in Astronomy III.*

Haynes, R., Content, R., Allington-Smith, J. R., & Lee, D. (1998b). Smirfs-ii: multiobject and integral field near-ir spectroscopy. In Fowler, A. M., editor, *Infrared Astronomical Instrumentation*, volume 3354.

Haynes, R., Content, R., Allington-Smith, J. R., & Lee, D. (1998c). Teifu: a thousand element integral field unit for the wht. In *Fibre optics in Astronomy III.*

Haynes, R., Content, R., Allington-Smith, J. R., & Lee, D. (1998d). Teifu: a thousand element integral field unit for the wht. In D'Odorico, S., editor, *Optical Astronomical Instrumentation*, volume 3355.

Herbst, T. M. (1998). A micro-pupil based near-infrared imaging spectrograph. In Fowler, A. M., editor, *Infrared Astronomical Instrumentation*, volume 3354. SPIE.

Hilton, J. W. & Hilton, W. A. (1973). *American Journal of Physics*, 41, 702–705.

Hoose, J., Loewen, E., Wiley, R., Blasiak, T., Zheleznyak, S., & Sroda, T. (1995). *Photonics Spectra*, pages 118–120. December issue.

Hulthen, E. & Neuhaus, H. (1954). *Nature*, 173, p442–443. Letters to the editor.

Hunter, W. R. (1985a). Measurement of optical constants in the vacuum ultraviolet spectral region. In Palik, E. D., editor, *Handbook of Optical Constants of Solids*. Academic Press.

Hunter, W. R. (1985b). Optical constants of aluminium. In Palik, E. D., editor, *Handbook of Optical Constants of Solids*. Academic Press.

Hutley, M. C. (1982). *Diffraction Gratings*, volume 6 of *Techniques of Physics*. Academic Press.

Hutley, M. C. (1991). *Microlens Arrays*, volume 30 of *IOP short meetings series*. Institute of Physcics.

Hutley, M. C., Daly, D., & Stevens, R. F. (1991). The testing of microlens arrays. In Hutley, M. C., editor, *Microlens arrays*, pages 67–81.

James & Sternberg (1969). *The Design of Optical Spectrometers*. Chapman and Hall.

Jenkins, F. A. & White, H. E. (1976). *Fundamentals of optics*. McGraw-Hill, fourth edition.

Johnston, H., Gray, P., Stathakis, R., & Robinson, R. (1986). *Efficiencies of the AAO Diffraction Gratings*, AAO UM 19 edition.

Kaufl, H. U. (1994). *The Messenger*, 78, p4–7.

Keel, W. C. (1996). *ApJS*, 106.

Knop *et al.* (1996). *AJ*, 112(1), 81–90.

Lee, D., Haynes, R., Content, R., & Allington-Smith, J. R. (1998). Characterisation of microlens arrays for use in integral field spectroscopy. In D'Odorico, S., editor, *Optical Astronomical Instrumentation*, volume 3355.

Levin, K. H., Tran, D. C., Kindler, E., Glenar, D., & Joyce, R. (1993). Infrared fibre arrays for low background infrared astronomy. In Gray, P. M., editor, *Fibre optics in Astronomy II*, volume 37 of *ASP conference series*, pages 295–309.

Lewis, I. (1996). *Investigations of tube-array fibre holders*. Durham University, AIG, technical note.

Lewis, I. J. (1993). *Fibres in Astronomy*. PhD thesis, University of Durham.

Loewen, E. G., Neviere, M., & Maystre, D. (1977). *Applied Optics*, 16(10), 2711–2721.

Longhurst, R. S. (1973). *Geometrical and Physical Optics*. Longman Scientific and Technical, third edition.

Mahajan, V. N. (1991). *Aberration Theory Made Simple*, volume TT6 of *Tutorial texts in optical engineering*. SPIE Press.

Maillard, J. P. (1994). 3-D spectroscopy with a Fourier Transform Spectrometer. In Comte, G. & Marcelin, M., editors, *Tridimensional optical spectroscopic methods in astrophysics*, volume 71 of *A. S. P. Conf. Ser.*, pages 316–327. A.S.P. IAU colloquium 149.

Malacara, D. (1978). *Optical shop testing*. Pure and applied optics. Wiley-Interscience.

Mauder, W. *et al.* (1994). *ApJ*, 285, 44–50.

Maystre, D., Neviere, M., & Petit, R. (1980). Experimental verifications and applications of the theory. In Petit, R., editor, *Electromagnetic Theory of Gratings*. Springer-Verlag.

Mersereau, K., Crisci, R. J., Nijander, C. R., Townsend, W. P., Daly, D., & Hutley, M. C. (1993). Testing and measurement of microlenses. In *Miniature and micro-optics and micromechanics*, volume 1992, pages 210–215.

Monnet, G. (1994). 3D spectroscopy with large telescopes: past, present and prospects. In Comte, G. & Marcelin, M., editors, *Tridimensional optical spectroscopic methods in astrophysics*, volume 71 of *A. S. P. Conf. Ser.*, pages p12–17. A.S.P. IAU colloquium 149.

Nelson, J. E. & Mast, T. S. (1986). Optical design and Instrumentation of the Keck Observatory. In Barr, L. D., editor, *Advanced technology optical telescopes III*, volume 628, pages p207–212. SPIE.

Nussbaum, P., Volkel, R., Herzing, H. P., Eisner, M., & Haselbeck, S. (1997). *Pure and Applied Optics*, 6(6), 617–636.

Ohtani, H. *et al.* (1994). Spectrograph with multimode of area spectroscopy for faint extended objects. In Crawford, D. L. & Craine, E. R., editors, *Instrumentation in Astronomy VIII*, volume 2198, pages 229–238. SPIE.

Oke, J. B. *et al.* (1995). *Publications of the Astronomical Society of the Pacific*, 107(710), 375–385.

Parry, I. R., Kenworthy, M. K., & Taylor, K. (1997). SPIRAL Phase A: a prototype integral field spectrograph for the AAT. In Ardeberg, A. L., editor, *Optical telescopes of today and tomorrow*, volume 2871, pages 1325–1331.

Pasquini, L., Storm, J., & Dekker, H. (1994). *The Messenger*, 78, p5–6.

Pedrotti, F. L. & Pedrotti, L. S. (1993). *Introduction to Optics*. Prentice Hall, second edition.

Peletier, R. (1997). *IRAF linemap IFU data reduction software*. Personal communication.

Piche, F. *et al.* (1997). COHSI: the Cambridge OH Suppression instrument. In Ardeberg, A. L., editor, *Optical telescopes of today and tomorrow*, volume 2871, page 1332.

Pilachowski, C., Dekker, H., Hinkle, K., Tull, R., Vogt, S., Walker, D. D., Diego, F., & Angel, R. (1995). *PASP*, 107, 983–989.

Puxley, P. & Boroson, T. (1997). Observing with a 21st century ground-based telescope - or how to do unique science with the Gemini telescopes. In Ardeberg, A. L., editor, *Optical telescopes of today and tomorrow*, volume 2871, pages 744–754.

Radley, A. S., Szumski, R., Diego, F., & Walker, D. D. (1994). *Design Study For An Unfolded Cryogenic Camera and Immersed Echelle For HROS, Final Report.* OSL technical report.

Ramsay-Howat, S. *et al.* (1998). UIST: An Imaging Spectrometer for the UKIRT Infrared telescope. In Fowler, A. M., editor, *Infrared Astronomical Instrumentation*, volume 3354.

Ramsay-Howat, S. K. (1994). Image quality with array spectrometers. In Crawford, D. L. & Craine, E. R., editors, *Instrumentation in Astronomy VIII*, volume 2198, page 467.

Rasilla, J. L., Marin, A. G., Arribas, S., Gellatly, D., & Carter, D. (1993). Multi-object spectroscopy with the isis spectrograph at the william herschel telescope. In Gray, P. M., editor, *Fibre optics in Astronomy II*, volume 37 of *ASP conference series*, pages 203–208.

Robertson, D. & Mountain, M. (1997). Gemini instrumentation. In Ardeberg, A. L., editor, *Optical telescopes of today and tomorrow*, volume 2198, pages 143–152.

Ruther, P., Gerlach, B., Gottert, J., Ilie, M., Mohr, J., Muller, A., & Obmann, C. (1997). *Pure and Applied Optics*, 6(6), 643–653.

Ryan, S. G. & Fish, A. C. (1995). *The UCL coude echelle spectrograph*, AAO UM 25 edition.

Salmon, D. (1996). *Report on Sol-Gel coating development at D.A.O.* Dominion Astrophysical Observatory. Private communication.

Schectman, S. A. (1993). Fibre-optic spectroscopy at the las campanas 2.5m telescope. In Gray, P. M., editor, *Fibre optics in Astronomy II*, pages 26–35.

Schroeder, D. J. & Hilliard, R. L. (1980). *Applied Optics*, 19(16), 2833–2841.

Seifert, W. *et al.* (1997). FORS - a workhorse instrument for the ESO VLT. In Ardeberg, A. L., editor, *Optical telescopes of today and tomorrow*, volume 2198, pages 213–218.

Shiles, E. (1980). *Physical Review B*, 22, 1612.

Simmons, D. A. *et al.* (1997). CFHT's imaging fourier transform spectrometer. In Ardeberg, A. L., editor, *Optical telescopes of today and tomorrow*, volume 2198, pages 185–193.

Simmons, J. H. *et al.* (1994). *Journal of non-crystalline solids*, 178, 166–175.

Simpson, C. *et al.* (1996). *MNRAS*, 283, 777–797.

Suntzeff, N. B. (1995). *PASP*, 107, p990–993.

Szumski, R. (1995). *MNRAS*. submitted.

Taylor, K. & Atherton, P. D. (1980). *MNRAS*, 191.

Taylor, K. *et al.* (1997). The Anglo-Australian Telescope's 2dF Facility. In Ardeberg, A. L., editor, *Optical telescopes of today and tomorrow*, volume 2871, pages 145–149.

Tecza, M. (1997). Personal communication regarding the sinfoni instrument.

Thomas, I. M. (1992). *Applied Optics*, 31(28), 6145–6149.

Vanderriest, C. (1980). *PASP*, 92, 858–862.

Vanderriest, C., Bacon, R., Georgelin, Y., Lecoarer, E., & Monnet, G. (1994). Astronomical uses of Integral Field Spectrography: present applications at CFHT and future developments. In Crawford, D. L. & Craine, E. R., editors, *Instrumentation in Astronomy VIII*, volume 2198, pages 1376–1384.

Verrill, J. F. (1978). *Optica Acta*, 25(7), 531–547.

Walker, D. D. *et al.* (1994). Hros. In Crawford, D. L. & Craine, E. R., editors, *Instrumentation in Astronomy VIII*, volume 2198, page p1083. SPIE.

Watson, F. G. & Terry, P. (1995). Fibre characterization at fast focal ratios. In Barden, S. C., editor, *Fibre Optics in Astronomical Applications*, volume 2476. SPIE.

Weast, R. C. (1978). *Handbook of Chemistry and Physics*. CRC press, 58 edition.

Weitzel, L. *et al.* (1996). *Astronomy & Astrophysics Supplement Series*, 119, 531–546.

Wiedemann, G. (1994). Very large telescope instrumentation - infrared immersion gratings. In *Scientific and Engineering Frontiers for 8-10 m Telescopes*. Papers submitted to an international conference held in Tokyo.

Wiedemann, G. & Jennings, D. E. (1993). *Applied Optics*, 32(7), 1176–1178.

Worswick, S. P. *et al.* (1995). Integration and testing of the WYFFOS fibre-fed spectrograph for the William Herschel Telescope. In Barden, S. C., editor, *Fiber Optics in Astronomical Applications*, volume 2476. SPIE.

Wright, G. S. (1993). The CGS4 experience two years later. In Fowler, A. M., editor, *Infrared Detectors and Instrumentation*, volume 1946, page 547.

Wynne, C. G. (1989). *Optics Communications*, 73(6), pp419–421.

Wynne, C. G. (1990a). *Optics Communications*, 75(1), pp1–3.

Wynne, C. G. (1990b). *Optics Communications*, 77(5), pp355–359.

Wynne, C. G. (1991). *Monthly Notices Royal Astronomical Society*, 250, pp796–801.

Wynne, C. G. (1992). *MNRAS*, 254, pp7–10. Short Communication.

Yoder, P. R. (1995). *Mounting lenses in optical instruments*, volume TT21 of *Tutorial texts in optical engineering*. SPIE Press.

Yoldas, B. E. & Partlow, D. P. (1984). *Applied Optics*, 23, 1418–1424.

Zombeck, M. V. (1989). *Handbook of Space Astronomy and Astrophysics*. Cambridge.